Numerical Evaluation (FEA) of End Stop Impact Forces for a Crane Fitted with Hydraulic Buffers

IFEOLU MOBOLAJI IDOWU

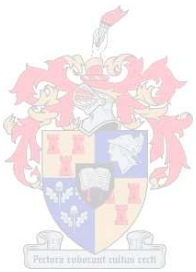

Thesis presented in partial fulfilment of the requirement for the degree of Masters in Civil Engineering at the University of Stellenbosch.

Supervisor: **Dr T.N Haas**

December 2010

Declaration

By submitting this thesis electronically, I declare that the entire of the work contained therein is my own original work and that I have not previously in its entirety or in part submitted it for obtaining any qualification.

December 2010

Signature: _____

Synopsis

Numerical Evaluation (FEA) of End Stop Impact Forces for a Crane Fitted with Hydraulic Buffers.

End stop impact forces are horizontal longitudinal forces imposed by the crane on the end stops. Both the previous South African loading code SABS 0160:1989 and the current South African loading code SANS 10160 , classify end stop impact force as an accidental load case , hence they are not expected to occur within the expected lifetime when the guide lines for crane operation are strictly adhered to.

In the estimation of end stop impact force, the previous South African loading code SABS 0160:1989 gives two guidelines for estimating the end stop impact force. The first guideline is simplistic in its approach and it's based on the assumption that the crane and its supporting structure act as rigid bodies; hence calculation is based on rigid body mechanics. Literature reviewed reveals that this is not correct. The second guideline is more explicit in its approach as it takes into account the crane speed, resilience of the buffers and resilience of the end stops.
The current South African loading code, SANS 10160 gives a better representation of the dynamics of the crane movement. However, the dynamic factor recommended for the estimation of end stop impact force is empirical in nature and thus lacks adequate scientific backing.

One of the purposes of this research was to investigate the influence of the stiffness of the crane bridge on the end stop impact force. This was achieved by conducting a series of FEA simulations on the double bridge EOHTC fitted with elastomeric buffers. For this set of simulations, the effect of each influencing parameter on the end stop impact force was investigated, and the maximum end stop impact force was obtained using a constraint optimization technique. From the results obtained, comparison was then made with the existing maximum end stop impact force for a single bridge EOHTC fitted with elastomeric buffers.

Another purpose of this research was to investigate the end stop impact force for an electric overhead travelling cranes (EOHTC) fitted with hydraulic buffers taking into account the dynamics involved in the movement of the EOHTC. This was achieved by a series of experimental and numerical investigation. The numerical investigation was conducted using an existing numerical model of an EOHTC which captures the crane and its supporting structure as a coupled system.

Finite element analysis (FEA) impact force histories obtained were calibrated to the base experimental impact force histories. Thereafter, a series of FEA simulations were conducted by

changing the parameters which have a substantial effect on the end stop impact forces. This yielded various maximum impact peaks for various parameters. The maximum impact force was then mathematical obtained from the FEA impact force histories for a given level of reliability using a constraint optimization technique. Also, codified end stop impact forces were calculated for the SABS 0160:1989 and SANS 10160-6:2010. From the results obtained, comparison was made between the codified end stop impact force and the maximum impact force obtained from the constraint optimization technique.

Opsoming

Ent buffer impak kragte is horisontale kragte wat deur die kraan op die entbuffers aangewend word. Beide die Suid Afrikaanse las kode SABS 0160:1989 en die voorgestelde Suid Afrikaanse las kode SANS 10160, klasifisseer die entbuffer impak kragte as ‘n ongeluks las geval, dus word die kragte nie verwag tydens die verwagte leeftyd van die kraan wanneer die riglyne van die kraan prosedures streng gevolg word nie.

Volgens die Suid-Afrikaanse las kode SABS 0160:1989 word daar twee riglyne voorgestel om die entbuffer kragte te bepaal. Die eerste riglyn is ‘n eenvoudige riglyn en word gebaseer op die aaname dat die kraan en die ondersteunende struktuur as ‘n starre ligame reageer en dus word die kragte bereken deur star ligaam meganika, alhoewel, uit die literatuur word dit bewys as inkorrek. Die tweede riglyn is ‘n meer implisiete benadering aangesien dit die kraan snelheid, elastisiteit van die buffers sowel as die elastisiteit van die end stoppe in ag neem.

SANS 10160-6:2019 gee ‘n beter benadering van die dinamiese beweging van die kraan. Die voorgestelde dinamiese faktor waarmee die ent_buffer_kragte bereken word, is empiries van natuur .

Een van die doelstellings vir die navorsings projek was om te bepaal wat die invloed van die kraan brug se styfheid op die entbuffer kragte is. ‘n Aantal Eindige Element Analise (FEA) simulasies is uitgevoer op ‘n dubbel brug elektriese aangedrewe oorhoofse kraan met elastomeriese buffers. Van die stel FEA simulasies kan die invloed van elke parameter op die entbuffer impak_kragte bepaal word. Die maksimum entbuffer impak_kragte is bepaal met behulp van ‘n beperking optimiserings tegniek. Vanaf hierdie resultate is ‘n vergelyking gemaak met die bestaande maksimum ent_buffer impak_kragte vir ‘n enkel brug elektriese oorhoofse aangdrewe kraan met elastomeriese buffers.

‘n Tweede doel rede vir die navorsing was om te bepaal wat die ent buffer impak_kragte op ‘n elektriese aangedrewe oorhoofse kraan met hidrouliese buffers is. Dit is bepaal deur ‘n aantal eksperimentele en numeriese toetse uit te voer. Die numeriese toetse is uitgevoer deur gebruik te maak van ‘n huidige numeriese model van ‘n elektriese aangedrewe oorhoofse kraan wat die kraan en die ondersteunende struktuur as ‘n.

Die Eindige Element Analise impak_kragte is gekalibreer teen die eksperimenteel bepaalde impak- kragte. Daarna is ‘n reeks Eindige Element Analise simulasies uitgevoer en sodoende die parameters te verander wat die mees beduidende invloed op die end stop impak_kragte het. Dit het verskeie impak_krag pieke vir verskillende parameters meegebring. Die maksimum impak

kragte is bepaal van die impak kragte van die Eindige Element Analise vir ‘n gegewe vlak van betroubaarheid deur gebruik te maak van die beperking optimiserings tegniek. Daarmee saam is die gekodifiseerde ent buffer impak kragte bereken volgen SABS 0160:1989 en die SANS 10160-6:2010. Vanaf hierdie resultate is ‘n vergelyking gemaak tussen die gekodifiseerde entbuffer impak_kragte en die maksimum impak_kragte wat bepaal is deur die (beperking optimiserings tegniek).

Acknowledgements

My first appreciation goes to God Almighty, without whom I can do absolutely nothing, thank you Father.

This work came to be by the help and support of so many people much more than I can document. However, the contribution of the following people can not go unmentioned.

To my parent:
Thank you for always going all the way to give me the best in life. I'm extremely blessed to be your daughter.

To my supervisor: Dr T.N Haas.
Thank you for your guidance through this work. I'm particularly grateful for your patience, readiness and availability to help solve problems.

To Prof Dunaiski:
Thank you for giving me the opportunity to have a funded research.

To my sibling: Dayo, Anu, Dimimu, Lara, Emma
Thank you guys for being so supportive. Your constant calls, chats and emails kept me going when life looked unbearable.

To the staff at the structures' laboratory: Charlton, Adrian, Godwin and Deon. Thank you all for helping me with my experimental tests.

To all the staff and students in the structural engineering division, thanks for your support

Finally to all my friends and loved ones, thank you all for being there.

1st Corinthians' 1:28

Table of Contents

List of Tables

List of Figures

CHAPTER 1: INTRODUCTION

1.1 Review of the Codes of Practice

There are various structural design codes employed by civil engineering professionals for the design of infrastructural projects. The Canadians use CAN/CSA-S-16, EURO CODE is the recognised code of practice in Europe, while the SABS/SANS codes are employed in South Africa. These design codes are based on different design philosophies, thus yielding varying responses.

In the analysis and design of structures, structural design codes are employed to obtain the most adverse loading condition(s) the structure would be subjected to through its design life, for a specified level of reliability. Therefore, the loading and design codes must be harmonised.

In South Africa, the majority of infrastructure is built using steel and concrete. The design codes for concrete and steel are based on the British and Canadian codes, respectively. However, both codes refer to the South African loading code for limit state design. This makes the codes of practice lack the desired harmonisation. As a result, the previous South African loading code SABS 0160:1989 was revised and published as SANS 10160 in 2010 such that the loading codes and the design codes are harmonised.

Bearing in mind the necessity of achieving a level of international harmonization without loosing functionality with the South African environment, the standard for revision of the code was derived from relevant ISO standards, using the Euro code as a primary reference. This helps both in maintaining international consistency and achieving a safe level of reliability for design. The revised code consists of eight parts. Amongst these revised parts, of particular interest to the author is SANS 10160: Part 6. “Action induced by cranes and machinery”

1.2 Research Overview

A research group at the Institute of Structural Engineering, at Stellenbosch University, conducts research on actions induced by Electric Overhead Travelling Cranes (EOHTC) on the supporting structure. This research project forms part of an ongoing investigation into the EOHTC.

EOHTC induce actions on both the supporting structures and the building in which it operates. New standards for these actions are currently being introduced based on the EN1991-3 of the Euro code. Part 6 of the current South African loading code SANS 10160-6:2010 classifies action

induced by EOHTC as either variable actions, test loads or accidental actions which are represented by different load models. The variable actions being gravity loads including hoist loads, inertia forces caused by acceleration/deceleration of the EOHTC, skewing and misalignment of crane wheels, and other dynamic effects. The accidental actions are due to the collision of the EOHTC with the end stops, i.e. end stop impact forces, or tilting forces caused by the collision of the payload with obstacles. Actions which are categorised as accidental, result in horizontal longitudinal forces.

For the purpose of this study, the author is interested in investigating accidental actions on the crane supporting structure when the EOHTC collides with the end stops.

1.3 Aim of Study

This study is a continuation of the work done by Haas (2007) at the Institute of Structural Engineering, at Stellenbosch University.

- The investigation was conducted to determine the effect of the lateral stiffness of the crane bridge on the end stop impact force. The South African loading code, SANS 10160 does not take the lateral flexibility of the crane bridge into account in determining the end stop impact force. Typically, structural flexure dissipates at least 5 percent of the kinetic energy before the buffer starts to deform, Kit (1996).

- Also, this investigation is aimed at determining the maximum end stop impact force when the EOHTC which is fitted with hydraulic buffers collides with the end stops.

1.4 Methodology

To achieve the aim of this investigation, a series of experimental and numerical tests were conducted. All numerical analysis were conducted using a modified finite element analysis (FEA) model developed by Haas (2007). The methodology used in this investigation is presented below:

- FEA simulations were conducted to determine the effect of the lateral stiffness of the crane bridge on the impact forces. This was achieved by:
  - Varying the lateral stiffness of a single bridge EOHTC.
  - By using the original flexural stiffness and replacing the single bridge with a double bridge EOHTC. For the double bridge EOHTC, the distance between the crane bridges

was varied and a representative distance was chosen.

- Since hollow box sections are used for double bridge EOHTC, the crane bridge and the end carriages were replaced with hollow box sections.

- FEA simulations were conducted on a double bridge EOHTC fitted with elastomeric buffers. From literature studied, certain parameters were identified to have significant influence on the end stop impact force, Haas (2007). For this set of simulations, sensitivity analysis was conducted to investigate the influence of the identified parameters on the impact force. Since it is not feasible to consider all of these parameters occurring simultaneously at their maximum values, it was unrealistic to consider that all the parameters would occur simultaneously. The maximum impact force was obtained using a constraint optimization technique which will be discussed in details in chapter 3 of this documentation.

- Experimental tests were conducted to determine the elastic and the damping characteristics of an adjustable DPH 25 hydraulic buffer.

- The elastomeric buffer's characteristics were replaced with the hydraulic buffer's characteristics in the FEA model.

- Experimental impact tests and FEA simulations were conducted for the single bridge EOHTC fitted with the hydraulic buffers.

- The maximum end stop impact force was determined for various levels of reliability using the FEA impact histories obtained for the single bridge EOHTC fitted with hydraulic buffers.

- The maximum end stop impact force obtained was compared with the codified end stop impact forces.

CHAPTER 2: LITERATURE REVIEW

2.1 General Review

The earliest cranes did not have buffers attached to them as found in current practice. End of travel limits were typically steel to steel collisions between framed members, Kit (1996). Little damage was experienced due to the low impact velocity of the cranes. In the past, several cushioning devices, such as oak timbers, were employed to absorb the energy produced from the collisions. However, these cushioning devices did not provide the required damping effect. As a result, buffers were developed to adequately offer the required damping effect. Just as many aspects of cranes, the concept of buffering impact forces was adopted from rail road mechanics. In the operation of trains, buffers are used as a device to prevent trains from going past the end of a section of a track.

Buffers are supplied in different types with each offering different efficiency levels and condition of service. Hydraulic buffers, elastomeric buffers, spring buffers and rubber buffers are types of buffers which are commonly fitted to overhead travelling cranes.

Kit (1996), relates impact forces to kinetic energy using efficiency diagrams. The efficiency diagram is defined as the ratio of the areas under the force-displacement graph for a particular buffer to the area under the theoretical force-displacement graph of an ideal buffer. The theoretical area for an ideal buffer is rectangular in shape under maximum force. However, the efficiency diagram does not give the energy absorption measured empirically.
Using the efficiency diagram, Kit (1996) estimates the efficiency for different buffers as:

- Solid elastomeric buffers: 45%
- Coils spring: 50%
- Rubber buffer: 30%
- Hydraulic buffer: 90%.

Kohlhaas (2004), conducted investigations to determine end stop impact forces for electric overhead travelling crane supporting structures. In this investigation, the end stop impact force histories of a 5-ton EOHTC fitted with elastomeric buffers were experimentally investigated. The results obtained yielded useful insight into the behaviour of end stop impact forces.

Haas (2007), worked on the numerical analysis of crane end buffer impact forces. This was achieved by developing a FEA model of the full scale experimental configuration of a 5-ton EOHTC

and its supporting structure. This will be discussed extensively in subsequent sections as some of the results form the basis for comparison in this investigation.

2.2 Buffers

Buffers are energy absorbing devices, which offer resisting forces to objects in motion. There are several energy absorbing devices that can be used to dissipate the impact energy from cranes when the EOHTC collides with the end stops. All of these devices differ in physical characteristics, design, function and efficiency.

The damping characteristics of a buffer defines the amount of energy it dissipates, which reflects its efficiency. The greater the damping percentage, the less strain energy it stores.
Generally, the process of damping is usually classified as either, (Taylor Devices Inc):

- Hysteretic/friction dampers: This is a damping device where a fixed damping force is generated under any deflection. It is an on-off constant force device, where the resisting force to any motion large or small, is a fixed value.
- Rubber/visco-elastic dampers: These dampers behave as a complex spring and damper combination. As a result of this complexity, no single out-put function exists to determine the performance of these dampers. The output has a non-linear force/deflection relationship and it varies with the type of rubber used, shape of the rubber and ambient temperature. An example of a buffer with this damping characteristic is an elastomeric buffer.
- Viscous/fluid dampers: This is a damping device which varies its force absorption only with impacting velocity. This provides a response that is inherently out of phase with stresses. An example of a buffer with this damping characteristic is an hydraulic buffer.

Figures 2.2.1, 2.2.2 and 2.2.3 provide representative force vs. displacement graphs of these three damper types.

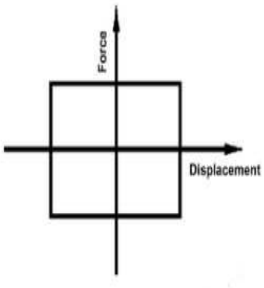

Figure 2.2.1 Friction output

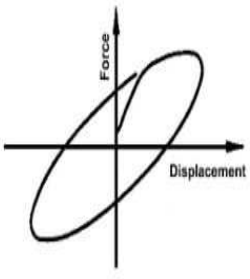

Figure 2.2.2 Visco-elastic output

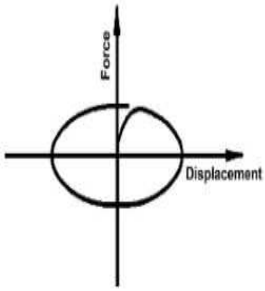

Figure 2.2.3 Fluid/Viscous output

The energy absorbed or dissipated by the buffers from a crane is a function of the kinetic energy of the crane at the point of impact. The deformation energy of a system is the area under the force-deflection curve. The energy absorbed by the buffers is usually as a result of its damping and elastic characteristics. An exception to this is a buffer which is simply a spring element and thus has no damping characteristic. The area under the stiffness curve is a combination of the strain energy “absorbed and stored” and the damping energy “dissipated”. In other words, the crane buffer absorbs the kinetic energy from an impact by applying a resistive force over the deflection, which implies that some strain energy is stored and capable of providing a return force once the buffer expands.

There are numerous types of buffers used for electric overhead travelling cranes. The most commonly used are elastomeric and hydraulic buffers. A good description of elastomeric buffers is documented in the investigation by Haas (2007). The present research was conducted on hydraulic buffers, hence a detailed description is provided.

2.3 Hydraulic Buffers

Hydraulic buffers are energy dissipating devices in compliance with the standard EN81-1:1998. Hydraulic buffers vary between manufacturers. However, the basic design and concept guiding its operation remains the same. Figure 2.3.1 shows a section through a hydraulic buffer.

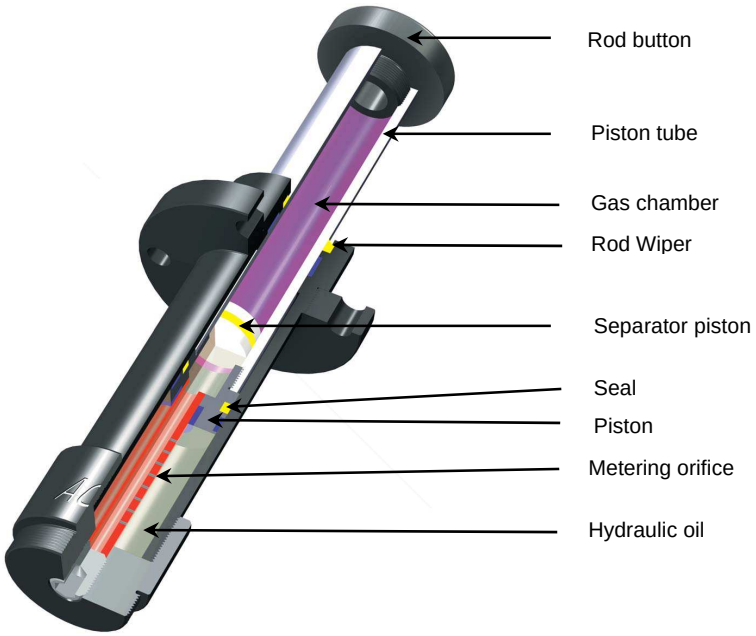

Figure 2.3.1 A section of an ACE hydraulic buffer

A hydraulic buffer is a device that mechanical removes energy from a system by converting the energy to heat. The hydraulic buffer consists of a damping element with a reset mechanism classified as a spring element. This spring element controls the rate of reset after impact. The reset mechanism can be identified by a static resistance curve. At the start of the operation, the piston rod is fully extended. As the impacting load strikes the buffers, the hydraulic oil behind the piston is forced through a series of metering orifices, thereby applying a dissipative force over a specified displacement. The metering orifice reduces proportionally through the stroke and the load; thereby reducing the velocity smoothly to zero. In the course of impact and the deceleration of the crane's velocity, the internal pressure remains constant. The displaced oil is stored in the piston accumulator. For the rod to return to its extended position after each impact, the low pressure nitrogen in the integrated gas chamber provides the return force to reset the rod. The force output is a function of the velocity of the hydraulic fluid through the orifice. According to Kit (1996), hydraulic buffers have a non-linear stiffness curve. Its non-linearity allows only the hydraulic buffer to change its resisting force as a function of the impacting velocity. That is, an increase in impacting velocity yields an increase in the resisting force capacity of the buffer. This makes the hydraulic buffer the only known buffer with a force output that is only velocity dependent. This is unlike the elastomeric buffer which has a forcing function dependent of both displacement and velocity. The kinetic energy to be dissipated by the buffer has a velocity squared function. This implies that, when the metering device of a hydraulic buffer is designed to provide buffer forces as a function of velocity square, the buffer forces will always be in the correct magnitude to effectively dissipate the impacting force.

Literature reviewed reveals that hydraulic buffers designed by different manufactures usually falls in two types of metering devices. Kit (1996), identified these two types of metering devices as;

- Metering pin/tube buffers: Buffers with this kind of metering device have a force velocity relationship where the capacity of the buffer to resist the force for a particular impact velocity is constant through the entire stroke of the buffer. In other words, the capacity of such a buffer is entirely dependent on the impact velocity. The force velocity relationship of the metering pin/tube buffer makes it possible for it to accommodate varying velocities by adjusting its end force.

- Metering fluidic buffers. Buffers with this kind of metering device have a force velocity relationship where the capacity of the buffer to resist an impact velocity varies along the stroke of the buffer. This implies that an increase in the end force of the buffer is dependent both on the impact velocity and the buffers' stroke. This indicates that a fluidic buffer is not exactly velocity sensitive, thereby making it impossible for it to maximise its full stroke under partial velocity. The inability of the buffers to maximize the full stroke prevents the buffers from having a minimum end force.

The metering tube / metering pin buffer has a force-velocity function represented by equation 2.3.1 while the metering fluidic buffer has a different force-velocity function represented by equation 2.3.2

$$F = Cv^2 \qquad 2.3.1$$

$$F = Cv^n \qquad 2.3.2$$

(Where n varies from 0.5 to 0.7 depending on specific design configuration and C is the Damping Constant,) kit (1996)

Figures 2.3.2 and 2.3.3 show a graphical representation of the force-velocity curve for the metering pin/tube and metering fluidic hydraulic buffers respectively.

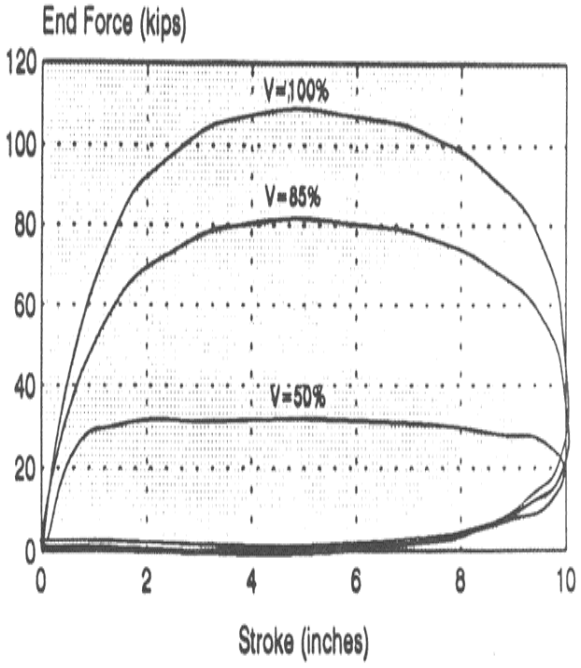

Figure 2.3.2 A metering pin hydraulic buffer.

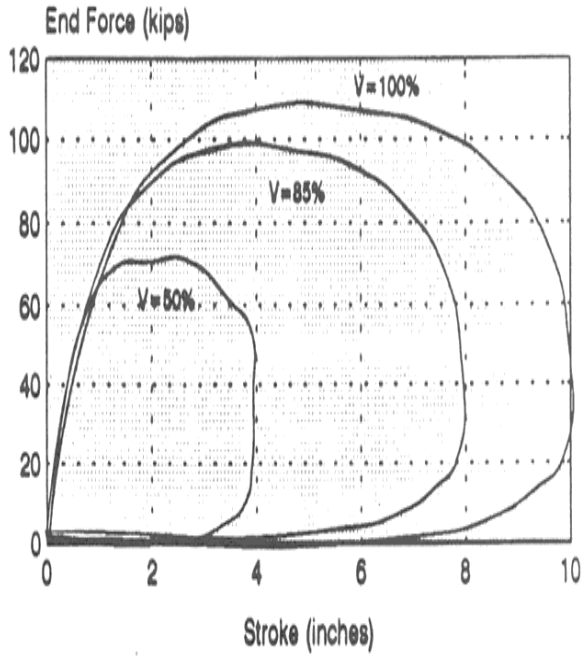

Figure 2.3.3 A metering fluidic hydraulic buffer.

Both metering devices are employed by different manufactures. The AISE Technical Report No 6 (1991), suggests a deceleration rate of 4.9m/sec at 50% of full rated travel speed for hydraulic buffers. Additionally, the buffer must be capable of absorbing the energy of the unloaded crane at 100% travel speed with corresponding increase in its deceleration, i.e. 19.6m/sec. Kit (1996) specifies that only a hydraulic buffer with a metering tube/pin device can effectively meet such specifications. For the purpose of this investigation**,** a DEMAG DPH 25 adjustable buffer was used. The manufactures of this buffer gives no information on the type of metering device used in its

design. Hence, limited information exists on the damping characteristics of this buffer. The only information given of the buffer is its energy absorption capacity. For the purpose of this research, the specific characteristics of the buffer was determined from experimental tests and documented in consequent chapters.

2.4 EOHTC Research at the Stellenbosch University

The Centre for Development of Steel Structures at Stellenbosch University is conducting research on the EOHTC with the aim of providing guidelines for the design of crane supporting structures. For this purpose, a 5-ton EOHTC with its supporting structure was erected in the structural laboratory of the civil engineering department.

Barnard (1999), was responsible for the design and construction of a full-scale EOHTC testing facility in the structural laboratory with the provision of adjusting various parameters during experimental tests.

Perez-Winkler (2003), studied the interaction between the crane wheels, rail and girder using experimental tests and numerical simulations.

Viljoen P (2004), conducted numerical investigation into the top flange and web deformation of a crane girder panel.

Kohlhaas (2004), carried out experimental investigations on the 5-ton EOHTC to obtain the end buffer impact forces when the EOHTC collides with the end stops. The results obtained show large discrepancies from the end buffer impact forces obtained by various codes of practice.

Dymond (2006), conducted a reliability based codefication for the design of overhead travelling crane supporting structures. The crane load models in the current South African loading code SANS 10160-6:2010 was adopted from the Euro code crane loading code, prEN 1991-3. Hence, the study focused on the crane load models from prEN 1991-3**.** The investigation revealed that prEN 1991-3 calculates vertical forces conservatively while the horizontal forces were underestimated.

De Lange (2007), worked on the calibration of the experimental setup developed by Barnard. The investigation also covered experimental tests for studies used by Haas and McKenzie.

McKenzie (2007), conducted a numerical analysis using FEA simulations to determine the wheel loads induced by the crane on the crane supporting structure through hoisting, normal longitudinal travel, skewing and rail misalignment.

Haas (2007), was responsible for the development of a numerical model to evaluate the crane end buffer impact forces taking into account the interaction between the crane and its supporting structure. This was achieved through a series of experimental tests and FEA simulations. The maximum end buffer impact force was determined using the results from the FEA simulations together with a constraint optimization technique.

2.5 Description of the EOHTC

Figure 2.5.1 shows a picture of the full scale 5-ton EOHTC at Stellenbosch University. The same experimental configuration was used for this investigation. For a detailed understanding of its basic make up and its components, the reader is referred to Haas (2007).

Figure 2.5.1 EOHTC in the laboratory of the structural division at Stellenbosch University.

2.6 Estimation of the Member Forces on the Crane Supporting Structure as Given by the South African Loading Codes

The previous South African loading code of practice, SABS 0160-1989, provides the following loading situation for the design of the crane supporting structure:

I. Vertical wheel loads: Clause 5.7.3 states that *"Take the vertical wheel loads imposed on the gantry by a crane as the values provided by the crane's manufacturer or specified by the owner. These are referred to as the static wheel loads. Allowance should be made for impact and other dynamic effects in the vertical direction by multiplying the static wheel loads by the appropriate factors depending on the class of the crane"*

II. Horizontal transverse wheel loads: Clause 5.7.4 states that *"Take the horizontal forces imposed on the gantry by a crane and acting at the top of the crane rails in a direction transverse to the direction of the travel of the crane, to be the most adverse of the following*"

(a) Allowance for acceleration or braking of the crab: Apply a force equal to the combined weight of the crab and the load lifted, to be multiplied by the appropriate factor depending on the class of the crane.

(b) Allowance for possible misalignment of crane wheels or gantry rails: Apply at each wheel a force

$$P_1 = \frac{xm}{N}$$

Where x = is the appropriate factor depending on the class of the crane

m = combined weight of the crane bridge, crab and load lifted

N = total number of crane travel wheels

(c) Allowance for skewing of crane in plan: Caused by wheel or gantry rail misalignment or by braking or acceleration of the crane with the crab at the extremity of travel.

III. Horizontal longitudinal loads: "Clause 5.7.5 states that "*Take the horizontal force imposed by a crane on each line of the rails, acting longitudinally in the direction of travel and caused by acceleration or braking, to be 0.10 times the sum of the maximum static wheel loads on that line of rails"*

IV. Forces on the end stops are regarded as an accidental load situation. These forces are used to design the end stop, gantry and the bracing system:
Clause 5.7.6 of the loading code provides two alternative methods of calculating end stop impact forces. Both of these methods are presented below.

"Take the horizontal force imposed on each end stop by a crane in the direction of travel to be lesser of the following"

a) A force equal to the combined weight of the crane bridge and the crab.
b) A force calculated on the assumption that the crane strikes the end stop while travelling at its full rated speed, taking into account the resilience of the end stops and crane buffers.
Note: In (a) and (b), the weight of the load carried by the crane may be ignored unless it is restrained in a horizontal direction as in a mast or claw crane.

To obtain the most severe buffer impact force SABS 0160-1989 states that*;*

"In determining the crane loads set out in clause 5.7.4- 5.7.6 assume the magnitude of the load lifted by the crane (up to its rated capacity), the position of the crab on the crane bridge, and the position of the crane on the crane supporting structure, to be such as will produce the most adverse effect upon the building or part of the building being designed".

Part 6 of the current South African loading code SANS 10160-6:2010 gives a more detailed method of estimating the end stop impact force. According to clause 4.12.1 of the code, end stop impact forces related to crane movement can be calculated as follows:

"(1) Where buffers are used, the forces on the crane supporting structure arising from the collision with the buffers shall be calculated from the kinetic energy of all relevant parts of the crane moving at 0.7 to 1.0 times the nominal speed.

"(2) The buffer forces multiplied by Φ_7 according to Table 9 of the South African loading code SANS 10160 to make allowance for the dynamic effects may be calculated taking into account the distribution of relevant masses and the buffer characteristics;

$$H_{B,1} = \Phi_7 \times V_1 \times \sqrt{m_C \times S_B}$$

Where;

$H_{B,1}$ = Horizontal longitudinal forces due to impact

Φ_7 = Dynamic factor obtained from Table 9 of SANS 10160

V_1 = Is 70% of the maximum longitudinal velocity (m/s) (where automated speed retarding mechanism is provided)

m_C = Mass of crane and hoist load (kg*)*

S_B = Spring constant of the buffer (N/m).

Table 9 of the code estimates the dynamic factors Φ_7 as a function of the buffer's strain value / buffer deformation (ξ_b) and is presented in Table 2.6.1:

Table 2.6.1 Dynamic factor Φ_7

Table 9 : SANS 10160:6-2010	
$\Phi_7 = 1.25$	*If* $0.0 \leq \xi_b \leq 0.5$
$\Phi_7 = 1.25 + 0.7 * (\xi_b - 0.5)$	*If* $0.5 \leq \xi_b \leq 1.0$

According to the code, ξ_b can be approximately determined from Figure 2.6.1 depending on the buffer's characteristics.

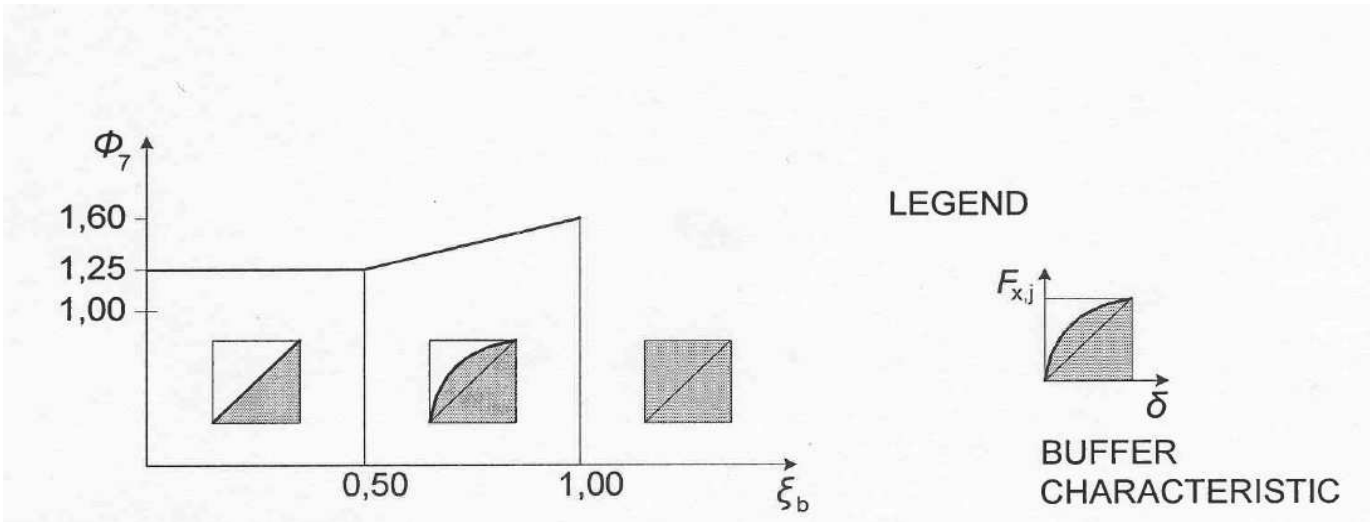

Figure 2.6.1 Definition of ξ_b

2.7 Estimation of End Stop Impact Force as Specified by Various Codes

As stated earlier, there are various design codes of practice employed for structural design based on acceptable standards in different countries. However, under the same conditions such as impact velocity, end stop resilience and impacting mass, it is expected that the end stop impact force will vary only according to the buffers' elastic and damping characteristics. However literature reviewed reveals that a number of other variables influence the impact force history (Haas, 2007).

Kohlhaas (2004), calculated the end stop impact force at an impact velocity of 0.55m/s using four different design codes of practice, that is, the previous South African code SABS 0160:1989, the European code EN 1991-3:2003 , and two Australian codes of practice vis-à-vis AS 1418.18-2001 and AS 1418.1-1994 . The results obtained revealed great variance in the estimated codified values. This influenced the criterion under which further experimental investigations were carried out. Kohlhaas (2004) conducted experimental investigation on the end stop impact force under different conditions. In the experimental tests, impact force histories were obtained for the following four conditions.

- Experimental tests with payload
- Experimental tests without payload
- Experimental tests with misalignment of the left hand side (LHS) end stop by 20mm.
- Experimental tests with an eccentric position of crab and payload

.

The result shows a 34% increase in the maximum impact force obtained for the test with payload, when compared with that obtained for the test without payload. An average of 37% increase in impact force was obtained when one of the end stops was misaligned by 20mm. For the experimental test with an eccentric position of the crab and payload, the impact force increased on the eccentric side by 55%. For an experimental test where one of the end stops was misaligned by 20mm and the crab and payload were eccentric on the crane bridge, the impact force increased by 71%. Results obtained not only show variation in the end stop impact forces under the varying conditions, but also, the impact force history obtained for the experimental tests without payload reveals two additional impacts. This was not expected since no gravitational load exists to drive the crane back into the end stops after the 1st impact. These additional peaks were identified to be as the result of the variable-adjusted-residual torque present in the drive motors during impact. It is observed that the torque is capable of driving the crane back into the end stops after the release of the acceleration button on the crane's pendant at impact. However, the magnitude and the duration of the residual torque are not provided by the crane manufacturer. Hence the investigation of the influence of residual torque on the impact force history was included in Kohlhaas's work.

Haas (2007) confirmed the variation in the codified result as observed by Kohlhaas, (2004). In his research, end buffer impact forces were determined based on the guidelines given by eight different codes of practice. The impact forces were obtained for various impact velocities using the experimental configuration data. Table 2.7.1 shows the end buffer impact forces obtained by Haas (2007) at various impact velocities for the following codes of practice:

- DEMAG: The manufacturer's guidelines for the estimation of end stop impact force which is based upon the German codes of practice, DIN 15018.
- SABS 0160:1989 (As amended in 1989): South African Standard Code of Practice for: The general procedure and loadings to be applied in the design of buildings.
- SAN10160: 2010; South African National Standards: Basis of structural design and actions for buildings and industrial structures. Part 6, Actions induced on cranes and machineries"
- AS 1418.18:2001; Australian Standards: "Cranes (including hoist and winches), Part 18: Crane runways and monorails.
- AS 1418.1: 1994; Australian Standards, "Cranes (including hoist and winches). Part 1: General requirements.
- AISE (Association of Iron and Steel Engineers) Technical report 13, 1997; Specification for electric over head travelling cranes for steel mill services.

Table 2.7.1 Summary of the end stop impact forces at various velocities based upon eight codes and guidelines for a DPZ 100 cellular plastic buffer.

Impact Velocity (m/s) / **Codes / Guidelines**	**Estimated End Buffer Impact Force as a Function of Impact Velocity (kN)**							
	0.3	0.4	0.5	0.6	0.7	0.8	0.9	1.0
DEMAG	2.4	6.1	8.1	9.4	15.0	23.3	27.6	-
SABS 0160-1989 (method a)	21.9	21.9	21.9	21.9	21.9	21.9	21.9	21.9
SABS 0160-1989 (method b)	3.3	9.1	11.9	15.0	21.9	37.3	-	-
Lesser of methods (a) & (b)	3.3	9.1	11.9	15.0	21.9	21.9	21.9	21.9
EN 1991:3 & SANS 10160	7.1	19.6	23.9	30.1	-	-	-	-
AS 1418.18.2001	5.7	6.8	8.1	10.9	14.3	18.2	22.4	50.3
AS 1418.1. 1994	3.5	5.1	6.1	7.6	11.7	13.9	20.3	27.8
AISE No 13: 1997	2.8	7.5	9.1	10.8	14.8	19.3	24.4	30.1

The divergence in impact forces reveals that the basis of the guidelines given by these codes is not properly understood. This necessitated a proper investigation into the ideas and philosophies on which the given guidelines of the codes of practice are based. Haas (2007), conducted FEA simulations to obtain the end stop impact forces. From the simulations, he was able to identify certain parameters which have a significant effect on the end stop impact force histories. These parameters are listed below.

- The horizontal position of payload in relation to the EOHTC at impact.
- The height of the payload beneath the crane bridge.
- The eccentric position of the crab and payload at the moment of impact.
- The flexibility of the crane supporting structure.
- The velocity of the crane at the moment of impact.
- The elastic characteristics of the crane's end buffers.
- The crane buffer's damping characteristics.
- The misalignment of the end stops.
- The influence of torque from the drive motors throughout impact on the impact force.

De Lange (2007) conducted an experimental investigation into the behaviour of the 5-ton EOHTC and its supporting structure. In the course of the investigation, experimental tests were conducted for two conditions termed as "No Payload, Power-On" and "No Payload, Power-Off with residual torque". For the condition of No Payload, Power On, the control button for the longitudinal movement of the crane was engaged for 6.5seconds. Result shows continuous impact peaks through out impact. For the condition of Power Off with residual torque, the control button for the longitudinal movement of the crane was released at impact. For this condition, the result showed two additional peaks. This is due to the residual torque present in the electric drive motor of the crane. The experimental test by De Lange (2007) revealed that the electric motor that drives the crane in the longitudinal direction has a step-down function. This step down function decreases the power gradually from the electric drive motors from the moment the acceleration control button on the crane's pendant is released. To investigate the effect of the step down function on impact force, the step down function on the drive motors was deactivated and impact tests were conducted. This test was termed as "No Payload, Power off without residual torque". This implies that for this condition, consequent impacts after 1st impact are solely due to inertia of the EOHTC. Results obtained for this condition shows that no further impact occurred after the first impact. The results obtained by De Lange (2007) yielded similar result as obtained by Kohlhlaas (2004), revealing the effect of residual torque on the end stop impact force history.

Based on the tests conducted by De Lange (2007) and Kohlhaas (2004), Haas (2007) was able to identify a set of criteria influencing the estimated end stop impact force under which the observed influencing parameters stated earlier were analysed. These identified criteria are:

- Payload Bottom, Power Off: For this condition, the residual torque from drive motor was disengaged before the impact test. The payload was hoisted 0.15m above ground level.
- Payload Bottom, Power On: For this condition, the drive torque was applied throughout the duration of impact. The payload was hoisted 0.15m above ground level.
- Payload Top, Power Off: This condition is the same as for “Payload Bottom Power Off” except that the payload was hoisted 2.2m above ground level.
- Payload Top, Power On: This condition is the same as for “Payload Bottom Power On” except that the payload was hoisted 2.2m above ground level.

2.8 FEA Simulation and Sensitivity of End Stop Impact Force

A numerical model of the EOHTC and its supporting structure was developed using ABAQUS. The same model was used for the numerical analysis in this investigation. The reader is referred to Haas (2007) for a detailed description of the model.

Using this model, Haas (2007) conducted FEA simulations on the parameters identified to determine its influence on the end stop impact force history. The simulations were conducted for each condition of Power On/Off and the vertical position of the payload above the ground. Under each of these conditions, a parameter was varied, while the remaining parameters were left constant. Each parameter was varied at an estimated standard deviation. It must be noted that the estimate of standard deviation for variation is based on observations made from experimental tests. Table 2.8.1 shows the influence of each identified parameter on the impact force history as obtained by Haas (2007).

Table 2.8.1 Influence of identified parameters on impact force history.

Parameters	Condition where Maximum Impact Occurs	Occurrence of Maximum Impact Force	Impact Force when all Parameters were at Base Value (kN)	Maximum FEA Impact Force (kN)
Lag Angle	Payload Bottom Power-On	1st Impact	7.26	10.03
Crab and Payload Eccentricity	Payload Top Power-On	1st Impact	7.48	9.39
Crane's Supporting Structure's Flexibility	Payload Top Power-On	2nd Impact	8.05	9.01
Crane Impact Velocity	Payload Top Power-On	2nd Impact	8.05	10.34
End Stop Misalignment	Payload Top Power-On	2nd Impact	8.05	10.11
Modified Buffers' elastic characteristics	Payload Top Power-On	2nd Impact	8.05	8.04
Modified Buffers' Damping characteristics	Payload Bottom Power-On	2nd Impact	4.61	14.33

2.9 Estimation of Maximum End Stop Impact Force.

The estimation of the end stop impact force shown in Table 2.8.1 gives different impact responses obtained under the influence of individual parameters. However, it is not feasible that only one of these influencing parameters would vary nor is it likely that all the parameter would vary by the maximum amplitude at the same time. The maximum end stop impact force was determined using a constraint optimization technique, namely the LaGrange Multipliers. The maximum end stop impact force was obtained for three levels of reliability. Tables 2.9.1 and 2.9.2 show the estimated end stop impact forces for the 1st and 2nd impacts respectively.

Table 2.9.1 Estimated maximum end stop impact force from the 1st Impact responses

Levels of Reliability (β)	Payload Bottom "Power-Off"	Payload Bottom "Power-On"	Payload Top "Power-Off"	Payload Top "Power-On"
$\beta = 1$	7.64	9.05	8.44	9.83
$\beta = 2$	8.93	10.83	10.23	12.19
$\beta = 3$	10.22	12.62	12.03	14.54

Table 2.9.2 Estimated maximum end stop impact force from the 2nd Impact responses

Levels of Reliability (β)	Payload Bottom "Power-Off"	Payload Bottom "Power-On"	Payload Top "Power-Off"	Payload Top "Power-On"
β = 1	1.96	1.51	9.11	9.95
β = 2	-0.57	-1.59	11.35	11.85
β = 3	-2.98	-4.69	13.58	13.75

A level of reliability of β=3 is used in South Africa. The probability of exceedance is related to the reliability indices represented by equation 2.9.3. Table 2.9.3 shows the probability of exceedance for each level of reliability. At a level of reliability β = 3 a maximum end stop impact force of 14.54kN occur for the condition of Payload Top Power-On

$$P = \Phi(-\beta) \qquad (2.9.3)$$

Where P = Probability of exceedance

Φ = Gaussian cumulative distribution

β = Level of reliability

Table 2.9.3 Level of probability for various level of reliability

β	Probability %
1	1.6×10^{-1}
2	2.3×10^{-2}
3	1.4×10^{-3}

CHAPTER 3: FINITE ELEMENT ANALYSIS OF A DOUBLE BRIDGE EOHTC

3.1 Horizontal Stiffness of the Crane Bridge Section.

The South African loading code, SANS 10160-6:2010 makes provision for a number of parameters that might possibly influence the end stop impact force. However, no provision is made for the influence of the lateral stiffness of the structure as a coupled system. The end stop impact force is expected to vary in proportion to the impact velocity, resilience of the buffers and the mass of the crane bridge. This assumption neglects the flexibility of the EOHTC as it collides with the end stops. Literature specifies that not less than 5% of impact force is absorbed by the structure's flexibility, Kit (2004). Numerical investigation on the end stop impact force reveal that the flexibility of the crane supporting structure has a significant influence on the impact force history, Haas (2007). Another component of the EOHTC where structural stiffness is likely to influence end stop impact force is the crane bridge. As the crane collides into the end stops, the crane bridge is capable of deflecting laterally, thereby influencing the end buffer deformation and ultimately the impact force history.

In South Africa, when the span between the crane's supporting structure is large or where the payload to be hoisted is substantial, the crane usually has a double bridge with box section, Haas (2007). Also the double bridge EOHTC provides a better lifting height for the payload. Double bridge EOHTC provides horizontal lateral stiffness that varies both with distance between the crane bridges and section used. According to the American Institute of Steel Construction (AISC), section to be used for a double bridge EOHTC shall be structural steel plate box sections or standard hot rolled section shapes.

To determine the effect of the horizontal lateral stiffness on end stop impact force, numerical simulations were conducted for a double bridge EOHTC with varying lateral stiffness. For the first set of simulations, the original web dimensions were used while the width of the flanges were adjusted to increase the lateral stiffness of the crane bridge girder. The result obtained reveals that the lateral stiffness of the crane bridge has a significant influence on impact force history. However, since the crane bridge girders are designed based on design codes and guide lines, certain limits are placed on the size of the flanges and webs of the steel sections to ensure serviceability and safety. Hence, for an H section, it is not feasible to increase the width of the flanges while keeping the same depth. Thus, a double bridge EOHTC with the original H-section for both the crane bridge girders and the end carriages was investigated. Influence of the lateral stiffness was investigated by varying the distance between the crane bridge girders. The impact force history obtained from these simulations is presented in Figure 3.1.1.1.

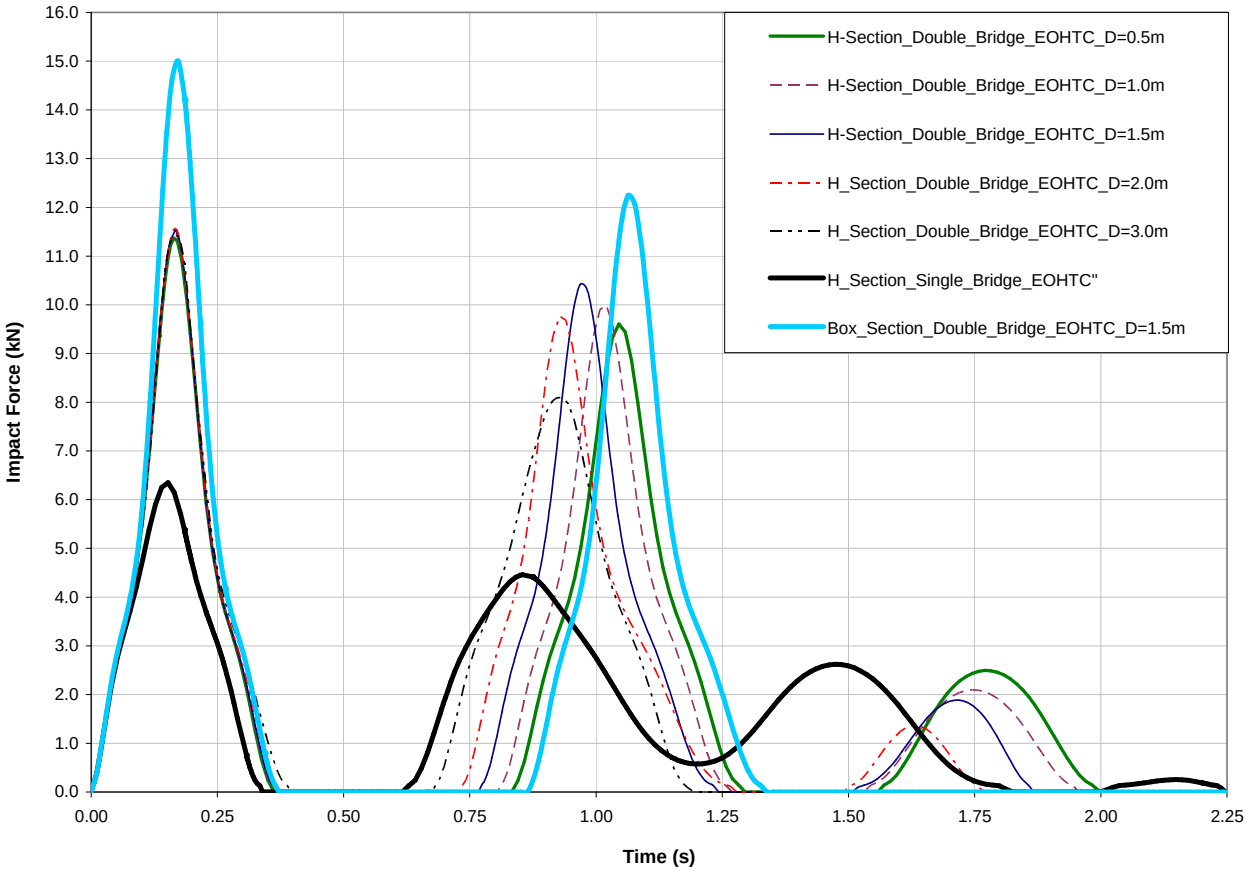

Figure 3.1.1.1 Effect of crane bridge spacing for a double bridge EOHTC**.**

Figure 3.1.1.1 compares the impact force histories of a 305x305x118 H-section single bridge EOHTC and a double bridge EOHTC of the same H-section. It must be noted that letter “D” in the legend of Figure 3.1.1.1 represents the distance between the crane bridge girders for the double bridge EOHTC. The results show that the spacing of the crane bridge girders has no significant influence on the 1st impact force. It however influences the magnitude of the 2nd impact peaks and time of occurrence significantly. The maximum impact forces and the time of occurrence obtained at both the 1st and 2nd impact for each girder spacing are presented in Table 3.1.1.2**.** Another analysis was conducted for a double bridge box section EOHTC. For this analysis, a hollow box girder of section 315 x 205 x 18 was used for each of the crane bridges, while a hollow box girder of section 205 x 205 x 14 was used for each end carriage. The crane bridges were spaced 1.5m apart. Superimposed on Figure 3.1.1.1 is the FEA impact force history obtained for the analysis of the box section, double bridge EOHTC. The result obtained shows that at 1st impact, the impact force increases for both the H-section and Box-section double bridge EOHTC with percentages significantly greater than the increase in their individual mass contribution. This shows that the end stop impact force does not increase in direct proportion to change in the impacting mass under the same condition of buffer characteristics. This is as a result of the non-linear stiffness curve of the elastomeric buffers. It must be noted that elastomeric buffers have damping characteristics that vary

along the stroke of the buffers. Results from the experimental test conducted by De Lange (2007), show that the loading damping curve of an elastomeric buffer has a logarithmic trend that first increases and reduces progressively along the buffer's stroke. This indicates that the buffers' ability to dissipate energy from the impacting mass at any point is largely dependent on the fraction of the buffer's stroke that undergoes compression. It is expected that the greater the impacting mass, the more the fraction of the buffer that would be compressed. Hence less energy is being dissipated. This yields to greater end stop impact force.

.

Thus it was necessary to investigate the influence of change in the impacting mass and that of change in the lateral stiffness of the crane girder on the impact force under the identified influencing parameters. Table 3.1.1.2, shows that the maximum 2nd impact force occurred when the crane bridges are 1.5m apart. Thus, a representative distance of 1.5m between the crane girders was chosen for further investigations.

It must be noted that since the maximum impact force would always occur for the conditions of Power-On, this investigation considered only the condition of Power-On.

Table 3.1.1.2 Results of impact force for double bridge EOHTC with varying distance.

Distances Between Crane Bridges (m)	1st Impact Force (kN)	Time of Occurrence of 1st Impact (secs)	2nd Impact Force (kN)	Time of Occurrence of 2nd Impact (secs)
0.5	11.43	0.17	9.62	1.05
1.0	11.45	0.17	9.99	1.00
1.5	11.43	0.16	10.42	0.98
2.0	11.50	0.17	9.68	0.94
3.0	11.29	0.17	8.10	0.93

.

3.2 Sensitivity Study of the Effect of the Parameters on the Impact Force History for a Double Bridge EOHTC (Elastomeric Buffers)

A finite element analysis was conducted on a double bridge EOHTC to investigate the effect of each influencing parameter (identified in chapter 2) on the impact force history. For this investigation, a 315 X 205 X 18 hollow box section was used for each of the crane girders while a 205 x 205 x 14 hollow box section was used for each of the end carriages. The influence of each parameter on the impact force history was determined by varying only the parameter under investigation, while the others were kept constant. All the parameters listed in section 2.7 were considered with the exception of elastic characteristic of buffers. Literature reveals that the elastic characteristics of buffers have an insignificant effect on impact force Haas, (2007). The range of variation of each parameter used for the analysis is based on that used by Haas (2007). A summary of how each of this variation was modelled in the FE simulations is presented below.

3.2.1 Description of the Variation of the Parameters

- Lag angle of the payload: The base value for this parameter is when the payload is positioned directly under the crane girders at the moment of impact. At the base value, the lag angle is 0°. For this parameter, the FEA simulations were conducted for a variance of $\pm 1.25^{\circ}$ of the payload angle in the direction of crane travel.
- Crab and payload eccentricity: The base value for this parameter is when the payload and the crab are positioned symmetrically on the crane bridge which is at 4.14m from either ends of the crane girders. The FEA simulations for this parameter were conducted by moving the crab and payload by a distance of 1.695m and 3.39m from the mid span of the crane girders.
- End stop misalignment: The base value for this parameter is when the two end stops are aligned. Possible misalignment could occur when the 150mm wooden block on the end stops is removed from the face of one of the end stops. Hence FEA simulations for this parameter were conducted by misaligning one end stop by 25mm, 50mm and 150mm with respect to the other end stop.
- Impact velocity: The base value for this parameter is an impact velocity of 0.55m/s which is the impact velocity of the crane. Results obtained from the encoder however revealed that the average velocity of the crane can vary by $\pm 9\%$ of the full rated velocity of the crane. Also the South African loading code states that the crane velocity can be reduced by 30% when a velocity retarding mechanism is used. Hence FEA simulations for this parameter were conducted for a variation of $\pm 9\%$ and 70% of the full rated velocity of the crane.
- Gantry's stiffness: The base value is when the gantry is horizontally and longitudinally braced at the top of the crane columns thus preventing horizontal longitudinal displacement of the end stops. For the variation in the FEA simulations, the bracing system was replaced with a horizontal longitudinal spring. A simplification was made to the model by adjusting the stiffness of

the spring to prevent horizontal longitudinal translation. This was achieved by using a very stiff spring with a stiffness value of 1.75 x 10^7 N/m. To investigate the influence of the gantry's stiffness, an intermediate and a weak spring were created by reducing the stiffness of the spring to 1.75 x 10^6 N/m and 1.75 x 10^5 N/m respectively.

- Buffer's damping characteristics: The base value for this parameter is when the buffer was modelled with damping characteristics obtained from experimental tests. The manufacturer of the buffers gives no information on the damping characteristics of the buffers. Hence for this parameter, FEA simulations were conducted for buffers modelled without damping characteristics.

Table 3.2.1 shows the range of variation of each parameter investigated with the corresponding standard deviation used by Haas (2007), and which was used for this investigation.

Table 3.2.1 Estimated standard deviation of each parameter

Parameter	Base Value	Estimated Standard Deviation
Payload Lag Angle	0°	0.022 Radians (1.25°)
Crab and Payload Eccentricity on Crane Bridge	At mid span of the crane bridge	1.13m
End Stop Misalignment	0m	0.04125m (41.25mm)
Impact Velocity	0.55m/s	0.05m/s
Gantry's Stiffness	Rigid bracing (Longitudinal displacement = 0)	Weak, Intermediate, and Stiff Spring
Buffer's Damping Characteristics	Damping Characteristics used in FEA	No damping

3.3 Interpretation of the FEA Simulations

This section deals with the results obtained for each parameter from the FEA simulations conducted for the double bridge EOHTC. For these simulations, a 315 x 205 x18 hollow box section was used for each crane girder, while a 205 x 205 x14 hollow box section was used for each end carriage. To determine the effect of the identified influencing parameters on the double bridge box girder EOHTC, comparison is made of the impact histories obtained for the double bridge box girder EOHTC and the single bridge H-section EOHTC. The total mass of the double bridge box girder EOHTC is 3648Kg, while the total mass of the single bridge H-section EOHTC is 2233kg. This

implies a 63% increase in the impacting mass**.** Sensitivity study of the identified parameters on impact forces for both the double bridge box girder and the single bridge H-sections are documented in the subsequent section.

It must be noted that for ease of documentation, when payload is hoisted 0.15m above ground level, the condition is termed as “Payload Bottom”. When the payload is hoisted 2.20m above ground level the condition is termed as “Payload Top”

3.3.1 Effect of the Lag Angle on the Impact Force History

Figures 3.3.1.1 and 3.3.1.2 show the effect of the horizontal lag angle of the payload at impact on the impact force history for the double bridge and the single bridge EOHTC respectively. The results presented here are for the condition of Payload Bottom.

The significant information which can be extracted from Figure 3.3.1.1: Payload Bottom: Double Bridge EOHTC are:

- The impact force histories for the double bridge EOHTC follows a similar trend as obtained for the single bridge EOHTC where the impact force is influenced by the lag angle.
- As the positive lag angle of the payload increases, there is a corresponding increase in the 1st impact force peak. The opposite holds for an increase in the negative lag angle.
- The 2nd impact peak is minimally affected for this parameter.

The numerical differences between the impact forces for the double and single bridge EOHTC are presented in Table 3.3.1.1

Table 3.3.1.1 Influence of the payload lag angle on the impact force history for payload bottom

Payload Lag Angle (°)	Single Bridge EOHTC		Double Bridge EOHTC		Percentage Difference in Impact Force between the Double and Single Bridge EOHTC (%)		Percentage Difference in Impact Force for the Double Bridge EOHTC Relative to the Base Value (%)	
	1st Impact Force (kN)	2nd Impact Force (kN)	1st Impact Force (kN)	2nd Impact Force (kN)	1st Impact	2nd Impact	1st Impact	2nd Impact
Base value 0°	7.26	4.61	16.34	16.03	125.1	247.1	NA	NA
-1.25°	6.20	5.00	14.00	16.29	125.0	225.8	-14.6	1.6
-2.50°	5.36	5.95	12.04	17.14	124.6	188.1	-26.3	7.0
+1.25°	8.80	4.51	18.71	16.05	112.0	255.9	14.5	0.3
+2.50°	10.02	4.60	21.13	16.13	110.9	250.7	29.3	0.6

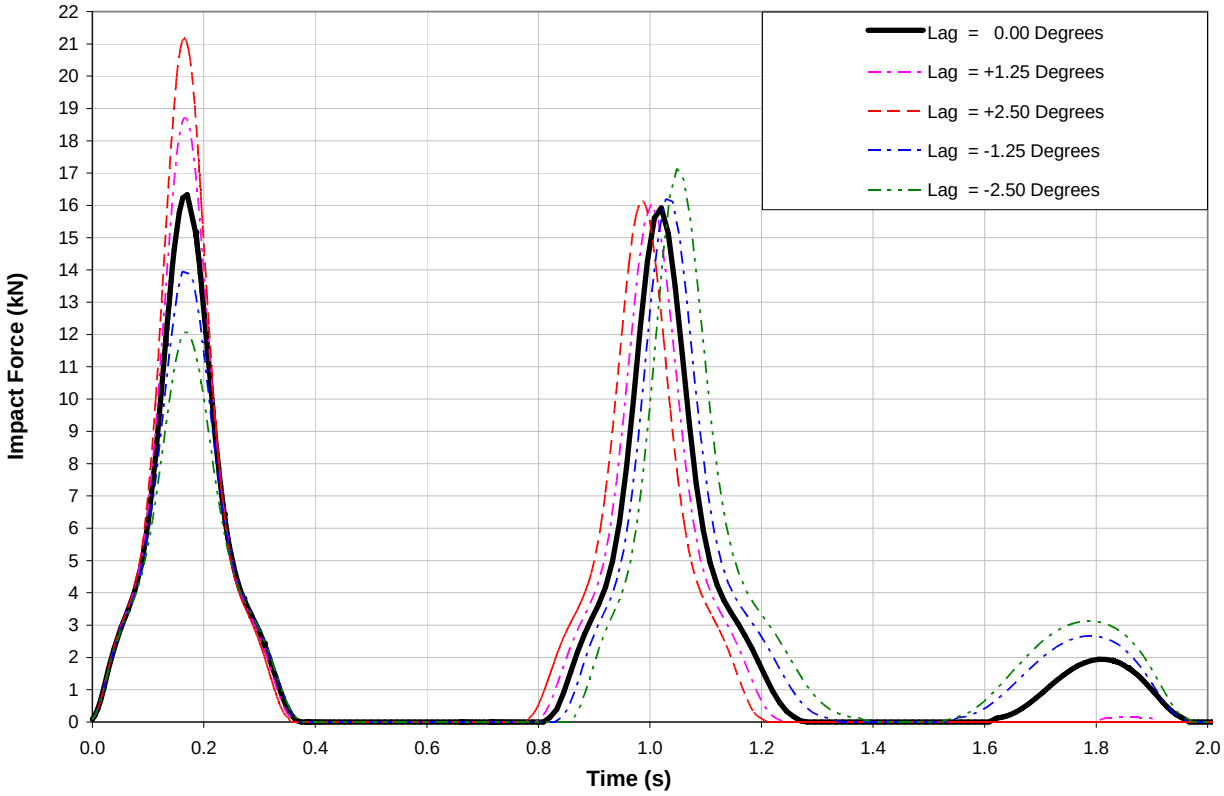

Figure 3.3.1.1 Parameter = Payload Lag: Payload Bottom "Double Bridge EOHTC"

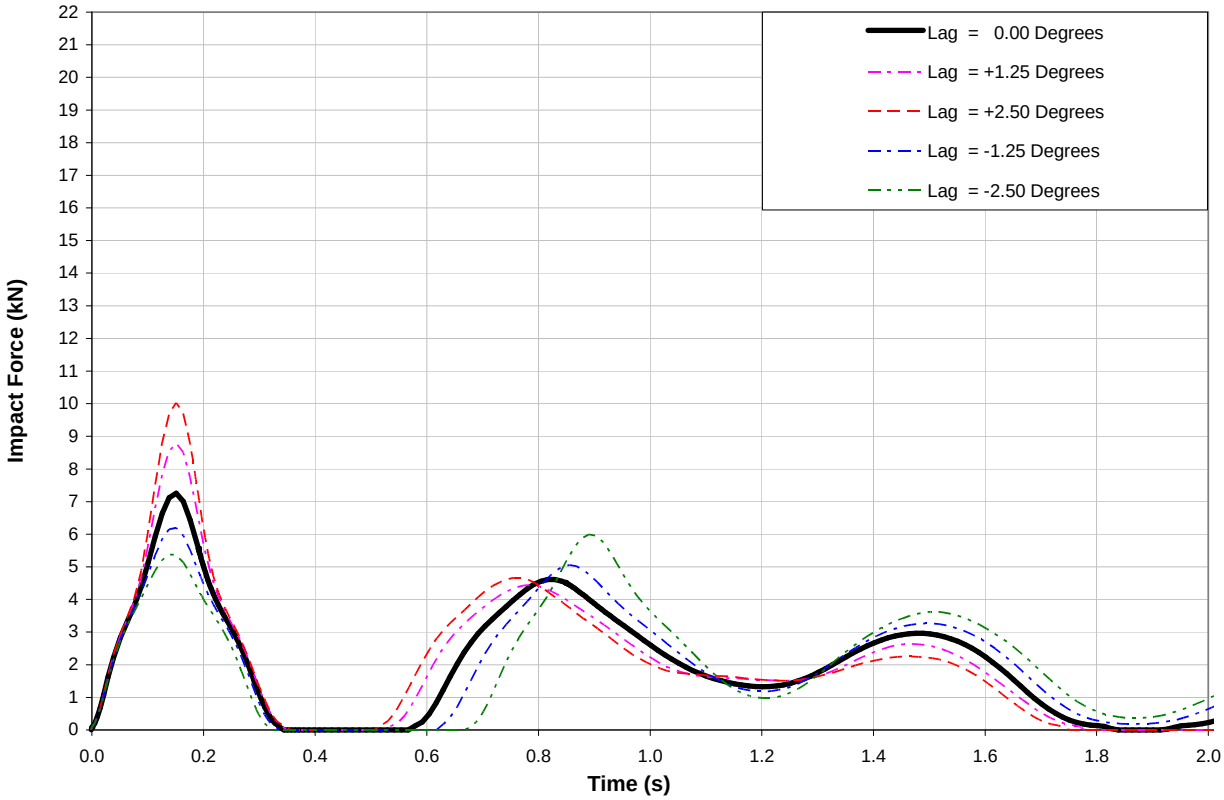

Figure 3.3.1.2 Parameter = Payload Lag: Payload Bottom "Single Bridge EOHTC"

Figures 3.3.1.3 and 3.3.1.4 show the effect of the horizontal lag angle of the payload at impact on the impact force history for the double bridge and the single bridge EOHTC respectively. The results presented here are for the condition of Payload Top.

The significant information which can be extracted from Figure 3.3.1.3: Payload Top: Double Bridge EOHTC are:

- The 1st impact force obtained follows the same trend as obtained for the condition of Payload Bottom where an increase in the lag angle yield a corresponding increase in the impact force and vice versa.
- For this condition, the 2nd impact peak is significantly lower than the 1st impact peak for the double bridge EOHTC.

The numerical differences between the impact forces for the double and single bridge EOHTC are presented in Table 3.3.1.2

Table 3.3.1.2 Influence of the payload lag angle on the impact force history for payload top

Payload Lag Angle (°)	**Single Bridge EOHTC**		**Double Bridge EOHTC**		**Percentage Difference in Impact Force Between the Double and Single Bridge EOHTC (%)**		**Percentage Difference in Impact Force for the Double Bridge EOHTC Relative to the Base Value (%)**	
	1st Impact Force (kN)	**2nd Impact Force (kN)**	**1st Impact Force (Kn)**	**2nd Impact Force (kN)**	**1st Impact**	**2nd Impact**	**1st Impact**	**2nd Impact**
Base value 0°	7.48	8.05	16.85	6.95	125.3	-13.7	NA	NA
-1.25	6.04	7.14	14.60	6.87	141.7	-3.8	-13.4	-1.2
-2.50	5.63	7.96	14.10	9.37	150.4	17.7	-16.3	34.8
+1.25	8.64	8.31	20.00	6.97	131.5	-16.1	18.7	0.3
+2.50	9.92	8.52	20.20	7.00	103.6	-17.8	19.9	0.7

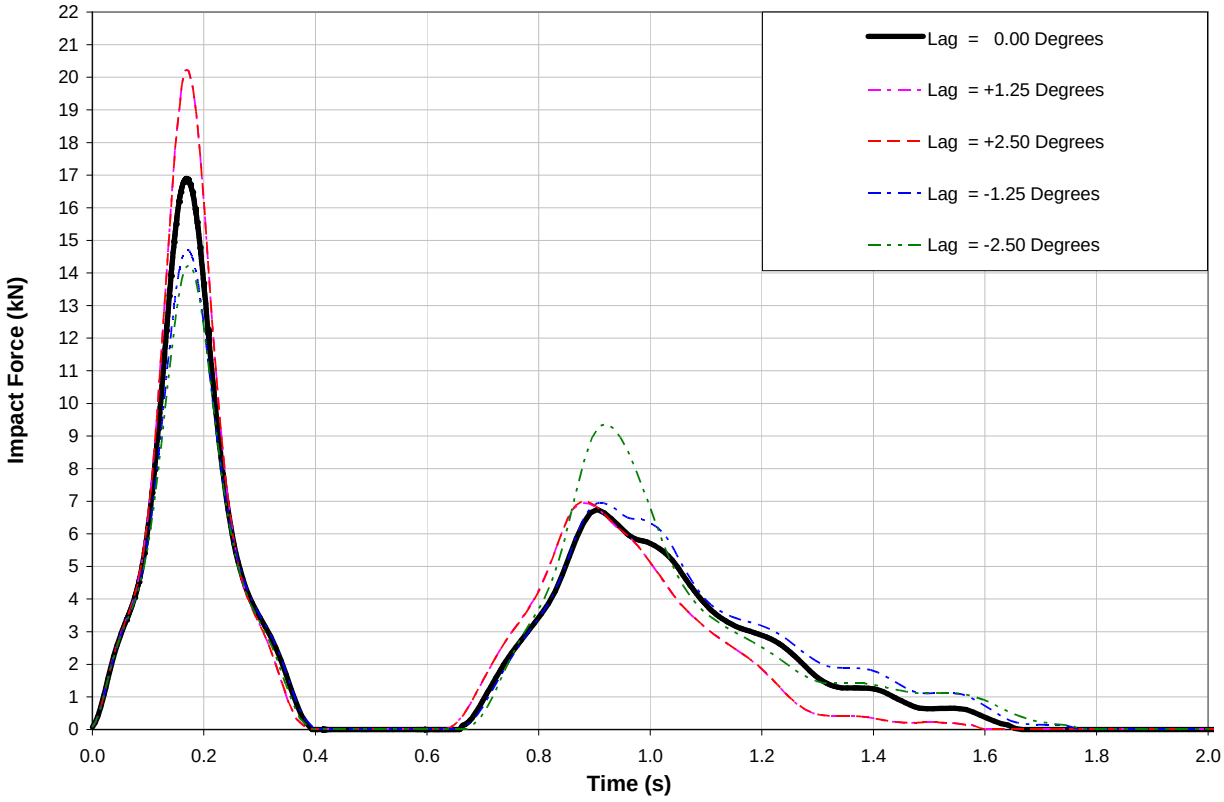

Figure 3.3.1.3 Parameter = Payload Lag: Payload Top "Double Bridge EOHTC"

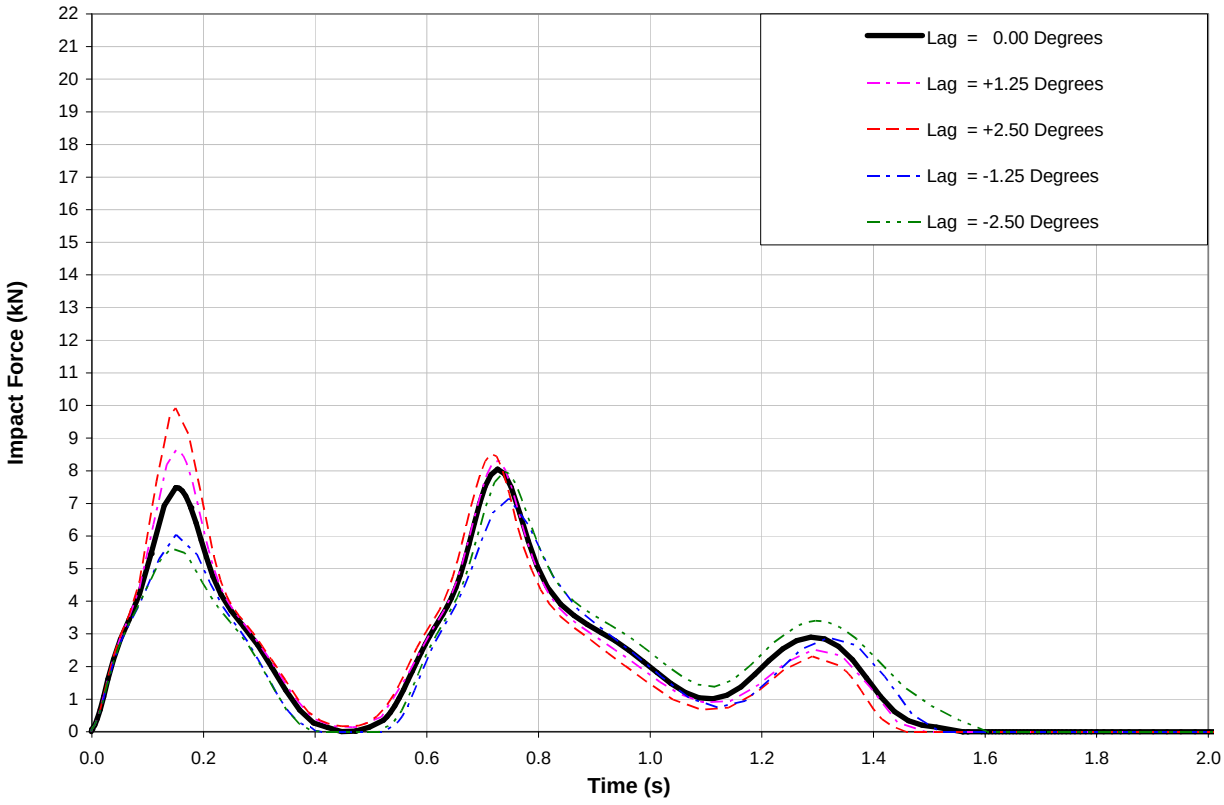

Figure 3.3.1.4 Parameter = Payload Lag: Payload Top "Single Bridge EOHTC

3.3.2 Effect of the End Stop Misalignment on the Impact Force History

For this parameter, the left hand side end stop (LHS) was misaligned by 25mm, 50mm and 150mm in the direction of travel as shown in Figure 3.3.2.1.

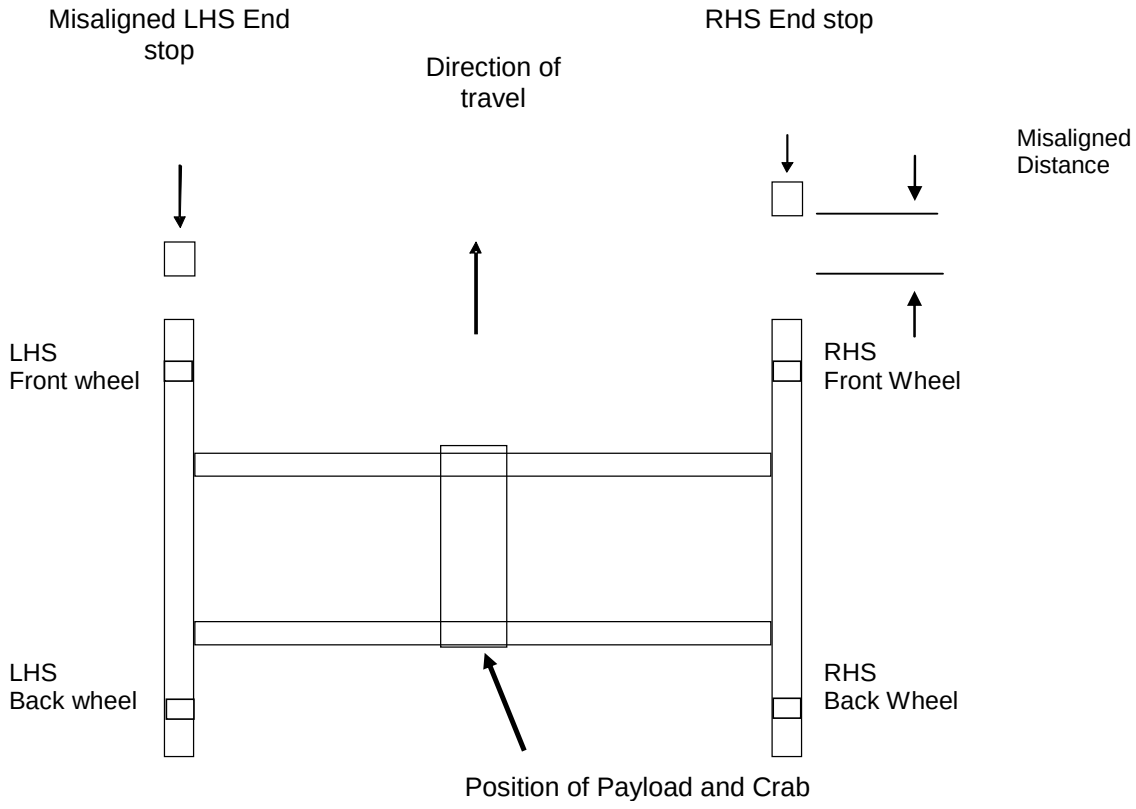

Figure 3.3.2.1 Layout of the misalignment of the Left hand side end stop.

Figures 3.3.2.2 and 3.3.2.3 show the effect of the end stop misalignment on the impact force history for the double bridge and the single bridge EOHTC respectively. The results presented here are for the condition of Payload Bottom.

The significant information which can be extracted from Figure 3.3.2.2: Payload Bottom: Double Bridge EOHTC are:

- The result obtained shows that the impact forces increase at the LHS end stop (misaligned side) with a corresponding increase in the misalignment of the end stop.
- It was observed that for the double bridge EOHTC, the parameter has a greater influence on impact force than that obtained for the single bridge EOHTC. This can be attributed to the increase in the stiffness of the crane bridge for the double bridge EOHTC where significant skewing of the EOHTC was prevented. This will be discussed extensively in chapter 6

- Also the result shows an unexpected trend for the double bridge EOHTC when the end stop was misaligned by 150mm. The result shows that after the 1st impact, the buffers take a longer time to expand and does not loose contact with the end stops throughout impact. The author is of the opinion that due to the increase in the impacting mass on the LHS end stop, the return force from the buffer at the misaligned side was insufficient to push the EOHTC backwards thus preventing loss of contact between the buffer at the misaligned side and the end stop.

The numerical differences between the impact forces for the double and single bridge EOHTC are presented in Table 3.3.2.1

Table 3.3.2.1 Influence of end stop misalignment on the impact force history for payload bottom

End Stop Misalignment (mm)	**Single Bridge EOHTC**		**Double Bridge EOHTC**		**Percentage Difference in Impact Force Between the Double and Single Bridge EOHTC (%)**		**Percentage Difference in Impact Force for the Double Bridge EOHTC Relative to the Base Value (%)**	
	1st Impact Force (kN)	**2nd Impact Force (kN)**	**1st Impact Force (kN)**	**2nd Impact Force (kN)**	**1st Impact**	**2nd Impact**	**1st Impact**	**2nd Impact**
Base value	7.26	4.61	16.34	16.03	125.0	248.0	NA	NA
Misalignment =25mm	8.69	7.10	16.34	12.85	88.0	81.0	0.0	-20.0
Misalignment =50mm	8.65	5.33	21.0	19.46	143.0	265.0	28.0	21.4
Misalignment =150mm	9.69	6.33	25.02	6.52	158.2	3.0	53.12	-59.33

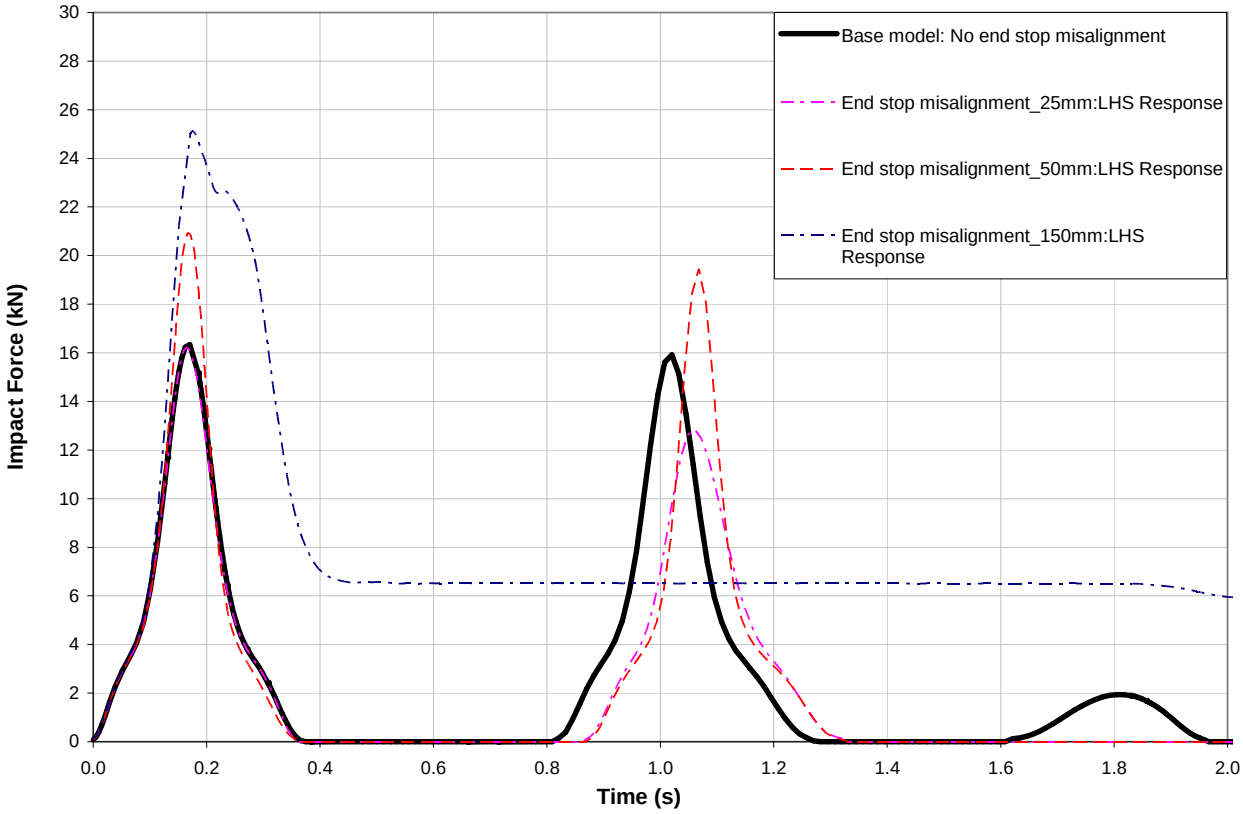

Figure 3.3.2.2 Parameter = End stop misalignment: Payload Bottom "Double Bridge EOHTC"

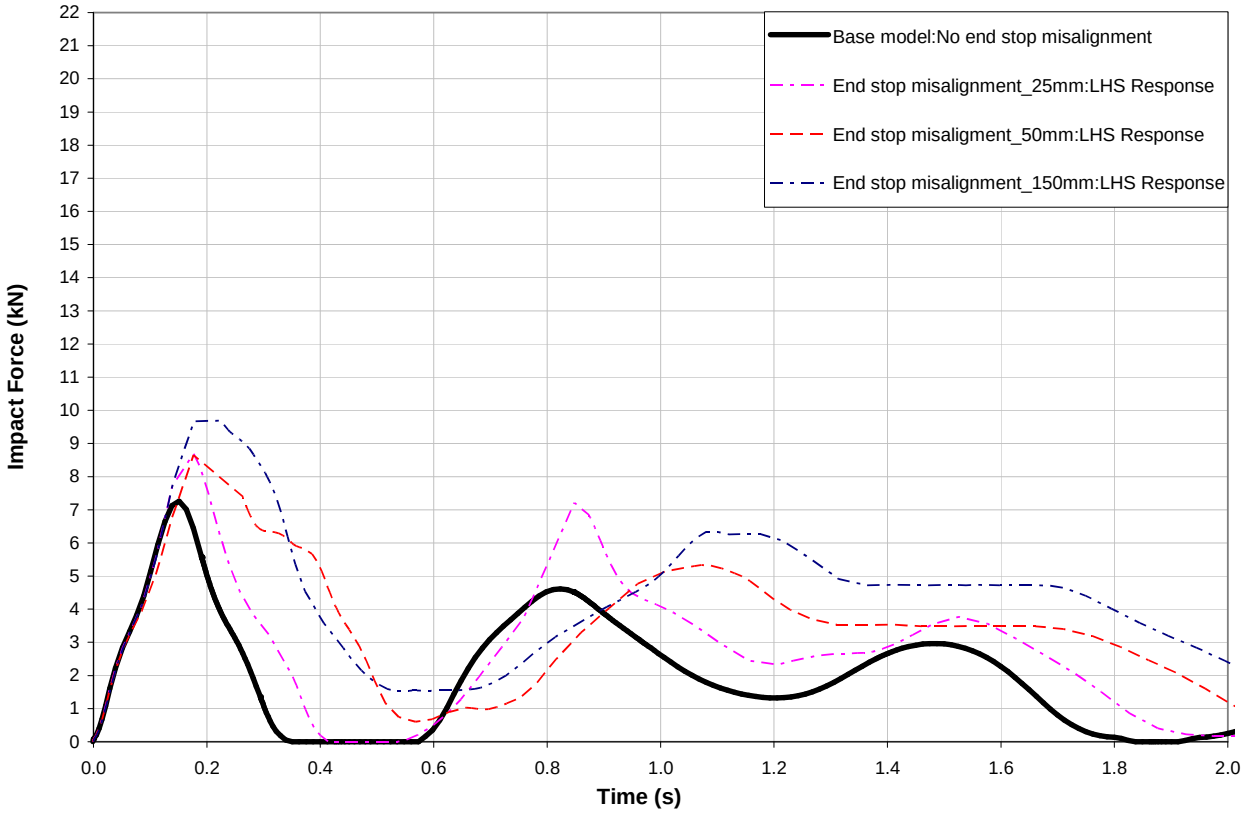

Figure 3.3.2.3 Parameter = End stop misalignment: Payload Bottom "Single Bridge EOHTC"

Figures 3.3.2.4 and 3.3.2.5 show the effect of the end stop misalignment on the impact force history for the double bridge and the single bridge EOHTC respectively. The results presented here are for the condition of Payload Top. The result follows the same trend as obtained for the condition of Payload Bottom.

The significant information which can be extracted from Figure 3.3.2.4: Payload Top: Double Bridge EOHTC are:

- The impact force history obtained follow a trend similar to that obtained for the condition of Payload Bottom where impact force increases with a corresponding increase in the end stop misalignment on the LHS end stop (misaligned side).

- For the double bridge EOHTC, the result obtained for 150mm misalignment of one of the end stops follows a similar trend to that obtained for the condition of payload Bottom.

The numerical differences between the impact forces for the double and single bridge EOHTC are presented in Table 3.3.2.2

Table 3.3.2.2 Influence of end stop misalignment on the impact force history for payload top

End Stop Misalignment (mm)	**Single Bridge EOHTC**		**Double Bridge EOHTC**		**Percentage Difference in Impact Force Between the Double and Single Bridge EOHTC (%)**		**Percentage Difference in Impact Force for the Double Bridge EOHTC Relative to the Base Value (%)**	
	1st Impact Force (kN)	**2nd Impact Force (kN)**	**1st Impact Force (kN)**	**2nd Impact Force (kN)**	**1st Impact**	**2nd Impact**	**1st Impact**	**2nd Impact**
Base value	7.48	8.05	16.85	6.95	125.3	-13.7	NA	NA
Misalignment =25mm	9.10	10.11	17.92	13.00	96.9	28.6	6.4	87.0
Misalignment =50mm	9.78	7.04	22.40	19.46	129.0	176.4	33.0	180.0
Misalignment =150mm	9.72	8.11	23.74	6.03	144.2	-25.6	41.0	-13.23

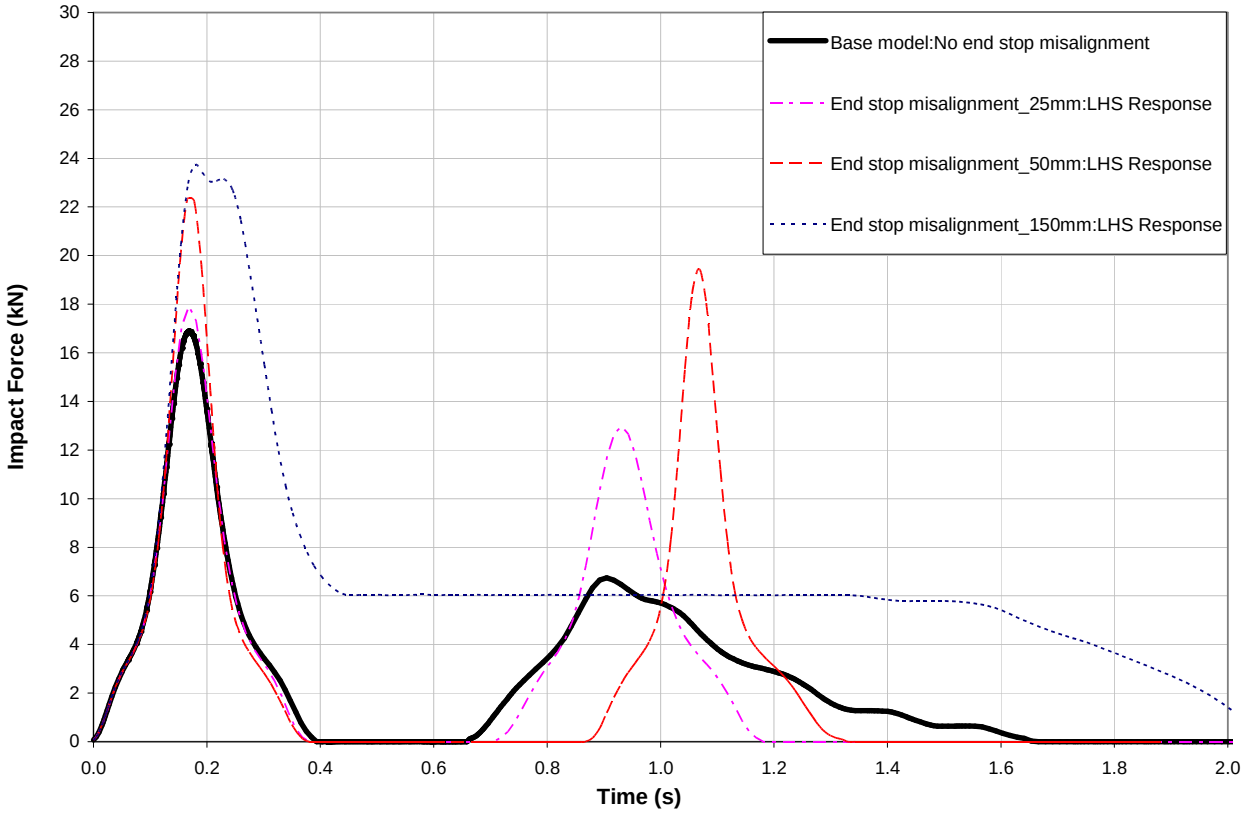

Figure 3.3.2.4 Parameter = End Stop Misalignment: Payload Top “Double Bridge EOHTC"

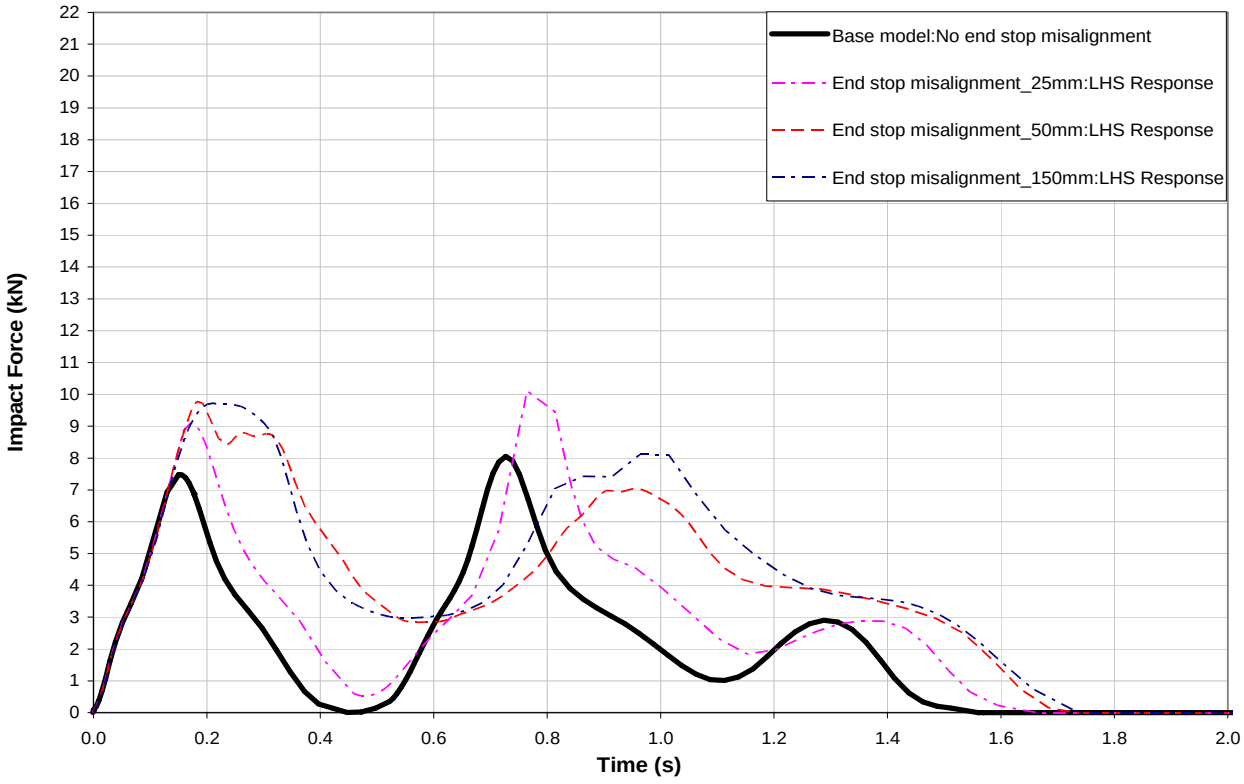

Figure 3.3.2.5 Parameter = End Stop Misalignment: Payload Top “Single Bridge EOHTC”.

3.3.3 Effect of the Crab and Payload Eccentricity on the Impact Force History

Figures 3.3.3.1 and 3.3.3.2 show the effect of the crab and payload eccentricity on the impact force history for the double bridge and the single bridge EOHTC respectively. Eccentricity of the crab and payload is to the left hand side (LHS) of the midpoint of the crane girders. The results presented here are for the condition of Payload Bottom.

The significant information which can be extracted from Figure 3.3.3.1: Payload Bottom: Double Bridge EOHTC are:

- 1st and 2nd impact peaks are minimally affected.
- A notable observation is the reduced effect of the crab and payload eccentricity on the impact peaks for the double bridge EOHTC. This occurs because the increase in the lateral stiffness for the double bridge EOHTC prevents a significant skewing of the EOHTC, which the eccentricity of the crab and payload would have induced.

The numerical differences between the impact forces for the double and single bridge EOHTC are presented in Table 3.3.3.1

Table 3.3.3.1 Influence of crab and payload eccentricity on the impact force history for payload bottom

Crab and Payload Eccentricity (m)	**Single Bridge EOHTC**		**Double Bridge EOHTC**		**Percentage Difference in Impact Force Between the Double and Single Bridge EOHTC (%)**		**Percentage Difference in Impact Force for the Double Bridge EOHTC Relative to the Base Value (%)**	
	1st Impact Force (kN)	**2nd Impact Force (kN)**	**1st Impact Force (kN)**	**2nd Impact Force (kN)**	**1st Impact**	**2nd Impact**	**1st Impact**	**2nd Impact**
Base value	7.26	4.61	16.34	16.03	125.1	247.7	NA	NA
Eccentricity from Reference point= 1.695m	7.94	5.28	16.69	16.72	110.2	216.7	2.1	4.3
Eccentricity from Reference point= 3.39m	8.85	6.05	17.05	17.29	92.7	185.8	4.3	8.0

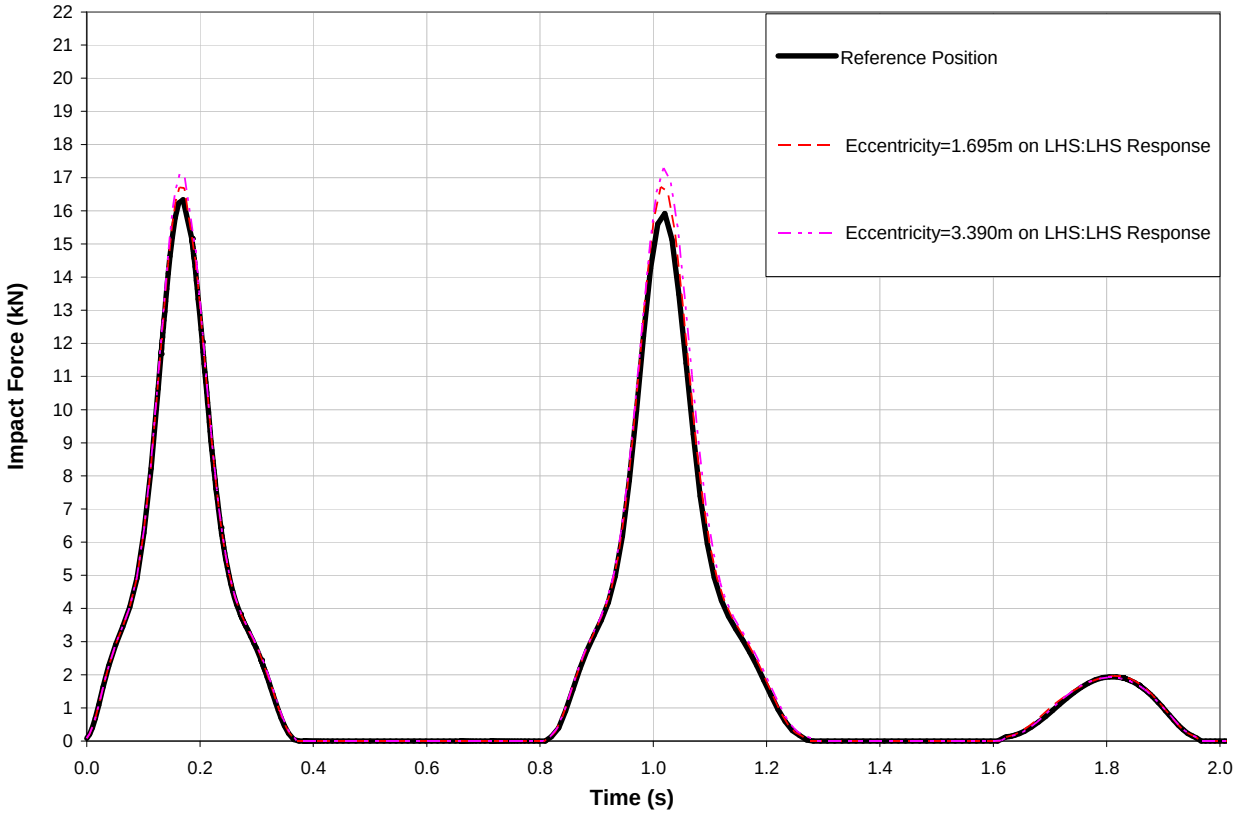

Figure 3.3.3.1 Parameter = Crab and Payload Eccentricity: Payload Bottom "Double Bridge EOHTC"

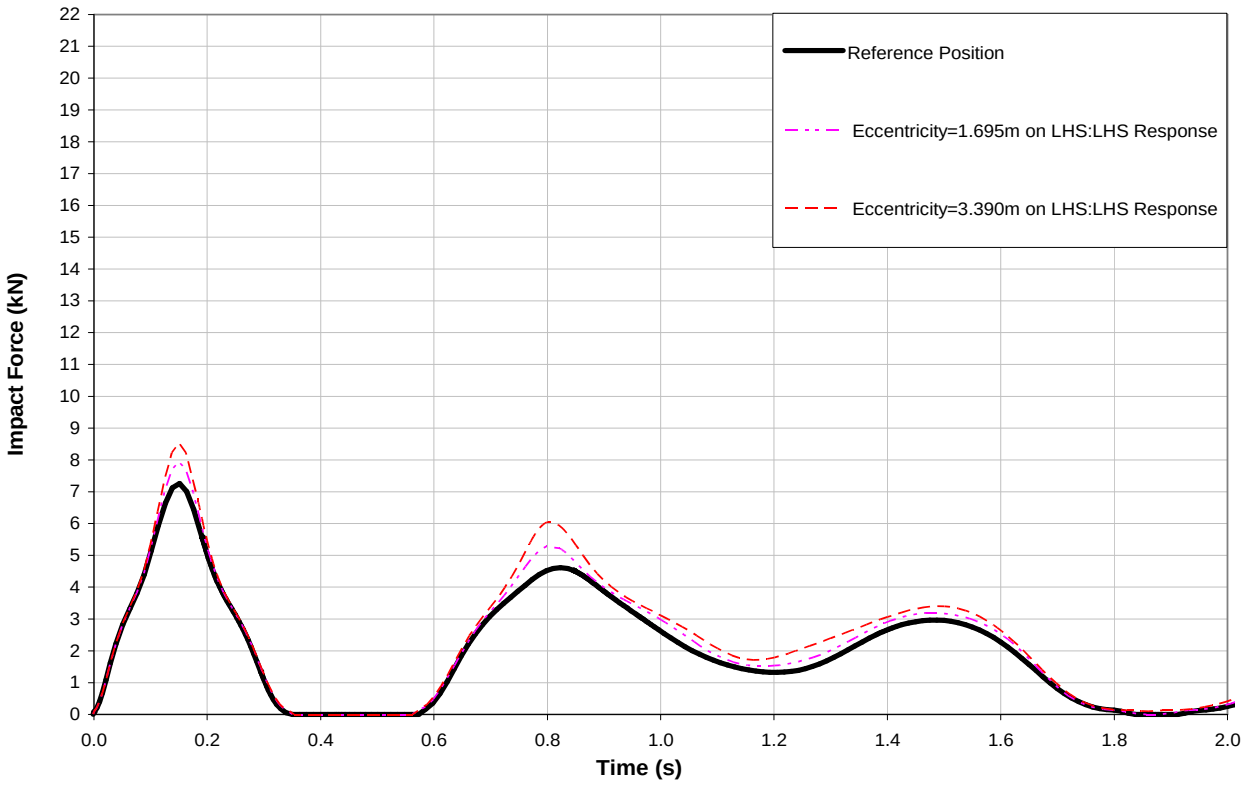

Figure 3.3.3.2 Parameter = Crab and Payload Eccentricity: Payload Bottom "Single Bridge EOHTC"

Figures 3.3.3.3 and 3.3.3.4 show the effect of the crab and payload eccentricity on the impact force history for the double bridge and single bridge EOHTC respectively. The results presented here are for the condition of Payload Top.

The significant information which can be extracted from Figure 3.3.3.3: Payload Top: Double Bridge EOHTC are:

- 1st impact peak is minimally affected.
- The 2nd impact history follows a trend different from the base value. It was observed that at an eccentricity of 3.39m, the 2nd impact peaks was significantly higher than the base value. For this condition, the displacement and the velocity histories obtained from the FEA simulations reveals that, at an eccentricity of 3.39m, both the impact velocity and the displacement of the buffer at 2nd impact are significantly greater than values obtained at the base value. The impact velocity and the displacement of the buffers obtained at 2nd impact at an eccentricity of 1.695m were very close to the those obtained at the base value

The numerical differences between the impact forces for the double and single bridge EOHTC are presented in Table 3.3.3.2

Table 3.3.3.2 Influence of crab and payload eccentricity on the impact force history for payload top

Crab and Payload Eccentricity (m)	**Single Bridge EOHTC**		**Double Bridge EOHTC**		**Percentage Difference in Impact Force Between the Double and Single Bridge EOHTC (%)**		**Percentage Difference in Impact Force for the Double Bridge EOHTC Relative to the Base Value (%)**	
	1st Impact Force (kN)	**2nd Impact Force (kN)**	**1st Impact Force (kN)**	**2nd Impact Force (kN)**	**1st Impact**	**2nd Impact**	**1st Impact**	**2nd Impact**
Base value	7.48	8.05	16.85	6.95	125.3	-13.7	NA	NA
Eccentricity from Reference point = 1.695m	8.56	8.83	17.11	4.12	99.9	-53.3	1.5	-41.0
Eccentricity from Reference point = 3.39m	9.39	9.04	17.69	15.09	88.4	66.9	5.0	117.1

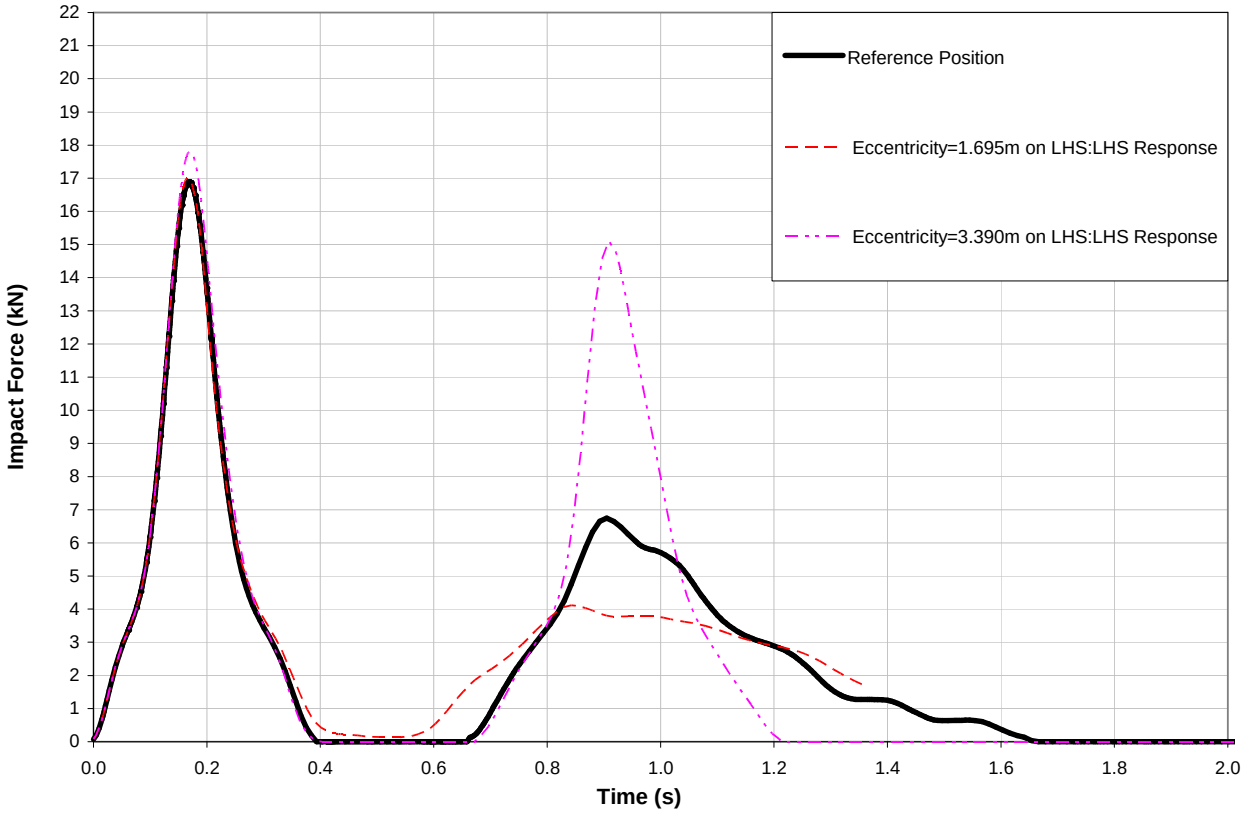

Figure 3.3.3.3 Parameter = Crab and Payload Eccentricity: Payload Top" Double Bridge EOHTC"

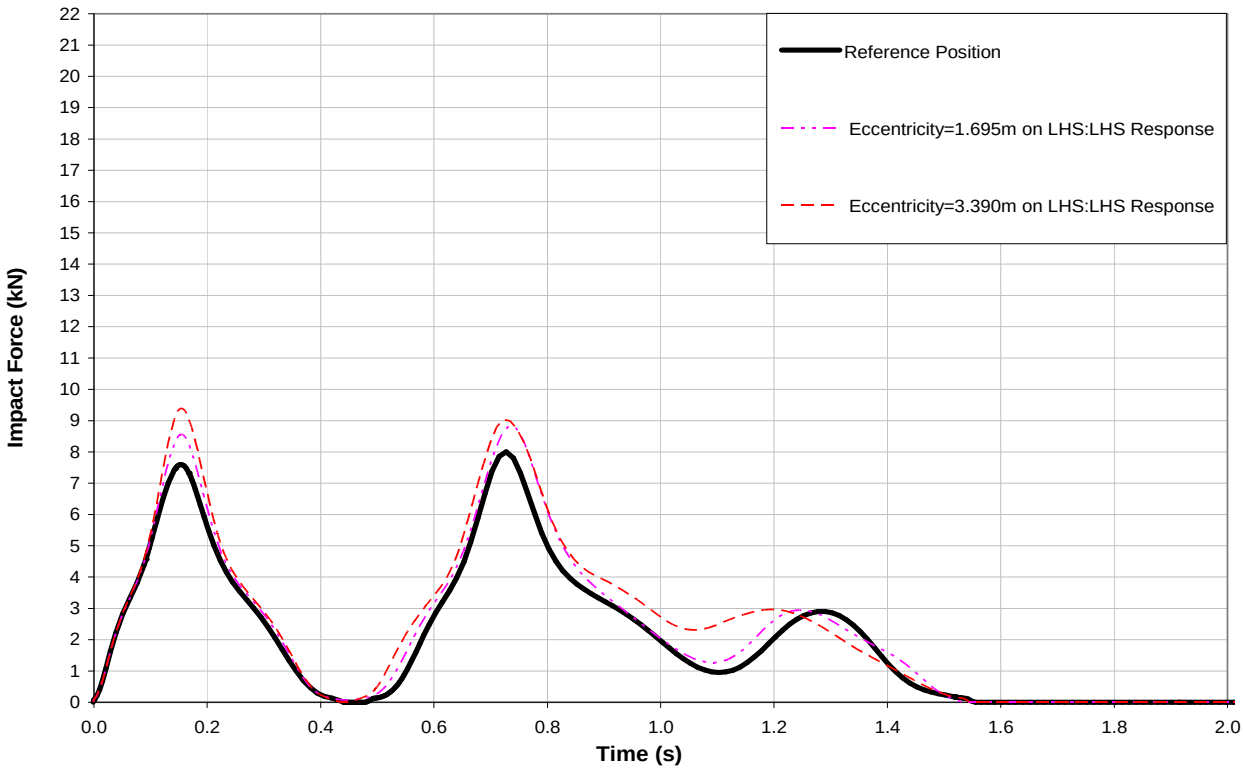

Figure 3.3.3.4 Parameter = Crab and Payload Eccentricity: Payload Top" Single Bridge EOHTC"

3.3.4 Effect of the Impact Velocity on the Impact Force History

Figures 3.3.4.1 and 3.3.4.2 show the effect of the impact velocity from the time of impact on the impact force history for the double bridge and single bridge EOHTC respectively. The result represented here are for the condition of Payload Bottom.

The significant information which can be extracted from Figure 3.3.4.1: Payload Bottom: Double Bridge EOHTC are:

- The 1st impact force increases with an increase in the impact velocity.
- The same trend occurs at 2nd impact
- A notable observation is the increase in the effect of the impact velocity on impact force for the double bridge EOHTC. This is as a result of the non-linear characteristics of the elastomeric buffers and the increase in the impacting mass yielding greater impact peaks as the buffers are compressed.

The numerical differences between the impact forces for the double and single bridge EOHTC are presented in Table 3.3.4.1

Table 3.3.4.1 Influence of the impact velocity on the impact force history for payload bottom

Impact Velocity (m/s)	**Single Bridge EOHTC**		**Double Bridge EOHTC**		**Percentage Difference in Impact Force Between the Double and Single Bridge EOHTC (%)**		**Percentage Difference in Impact Force for the Double Bridge EOHTC Relative to the Base Value (%)**	
	1st Impact Force (kN)	**2nd Impact Force (kN)**	**1st Impact Force (kN)**	**2nd Impact Force (kN)**	**1st Impact**	**2nd Impact**	**1st Impact**	**2nd Impact**
Base value 0.55 (m/s)	7.26	4.61	16.34	16.03	125.1	247.7	NA	NA
0.385 (m/s)	3.90	2.72	6.36	5.18	63.1	90.4	-61.1	-67.7
0.50 (m/s)	5.82	3.70	12.73	11.40	118.7	208.1	-22.1	-28.9
0.60 (m/s)	8.97	7.05	20.10	21.01	124.1	198.0	23.0	31.1

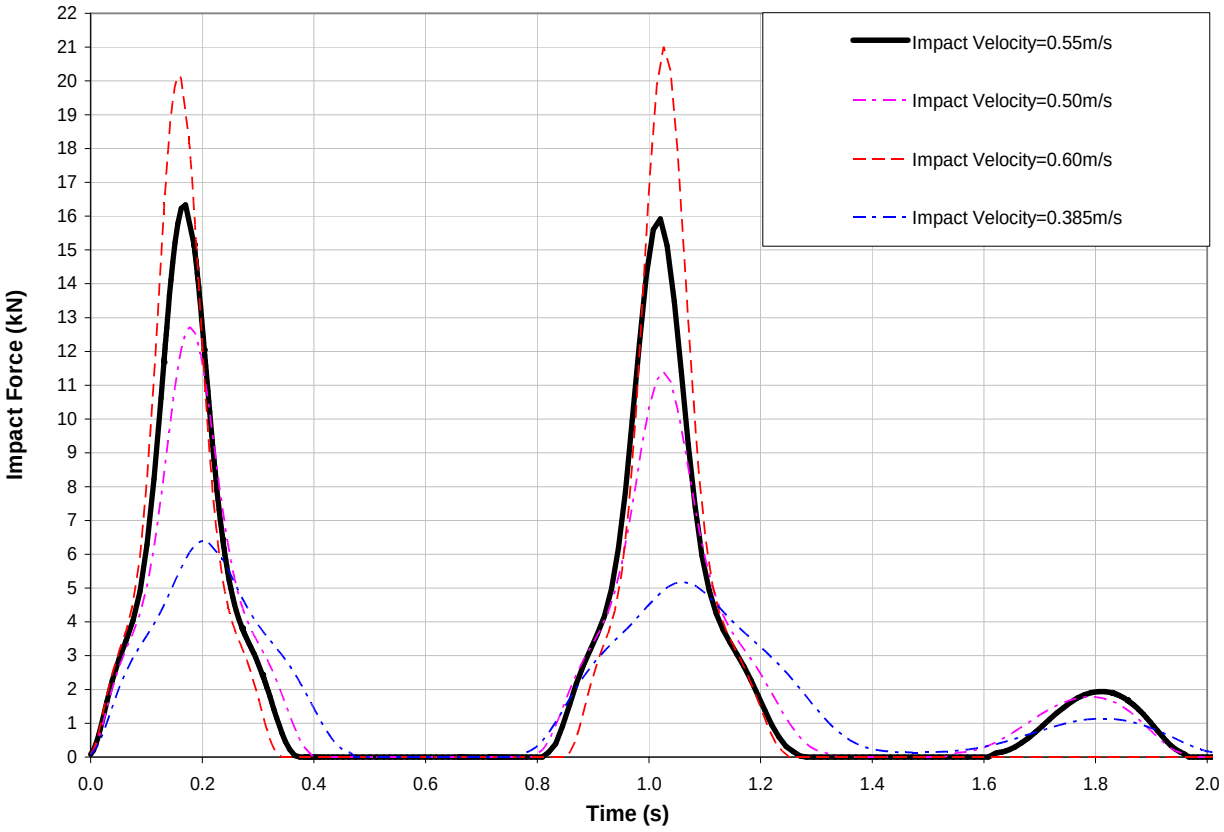

Figure 3.3.4.1 Parameter = Impact Velocity: Payload Bottom" Double Bridge EOHTC"

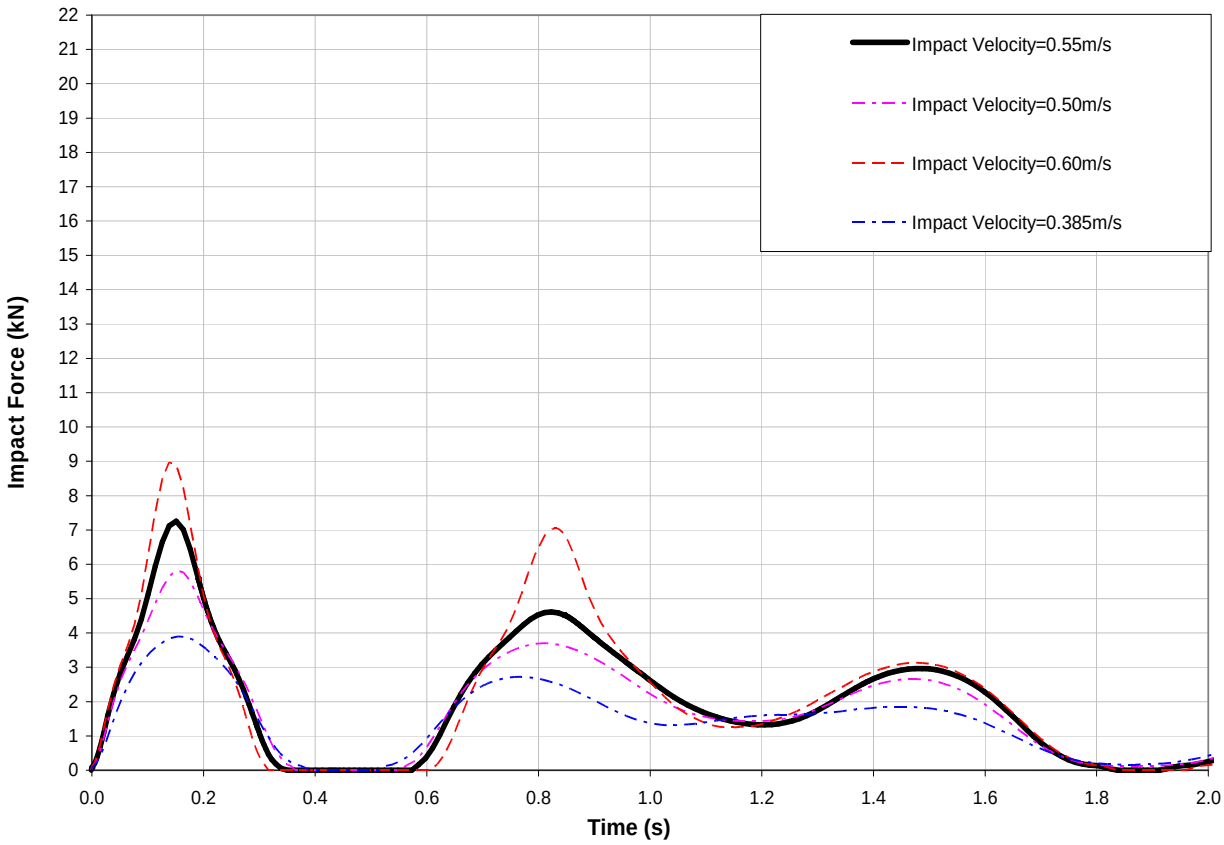

Figure 3.3.4.2 Parameter = Impact Velocity: Payload Bottom" Single Bridge EOHTC"

Figures 3.3.4.3 and 3.3.4.4 show the effect of the impact velocity from the time of impact on the impact force history for the double bridge and the single bridge EOHTC respectively. The results presented here are for the condition of Payload Top.

The significant information which can be extracted from Figure 3.3.4.3: Payload Top: Double Bridge EOHTC are:

- At 1st impact, the results follows a trend similar to that obtained for the payload bottom where impact force increases with a corresponding increase in the impact velocity
- The 2nd impact however follows an unexpected trend. It is observed that for each change in the impact velocity, the 2nd impact peaks were lower than the base value.

The numerical differences between the impact forces for the double and single bridge EOHTC are presented in Table 3.3.4.2

Table 3.3.4.2 Influence of the impact velocity on the impact force history for payload top.

Impact Velocity (m/s)	**Single Bridge EOHTC**		**Double Bridge EOHTC**		**Percentage Difference in Impact Force Between the Double and Single Bridge EOHTC (%)**		**Percentage Difference in Impact Force for the Double Bridge EOHTC Relative to the Base Value (%)**	
	1st Impact Force (kN)	**2nd Impact Force (kN)**	**1st Impact Force (kN)**	**2nd Impact Force (kN)**	**1st Impact**	**2nd Impact**	**1st Impact**	**2nd Impact**
Base value 0.55 (m/s)	7.48	8.05	16.85	6.95	125.3	-13.7	NA	NA
0.385 (m/s)	3.67	3.68	6.55	1.69	78.5	-54.1	-61.1	-75.7
0.50 (m/s)	6.06	6.17	13.12	3.85	116.5	-37.6	-22.1	-44.6
0.60 (m/s)	9.31	10.34	20.7	4.38	122.3	-57.6	22.8	-37.0

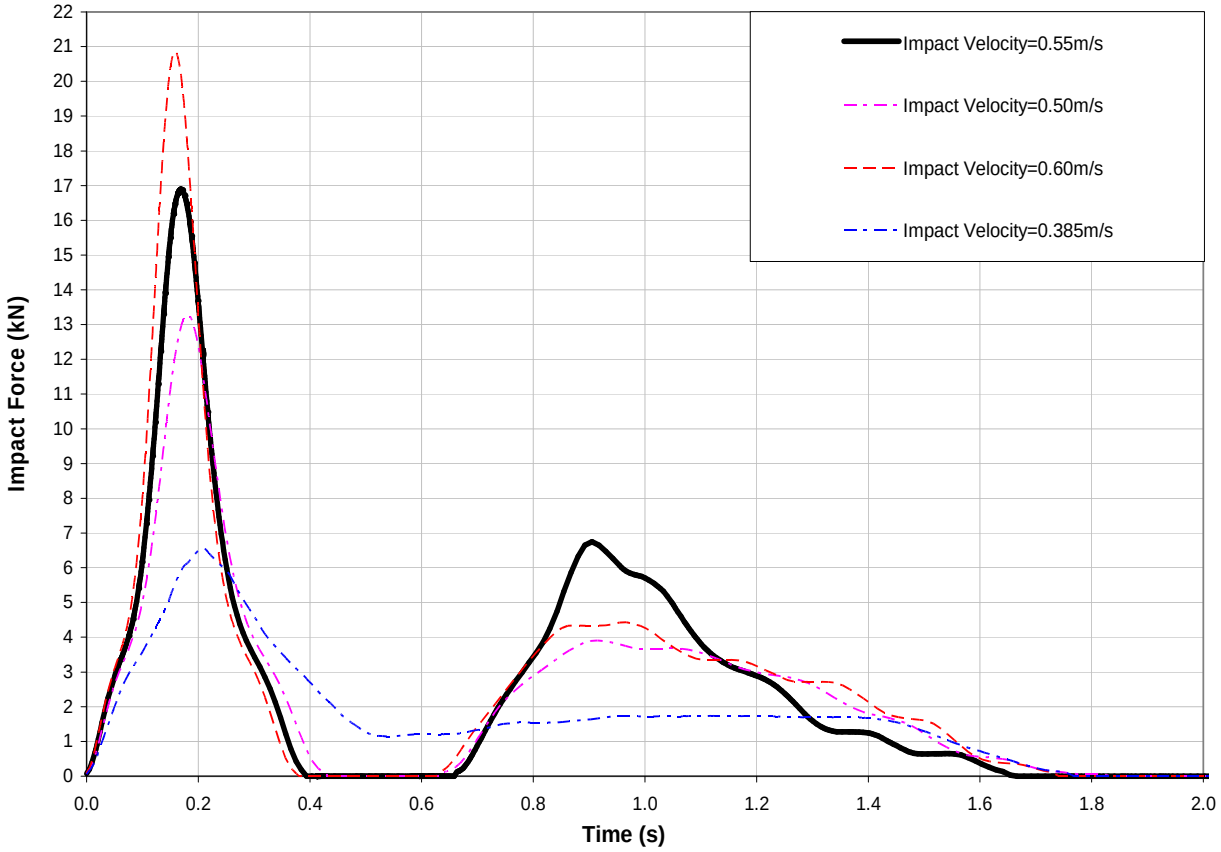

Figure 3.3.4.3 Parameter = Impact Velocity: Payload Top" Double Bridge EOHTC"

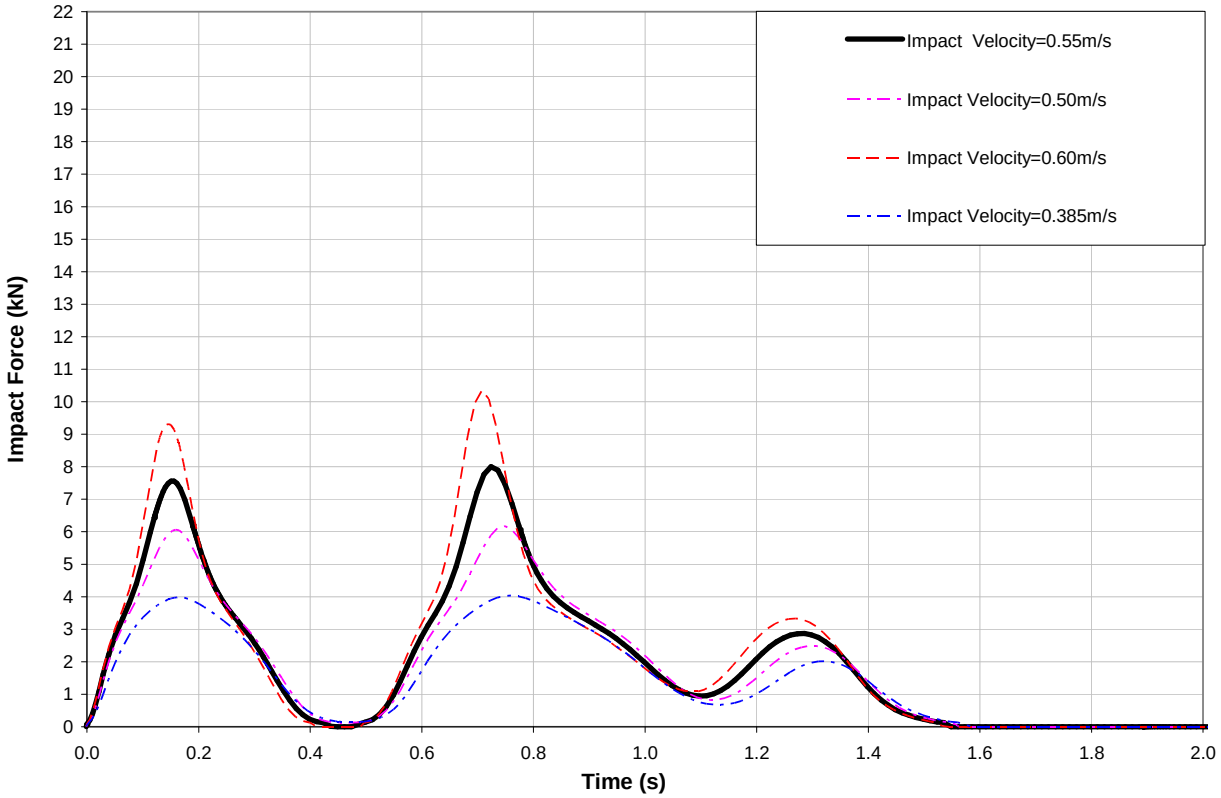

Figure 3.3.4.4 Parameter = Impact Velocity: Payload Top" Single Bridge EOHTC"

3.3.5 Effect of Buffers' Damping Characteristics on the Impact Force History

Figures 3.3.5.1 and 3.3.5.2 show the effect of buffer's damping characteristics on the impact force history for the double bridge and single bridge EOHTC respectively. The results presented here are for the condition of Payload Bottom. The significant information which can be extracted from Figure 3.3.5.1: Payload Bottom: Double Bridge EOHTC are:

- The 1st impact force yields a 12% increase when damping was omitted from the model.
- At 2nd impact, there is a significant shift in the time of impact when the damping characteristics were omitted from the model.
- Also it was observed that when the damping characteristics were omitted from the model, the 2nd impact yield a 25% increase for the Double Bridge EOHTC. However, for the single bridge EOHTC, the 2nd impact peak increased by 210% when the damping characteristics were omitted from the model.
- The author is of the opinion that the increased inertia of the double bridge EOHTC reduces the influence of the return force from the buffers with which the crane is pushed back after 1st impact. This results in the double crane EOHTC travelling at a reduced velocity before it returns for 2nd impact. The impact force history shown in Figures 3.3.5.1 and 3.3.5.2 reveals an increase in the time difference between the impacts peaks for the double bridge EOHTC when compared with the single bridge EOHTC

The numerical differences between the impact forces for the double bridge and single bridge EOHTC are presented in Table 3.3.5.1

Table 3.3.5.1 Influence of buffer's damping characteristics on the impact force history for payload bottom

Buffer's Damping Characteristics	**Single Bridge EOHTC**		**Double Bridge EOHTC**		**Percentage Difference in Impact Force Between the Double and Single Bridge EOHTC (%)**		**Percentage Difference in Impact Force for the Double Bridge EOHTC Relative to the Base Value (%)**	
	1st Impact Force (kN)	**2nd Impact Force (kN)**	**1st Impact Force (kN)**	**2nd Impact Force (kN)**	**1st Impact**	**2nd Impact**	**1st Impact**	**2nd Impact**
Base value	7.26	4.61	16.34	16.03	125.1	247.7	NA	NA
No Damping	8.71	14.33	18.24	20.00	109.4	39.6	11.6	25

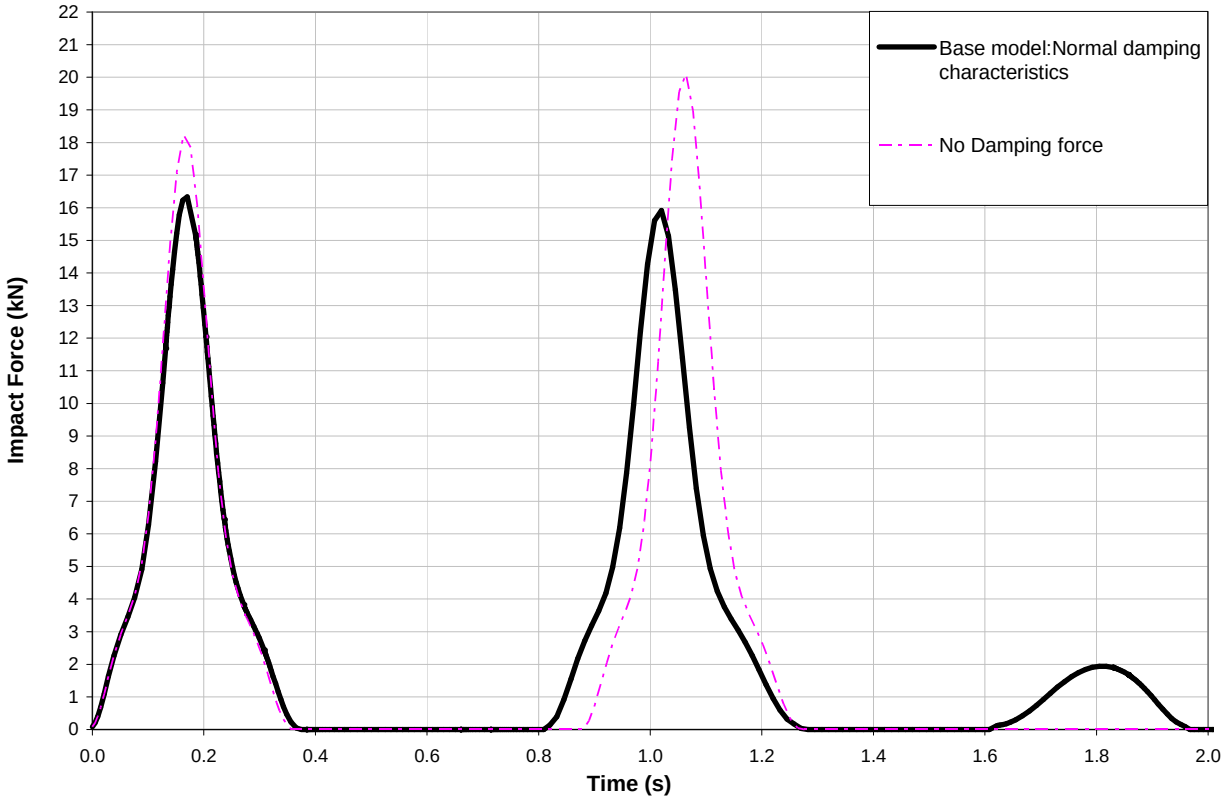

Figure 3.3.5.1 Parameter = Buffer's Damping Characteristics: Payload Bottom "Double Bridge EOHTC"

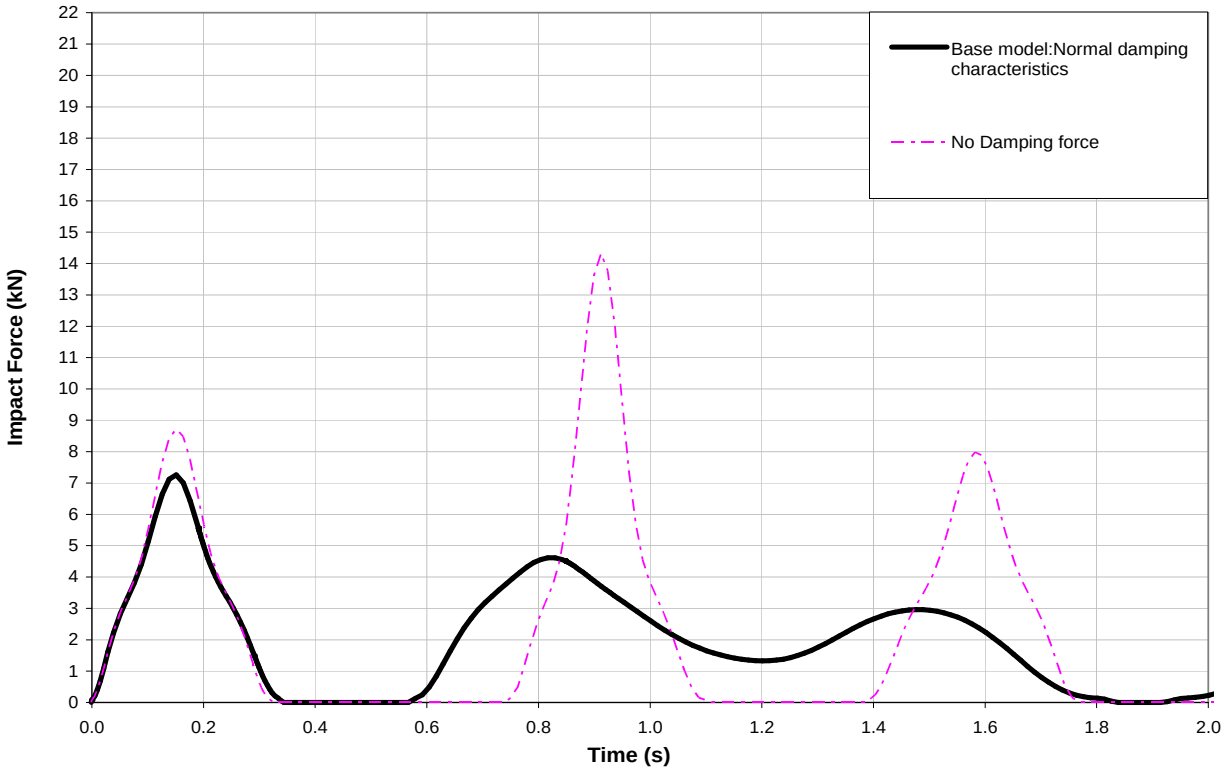

Figure 3.3.5.2 Parameter = Buffer's Damping Characteristics: Payload Bottom "Single Bridge EOHTC"

Figures 3.3.5.3 and 3.3.5.4 show the effect of the buffer's damping characteristics on the impact force history for the double bridge and single bridge EOHTC respectively. The results presented here are for the condition of Payload Top.

The significant information which can be extracted from Figure 3.3.5.3: Payload Top: Double Bridge EOHTC are:

- When the buffer's damping characteristics were omitted from the model, both the 1st and the 2nd impact peaks increased significantly.

The numerical differences between the impact forces for the double bridge and the single bridge EOHTC are presented in Table 3.3.5.2

Table 3.3.5.2 Influence of buffer's damping characteristics on the impact force history for payload top.

Buffer's Damping Characteristics	**Single Bridge EOHTC**		**Double Bridge EOHTC**		**Percentage Difference in Impact Force Between the Double and Single Bridge EOHTC (%)**		**Percentage Difference in Impact Force for the Double Bridge EOHTC Relative to the Base Value (%)**	
	1st Impact Force (kN)	**2nd Impact Force (kN)**	**1st Impact Force (kN)**	**2nd Impact Force (kN)**	**1st Impact**	**2nd Impact**	**1st Impact**	**2nd Impact**
Base value	7.48	8.05	16.85	6.95	125.3	-13.7	NA	NA
No Damping	9.01	12.48	19.83	9.50	120.1	-23.9	17.7	37.0

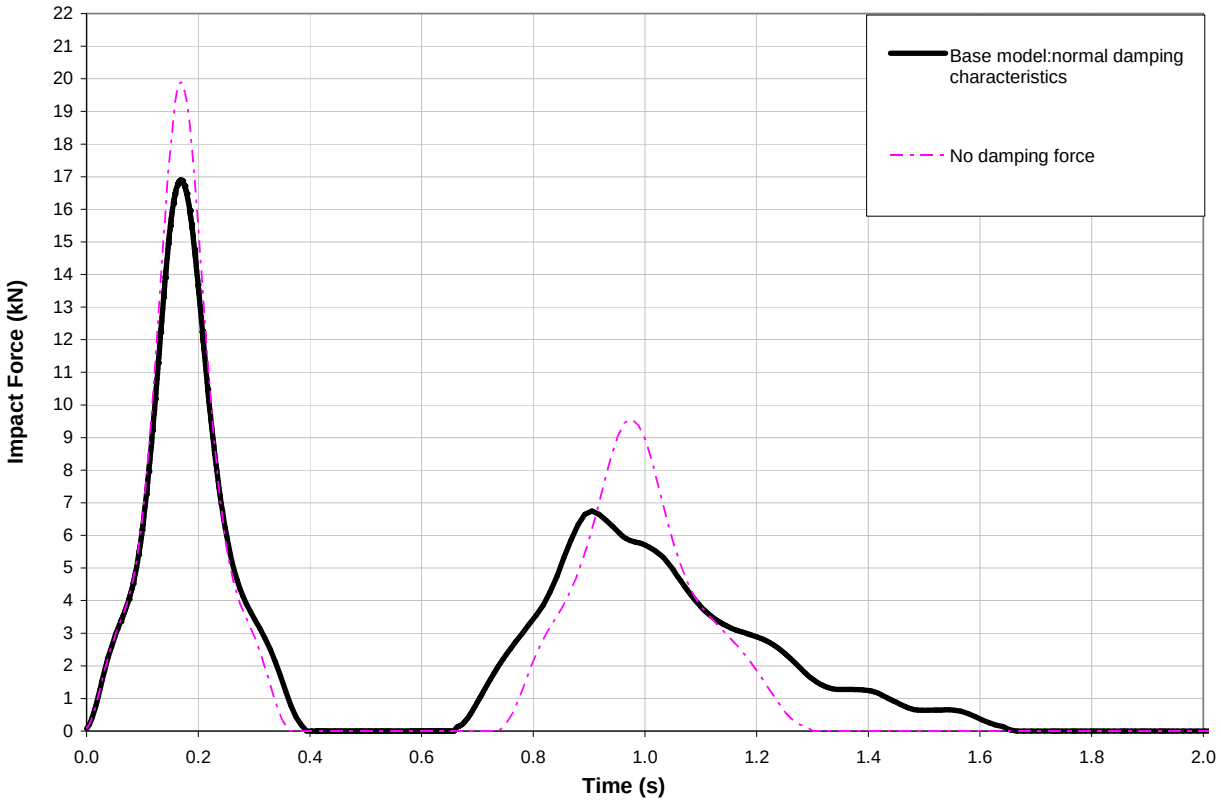

Figure 3.3.5.3 Parameter = Buffer's Damping Characteristics: Payload Top "Double Bridge EOHTC"

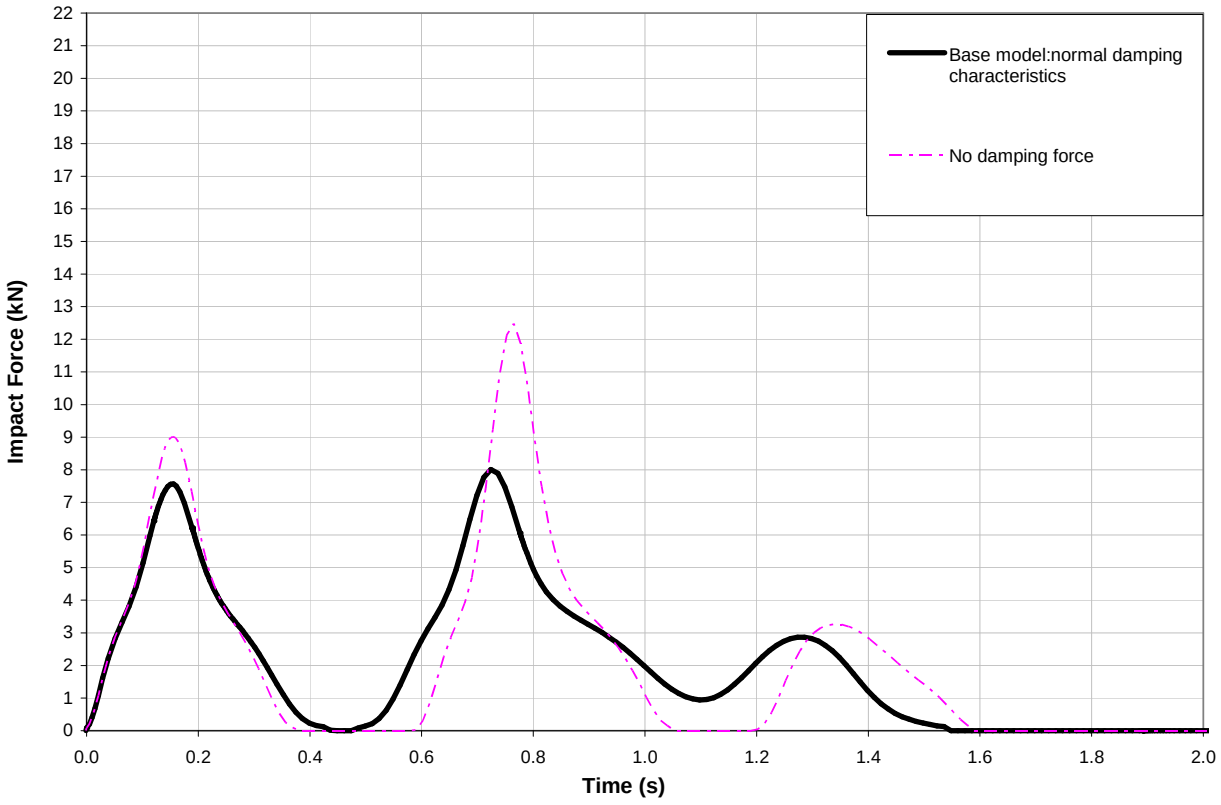

Figure 3.3.5.4 Parameter = Buffer's Damping Characteristics: Payload Top "Single Bridge EOHTC"

3.3.6 Effect of the Gantry's Stiffness on the Impact Force History

Figures 3.3.6.1 and 3.3.6.2 show the effect of the gantry's stiffness on the impact force history for the double bridge and single bridge EOHTC respectively. The results presented here are for the condition of Payload Bottom.

The significant information which can be extracted from Figure 3.3.6.1: Payload Bottom: Double Bridge EOHTC are:

- It was observed that for the double bridge EOHTC, an increase in gantry's stiffness has a reduced influence on the 2nd impact force
- It was also observed that for the double bridge EOHTC, the time difference between impact peaks increased significantly.

The numerical differences between the impact forces for the double and single bridge EOHTC are presented in Table 3.3.6.1

Table 3.3.6.1 Influence of the gantry's stiffness on the impact force history for Payload Bottom

Gantry's Stiffness (N/m)	**Single Bridge EOHTC**		**Double Bridge EOHTC**		**Percentage Difference in Impact Force Between the Double and Single Bridge EOHTC (%)**		**Percentage Difference in Impact Force for the Double Bridge EOHTC Relative to the Base Value (%)**	
	1st Impact Force (kN)	**2nd Impact Force (kN)**	**1st Impact Force (kN)**	**2nd Impact Force (kN)**	**1st Impact**	**2nd Impact**	**1st Impact**	**2nd Impact**
Base value	7.26	4.61	16.34	16.03	125.1	247.7	NA	NA
Weak Spring 1.75×10^5 N/m	5.03	6.85	7.49	7.13	48.9	4.10	-54.2	-55.5
Intermediate spring 1.75×10^6 N/m	6.62	5.01	10.34	12.36	56.2	146.7	-36.7	-22.9
Stiff Spring 1.75×10^7 N/m	7.65	4.65	16.00	14.51	109.2	212.0	-2.1	-9.5

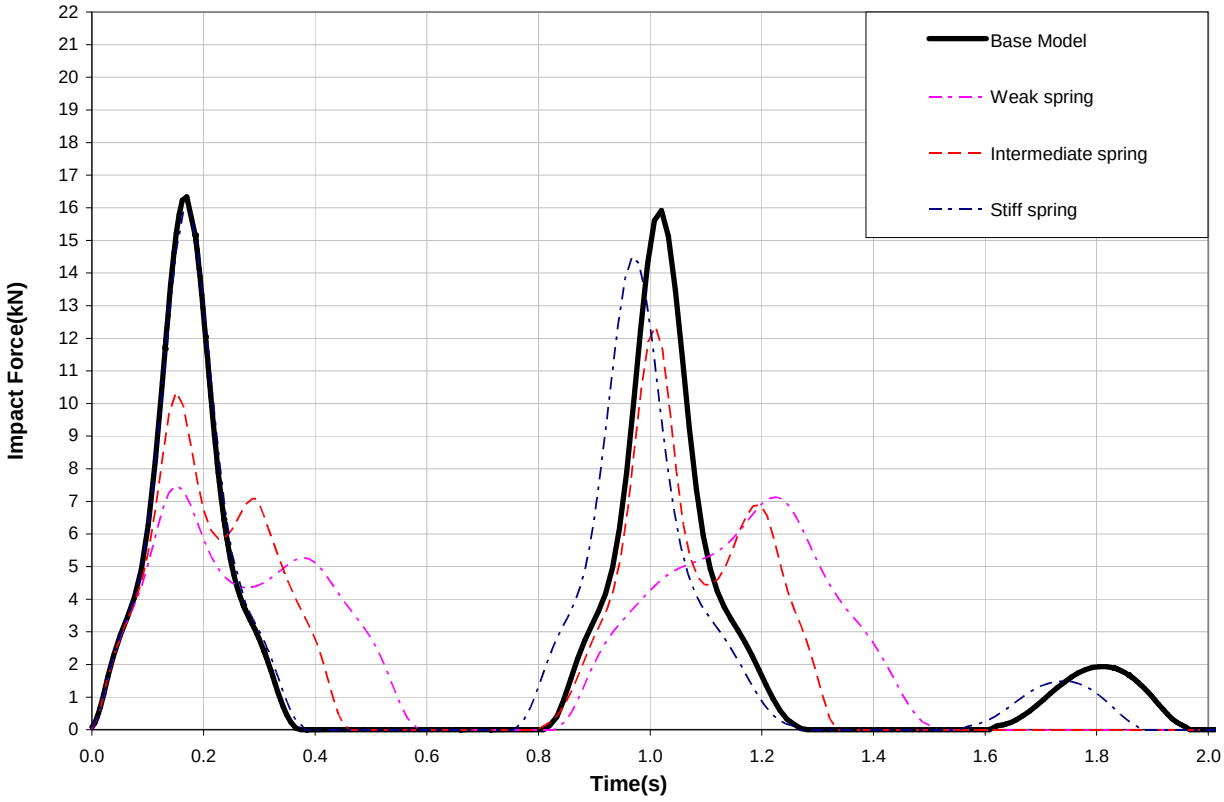

Figure 3.3.6.1 Parameter = Gantry's Stiffness: Payload Bottom "Double Bridge EOHTC"

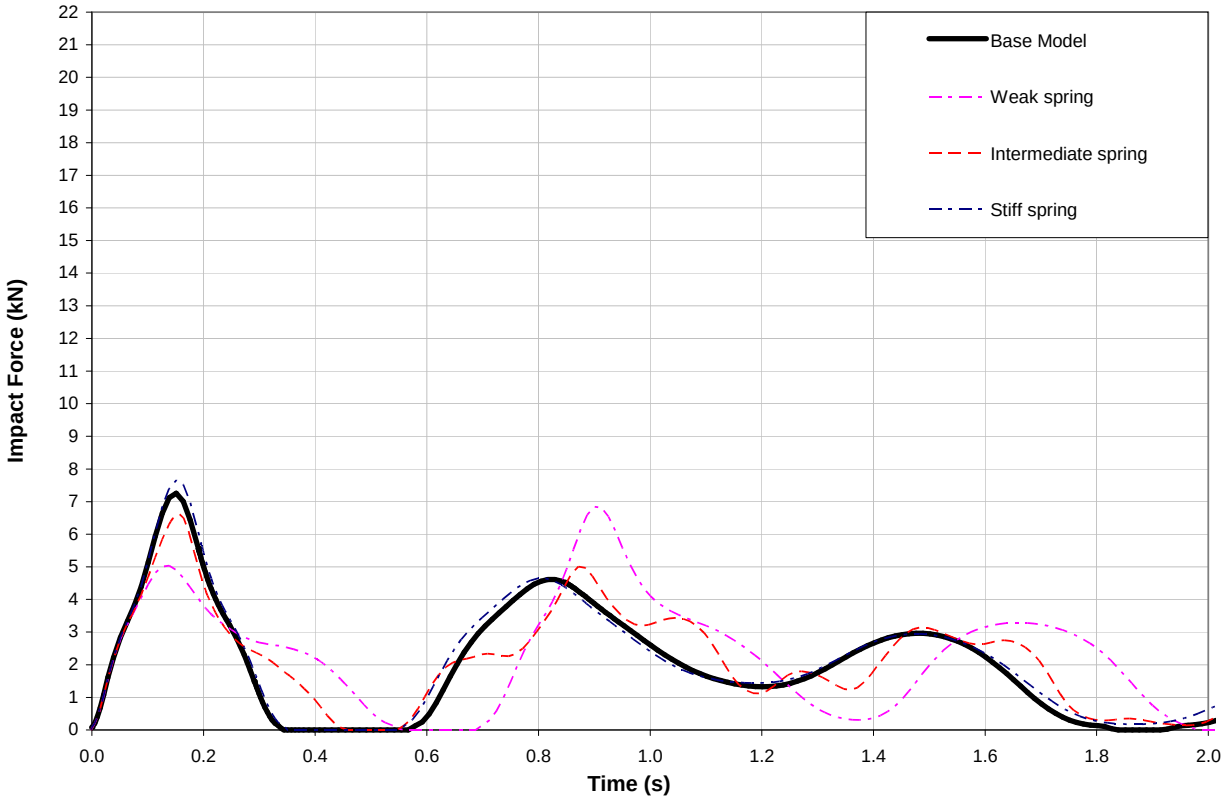

Figure 3.3.6.2 Parameter = Gantry's Stiffness: Payload Bottom "Single Bridge EOHTC"

Figures 3.3.6.3 and 3.3.6.4 show the effect of the gantry's stiffness on the impact force history for the double bridge and single bridge EOHTC respectively. The results presented here are for the condition of Payload Top.

The significant information which can be extracted from Figure 3.3.6.3: Payload Top: Double Bridge EOHTC are:

- The results obtained at 1st impact follows a trend similar to that obtained for the condition of payload bottom where impact peaks decreased with a corresponding decrease in the spring's stiffness
- The result obtained at 2nd impact follows a different trend. It was observed that for the model with the stiff spring, the 2nd impact peak increased significantly. The same occurred for the model with the intermediate spring.

The numerical differences between the impact forces for the double and single bridge EOHTC are presented in Table 3.3.6.2

Table 3.3.6.2 Influence of the gantry's stiffness on the impact force history for payload top

Gantry's Stiffness N/m	**Single Bridge EOHTC**		**Double Bridge EOHTC**		**Percentage Difference in Impact Force Between the Double and Single Bridge EOHTC (%)**		**Percentage Difference in Impact Force for the Double Bridge EOHTC Relative to the Base Value (%)**	
	1st Impact Force (kN)	2nd Impact Force (kN)	1st Impact Force (kN)	2nd Impact Force (kN)	1st Impact	2nd Impact	1st Impact	2nd Impact
Base value	7.48	8.05	16.85	6.95	125.3	-13.7	NA	NA
Weak Spring 1.75×10^5 N/m	4.92	9.01	7.98	6.77	62.2	-24.9	-52.6	-2.6
Intermediate spring 1.75×10^6 N/m	6.52	7.48	10.98	13.55	68.4	81.1	-34.8	95.0
Stiff Spring 1.75×10^7 N/m	7.48	7.9	17.41	14.02	132.8	77.5	3.3	101.7

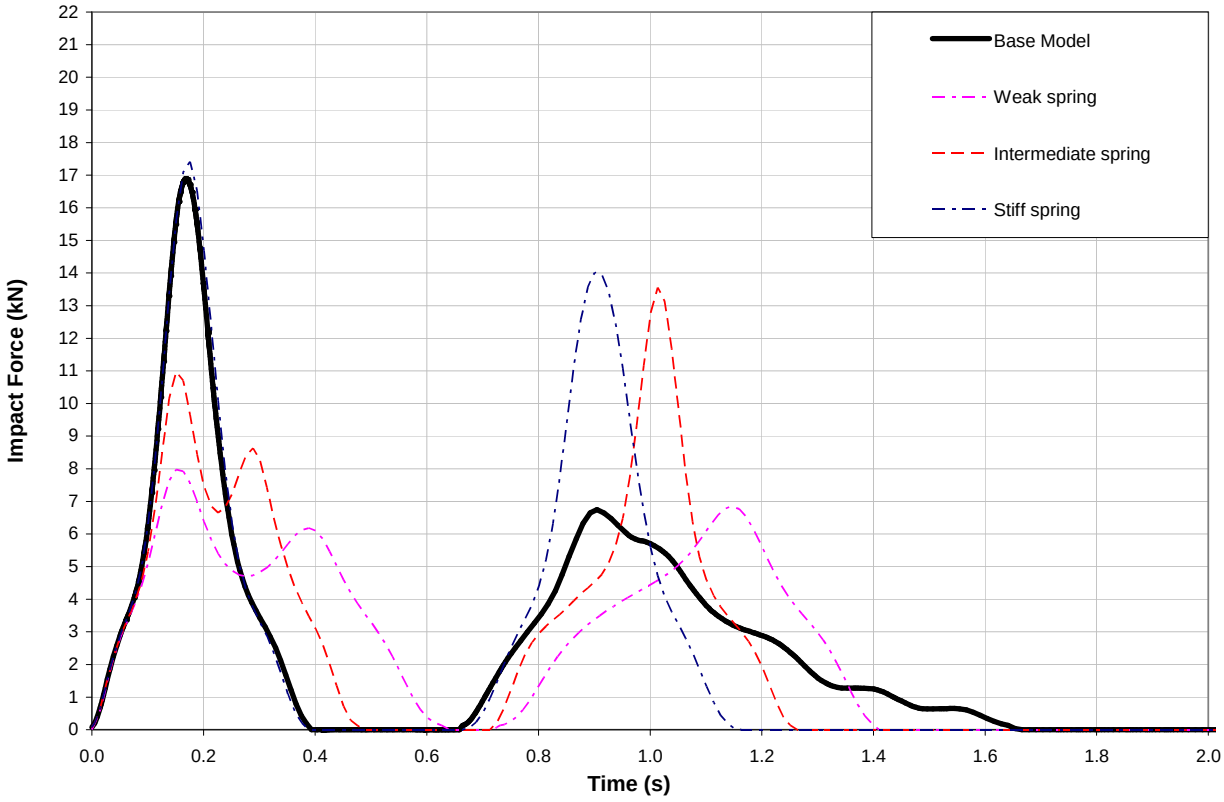

Figure 3.3.6.3 Parameter = Gantry's Stiffness: Payload Top "Double Bridge EOHTC"

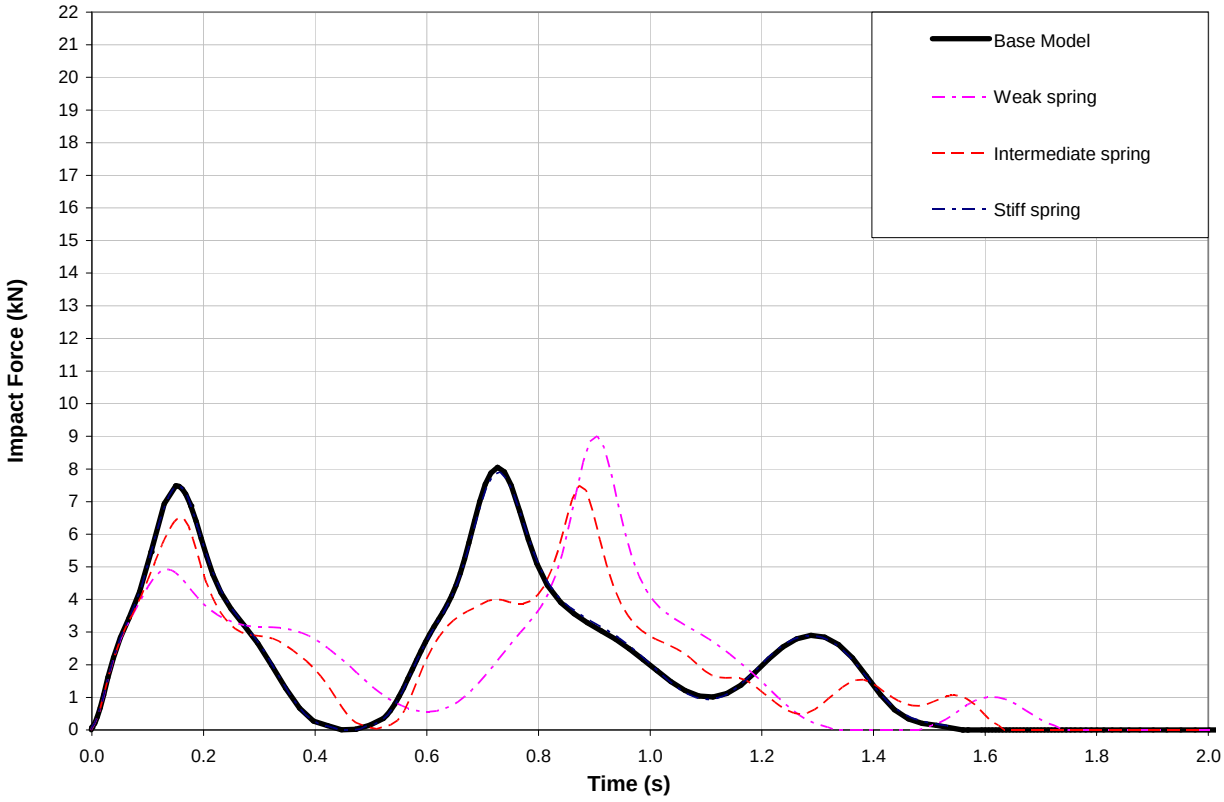

Figure 3.3.6.4 Parameter = Gantry's Stiffness: Payload Top "Single Bridge EOHTC"

3.4 Summary of Sensitivity Analysis (Double Bridge EOHTC)

From the sensitivity study conducted, the maximum impact force obtained for each parameter investigated is presented in Table 3.4.1

Table 3.4.1 Summary of sensitivity study for double bridge EOHTC.

PARAMETERS	CONDITION OF OCCURRENCE	BASE VALUE (kN)	MAXIMUM IMPACT (kN)
Lag Angle	Payload Bottom, 1st impact	16.34	21.13
End Stop Misalignment	Payload Bottom, 1st impact	16.34	25.02
Crab Eccentricity	Payload Top, 1st impact	16.85	17.69
Velocity at Impact	Payload Bottom, 2nd impact	16.03	21.01
Buffer's Damping Characteristics	Payload Bottom, 2nd impact	16.03	20.00
Gantry's Stiffness	Payload Top, 1st impact	16.85	17.41

The impact forces presented in Table 3.4.1 are the maximum impact forces obtained from the FEA simulations based on a given standard deviation of the parameters. For these simulations, only one parameter was varied a time, while the other parameters were kept at base value. To obtain the maximum end stop impact force from the results presented, it was required to determine the combination of parameters that would give the maximum and minimum impact force. This was achieved by using a constraint optimization technique namely the LaGrange Multipliers. This method can be used to determine the maximum and minimum values of an optimization function subjected to a constraint function. The summary of this technique is presented in the section below. The reader is referred to Haas (2007) for a detailed description of the technique.

3.4.1 Constraint Optimization Method

In the FEA analysis, one parameter was varied at a time. The variation of each of these parameters was in one increment at a time along the same direction for all parameters. This creates a situation where it was possible to only access the gradient of the impact force relative to the change in parameters; hence a linear model was employed. The linear model is represented by equation 3.4.1.1 The author is aware that due to the non linearity of the elastomeric buffers, the graph of change in impact force versus change in parameter is non-linear. Hence, the linear model is a simplistic approach.

$$f(\Delta P) = f(0) + \sum_{i=1}^{n} \frac{\partial fi}{\partial pi}.\Delta pi \quad = \quad f(0) + (\nabla_p f)^T . \Delta P \qquad (3.4.1.1)$$

Where $f(\Delta P) =$ End stop impact force (Optimization function).

$f(0)$ = Impact force at base value of all parameters (intercept of graph)

$\frac{\partial fi}{\partial pi}$ = Gradient of the change in impact force relative to the change in the parameter.

$(\Delta P) =$ Change in the parameters = $\overline{P}$ - $\overline{P}_0$

$\overline{P}_0$ = Is the nominal value of the parameter at which the gradient was assessed.

n = Number of parameters.

From the sensitivity analysis, it is possible to obtain a change in force f_0 for each change in parameter. Change in force is the product of the gradient of the change in impact force relative to change in parameter and the change in parameter at which the change in force is to be assessed.

i.e $f_0 = \frac{\partial fi}{\partial pi} (\Delta P)$ (for parameter n = i)

However, due to the non-linearity of the force versus change in parameter curve, the gradient for each change in parameter varied, i.e. the gradient along the graph is not constant. Hence the gradient of the change in force for each change in parameter was obtained and the average of the gradient was used in calculating f_0. The empirical rule is that, 99.73% of impact will occur at a standard deviation (σ) of 3 from the mean value. Hence, the change in the impact force was accessed at the change in the parameter (ΔP) at $\sigma = 3$. The change in force obtained for each parameter at a standard deviation of $\sigma = 3$ is presented in Table 3.4.1.1. The results presented here are for the 1st and 2nd impacts.

Table 3.4.1.1 The change in impact force f_0 obtained for each parameter when each parameter was varied by 3σ from the base value.

PARAMETERS	Payload Bottom		Payload Top	
	1st Impact (kN)	2nd Impact (kN)	1st Impact (kN)	2nd Impact (kN)
Base Impact Force *f(0)*	16.34	16.03	16.85	6.95
Lag Angle	6.95	-0.56	6.19	-0.81
End Stop Misalignment	6.23	5.69	8.24	4.17
Crab Eccentricity	0.73	1.36	0.68	1.24
Velocity at Impact	10.39	12.90	10.70	2.12
Buffer's Damping Characteristics	1.71	3.57	2.68	2.30
Gantry's Stiffness	0.16	0.17	0.12	-0.16

3.4.1.1 Probability Distribution of the Parameters

The change in force (f_0) obtained, is due to change in each parameter. However, it is very unlikely that all of these parameters will have its maximum effect on impact force simultaneously. Thus, it was necessary to obtain a probability distribution $p(\overline{\Delta P})$ for the change in parameter using a probability density function. However since the standard deviation of the changes in parameter is the only available parameter, a multinomial Gaussian distribution was employed as presented in equation 3.4.1.1.1. This type of distribution is used when information is limited to the mean and standard deviation of variables.

$$p(\overline{\Delta P}) = (2\pi)^{-\pi/2} \det(\overline{\overline{C}})^{1/2} \exp\left(-\frac{1}{2}\overline{\Delta P}^{T}.\overline{\overline{C}}^{-1}.\overline{\Delta P}\right) \qquad (3.4.1.1.1)$$

Where $(\overline{\overline{C}})$ is a diagonal matrix with the square of the deviation of each parameter as the diagonal coefficient.

3.4.1.2 Design Point

In order to obtain the design point, it was necessary to find the combination of parameters which will give the maximum probability function. However since the variables are subject to certain constraints, obtaining the maximum value from the probability distribution implies finding the combination of parameters which will give the maximum probability function with the lowest value for the constraint function $g(\overline{\Delta P})$ presented in equation 3.4.1.2.1,

$$g(\overline{\Delta P}) = \left(-\frac{1}{2} \overline{\Delta P}^T . \overline{\overline{C}}^{-1} . \overline{\Delta P} \right) \qquad (3.4.1.2.1)$$

To obtain the lowest value of $g(\overline{\Delta P})$, it is required to find the value of $(\overline{\Delta P})$ that minimizes $g(\overline{\Delta P})$ under the constraint f_C presented in equation 3.4.1.2.2

$$f(\Delta P) = f_C = f(0) + (\nabla_p f)^T . \Delta P \qquad (3.4.1.2.2)$$

This is a constrained minimization problem. A convenient way to solve this problem is to transform it into the unconstrained minimisation problem by means of LaGrange multiplier λ. According to Larson (1995), the above equation is equivalent to solving for $(\overline{\Delta P})$ and λ for which

$$g^*(\overline{\Delta P}) = -\frac{1}{2} \overline{\Delta P}^T . \overline{\overline{C}}^{-1} . \overline{\Delta P} + \lambda \left(\left(\overline{\nabla} pf \right)^T . \overline{\Delta P} + f(0) - fc \right) \qquad (3.4.1.2.3)$$

is extremal.

The change in parameter $\overline{\Delta P}$ obtained from equation 3.4.1.2.3 is the most probable combination of parameters that cause an end stop impact force equal to f_C in the constraint. This value of $\overline{\Delta P}$ is known in the theory of first order reliability method (FORM) as a design point**.**

3.4.2 Probability of Exceedance

The reliability index can be defined as

$$\beta = \sqrt{\overline{\Delta P}^T . \overline{\overline{C}}^{-1} . \overline{\Delta P}} \qquad (3.4.3.1)$$

According to the theory of first order reliability method, it can be proven that the probability of the end stop impact force f_C being exceeded, is equal to $p(f > f_C) = \Phi(-\beta)$

Where Φ = Gaussian cumulative distribution

3.4.3 The Results Obtained from the Constraint Optimization Technique

The results obtained from the constrained optimization technique for three levels of reliability are presented in Tables 3.4.3.1 and 3.4.3.2 for the 1st and the 2nd impact responses.

Table 3.4.3.1 Estimated maximum end stop impact force for the 1st impact.

Levels of Reliability (β)	Payload Bottom, Power On	Payload Top, Power On
β =1	17.49	18.16
β= 2	18.64	19.47
β= 3	20.00	21.00

Table 3.4.3.2 Estimated maximum end stop impact force for the 2nd impact.

Levels of Reliability (β)	Payload Bottom, Power On	Payload Top, Power On
β =1	14.00	5.37
β= 2	12.00	3.80
β= 3	10.00	2.22

From Tables 3.4.3.1 and 3.4.3.2, a maximum end stop impact force of 21kN occurred at 1st impact for the condition of Payload Top Power On.

3.4.4 Calculation of Codified End Stop Impact Force.

Haas (2007) considered eight different codes as a basis for comparison with the FEA impact force. For the purpose of this research, three different codes were of interest to the investigation and only these three were considered. Each of the codified impact force was determined as follows.

DEMAG's estimation of the end stop impact force is based on DIN 15018. Following the guidelines given by the manufacturer, the end stop forces were obtained based on the kinetic energy produced by the EOHTC at impact, when a rigidly connected load on the crane bridge is in the most

unfavourable position. DEMAG provides a table to be used to estimate the kinetic energy on the end buffer for different cases as presented in Table 3.4.4.1. For the case of this investigation, calculation of kinetic energy acting on a buffer was made for a crane system with the buffers in collision with rigid structure. Experimental test shows that the crane used for this investigation has a step down function which serves as a speed retarding mechanism. However, to have a conservative estimation of impact force, calculation of the kinetic energy for this system was carried out using the formular provided for the crane without a speed retarding mechanism. Also, DEMAG provides a flexibility vs. energy vs. buffer force graph. This is presented in Figure 3.4.4.1. Once the kinetic energy is obtained, the final end stop impact force can be obtained as illustrated on Figure 3.4.4.1.
It must be noted here that the formulae given in Table 3.4.4.1 is for a velocity measured in m/min.

Table 3.4.4.1 DEMAG estimation of energy acting on one end buffer

Determine the energy acting on one buffer E_{pu}

System	With/without speed reduction	Energy acting on one buffer E_{pu}		
		Collision against rigid structure	Collision against stop with buffer 1)	Collision between two units with the same buffers
Crane	without	$E_{pu} = \frac{m_{pu} \cdot v^2}{9965}$	$E_{pu} = \frac{m_{pu} \cdot v^2}{19930}$	$E_{pu} = \frac{m_{pu1} \cdot m_{pu2} \cdot (v_1 + v_2)^2}{19930(m_{pu1} + m_{pu2})}$
	with	$E_{pu} = \frac{m_{pu} \cdot v^2}{14694}$	$E_{pu} = \frac{m_{pu} \cdot v^2}{29388}$	$E_{pu} = \frac{m_{pu1} \cdot m_{pu2} \cdot (v_1 + v_2)^2}{29388(m_{pu1} + m_{pu2})}$
Crab	without	$E_{pu} = \frac{m_{pu} \cdot v^2}{7200}$	$E_{pu} = \frac{m_{pu} \cdot v^2}{14400}$	$E_{pu} = \frac{m_{pu1} \cdot m_{pu2} \cdot (v_1 + v_2)^2}{14400(m_{pu1} + m_{pu2})}$
	with	$E_{pu} = \frac{m_{pu} \cdot v^2}{14694}$	$E_{pu} = \frac{m_{pu} \cdot v^2}{29388}$	$E_{pu} = \frac{m_{pu1} \cdot m_{pu2} \cdot (v_1 + v_2)^2}{29388(m_{pu1} + m_{pu2})}$

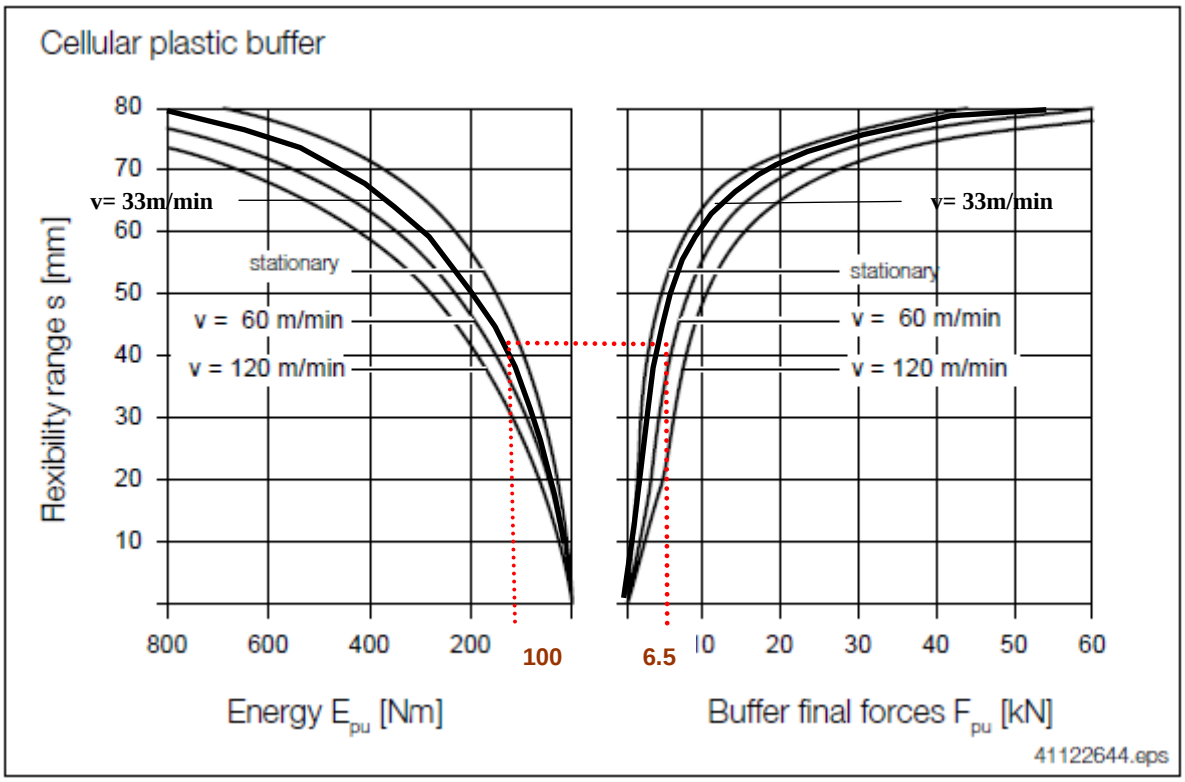

Figure 3.4.4.1 DEMAG'S Energy vs. flexibility vs. buffer final force graph for a DPZ 100 cellular plastic buffer (elastomeric buffers)

For the previous South African loading code, SABS 0160:1989, the end stop impact force was estimated using the two methods specified by the codes and described in section 2.6 of this document. For the two methods, the kinetic energy on each end buffer was obtained using the total mass of the crane and the crab. The second method for this code was obtained using the same method used by DEMAG. The only difference is that SABS 0160:1989 calculates the kinetic energy using the conventional formula

$$\text{K.E} = \frac{1}{2}mv^2$$ (which has a denominator of 7200 when the velocity is in m/min as opposed to 9965 used for DEMAG)

For the South African loading code, SANS 10160-6:2010, the kinetic energy was calculated using the total mass of the crane, crab and the payload. Using the energy vs. force graph supplied by the manufacturer, the kinetic energy of the crane was obtained. The corresponding force and the flexibility range at the obtained kinetic energy were used to estimate the buffer's spring constant. The final end stop impact force was then obtained using the method specified by the code and documented in section 2.6 of this document. This method considers the total mass of the crane bridge and the hoist load to estimate the kinetic energy on the end stops. However, unlike SABS

0160:1989, the current loading code, SANS 10160-6:2010 does not clearly state if the end stop impact force obtained from clause 4.12.1.2 of the code is for one end stop or should be divided between the two end stops. A conservative way will be to assume that the force due to the kinetic energy from the mass of the crane and payload will act on one end stop. The unconservative way will be to assume the force is shared between the two end stop. To estimate the end stop impact force for the worst case scenario, the force from the kinetic energy due to the total mass of the crane and payload was used to estimate the end stop impact force on each end stop. The results obtained are presented in Table 3.4.4.4 .It must be noted that a $\Phi_7 = 1.6$ was used to obtain the final end stop impact force. This was obtained by substituting a $\xi_b = 1$ into Table 9 of the code. The literature reviewed reveals that the elastomeric buffer has a non-linear stiffness curve

Table 3.4.4.2 Estimation of the end stop impact force per end stop according to DEMAG

DEMAG	Velocity(m/s)	E_{pu} = MV²/9965 (Nm)	Deflections (mm)	Force (kN)
Mass = 3648kg	0.3	119	34	4.5
	0.4	211	50	7.2
	0.5	329	60	11.5
	0.55	399	66	13.5
	0.6	474	69	17.5

Table 3.4.4.3 Estimation of the end stop impact force per end stop according to SABS 0160:1989

SABS 0160:1989 (method a) Mass = 3648kg	Force = mass x 9.81		Force = 35.8KN		
SABS 0160:1989 (method b) Mass = 3648kg	Velocity (m/s)	E_{pu} = MV²/7200 (Nm)	Deflections (mm)	Force (kN)	Lesser of methods (a)&(b)
	0.3	164	43	6.7	6.7
	0.4	292	55	8.2	8.2
	0.5	456	68	16.5	16.5
	0.55	552	73	19.5	19.5
	0.6	657	79	27.20	27.20
For the SABS 1989, use the lesser value between the two methods					

Table 3.4.4.4 Estimation of the end stop impact force per end stop according to SANS 10160

	Velocity(m/s)	E_K (Nm)	Deflections (mm)	Force (kN)	Stiffness (kN/m)	Impact Force on Each End Stop (kN)
SANS 10160-6:2010 Mass = (3648+5128) = 8776kg	0.3	194	49	7	143	11.8
	0.4	344	63	12	190	18.3
	0.5	538	72	22	306	28.9
	0.55	650	78	28	359	34.5
	0.6	774	80	40	550	44.5

To compare the codified end stop impact force with the FEA end stop impact force for the double bridge EOHTC, the maximum FEA impact force was superimposed on the codified impact force and presented in Figure 3.4.4.1

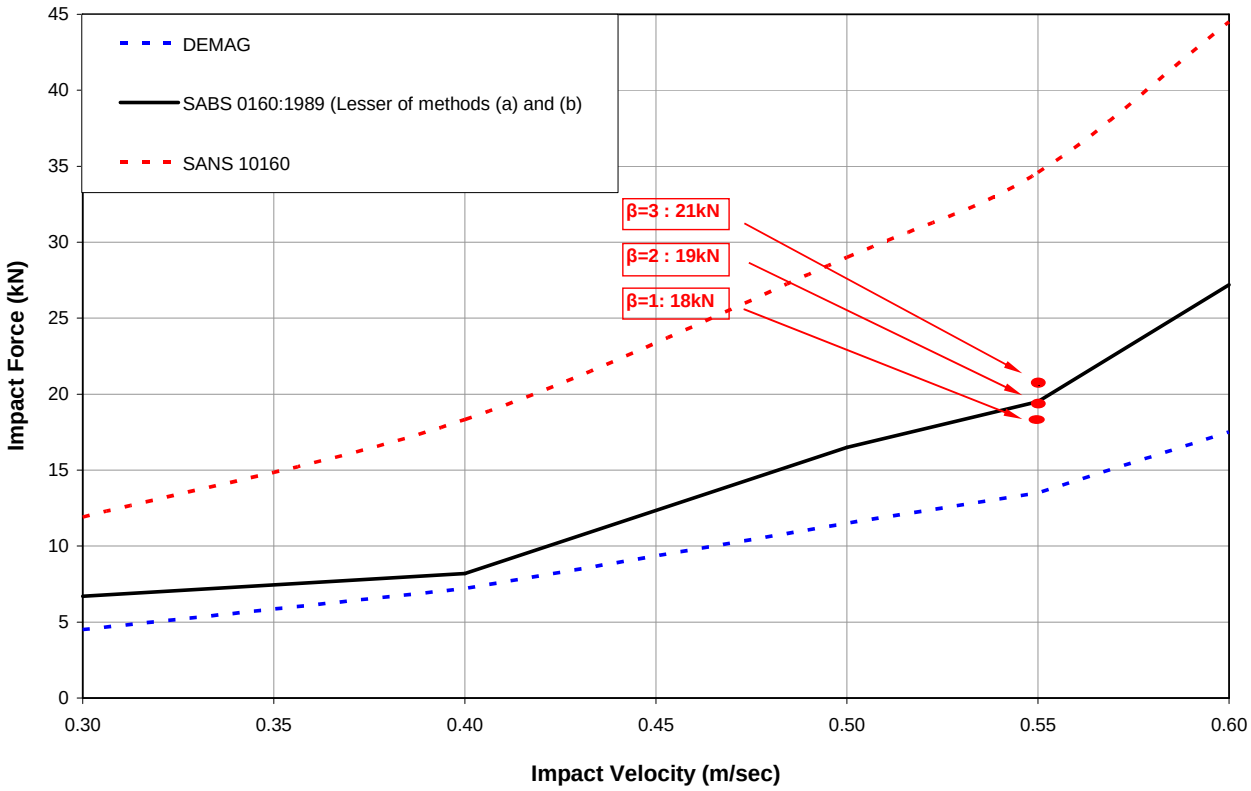

Figure 3.4.4.1 Codified and Constraint Optimization Impact Forces at Different Impact Velocity for the "Double Bridge EOHTC".

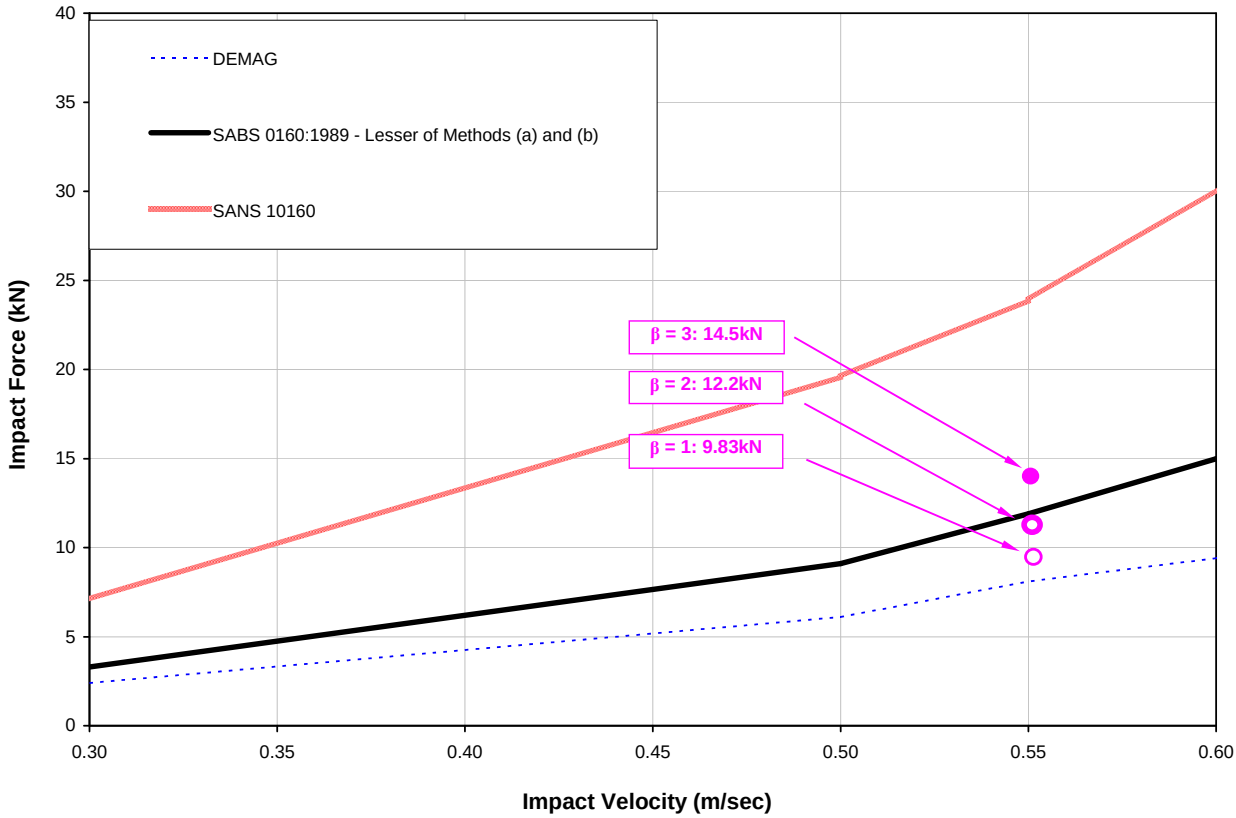

Figure 3.4.4.2 Codified and Constraint Optimization Impact Forces at Different Impact Velocity for the "Single Bridge EOHTC".

From Figure 3.4.4.1, it is observed that at an impact velocity of 0.55m/s, SANS 10160-6:2010 estimates end stop impact force as 35kN. At this same velocity, a maximum end stop impact force of 21kN was obtained using the constraint optimisation technique for a level of reliability of β =3. This implies that for the double bridge EOHTC, SANS 10160-6:2010 over estimates end stop impact force by 67%. For a level of reliability β =3, the previous loading code SABS 0160:1989 underestimates impact force by 7%. DEMAG underestimates impact force at all levels of reliability.

For the single bridge EOHTC, Figure 3.4.4.2 shows that at a velocity of 0.55m/s, SANS 10160-6:2010 estimates the end stop impact force as 23.9kN. This is a 64% increase to the maximum end stop impact force of 14.54kN that was obtained for a level of reliability of β =3. The previous loading code, SABS 0160:1989 estimates impact force as 12kN which is an 18.2% underestimation of the impact force obtained at a level of reliability β =3, using the constraint optimization technique. DEMAG underestimates impact force at all levels of reliability.

CHAPTER 4: FINITE ELEMENT MODELLING OF THE HYDRAULIC BUFFER

4.1 Introduction.

One of the major objectives of this investigation was to obtain the maximum end stop impact force (due to the identified influencing parameters) for an EOHTC fitted with hydraulic buffers. To achieve this goal, the hydraulic buffers' elastic and damping characteristics were obtained experimentally. These characteristics were used for the FEA modelling of the hydraulic buffers. For this study, a DEMAG's DPH 25 adjustable buffer was used. This section describes how the elastic and damping characteristics were obtained as well as a detailed description of the experimental configuration. This section also describes how the hydraulic buffer was modelled in the FEA model, together with the calibration of the FEA impact force history to the experimental impact force history.

4.1.1 Description of DEMAG's DPH 25 Hydraulic Buffer.

DEMAG is one of the leading companies in South Africa in the manufacture and supply of buffers and most crane components. Figure 4.1.1.1 shows a picture of a DEMAG DPH 25 adjustable hydraulic buffer.

Figure 4.1.1.1 DEMAG DPH 25 Adjustable Hydraulic Buffers.

The DEMAG DPH 25 adjustable hydraulic buffer has a piston with a stroke of 50.8mm and a diameter of 25mm. The buffer is an enclosed system consisting of a maintenance free hydraulic element. The hydraulic element has an almost uniform deceleration, hence making it possible for the buffer to achieve the smallest possible breaking force for the shortest possible breaking path. Permissible ambient operating temperature ranges from -12℃ to +90℃. As the name implies, the DEMAG DPH 25 adjustable hydraulic buffer can be adjusted for various damping capacities. The buffer has a dial setting ranging from 0 to 9 that can be used to control the force resisting capacity of the buffers. The setting of this dial controls the stiffness characteristics of the buffer. Experimental test conducted on the buffers in the course of this investigation reveal that the buffer yields the highest resistance to compression when its dial setting is set to dial 0, and the lowest resistance to compression when dial setting is set to dial 9. An example of the setting of the dial is shown in Figure 4.1.1.2 with the dial set to 0.

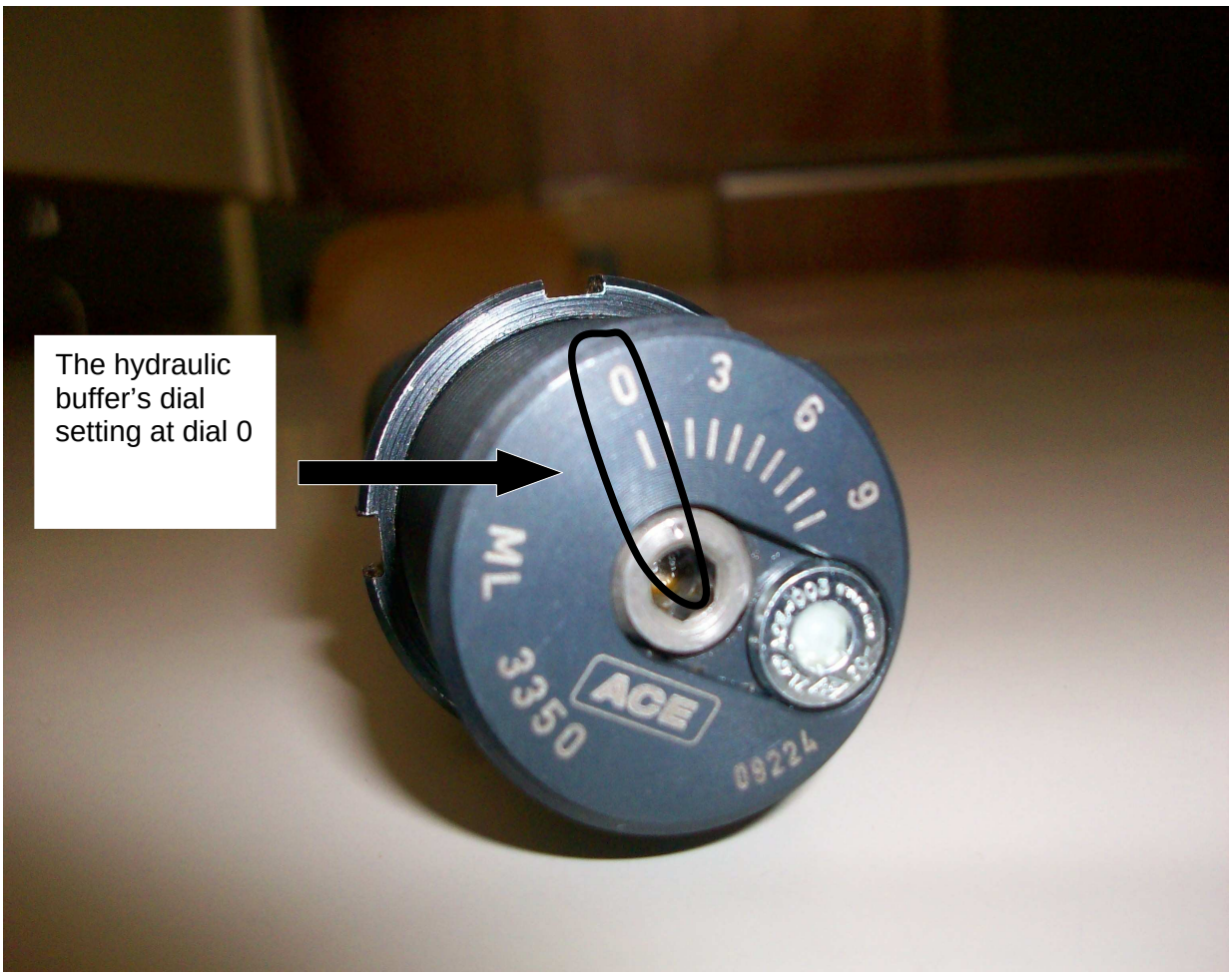

Figure 4.1.1.2 The Hydraulic Buffer Set to Dial 0

DEMAG provides a table to guide the selection of buffers for cranes. The table is presented as Table 4.1.1.1 in this document. The values given in the table are the maximum masses which the buffers can resist for a given travel velocity. For the DPH 25 adjustable buffer, DEMAG gives no information on the maximum mass that can be resisted when the travelling velocity of the crane is less than 12.5m/min and when it is higher than 40m/min.

Table 4.1.1.1 DEMAG's estimation of the hydraulic buffer's capacity at different velocities.

Hydraulic Buffer		**Travel Velocity in m/min**								
Limit Switch k=70%		to 14.3	to 17.9	to 22.9	To 28.6	to 35.7	to 45.0	to 57.1	to 71.4	to 90.0
Long travel k=85%		to 11.8	to 14.7	to 18.8	To 23.5	to 29.4	to 37.1	to 47.1	to 58.8	to 74.1
Cross Travel k=100%		to 10.0	to 12.5	to 16.0	To 20.0	to 25.0	to 31.5	to 40.0	to 50.0	to 63.0
DRS wheel Block Size	**Buffer**									
112-500	DPH 7	-	-	-	1000	790	600	370	-	-
112-500	DPH 25	-	10000	8000	6300	4000	2530	1590	-	-
112-500	DPH 80	-	-	-	8000	8000	8000	5000	3200	2010
400-500	DPH 350	-	-	-	-		10000	10000	8800	7300

Also DEMAG gives guidelines to be used in calculating the buffer's capacity. According to DEMAG, this guidelines should be adopted to determine the velocity to be considered for buffer selection in Table 4.1.1.1. According to the guideline, the required buffer energy absorption capacity must be calculated for the following cases:

a) For the maximum possible impact velocity. However, when a velocity reduction device (limit switch) is used, a value of k= 70% of the crane travel velocity can be used to calculate the kinetic energy.
b) For k = 85% of the travel velocity of the crane.
c) For k = 100% of the travel velocity of the crabs and travel/end carriages

Where k = buffer energy factor. (Table 4.1.1.1).

Since the buffer capacity being investigated is for the impact force on the end stop and not for the cross travel of the crab, the kinetic energy required is due to the longitudinal travel of the crane.
The top part of Table 4.1.1.1 shows the travel velocity of the crane. To have a clear understanding on how the mass to be resisted by a buffer was obtained, it is important to understand the concept presented in Table 4.1.1.1. The third column in Table 4.1.1.1 gives three different values of the travel

velocity of the crane. All three values refer to a mass capacity of 8000kg for the DPH 25 buffer. The primary idea here is that at a travel velocity of 16m/min, the DPH 25 can resist a maximum mass of 8000kg. Table 4.1.1.1 shows that at a velocity of 22.9m/min, for the case where k=70%, the buffer can resist the same mass of 8000kg. This is because for a crane where k = 70%, the travel velocity is reduced from 22.9m/min to 16m/min. The same applies for the situation where k= 85%, the travel velocity is reduced from 18.8m/min to 16.0m/min.

For the case of this investigation, the crane travels at a velocity of 33/min. By interpolation between the given travel velocities and the corresponding masses, the following values were obtained for the three values of k.

- For 70%: 4875kg
- For 85%: 3313kg
- For 100%: 2364kg

To have a conservative estimation of the mass to be resisted by the buffer, it was assumed that the crane will travel at full travel velocity. Hence at a travel velocity of 33m/min, the DPH 25 hydraulic buffer has the capacity to resist a maximum mass of 2364kg.

4.2 Description of Experimental Analysis.

All impact tests were conducted on the INSTRON universal actuator as shown in Figure 4.2.1.

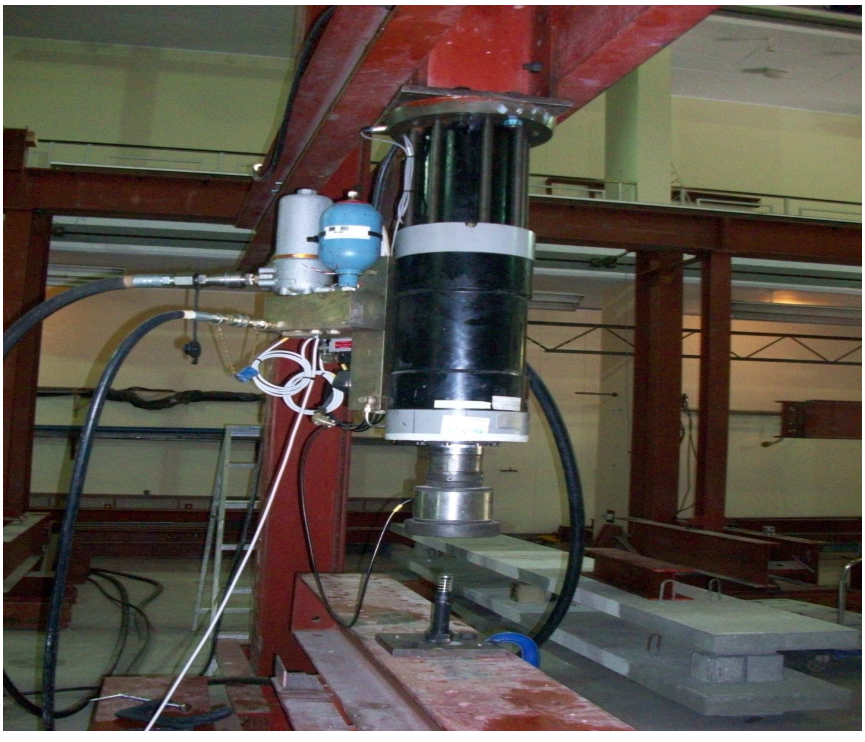

Figure 4.2.1 Impact Test on the Hydraulic Buffer Using the INSTRON

The INSTRON is an electronically controlled actuator system which can be used for both compression and tensile tests. To obtain the force-displacement relationship of the buffers, a displacement controlled experimental test was conducted on the buffers. For the experimental tests, a 5ton load cell was used. Two set of plates were attached to the load cells to ensure the impacting force was evenly distributed over the contact area, as shown in Figure 4.2.2. The two set of plates attached to the load cell were placed 5mm above the buffer and the displacement limit was set to a distance of 50mm. This implies that the set of plates only comes in contact with the buffer after it has moved by a distance of 5mm and the buffer will only compress by 45mm. The displacement of the buffer was limited to 45mm to prevent it from being damaged.

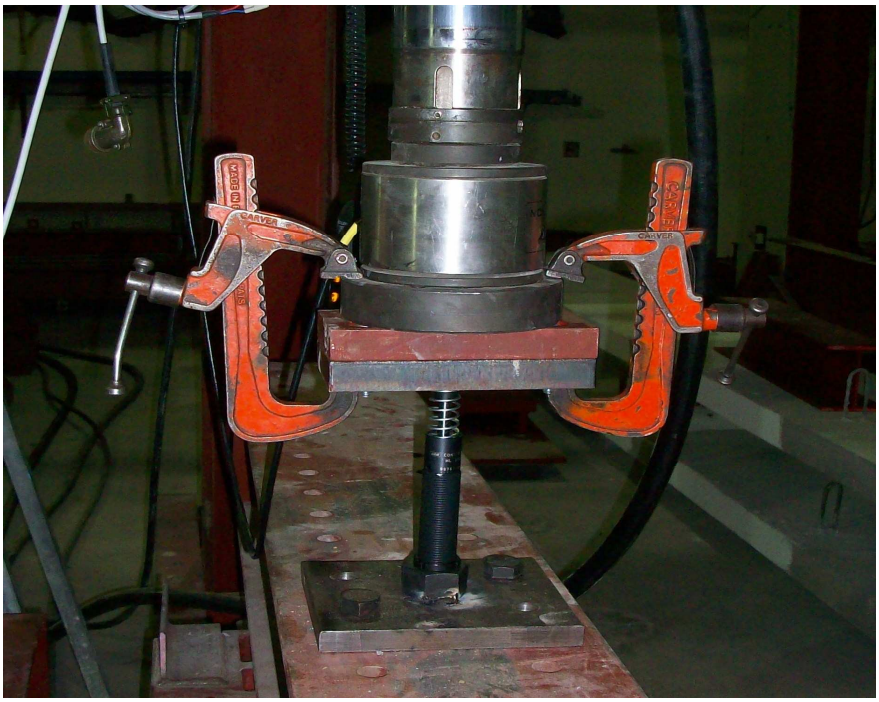

Figure 4.2.2 Two set of plates for uniform force contact on the buffers.

To determine the static resistance curve of the buffers, it was necessary to carry out a quasi-static test on the hydraulic buffers. For the purpose of the quasi-static experiment, four sets of experimental tests were conducted on the buffers. The first two sets of the experimental tests were conducted with the buffer's stiffness set to dial 1 at velocities of 5mm/min and 10mm/min respectively. The same was done when the buffer's stiffness was set to dial 9. The results obtained are presented in Figure 4.2.3. The results obtained from this set up reveal a preload of 40N even before the buffers starts to deform. The author is of the opinion that the preload is due to the plates attached to the load cells. To achieve an accurate force-displacement relationship of the buffer, the graph was plotted from the start of deformation of the buffer with the corresponding force causing the deformation. From the quasi static curve presented in Figure 4.2.3, it was observed that the

stiffness-curve obtained for each cycle has the same trend, establishing that the dial position has no effect on the stiffness of the mechanical spring of the buffers

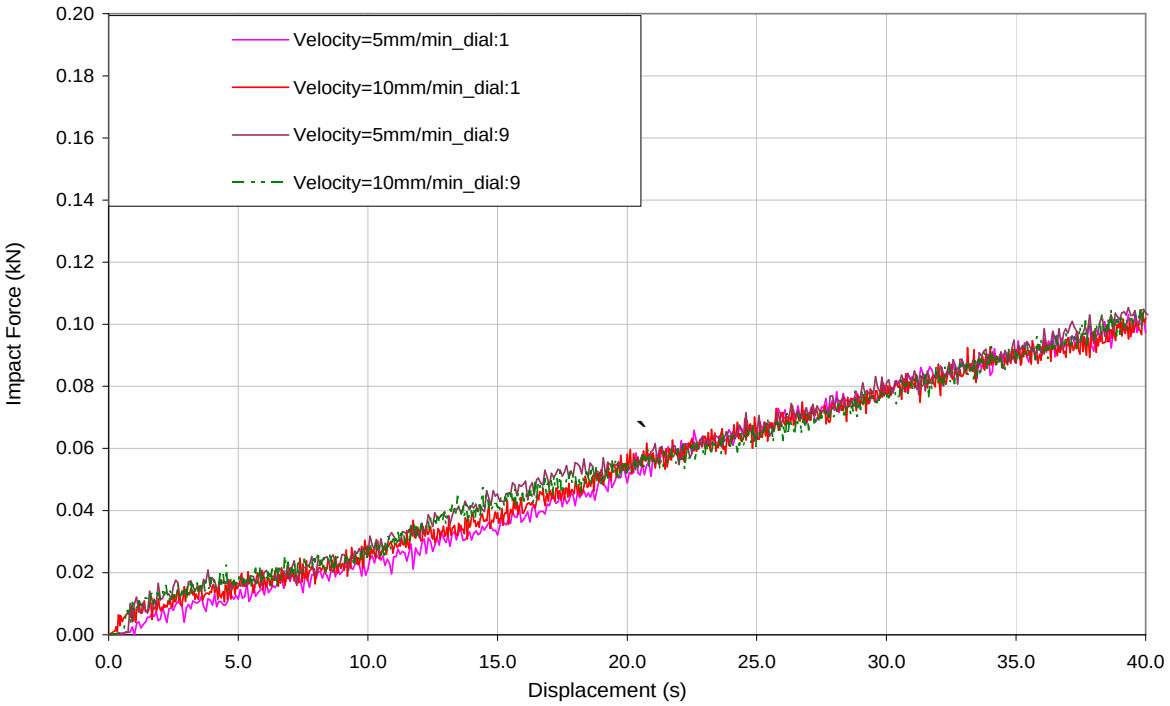

Figure 4.2.3 Quasi static experimental test on the hydraulic buffer

To obtain the damping characteristics of the buffers as it relates to its velocity, subsequent experimental tests were conducted on the buffers at various velocities. The impact tests were conducted for two cases where the buffer's stiffness was set to dial 0 and dial 9 respectively. For each of these cases, tests were conducted at impact velocities 150mm/sec, 112.5mm/sec, 75mm/sec and 37.5mm/sec. For this set of tests it was necessary to obtain the accurate velocity during impact as the damping capacity of a buffer is a function of its velocity. To ensure that the INSTRON would attain a given velocity when it impacts the buffers, the two set of plates attached to the load cell was placed 50mm above the buffer and the displacement limit on the INSTRON was set to a distance of 95mm. This implies that the set of plates only comes in contact with the buffer after it has moved by a distance of 50mm and the buffer will only compress by 45mm.The results obtained are presented in Figures 4.2.4 and 4.2.5. The results show that the capacity of the buffers to resist the force increased with an increase in the impact velocity. For the case where the buffers' dial setting was adjusted to dial 9, the buffers offered very little resistance to compression as shown on Figure 4.2.5. The highest resisting force obtained at a velocity of 150mm/sec for dial 9 is 0.417kN. At the same velocity, the buffers resisted a maximum impact force of 2.6kN when its dial setting was adjusted to dial 0. Hence it is inferred that the damping capacity of the buffer reduces with an increase in the dial number. The buffers' force-displacement curve gives a close relationship to an

exponential function where the resistance to force increases non-linearly along the stroke of the buffer. Thus, this particular buffer has a fluidic metering device. For a buffer with a fluidic metering device, its capacity to resist impact force increases along the stroke of the buffer (section 2.3). Hence, the damping capacity is dependent both on the velocity and the displacement of the buffer. Also it was observed from the results obtained that in spite of the attempt to attain a given velocity at the start of the loading test, this could not be achieved. Table 4.3.1 shows that for the tests conducted at a velocity of 150mm/sec, it was impossible to attain the given velocity at the start of the test. The velocity gradually increased and a constant velocity of 146mm/sec was only obtained after the buffers had compressed by 25mm. Another observation made from the results is that the capacity of the buffers suddenly increased at a displacement of 28mm and 36mm. The author is of the opinion that this is as a result of the deceleration rate of the hydraulic fluid through the orifices in the buffers. According to Kit (1996), a hydraulic buffer with a fluidic metering device compensates for changes in impact velocity by adjusting its stroke to attain a minimum end force. This is achieved by adjusting its deceleration rate with each impact velocity to attain a minimum end force. In chapter 2 of this document, it was stated that during impact, the hydraulic fluid flows through a series of metering orifices. The number, size and the relative positioning of the orifices controls the rate of flow of the hydraulic fluid through the orifices and thus controls the deceleration rate of the buffer. Usually, the number, size and spacing of these orifices are predetermined by manufactures to provide a desired resistance and deceleration rate such that the velocity at which the buffer's spring is being compressed reduces to zero at the end of the retraction stroke, Kamman (1975). According to Kamman (1975), the metering orifices are mostly arranged with a progressively diminishing space towards the end of the buffer to reduce the rate of flow of the hydraulic fluid and assure zero velocity at the end of the buffer's stroke. The implication of this is that, the resistance of the hydraulic fluid to flow will increase along the stroke of the buffer in a manner which is dependent on the arrangement of the metering orifice. The hydraulic buffers used for this investigation is an enclosed system. Hence, no information exists on the arrangement of the metering orifices. The result obtained and presented in Figure 4.2.4 however shows a sudden increase in the capacity of the buffer at different distances along the buffer. It must be noted that each result presented on Figure 4.2.4 is for a controlled experimental test where the buffer was compressed through its entire stroke at a constant velocity. Hence, the deceleration of the movement of the spring was impossible. Rather, the buffer's force resisting capacity varied along its stroke.

The unloading curve for all settings follows the same line which represents the return coil force from the buffer. After the 1st impact, the unloading force is solely a function of the capacity of the recoil spring of the buffers which in this case is found to be minimal when compared with its damping capacity.

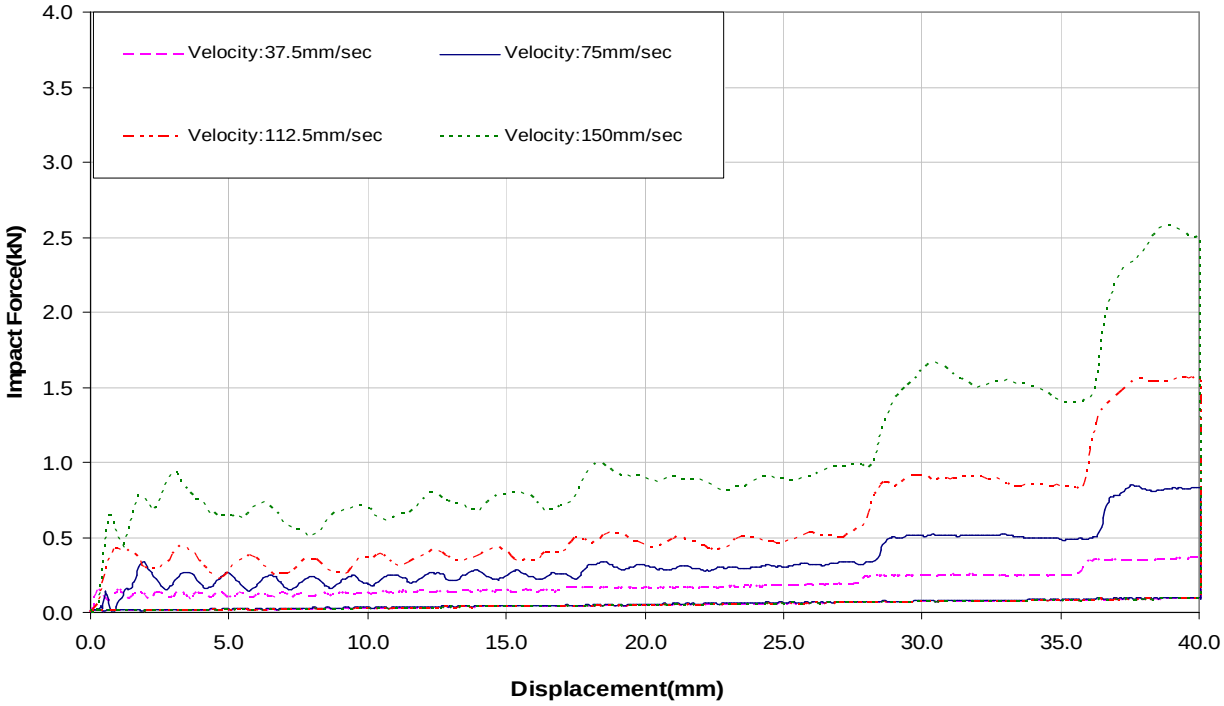

Figure 4.2.4 Impact resisting force when buffers' stiffness is set to dial: 0

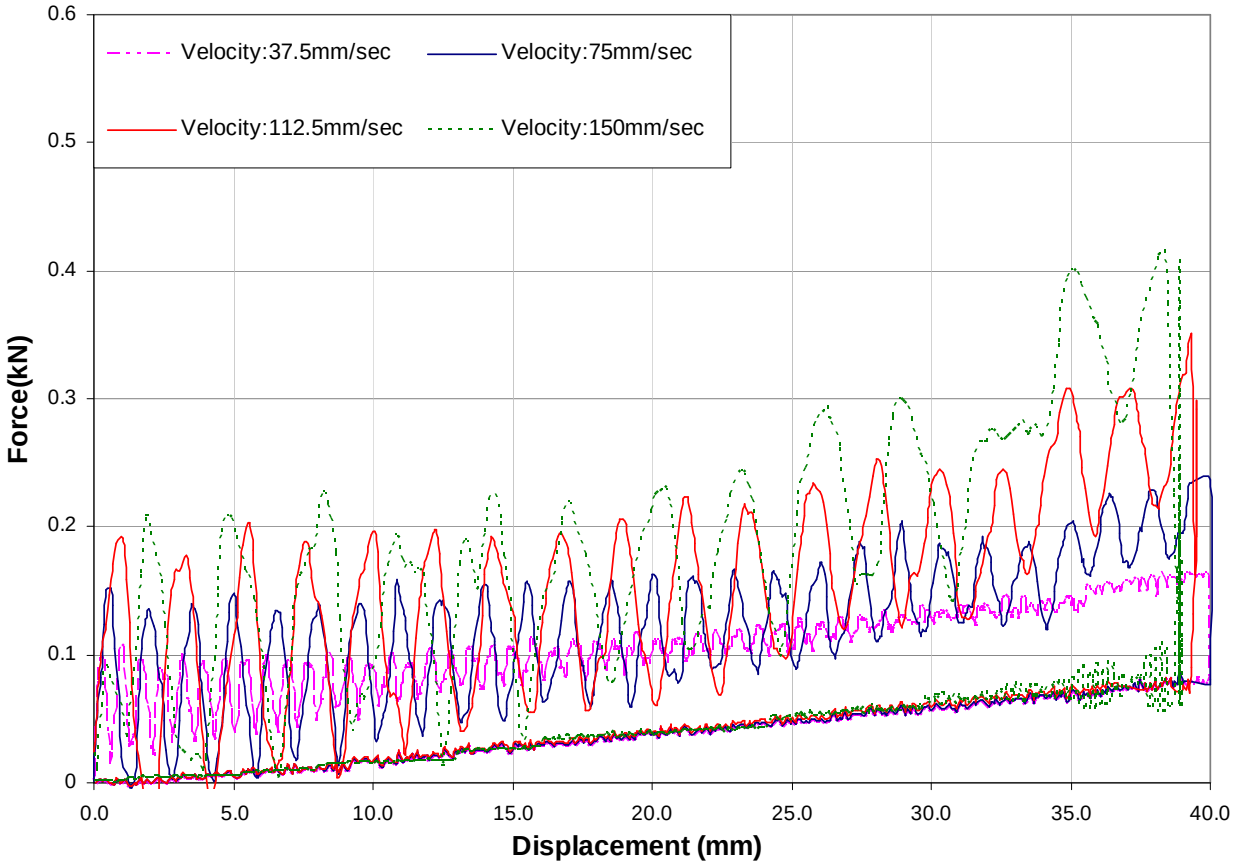

Figure 4.2.5 Impact resisting force when buffers' stiffness is set to dial: 9

4.3 The Characteristics of the Hydraulic Buffers Obtained from the Loading Test.

To have a clearly defined function of the hydraulic buffer's loading curve, it was required to draw a regression line through the loading curve obtained from the experimental tests. Due to the limited capacity of the valve controlling the velocity of the INSTRON, it was impossible to obtain a loading test for a velocity greater than 150mm/sec. Hence, the loading curve for a velocity of 150mm/sec was used and the results obtained are for the capacity of the buffer at this velocity. A regression line joining the points at 91% accuracy was drawn through the loading curve. Accuracy is based on the regression line's R^2 value. The result obtained gives a sixth order polynomial function as presented in Figure 4.3.1. This function is represented by equation 4.3.1

$$Y = -4*10^{-8}x^6 + 5*10^{-6}x^5 - 0.3*10^{-3}x^4 + 0.66*10^{-2}x^3 - 0.0792x^2 + 0.4223x \qquad (4.3.1)$$

The equation for the quasi-static curve as obtained from Figure 4.3.1 is represented by equation 4.3.2.

$$Y = 0.0347x^{0.3589} \qquad (4.3.2)$$

To obtain the damping capacity of the buffers at a velocity of 150mm/sec, the quasi static curve (elastic curve) is superimposed on the loading curve as shown in Figure 4.3.1. The difference between these two curves is the damping force of the buffer at this velocity. The result obtained for the damping force with the corresponding displacement and velocity is presented in Table 4.3.1.

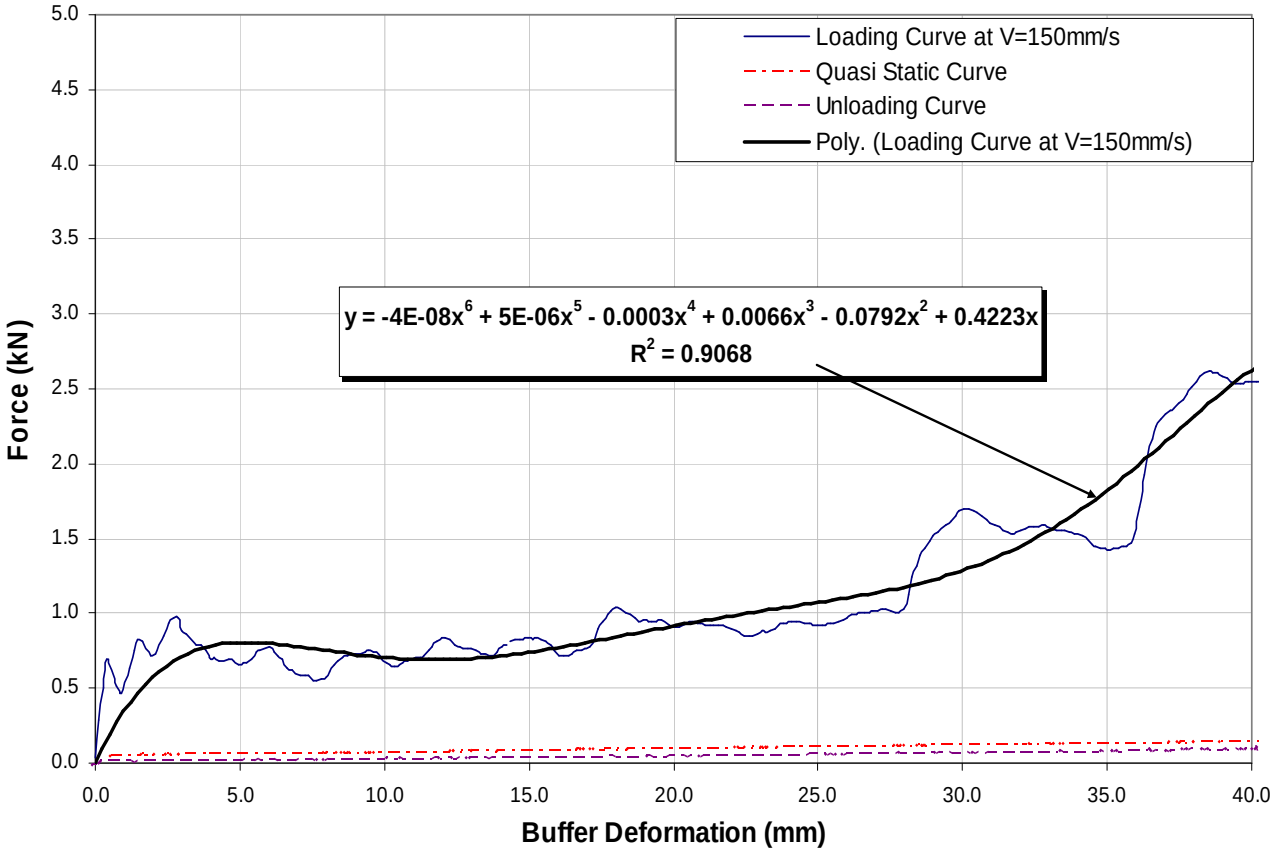

Figure 4.3.1 Comparison of loading; unloading and quasi static curve.

Table 4.3.1 Damping characteristics of the buffers at a velocity of 150mm/sec

Damping Force (kN)	Buffer's Deformation (mm)	Velocity (m/sec)
0	0	0.112
0.76	2.917	0.112
0.80	3.381	0.117
0.82	6.539	0.133
0.82	8.112	0.139
0.82	13.711	0.141
0.86	17.788	0.143
0.90	20.247	0.145
1.11	25.379	0.146
1.27	29.396	0.146
1.32	30.733	0.146
1.39	32.102	0.146
1.79	34.99	0.147
2.19	37.265	0.147
2.35	37.997	0.147
2.60	39.213	0.147

The force $f_{(t)}$ caused by mass moving at acceleration "a" at any time "t" is represented in Figure 4.3.2. Where $f_{(t)}$ is an external force acting in the positive direction, $f_{(s)}$ is the elastic resisting force and $f_{(D)}$ is the damping resisting force. The external force is taken to be positive in the x direction. The elastic and the damping forces are shown as acting in the opposite direction because they are internal forces that resist the deformation and velocity respectively.

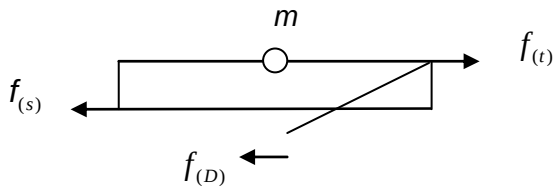

Figure 4.3.2 Force acting on a mass moving at a given acceleration

Using Newton's second law of motion, the resultant force f along the x axis due to mass moving at a given acceleration can be represented by equation 4.3.3.

$$f = f_{(t)} + f_{(D)} + f_{(s)} \qquad (4.3.3)$$

$f_{(t)} = m * a$

$f_{(D)}$ = damping force = $C * v$

$f_{(S)}$ = elastic force = $k * u$

The representation in Figure 4.3.2 can be used to show a relationship of the end stop impact force where the resultant force from the buffered mass of the crane causes a reaction force on the end stop.

Where f = resisting force (force on end stop)

m = Impacting mass (mass of the crane and payload)

a = Impacting acceleration

C = Damping coefficient of the buffer.

v = Velocity of deformation of the buffer.

k = Stiffness coefficient of the buffer.

u = Deformation of the buffer.

Using equation 4.3.3, a spring was modelled with the buffers' elastic and damping characteristics obtained for a constant velocity of 150mm/sec and incorporated into the EOHTC model.

4.4 Experimental Impact Tests on EOHTC fitted with the Hydraulic Buffers

To obtain the end stop impact force when the EOHTC is fitted with the hydraulic buffers, it was required to conduct impact test on the EOHTC. The first set of impact tests was to determine the response of the buffers under higher impact velocities. To conduct the impact test, the dial setting of the hydraulic buffers was adjusted to dial 0 and the buffers were fitted to the end carriages of the EOHTC. A 100mm linear variable displacement transducer (LVDT) was used to measure the deformation of each of the buffers and a 2ton load cell was used to measure the force on each end stop. The 1st set of experimental tests was conducted without payload at an impact velocity of 0.25m/s. The representative results obtained for this test are presented in Figure 4.4.1. From the results presented in Figure 4.4.1, it was discovered that even though both the left hand side (LHS) and the right hand side (RHS) buffers are of the same specifications, the damping capacity of each buffer differs significantly, yielding different end stop impact forces at the two end stops. Hence it was required to calibrate the buffers to offer the same resistance to impact.

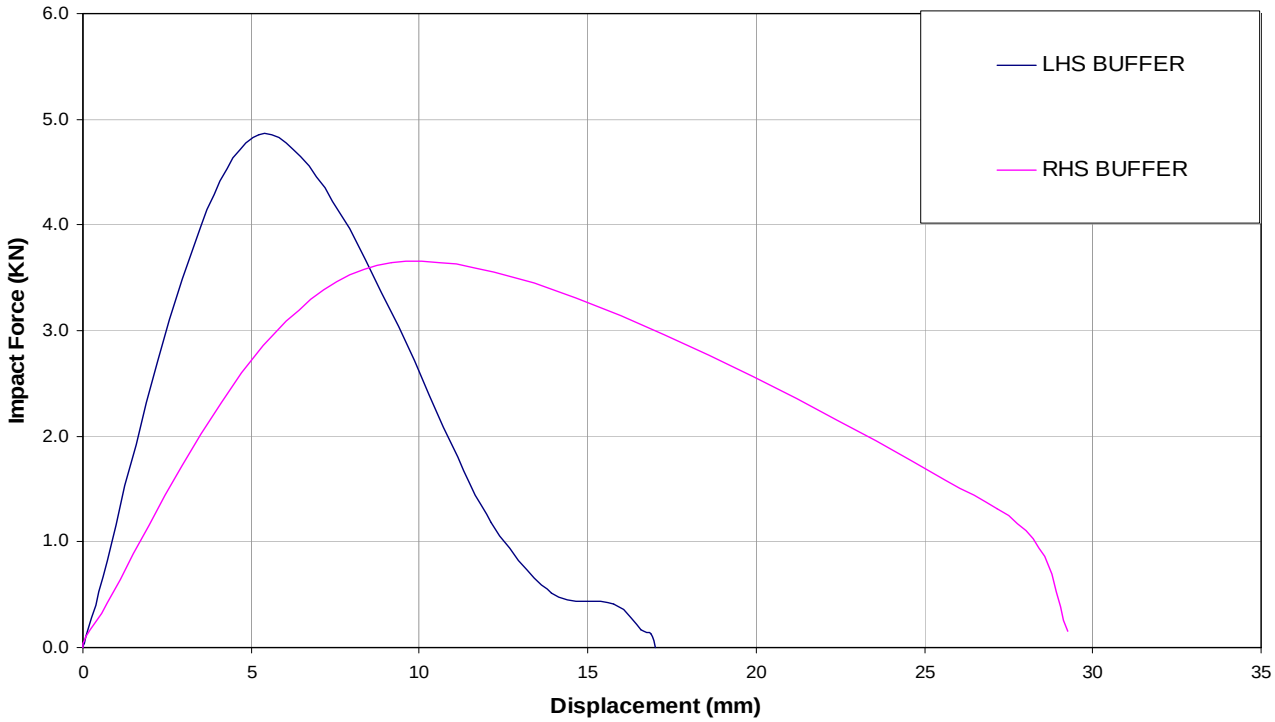

Figure 4.4.1 Impact force history of the EOHTC fitted with hydraulic buffers.

4.5 Calibration of the Hydraulic Buffers.

Calibration of the buffers was done on the Zwick Z250 in the structural laboratory of the department. To achieve the same capacity for the two buffers, the dial setting of each buffer was adjusted from dial 0 to dial 9. Loading tests were conducted on each buffer at a velocity of 10mm/sec for each of these dial settings. To ascertain that the correct capacity of the buffers was obtained, the buffers were subjected to a repetitive loading test. The results obtained from the tests do not only show a significant difference in the capacity of the two buffers but it also shows great inconsistency in the capacity of each of the buffers at a given dial setting. Figures 4.5.1 and 4.5.2 is a representative of the inconsistency in the damping capacity observed from the loading test.

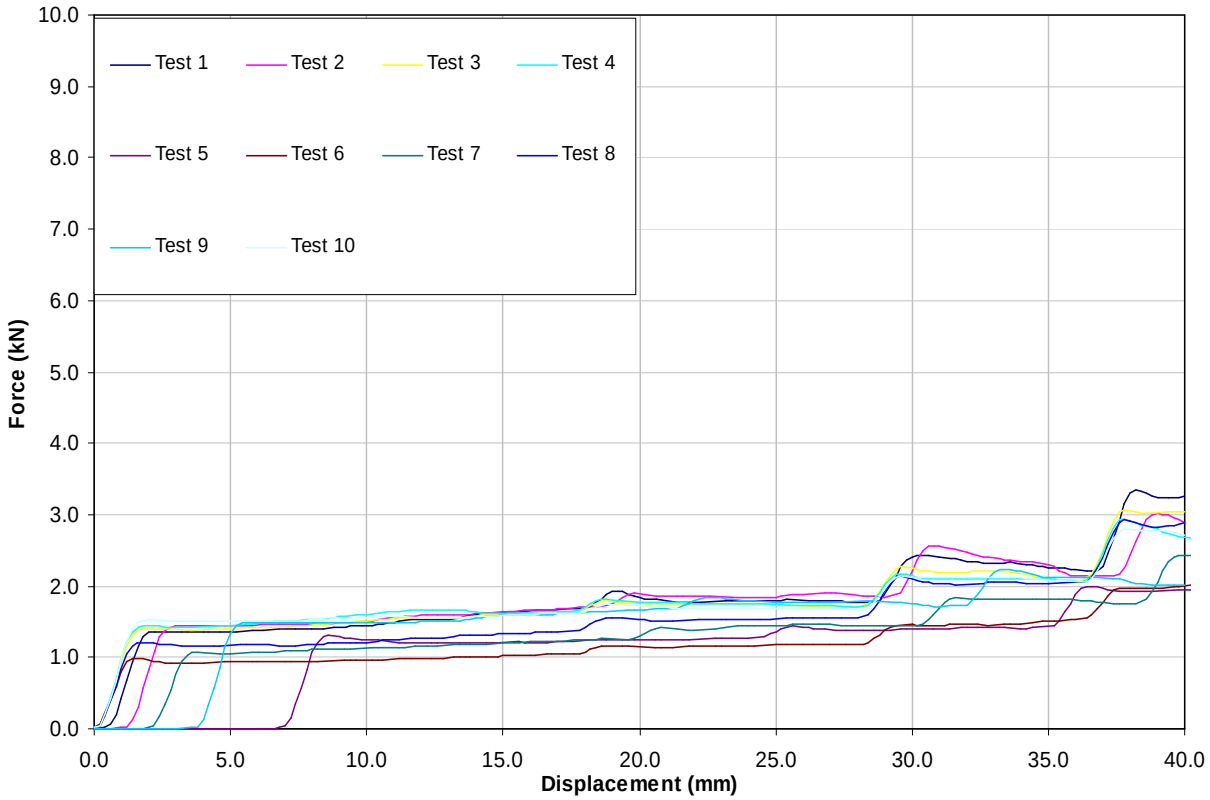

Figure 4.5.1 Force-displacement curve for a repetitive loading for LHS buffer: Dial 0

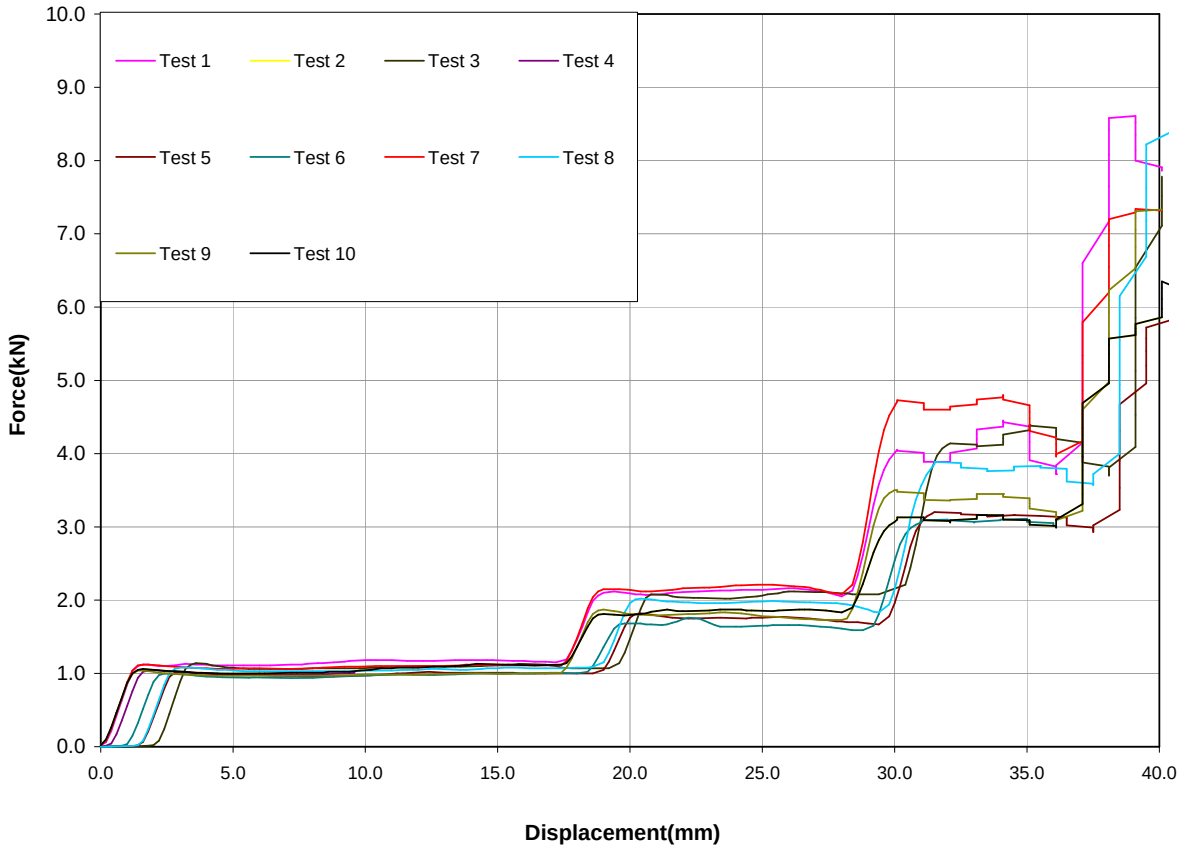

Figure 4.5.2 Force-displacement curve for a repetitive loading for RHS buffer: Dial 0

Figures 4.5.1 and 4.5.2 show the loading curve obtained at a dial setting of 0 for the left hand side (LHS) and the right hand side (RHS) buffers respectively. The results show that at the same dial setting of 0, the force resisting capacities of the two buffers varied significantly. The author is of the opinion that the difference between the capacities of the buffers is due to a manufacturing error. Also observed is the inconsistency in the capacity of each buffer at a given dial setting. This is particularly obvious in the RHS buffer. The reason for the erratic behaviour exhibited by each of the buffers maybe due to the behaviour of the hydraulic fluid in the buffers at a given time. The hydraulic buffer operates as a hydraulic system. Hence, the mechanism of its operation is such that the efficiency of the system at any point in time is largely dependent on the pressure, temperature, density, and ultimately the viscosity of the hydraulic fluid in the buffers. It must be noted that the temperature of the hydraulic fluid (which is influenced by its pressure) influences its density which in turn influences its viscosity. At high temperature, the viscosity of the fluid decreases and vice versa. Many points in a fluidic system can add heat, particularly points with high frictional resistance. An example of such, for a hydraulic buffer is the point where the hydraulic fluid is being pushed through the orifices. This causes frictional drag on the fluid as it passes through the restricted passages, E.C Fitch (2002). The larger the pressure, the greater the amount of heat generated, revealing that the temperature of the hydraulic fluid at any point in time would vary significantly. According to Fitch (2002), in his report on Temperature Stability of Lubricants and Hydraulic Fluid, the reduction in the fluid's viscosity is

one of the most obvious effects of high temperature operation. A fluid's temperature instability can therefore occur as a result of various operating factors such as design, maintenance and the severity of the duty cycle in terms of load application, duration and magnitude. The temperature and viscosity of hydraulic fluid are inversely related; this implies that, as the temperature of the hydraulic fluid increases, its viscosity decreases. At low viscosity, the hydraulic fluid can pass through the orifice at greater speeds. At high viscosity, the rate of flow of the hydraulic fluid is reduced; hence the capacity of the buffers is increased. DEMAG, specifies that the hydraulic buffer used for this investigation was manufactured using Newtonian fluid. Hence, the viscosity of this fluid is fully dependent on both its temperature and pressure. DEMAG gives no information on the temperature behaviour of the fluid. Also, due to the design of the buffer used for this investigation, it was impossible to accurately measure the temperature of the hydraulic fluid at any given time. To have a clear understanding of this, experimental tests were conducted in such a way to vary the pressure and temperature of the hydraulic fluid at different instances. This was achieved by testing the hydraulic buffers under repetitive loading and varying the time interval between each test. This was done for each buffer with the buffers set to ten (10) different dial settings, i.e. dials 0 to dial 9. Each buffer was tested through three sets of experimental tests with a time difference of 5 minutes between each set. For the 1st set of experiment, each buffer was subjected to a repetitive loading with an interval of 15 seconds between each impact. The same procedure was carried out for the 2nd and 3rd set of experiments with an interval of 1 minute and 2 minutes respectively. A representation of the trend of results obtained for both buffers are presented in Figures 4.5.3. It must be noted that these set of experimental tests were conducted under the same impact velocity of 10 mm/sec.

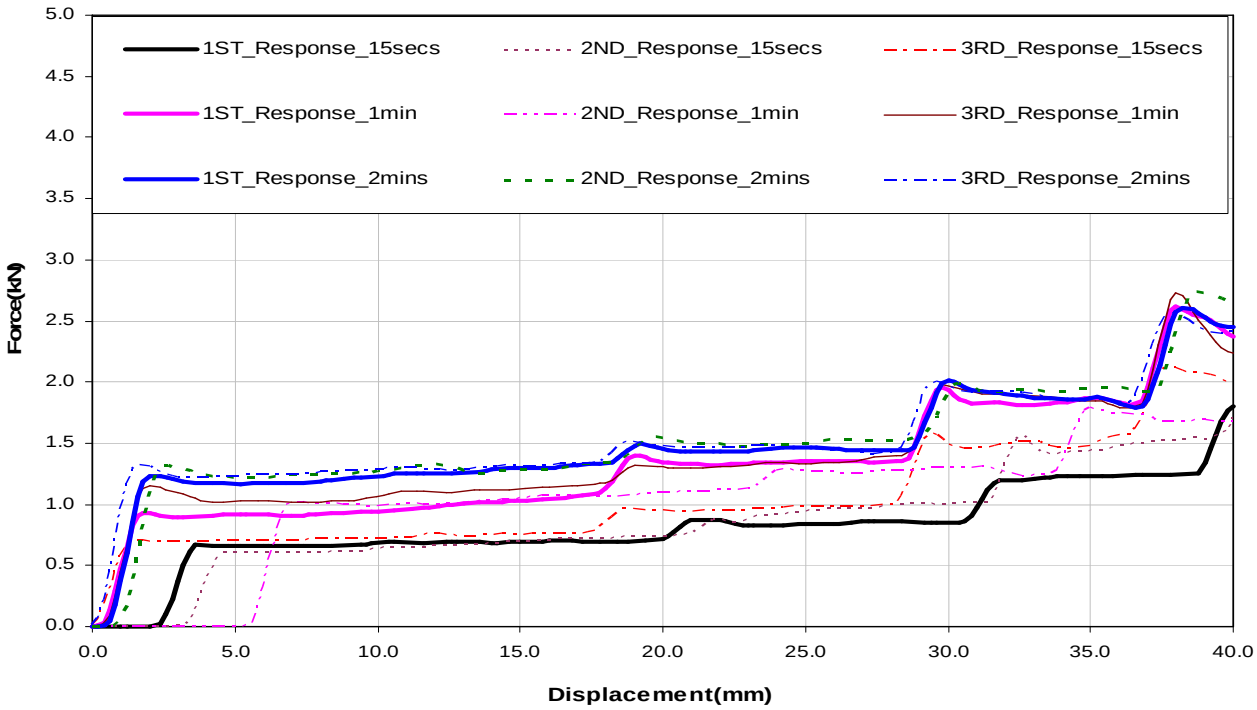

Figure 4.5.3 A representative force-displacement curve of the hydraulic buffers.

From the experimental tests, it was observed that the force-displacement curve of the buffers is erratic. Figure 4.5.3 shows that at the same dial setting, the buffers offers varying response to the repetitive loading with its force resisting capacity increasing progressively through the repetitive loading. Although the increase in force wasn't consistent through out the repetitive loading on the buffers, however, the consistent observation from the experimental test is that for both buffers, the lowest resistance to impact force occurred at the start of experiment, when the temperature and the pressure of the hydraulic oil in the buffer was expected to be minimal. From Figure 4.5.3, it is observed that at the start of the experiment, the buffer only started resisting force after a displacement of 2.6mm and eventually resist a force of 1.8kN. This implies that at the start of the experiment, the viscosity of the fluid was low causing the hydraulic fluid to flow through the orifices with little or no resisting force until the buffers had being compressed by 2.6mm. The second response after 15secs follows the same trend where the buffers compressed by almost 3.5mm before resisting the loading force and eventually resisted a force of 1.79kN. The third response (15 seconds after) however shows an increase in the viscosity of the fluid which was not expected. For this response, the buffer started resisting loading force of 0.71kN with only 0.04mm of the buffer's stroke being compressed and eventually resisted a loading force of 2kN. The second set of experiment was conducted exactly 5 minutes after the first set. The result shows high viscosity of the hydraulic fluid at the first response and a corresponding increase in the force resisting capacity of the buffer. The second response after 1min however shows a sudden reduction in the viscosity of the fluid and a corresponding reduction in the capacity of the buffers. The third response for this set of experiment shows an unexpected increase in viscosity of the fluid. The third set of experiments was conducted 5minutes after the second set. The result obtained for this set showed consistency in the viscosity of the fluid and the capacity of the buffers. Further experimental test revealed that the time it takes for the hydraulic fluid to cool off depends on the intensity of the load cycle (in terms of magnitude, frequency and velocity) and ambient temperature of the surrounding environment the buffer is subjected to. This made it difficult to estimate the capacity of the buffer at any point in time. One thing that is constant with the result obtained is that an increase in the viscosity of the buffer yielded a corresponding increase in the buffers capacity and vice versa.

4.5.1 Selection of Dial Setting from Calibration.

The results obtained and discussed above shows great inconsistency in the behaviour of the hydraulic fluid and a corresponding inconsistency in the capacity of the hydraulic buffers. Hence It was impossible to accurately estimate the capacity of the buffers. Also identified from the loading test is the significant difference in the capacity of the two buffers. However to obtain a similar capacities of the buffers, it was required to select the dial settings that shows similar capacities for the two buffers. From the calibrations, the response that offered the closest force resisting capacities

for the two buffers was for the test where the LHS buffer was set to dial 1 and the RHS buffer was set to dial 2. The results obtained for these two cases are presented in Figures 4.5.1.1 and 4.5.1.2 respectively. Although, these buffers have a capacity that varies by approximately 50N, however, these dial settings offered the closest buffer capacity. Hence, for the impact test, the LHS buffer was set to dial 1 while the RHS buffer was set to dial 2. Once the buffers had been calibrated, the hydraulic buffers were fitted to the EOHTC. Also, to have a consistent estimation of the buffer's capacity for impact, the buffers were left to cool off before conducting each impact test. This was achieved by conducting each test at an interval of 20minutes

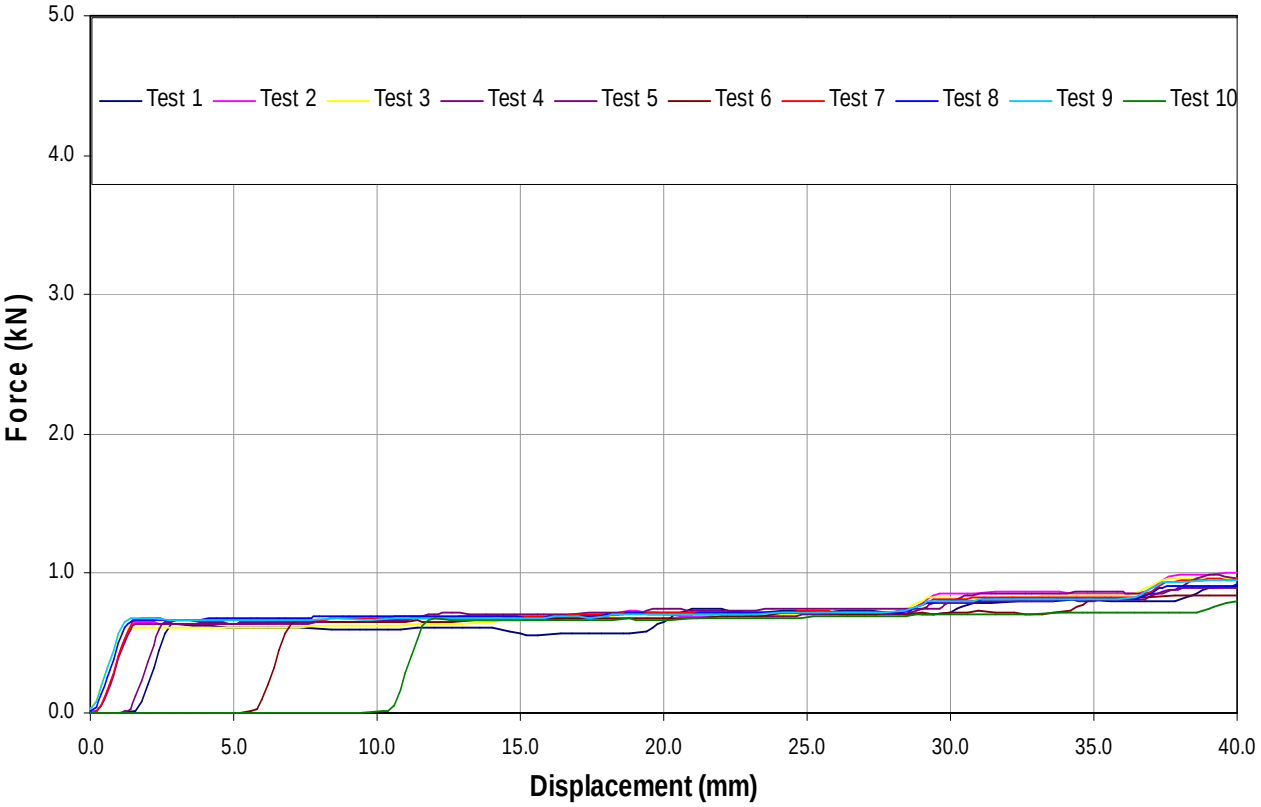

Figure 4.5.1.1 Force-displacement curve for a repetitive loading for LHS buffer: Dial 1

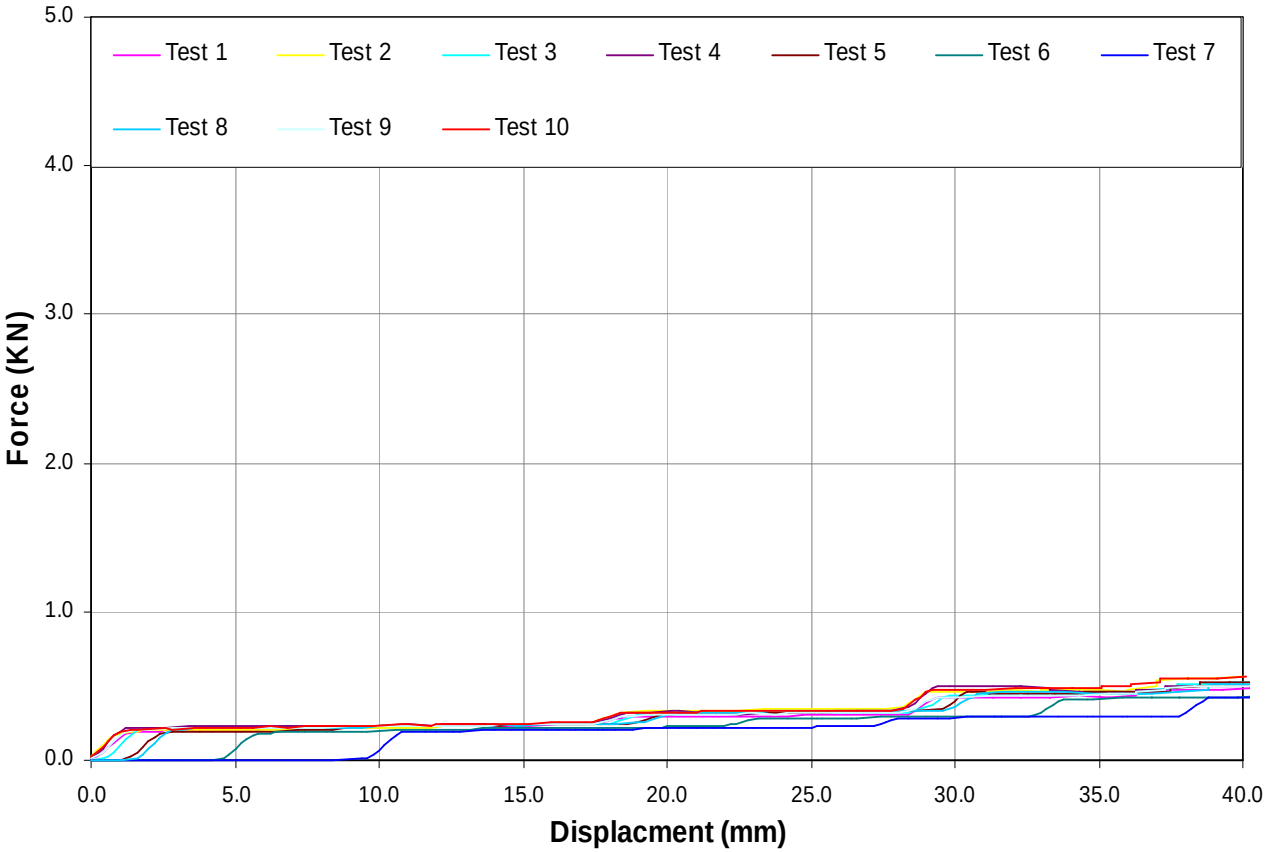

Figure 4.5.1.2 Force-displacement curve for a repetitive loading for RHS buffer: Dial 2

4.6 Description of the Experimental Impact tests on the EOHTC.

For the experimental tests, the first impact test was conducted without the payload. Also the residual torque function was disengaged before the tests commenced. This is the condition termed as Power Off no residual torque. The impact force on each of the end stops was measured with a 2 ton load cell, while the displacement of each buffer was measured with a 100mm LVDT. An encoder was connected to the crane wheels to measure the velocity before and during impact. Figure 4.6.1 shows the experimental set up. For this set of impact test, each test was conducted at an interval of 20minutes so as to achieve consistency in the impact force obtained. The results obtained for the first two impact tests are presented in Figure 4.6.2.

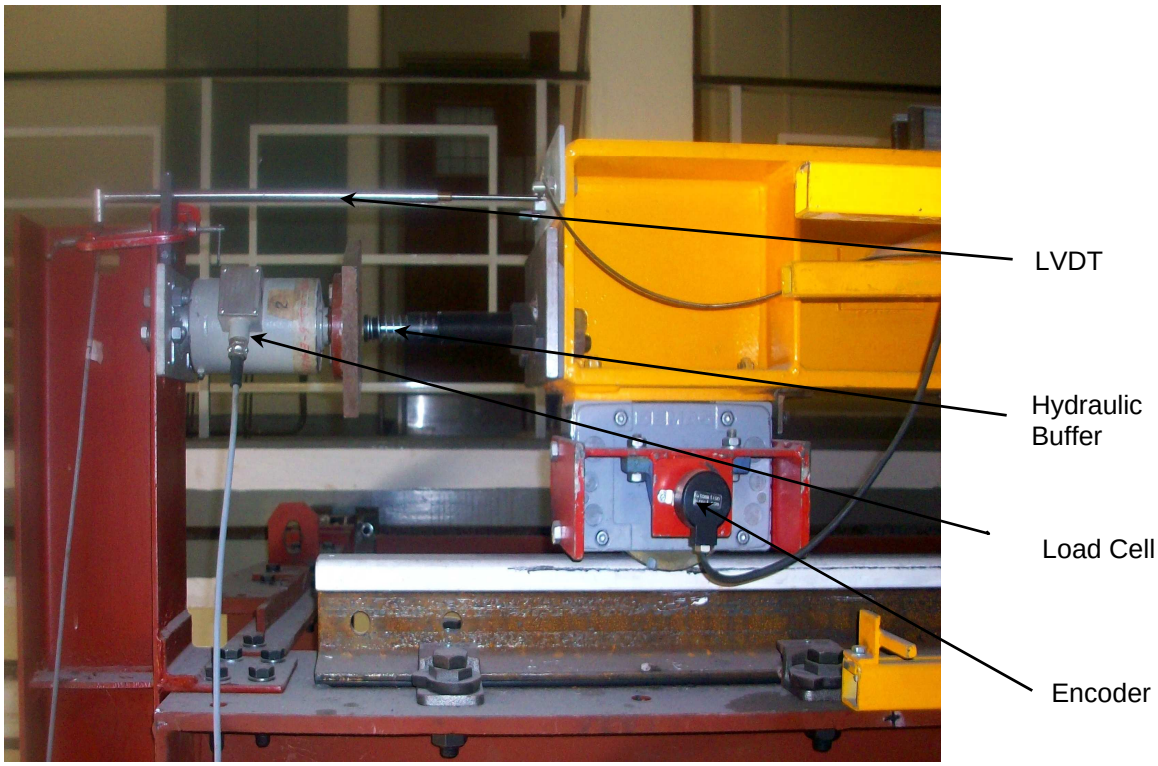

Figure 4.6.1 Experimental set up for impact test on the EOHTC fitted with hydraulic buffers.

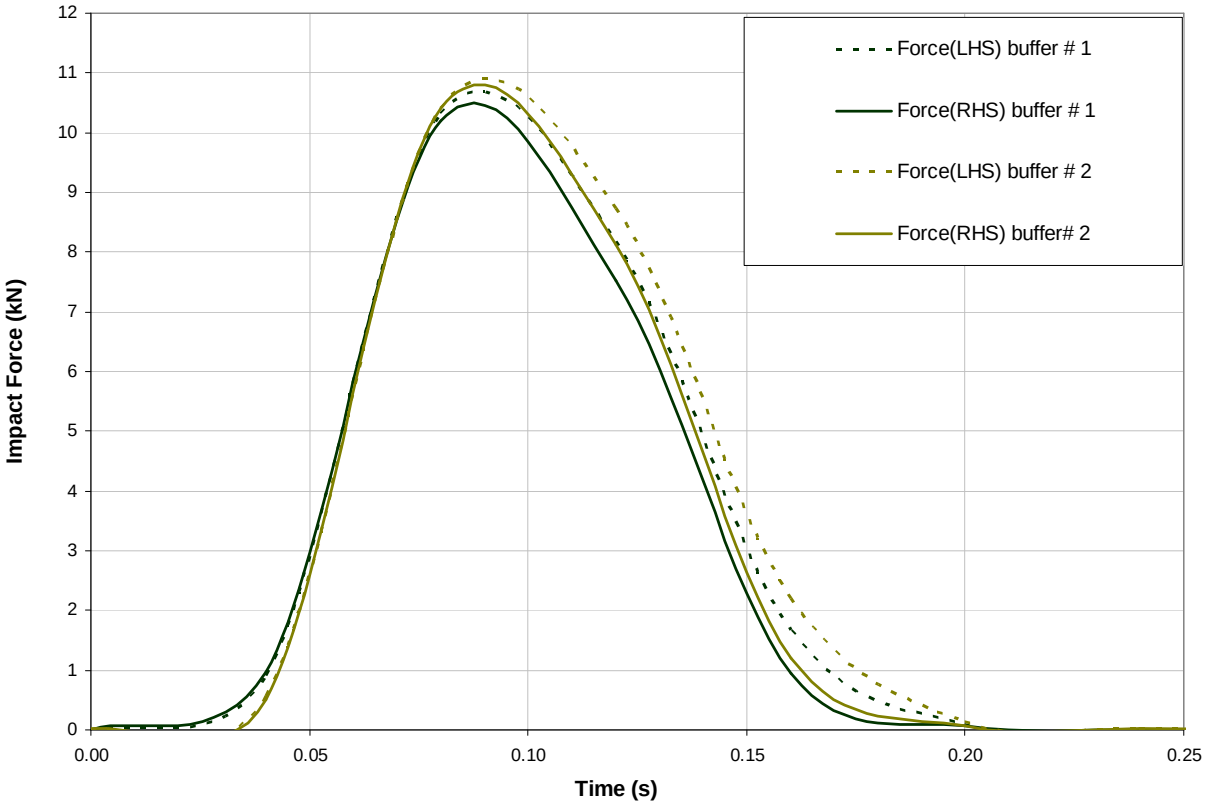

Figure 4.6.2 Impact force history for the condition of No Payload Power-Off

It can be seen from the results presented that after the calibration of the buffers, the impact force for both buffers yielded a good correlation. For this set of tests, the impact force and the displacement histories obtained were consistent; hence no further tests were conducted for this condition.

Further experimental impact test that were conducted on the EOHTC are:

- Impact test for the condition of No Payload Power On.
- Impact test for the condition of Payload Bottom Power Off.
- Impact test for the condition of Payload Bottom Power On.
- Impact test for the condition of Payload Top Power Off.

Test for the condition of No Payload Power On: For this condition, the impact tests were conducted with the power activated throughout out the tests. The representative impact force history obtained for this experiment is superimposed on that for the condition of Power Off and presented in Figure 4.6.3. The results show that impact force obtained for Power On is approximately 7% greater than that obtained for Power Off. Also for the condition of Power On, the EOHTC returns to impact the end stop after 1st impact. An experimental clip of the experimental tests for the condition of Power On shows that the rear wheels spins and lift up at impact; thus causing the crane to be propelled back into the end stop for consequent impacts. However, the results shows that the 2nd impact force is minimal when compared to the 1st impact force.

Test for the condition of Payload Bottom Power Off: For this experimental test, the payload was hoisted 0.7m above ground level with the power deactivated at impact. The payload could not be hoisted closer to the ground due to other experimental set up in the laboratory at the time of this experiment. The representative impact force history obtained is presented in Figure 4.6.4.

Test for the condition of Payload Bottom Power On: This experimental test was conducted in the same manner as described for the condition of Payload Bottom Power Off except that power was activated throughout the duration of the test. The representative impact force history obtained is superimposed on Figure 4.6.4. From Figure 4.6.4, it is observed that for the condition of Payload Bottom Power On, the 1st impact force increases by 3% compared to that obtained for the condition of Payload Bottom Power Off. Also consequent impacts for the two conditions were significantly lower than the 1st impact peaks.

Test for the condition of Payload Top Power Off: This experimental test was conducted in the same manner as described for the condition of Payload Bottom Power Off, except that the payload was hoisted 2.20m above ground level. The representative impact history obtained for this condition is presented in Figure 4.6.5. Superimposed on this is the impact force history obtained for the condition of Payload Bottom Power Off. From Figure 4.6.5, it was observed that for the condition of Payload

Bottom Power Off, the 1st impact force was 3% greater than that obtained for the condition of Payload Top Power Off.

No experimental results exist for the condition of Payload Top Power On. The capacity of the buffers to handle such an impact force was uncertain. DEMAG estimates that at an impact velocity of 33m/min, the DPH 25 hydraulic buffer has the capacity to buffer a maximum mass of 2364kg. The total mass of the payload and the crane investigated is 7361Kg. To have the payload hoisted closely to the crane bridge running at 100% of the impact velocity could yield large end stop impact forces. This was considered as unsafe thus, experimental tests were not performed for this condition.

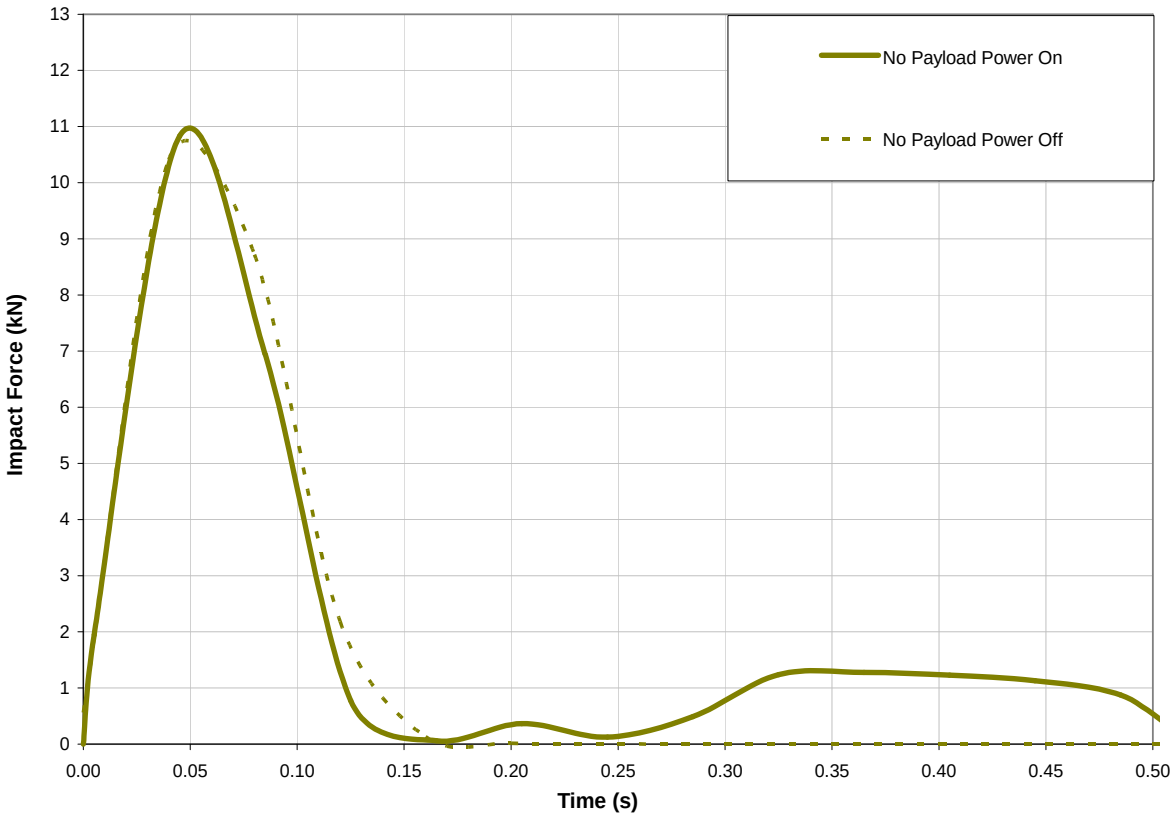

Figure 4.6.3 Comparison of impact force histories for the condition of Power On and Power Off without payload.

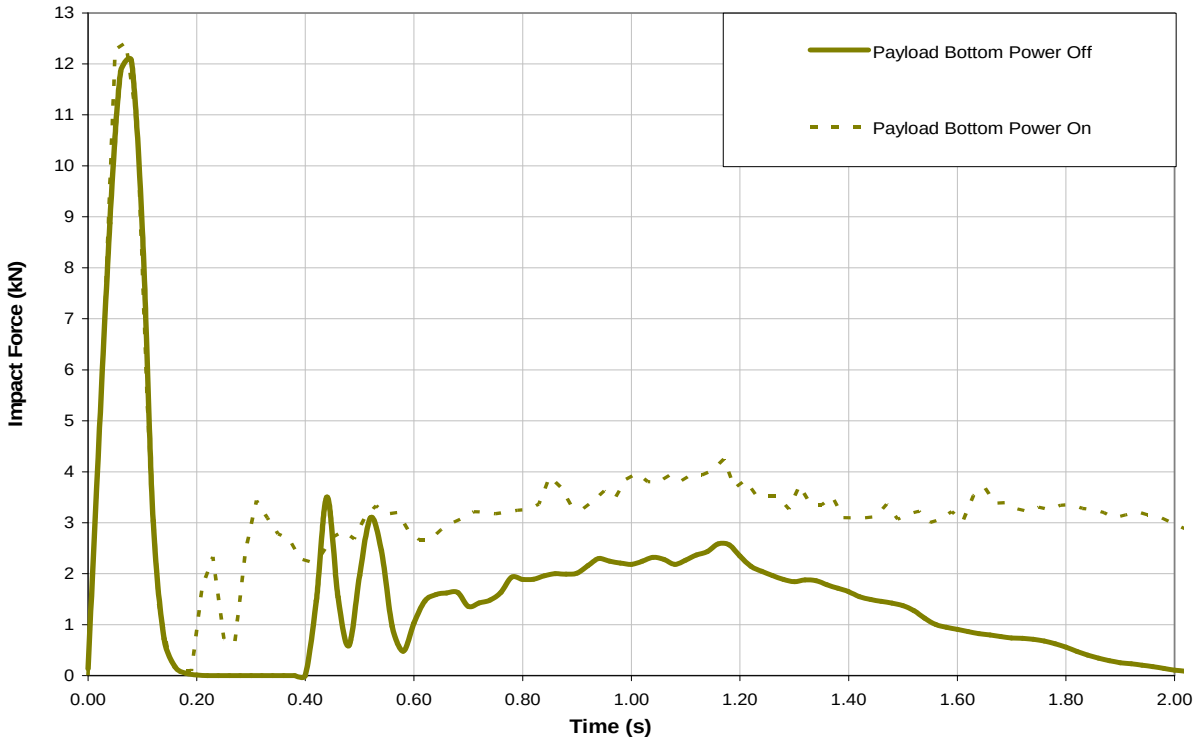

Figure 4.6.4 Comparison of impact force histories for the condition of Payload Bottom Power On and Payload Bottom Power Off.

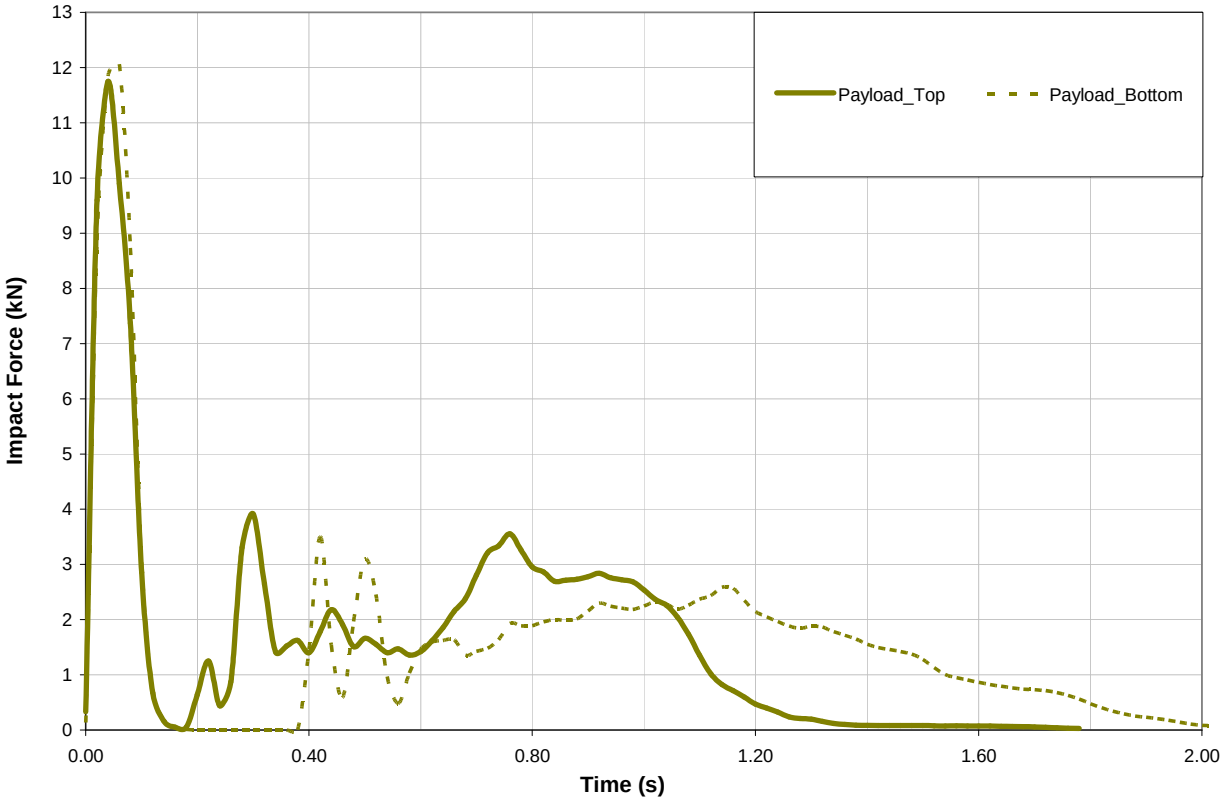

Figure 4.6.5 Comparison of impact force histories for the condition of Payload Top and Payload Bottom Power Off.

4.7 Finite Element modelling of the hydraulic buffers.

In order to obtain accurate end stop impact forces when the EOHTC is fitted with hydraulic buffers, it was necessary to accurately model the elastic and damping characteristics of the buffers. The EOHTC has a rated capacity of 0.55m/sec when travelling at full speed. Experimental loading tests were conducted on the buffers at constant velocities of 0.0375m/sec, 0.075 m/sec, 0.1125m/sec and 0.150m/sec. Due to the limited capacity of the INSTRON actuator, loading tests could not be conducted for velocities higher than 0.150m/sec.

The result obtained from the series of loading tests conducted shows that the buffers have a damping capacity related by equation 2.3.2, i.e. $F = Cv^n$ as shown in section 2.3. From the results obtained for the varying velocities, it is possible to simultaneously solve for the damping constant "C" and value of "n" which can be used to obtain the force capacity of the buffers at a constant velocity of 0.55m/s. However, the results obtained from the impact tests on the crane shows that the buffers have a non constant deformation rate (non constant strain) throughout impact. Hence the capacity of the buffers at a constant velocity of 0.55m/s could not accurately simulate its response under impact. According to Kohlhaas, (2004), the capacity of the buffers for a non constant strain could only be accurately obtained from impact tests on the crane. Using the response obtained from an impact test conducted on the EOHTC fitted with elastomeric buffers, Kohlhaas (2004), made comparisons with the buffer's capacity supplied by the manufacturer as presented in Figure 4.7.1. The result shows that at an impact velocity of 0.55m/sec (33m/min) the response of the buffer from the crane was very similar to that provided by the manufacturer.

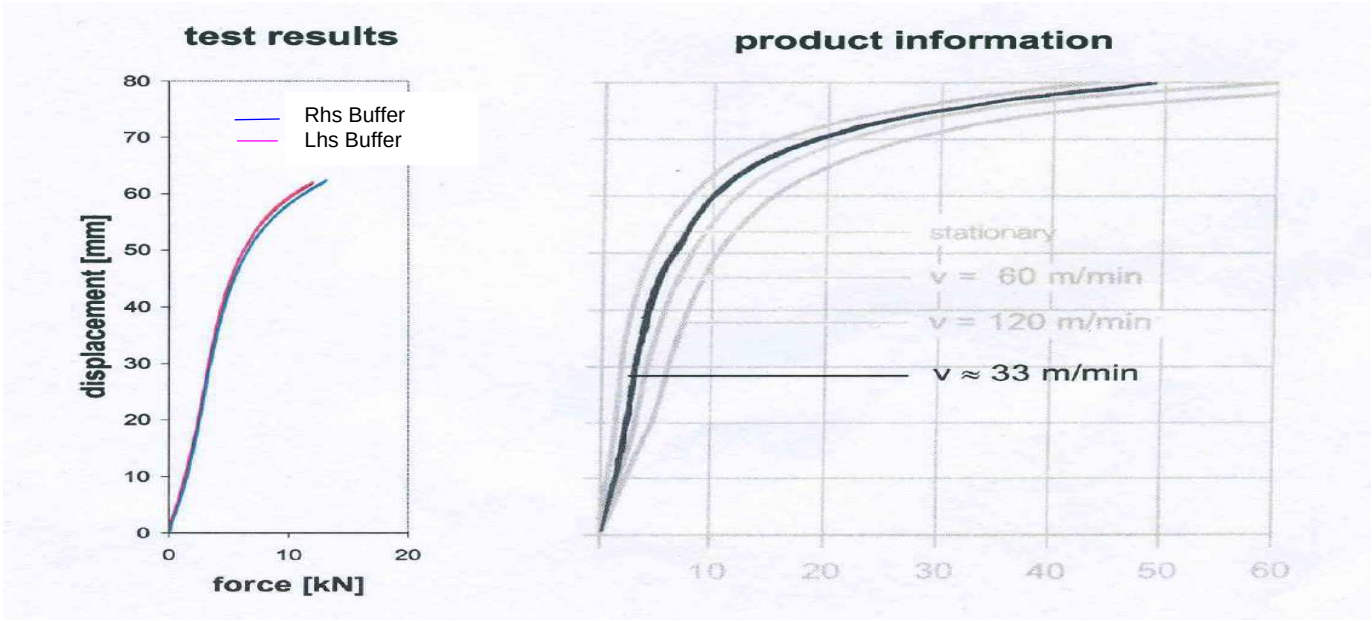

Figure 4.7.1 Comparison of the results from the impact tests of the crane with product the product's information.

Also for DPZ 100 elastomeric buffers, Haas (2007) compared the line joining the point of zero velocity obtained from impact tests conducted on the crane with the elastic curve supplied by the manufacturer. The line joining point of zero velocity is the line that joins the start of deceleration of the buffers to the point where the buffers starts to accelerate during impact test. The comparison made as presented in Figure 4.7.2 shows a close correlation between the results obtained and the manufacturer's curve.

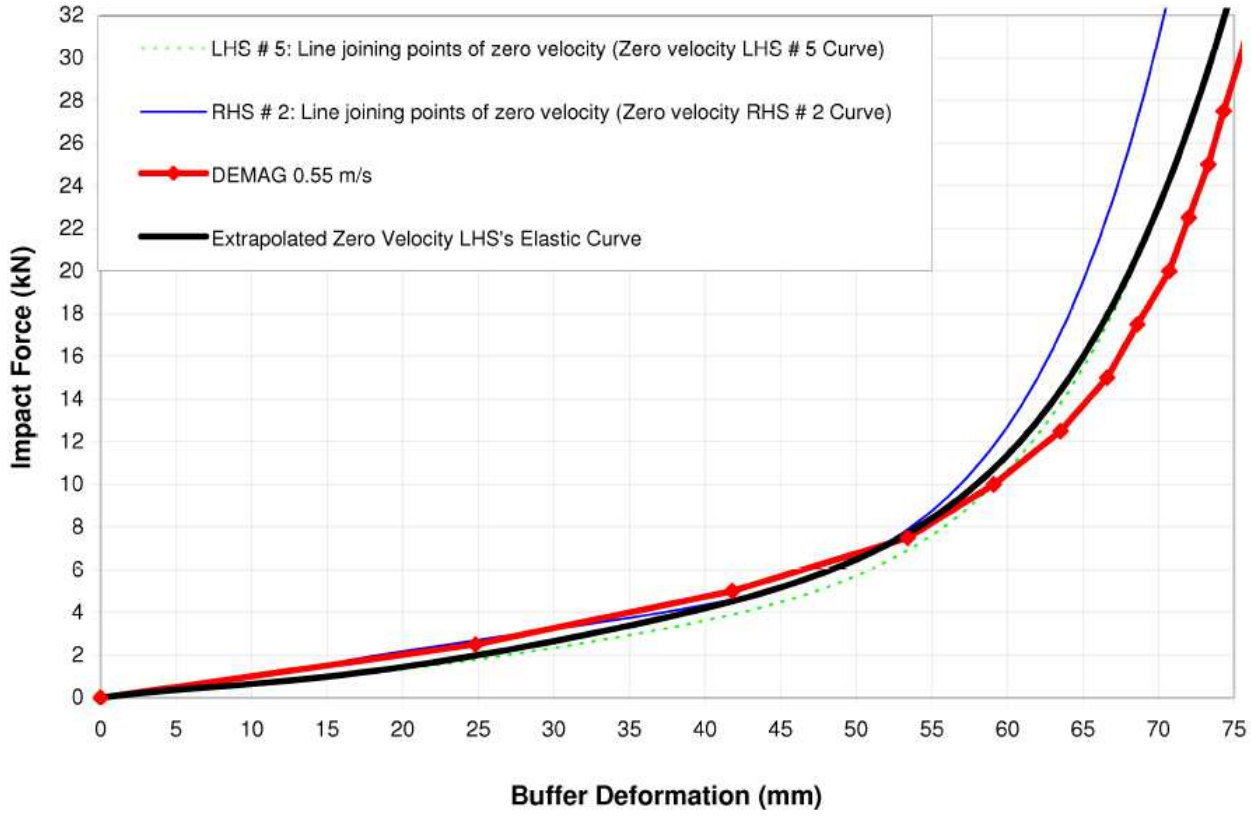

Figure 4.7.2 Comparison between DEMAG's elastic curve and the line joining the point of zero velocity resulting from the impact tests of the crane.

From the experimental impact tests conducted on the EOHTC fitted with the hydraulic buffers, the force vs. displacement curve was obtained and presented in Figure 4.7.3. The result presented in Figure 4.7.3 shows that during the impact tests, the buffers compressed by only 13mm before it started to expand. In order to obtain the force vs. displacement curve for the entire stroke of the buffers, the loading curve was extrapolated for a displacement of 50mm as shown in Figure 4.7.3. Also shown in Figure 4.7.3 is the line joining the point of zero velocity extrapolated for a displacement of 50mm. The result of the extrapolation presented in Figure 4.7.3 shows that the extrapolated loading curve has a linear function. Although the result obtained from the test shows that the loading curve is only linear until a displacement of 8mm after which the force reduces from

10.4kN to 2kN. However, the loading curve was assumed linear since the force increased in a linear trend till the maximum impact force obtained.

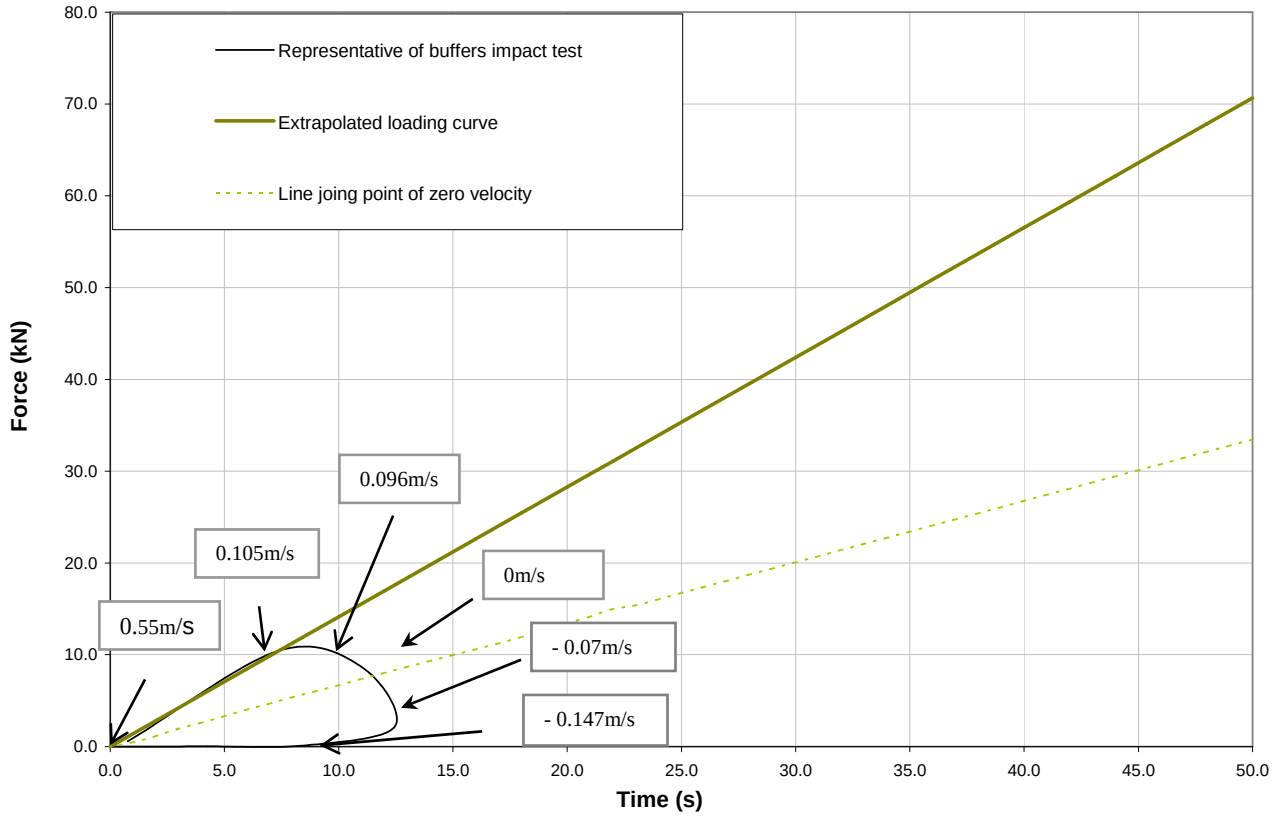

Figure 4.7.3 A representation of the force vs. displacement curve of the hydraulic buffers obtained from the experimental impact tests.

DEMAG gives no information on the force vs. displacement curve of the hydraulic buffers. However, DEMAG provides a force vs. energy curve for hydraulic buffers as presented in Figure 4.7.4. The manufacturer's curve presented shows that hydraulic buffers have a linear function

As earlier stated, the result from the impact tests from the crane was obtained for a displacement of 13mm. Hence, the rate at which the buffers compressed during impact tests were also obtained for a deformation of 13mm. According to Kit (1996), the deceleration of the buffer is only a function of the velocity and the stopping distance of the buffers. This is represented by Figure 4.7.5.

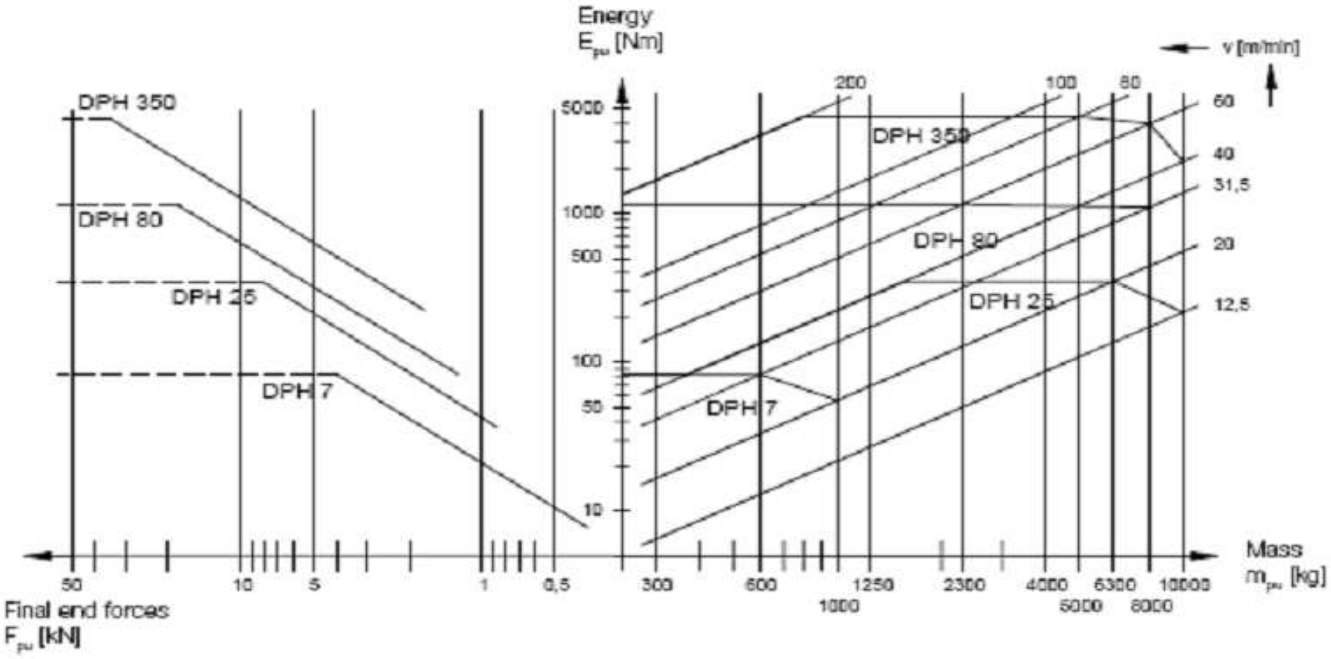

Figure 4.7.4 DEMAG's force vs. energy curve and energy vs. impact mass curve for hydraulic buffers.

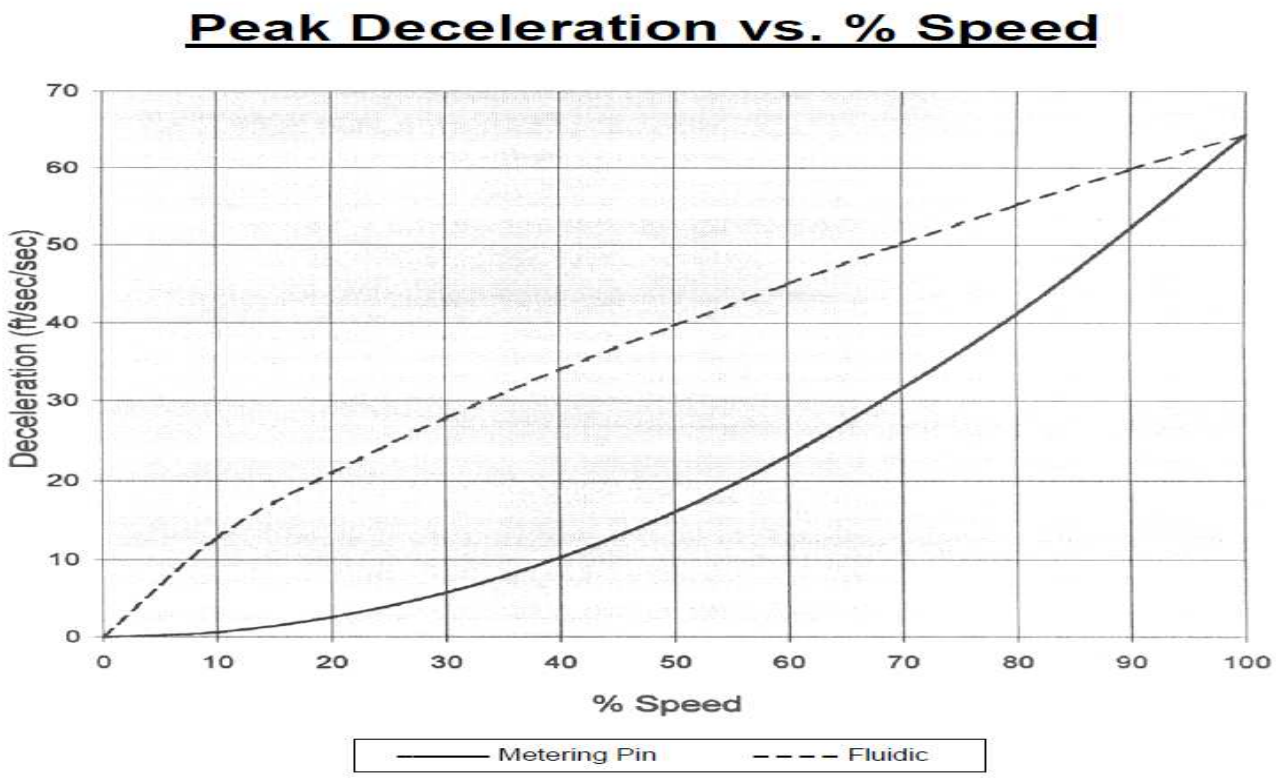

Figure 4.7.5 Peak Deceleration vs. Impact Speed**,** Kit (1996)

Kit, (1996) stated that the higher the impact velocity, the higher the deceleration of the buffers and the fraction of stroke compressed. The implication of this is that the deceleration of the buffers and the corresponding stroke of the buffer compressed is a function of the impact velocity. According to Kit, (1996) only an hydraulic buffer with a metering pin device uses all of its stroke under any given speed. For an hydraulic buffer with a fluidic metering device, the impact velocity determines the fraction of the buffer's stroke that is compressed at impact. Kit,(1996) illustrated this relationship with a force vs. displacement curve for different impact velocities as presented in Figures 2.3.2 and 2.3.3 of this document. The result of the impact tests conducted on the hydraulic buffers used for this investigation reveal that it has a metering fluidic device. At a rated crane travel velocity of 0.55m/s the results from all the impact tests from the crane shows that the EOHTC decelerates with a change in impact velocity from 0.55m/s to 0.096m/s with a corresponding buffer deformation of 10mm and the buffers eventually compressed to a maximum deformation of 13mm. Due to the relationship between the impact velocity and the deceleration of the buffers, it is not expected that the buffers will experience a higher deformation at the given velocity. However, to create a model where the effect of higher impact velocity can be investigated; the velocity was extrapolated for a displacement of 35mm. This was achieved by plotting the graph of the change in the velocity of the EOHTC vs. buffer deformation obtained from the impact test as presented in Figure 4.7.6. The regression line equation obtained in Figure 4.7.6, was used to extrapolate the velocity at which the buffers were compressed for a buffer deformation of 35mm. The deformation was limited to 35mm because velocities obtained beyond a buffer deformation of 35mm were infinitely small.

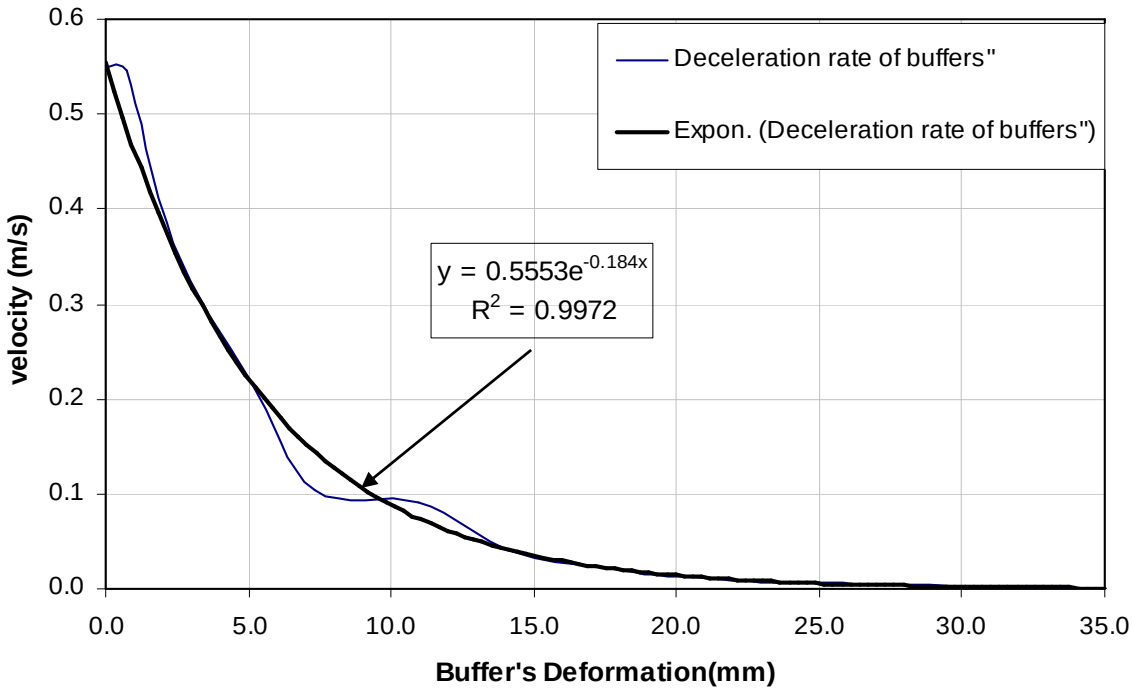

Figure 4.7.6 Velocity vs. Buffer Deformation Curve

The velocities obtained from the extrapolation for the loading curve is shown in Figure 4.7.7. Using Figure 4.7.7, the damping characteristics was modelled as the difference between the loading curve and the line joining the point of zero velocity as presented in Table 4.7.1

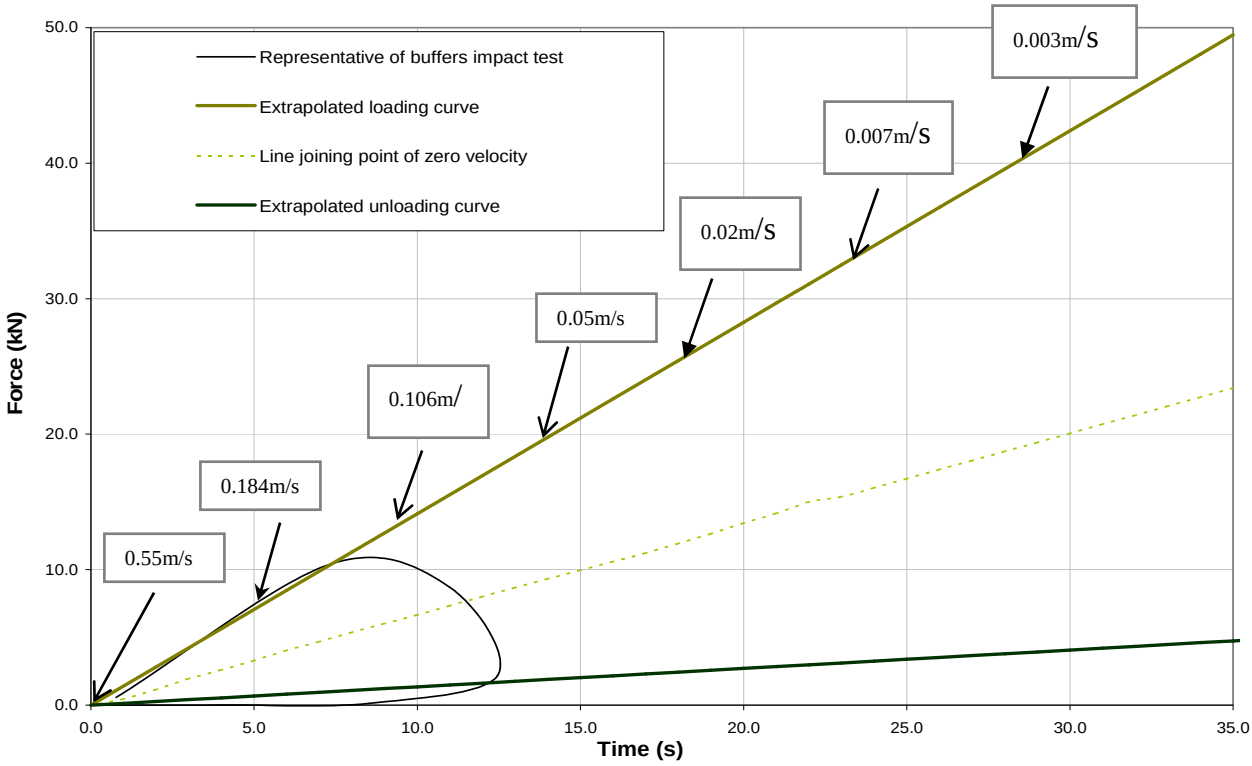

Figure 4.7.7 Extrapolated buffer's force displacement curve obtained from the impact test on the Crane

Table 4.7.1. Damping characteristics of the buffers obtained for a non constant strain

Force (kN)	Buffer Deformation (mm)	Velocity (m/sec)
0	0	0.55
0.95	1.0	0.46
2.27	3.0	0.32
4.42	6.0	0.184
6.99	9.0	0.106
9.68	13.0	0.05
13.50	18.0	0.02
17.86	24.0	0.007
21.83	28.0	0.003
24.60	33.24	0.001
26.80	35.0	0.0008

The damping and the elastic characteristics of the buffers obtained were incorporated into the FEA model of the EOHTC and FEA simulations was conducted to obtain the end stop impact force.

4.7.1 Calibration of the FEA results with the Experimental Result

Using the buffer's characteristics obtained, FEA simulations were conducted for the condition of "No Payload Power Off". The result obtained is superimposed on the experimental result as presented in Figure 4.7.1.1

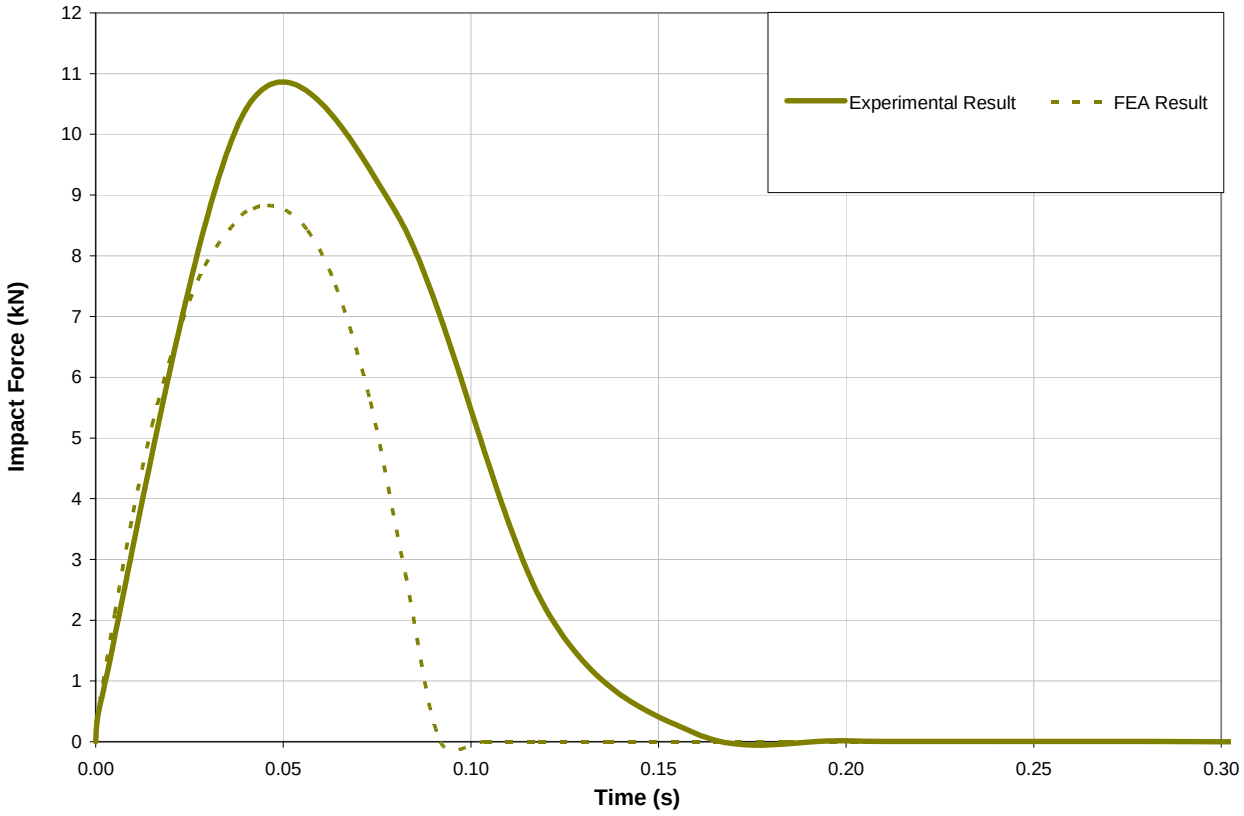

Figure 4.7.1.1 FEA impact force superimposed on the experimental result

From the comparison made, it can be seen that the FEA yielded a response that is significantly lower than the experimental result. To obtain an impact peak closer to the experimental result, the damping characteristics of the buffers were adjusted until a better impact history was obtained. Table 4.7.1.1 shows the calibrated damping characteristics.

Also the unloading curve obtained from the FEA result shows that the buffers expand at a faster rate in the FEA simulations than in the experimental tests. The expansion of the buffers is a function of the reset mechanism of the buffers. Hence to capture the rate of expansion of the buffers in the FEA model, an unloading damping characteristic was introduced to the FEA model of the buffers. This

was modelled as the negative difference between the line joining the point of zero velocity and the extrapolated unloading curve in Figure 4.7.7 with the corresponding rate of acceleration of the buffers during the expansion phase as presented in Table 4.7.1.2. From the experimental tests, the buffers expand from zero velocity to 0.147m/secs after which it starts to decelerate. Hence it was difficult to estimate the velocity change during the expansion phase. However to introduce the unloading damping characteristics into the model, a series of acceleration rate was assumed in the model and simulations were conducted until the unloading trend in the FEA result yielded a close fit to the experimental result

Table 4.7.1.1 Calibrated damping characteristics of the buffers

Force (kN)	Buffer Deformation (mm)	Velocity (m/sec)
0.64	1.0	0.55
1.38	1.3	0.45
2.17	7.0	0.35
3.05	11.0	0.28
3.62	14.5	0.2
3.96	17.5	0.15
4.92	20.5	0.12
5.32	23.5	0.1
5.72	27.0	0.098
6.31	29.0	0.094
6.70	33.0	0.086
6.90	35.0	0.05

Table 4.7.1.2 Unloading damping characteristics of the buffers

Force (kN)	Velocity(m/s)
0.00	-0.001
-0.35	-0.072
-1.00	-0.075
-2.20	-0.083
-6.30	-0.097
-10.90	-0.15
-11.70	-0.2
-12.37	-0.25
-12.46	-0.31
-12.59	-0.39
-12.82	-0.46
-12.91	-0.52
0.00	-0.55

Comparison of the damping characteristics in Table 4.7.1 and the calibrated damping characteristics in Table 4.7.1.1 shows that the originally obtained damping characteristics vary significantly from the calibrated values. This variation is particularly obvious after a deformation of 8mm where the maximum force occurred during the experimental test. The author is of the opinion that the significant difference is due to the assumption that the loading curve continues linearly after the maximum force obtained. However, the assumption that the loading curve is linear was only adopted as a starting point for the modelling of the buffers.

The calibrated damping characteristics of the buffers obtained were incorporated in the FEA model and finite element simulations were conducted to obtain the end stop impact force. Figure 4.7.1.2 presents the experimental impact force superimposed on the FEA impact force obtained using the adjusted damping characteristics for the condition of No payload power off

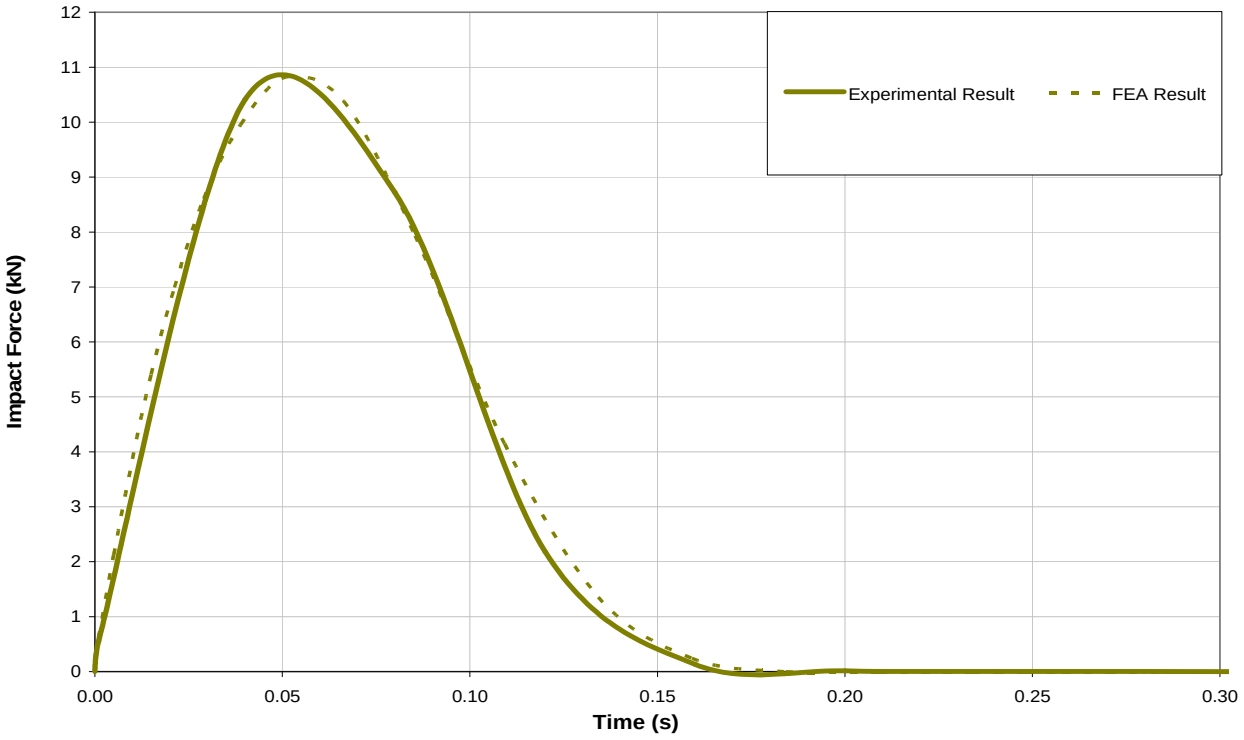

Figure 4.7.1.2 Comparison of the FEA impact force response for the condition of No Payload Power Off with the experimental result.

From Figure 4.7.1.2, it can be seen that there is an excellent correlation between the FEA and experimental impact force histories. Both impact force histories yield a maximum impact force of 10.8kN. The time difference between the impact peaks is 0.02 seconds

4.7.1.2 Comparison of the FEA impact force history with the experimental impact force for the condition of No Payload Power On

An FEA simulation was conducted for the condition of No Payload Power On. For this simulation, the original FEA model developed by Haas (2007) captures the constantly running motors of 55kW on the crane wheels. This was modelled by applying a force of 550N produced by the running motors to the rear wheels. A simplification was introduced to capture the loss of contact and the spinning of the conventional motorised experimental wheels. This was achieved by applying a time dependent amplitude function to the force on the wheels. The result obtained for this condition is superimposed on the experimental result and presented in Figure 4.7.1.2.1

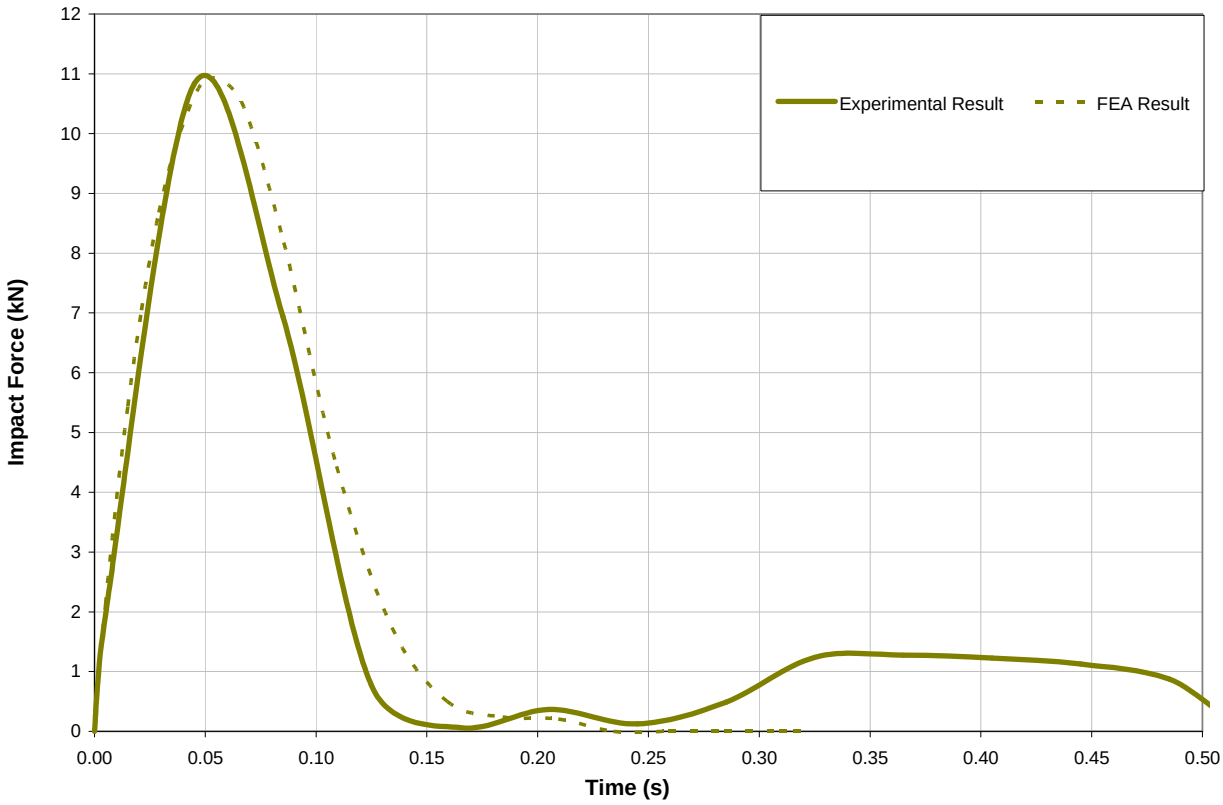

Figure 4.7.1.2.1 Comparison of the FEA impact force history for the condition of No Payload Power On with the experimental impact force history.

.

4.7.1.3 Comparison of the FEA impact force history with the experimental impact force for the condition of Payload Bottom Power On

Figure 4.7.1.3.1 presents the FEA impact force superimposed on the experimental result for the condition of Payload Bottom Power On. The comparison shows that FEA simulation gives an impact force which is 0.8kN lower than that obtained for the experimental result.

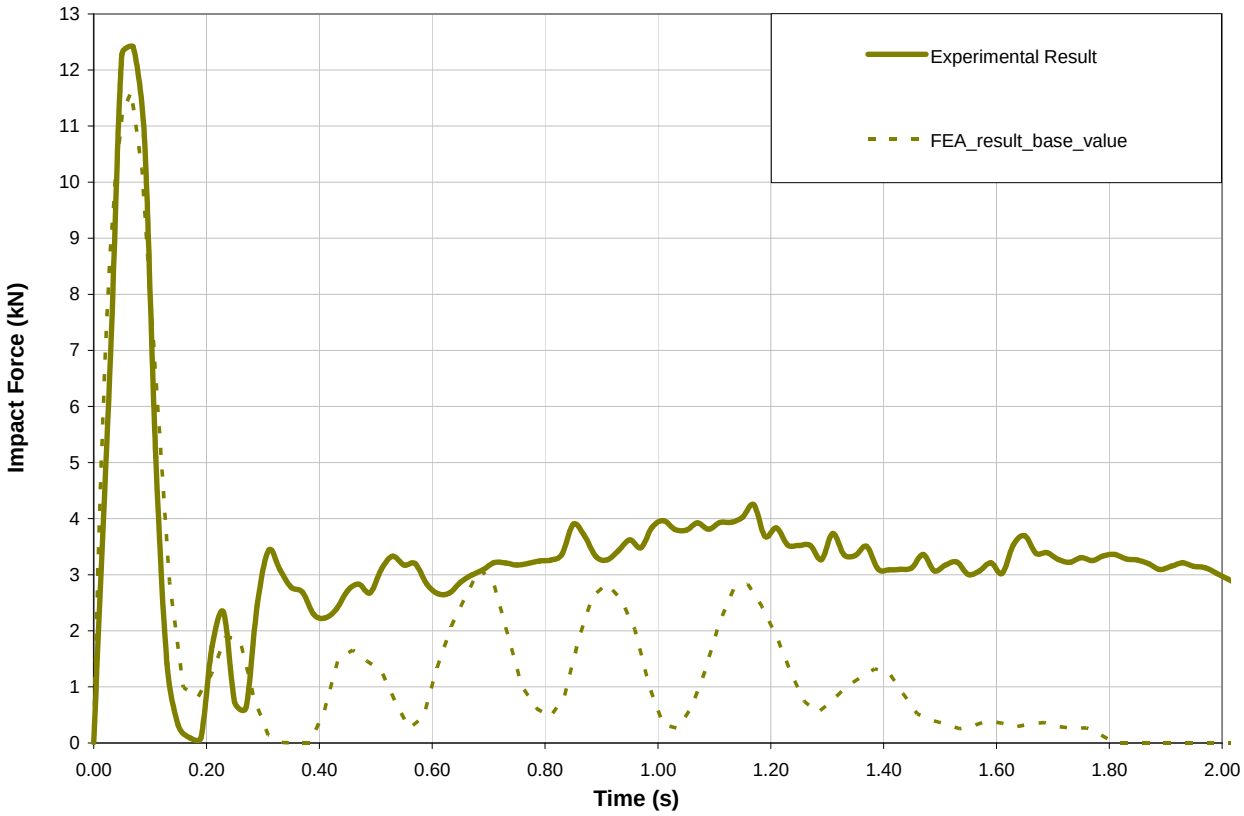

Figure 4.7.1.3.1 Comparison of the FEA impact force history for the condition of Payload Bottom Power On with the experimental impact force history.

4.7.1.4 Comparison of the FEA impact force history with the experimental impact force for the condition of Payload Bottom Power Off.

Figure 4.7.1.4.1 presents the FEA impact force superimposed on the experimental result for the condition of Payload Bottom Power Off. From the result presented, a difference of 0.9kN in the maximum impact force was observed. For this condition, the experimental clip revealed that the crane impacts the end stop at a positive payload lag angle. However, the FEA model has a predefined zero payload lag angle at impact for base value simulations. Further simulations conducted for a positive lag angle of 2.5º gives an impact force that offers a close correlation to the experiment impact force history. This is document in subsequent chapter.

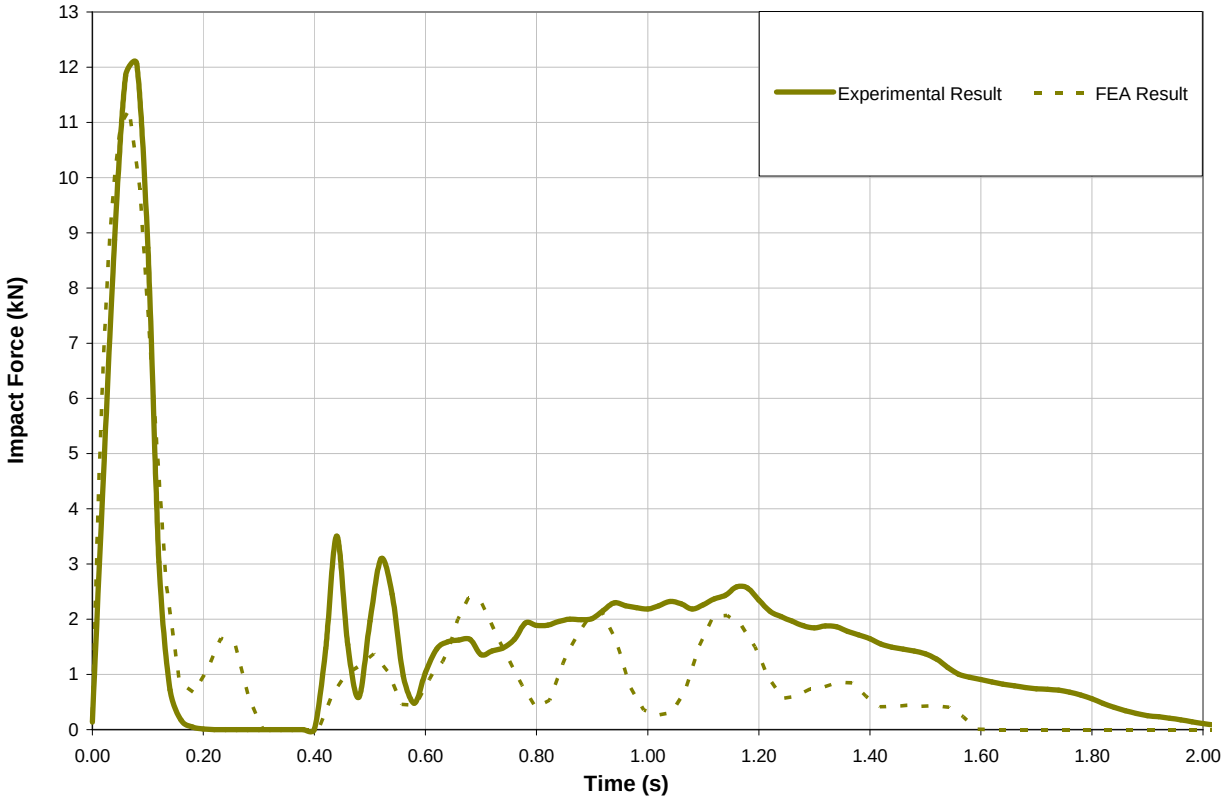

Figure 4.7.1.4.1 Comparison of the FEA impact force history for the condition of Payload Bottom Power Off with the experimental impact force history.

4.7.1.5 Comparison of the FEA impact force history with the experimental impact force for the condition of Payload Top Power Off.

Figure 4.7.1.5.1 presents the FEA impact force superimposed on the experimental result for the condition of Payload Top Power Off. The comparison made for the condition of Payload Top Power Off shows a closer correlation in the maximum impact force obtained. For this condition, the same maximum impact force value was obtained for both the experimental and FEA results. It must be noted that the trend of subsequent impacts after the 1st impact is highly dependent on the payload lag angle, bearing in mind that the hydraulic buffer does not have a large return force capacity to cause a significant 2nd impact force.

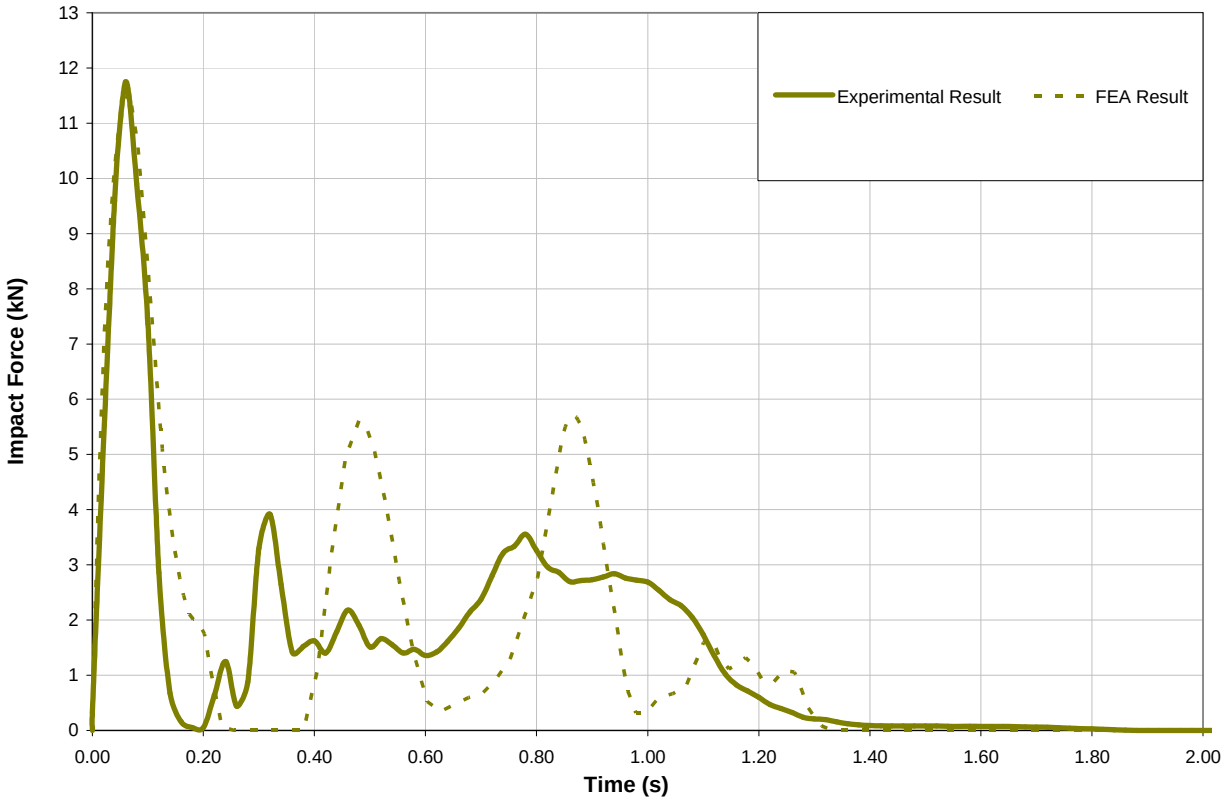

Figure 4.7.1.5.1 Comparison of the FEA impact force history for the condition of Payload Top Power Off with the experimental impact force history.

Since no experimental result exist for the condition of Payload Top Power, On, FEA simulations conducted for this condition could not be calibrated to experimental result

From the result obtained from the calibrations, it can be concluded that the FEA model of the hydraulic buffers yields a close representation of the operation of the hydraulic buffers. Hence the hydraulic buffer model was employed for further FEA simulations.

CHAPTER 5: SENSITIVITY STUDY

5.1 Sensitivity Study of the Effect of the Parameters on the End Stop Impact Force History for a Single Bridge EOHTC Fitted with Hydraulic Buffers

Another aim of this research project was to determine the maximum end stop impact force for an EOHTC fitted with hydraulic buffers. A finite element analysis of the EOHTC model fitted with the DPH 25 adjustable buffers was conducted. This was done to investigate the effect of each parameter identified in chapter 2 on the end stop impact force history. This section deals with the sensitivity of the parameters to the end stop impact force history.

It must be noted here that since the condition for Power On will always yield greater impact force, simulations were conducted only for the condition of Power On.

5.2 Interpretation of FEA Simulation

In the FEA simulations, each identified influencing parameter was analysed individually while the other parameters were kept constant. This section gives a description of the results obtained for each parameter. Also documented in this section are the comparisons made between the FEA impact force histories obtained for the single bridge EOHTC fitted with hydraulic buffers and that fitted with elastomeric buffers.

5.2.1 Effect of the Lag Angle on the Impact Force History

Figures 5.2.1.1 and 5.2.1.2 show the effect of the horizontal lag angle of the payload at impact on the impact force history for the single bridge EOHTC fitted with the hydraulic buffers and the single bridge EOHTC fitted with the elastomeric buffers respectively. The result presented here are for the condition of Payload Bottom.
The significant information which can be extracted from these results are:

- At 1st impact, the results obtained for both buffers follow the expected trend. As the positive lag angle of the payload increases, there is a corresponding increase in the impact force obtained. The opposite holds for an increase in the negative lag angle.
- The results presented shows that the effect of the parameter change is significantly reduced for the hydraulic buffer when compared with the elastomeric buffers.

The numerical differences between the impact forces for the single bridge EOHTC fitted with hydraulic buffers and the single bridge EOHTC fitted with elastomeric buffers are presented in Table 5.2.1.1

Table 5.2.1.1 Influence of the payload lag angle on the impact force history: payload bottom

Payload Lag Angle (°)	Hydraulic Buffers		Elastomeric Buffers		Percentage Difference in Impact Force w.r.t the Base Value for Hydraulic Buffers (%)		Percentage Difference in Impact Force w.r.t the Base Value for Elastomeric Buffers (%)	
	1st Impact Force (kN)	2nd Impact Force (kN)	1st Impact Force (kN)	2nd Impact Force (kN)	1st Impact	2nd Impact	1st Impact	2nd Impact
Base value 0°	11.57	1.95	7.26	4.61	NA	NA	NA	NA
-1.25	11.20	1.36	6.20	5.00	-3.2	-30.3	-14.6	8.5
-2.50	10.79	0.25	5.36	5.95	-6.7	-87.2	-26.2	29.1
+1.25	12.00	1.96	8.80	4.57	3.7	0.5	21.2	-0.9
+2.50	12.40	2.13	10.02	4.60	7.2	9.2	38.0	-0.2

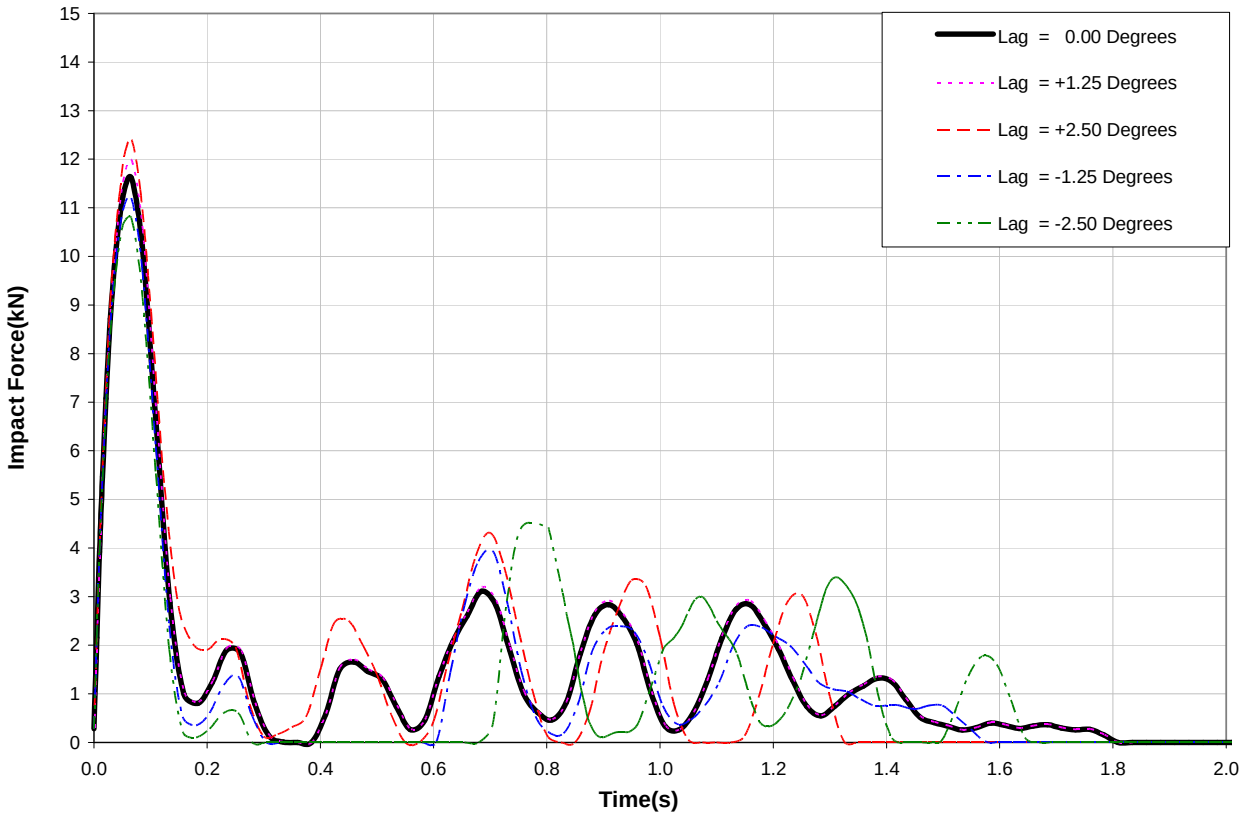

Figure 5.2.1.1 Parameter = Payload Lag Angle: Payload Bottom “Hydraulic Buffers”.

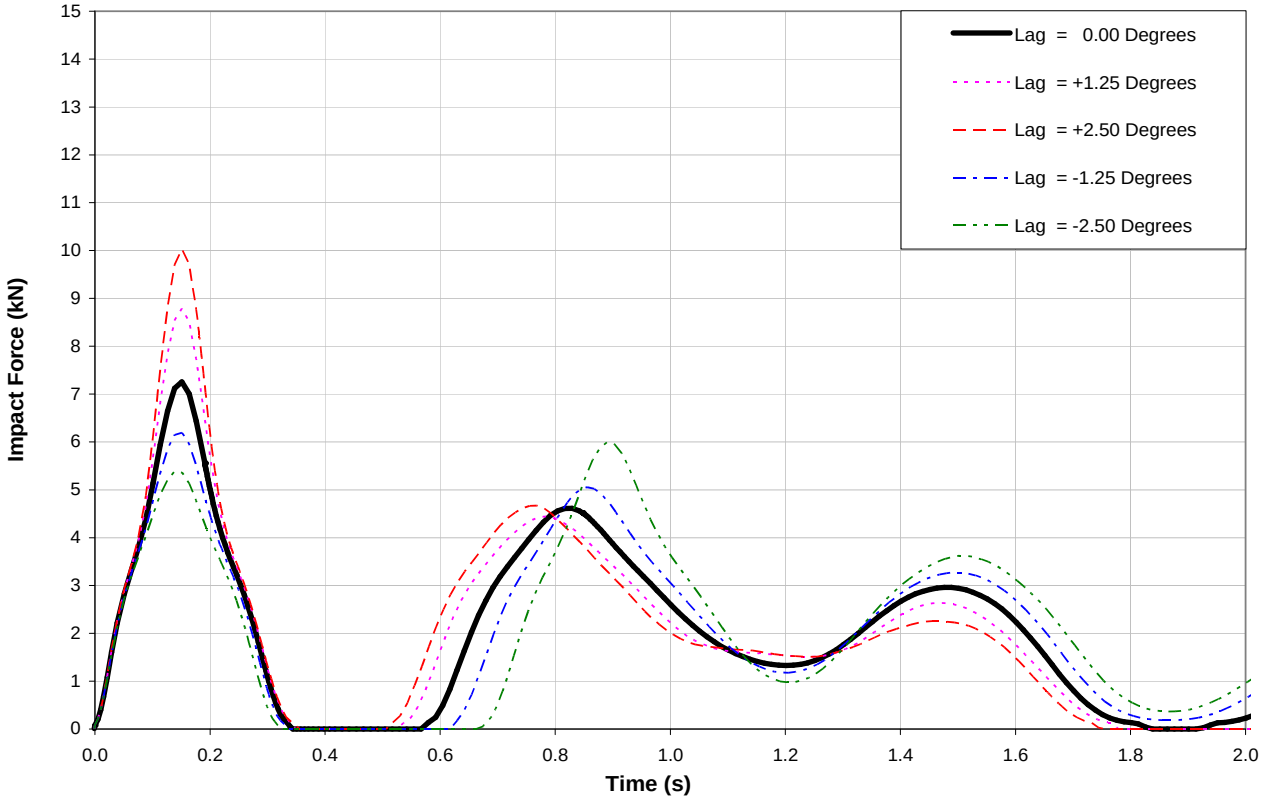

Figure 5.2.1.2 Parameter = Payload Lag Angle: Payload Bottom “Elastomeric Buffers”.

Figures 5.2.1.3 and 5.2.1.4 show the effect of the horizontal lag angle of the payload at impact on the impact force history for the single bridge EOHTC fitted with the hydraulic buffers and the single bridge EOHTC fitted with the elastomeric buffers respectively. The results presented here are for the condition of Payload Top.

The significant information which can be extracted from these results are:

- At 1st impact, results obtained for both the hydraulic and elastic buffers follow the expected trend where the impact peaks increases with a corresponding increase in the positive lag angle.
- The 2nd impact however follows a different trend. For the hydraulic buffers, the positive lag angle yield a corresponding reduction in the 2nd impact peaks. The opposite is true for the elastomeric buffers.

The numerical differences between the impact forces for the single bridge EOHTC fitted with hydraulic buffers and the single bridge EOHTC fitted with elastomeric buffers are presented in Table 5.2.1.2.

Table 5.2.1.2 Influence of the payload lag angle on the impact force history: payload top

Payload Lag Angle (ϑ)	Hydraulic Buffers		Elastomeric Buffers		Percentage Difference in Impact Force w.r.t the Base Value for Hydraulic Buffers (%)		Percentage Difference in Impact Force w.r.t the Base Value for Elastomeric Buffers (%)	
	1st Impact Force (kN)	2nd Impact Force (kN)	1st Impact Force (kN)	2nd Impact Force (kN)	1st Impact	2nd Impact	1st Impact	2nd Impact
Base value 0^0	11.56	5.61	7.48	8.05	NA	NA	NA	NA
-1.25	11.19	6.40	6.04	7.14	-3.2	14.1	-19.3	-11.3
-2.50	10.66	6.43	5.63	7.96	-7.8	14.6	-24.7	-1.1
+1.25	11.97	5.51	8.64	8.31	3.5	-1.8	15.5	3.2
+2.50	12.26	4.58	9.92	8.52	6.1	-18.4	32.6	5.8

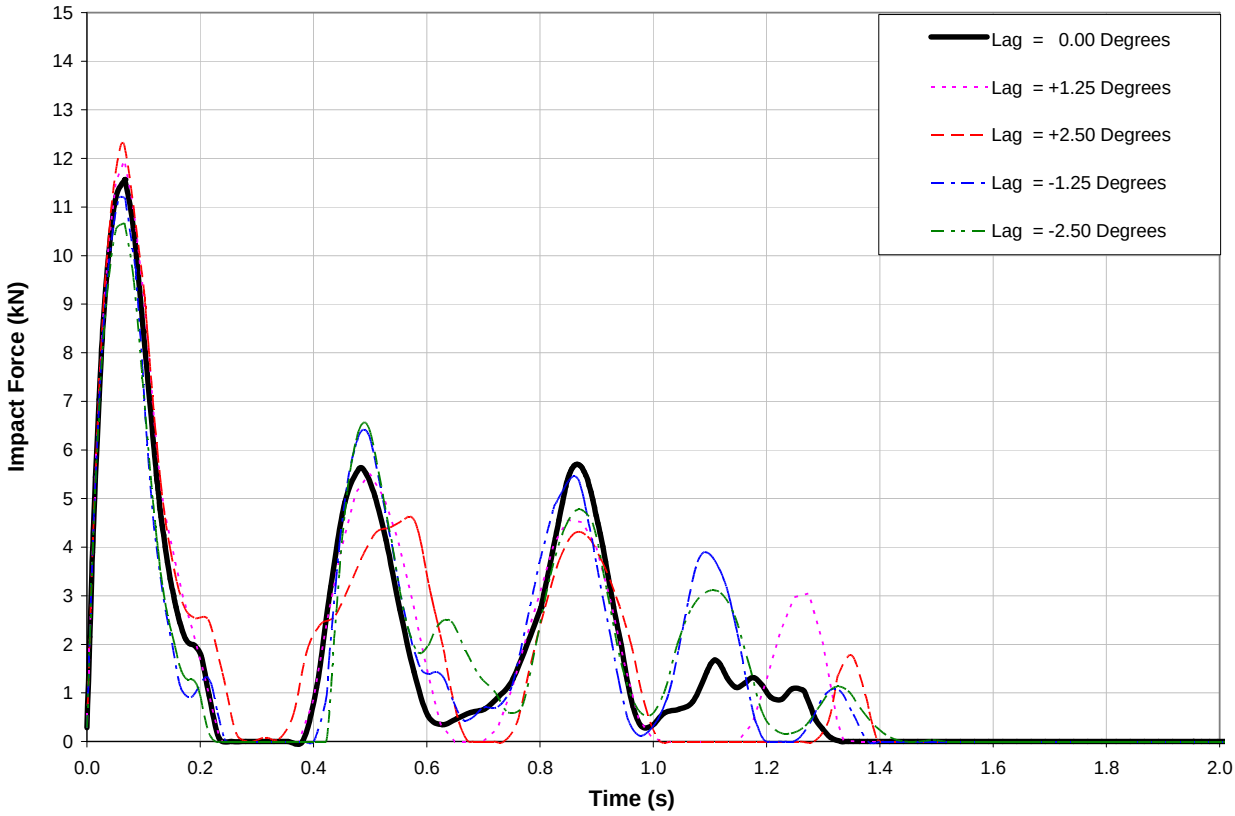

Figure 5.2.1.3 Parameter = Payload Lag Angle: Payload Top "Hydraulic Buffers".

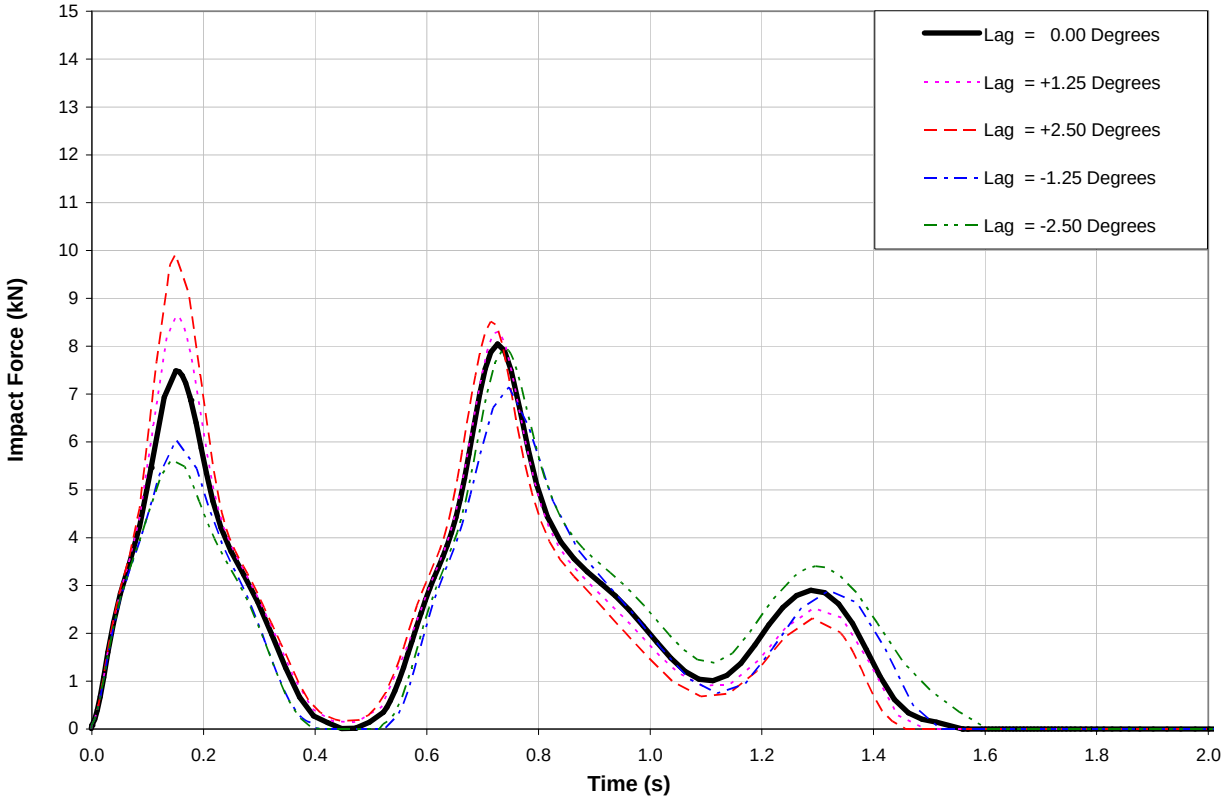

Figure 5.2.1.4 Parameter = Payload Lag Angle: Payload Top "Elastomeric Buffers".

5.2.2 Effect of End Stop Misalignment on the Impact Force History

For this parameter, the left hand side end stop (LHS) was misaligned by 25mm, 50mm 150mm in the direction of travel as shown in Figure 3.3.2.1. Figures 5.2.2.1 and 5.2.2.2 show the effect of the end stop misalignment on the impact force histories for the single bridge EOHTC fitted with the hydraulic buffers and the single bridge EOHTC fitted with the elastomeric buffers respectively. The result presented here is for the condition of Payload Bottom.

The significant information which can be extracted from the results obtained are:

- The results show that the misalignment of one end stop significantly influences the impact force histories obtained for both buffers. The impact force increases on the misaligned end stop.
- For the elastomeric buffers, it was observed that as the misalignment of the end stop increases, there is a corresponding increase in the impact force peaks. However, Figure 5.2.2.1 shows that for the hydraulic buffers, the impact peaks increases for a misalignment of 25mm. Further misalignments does not significantly increase the 1st impact peaks.

The numerical differences between the impact forces for the single bridge EOHTC fitted with hydraulic buffers and the single bridge EOHTC fitted with the elastomeric buffers are presented in Table 5.2.2.1

Table 5.2.2.1 Influence of the end stop misalignment on the impact force history: payload bottom

End Stop Misalignment (mm)	**Hydraulic Buffers**		**Elastomeric Buffers**		**Percentage Difference in Impact Force w.r.t the Base Value for Hydraulic Buffers (%)**		**Percentage Difference in Impact Force w.r.t the Base Value for Elastomeric Buffers (%)**	
	1st Impact Force (kN)	**2nd Impact Force (kN)**	**1st Impact Force (kN)**	**2nd Impact Force (kN)**	**1st Impact**	**2nd Impact**	**1st Impact**	**2nd Impact**
Base value	11.57	1.95	7.26	4.61	NA	NA	NA	NA
Misalignment = 25mm	12.10	4.30	8.69	6.84	4.5	120.5	19.7	48.4
Misalignment = 50mm	12.10	10.70	8.65	5.33	4.5	449.0	19.1	15.6
Misalignment = 150mm	12.10	10.8	9.69	6.33	4.5	453.8	33.4	37.3

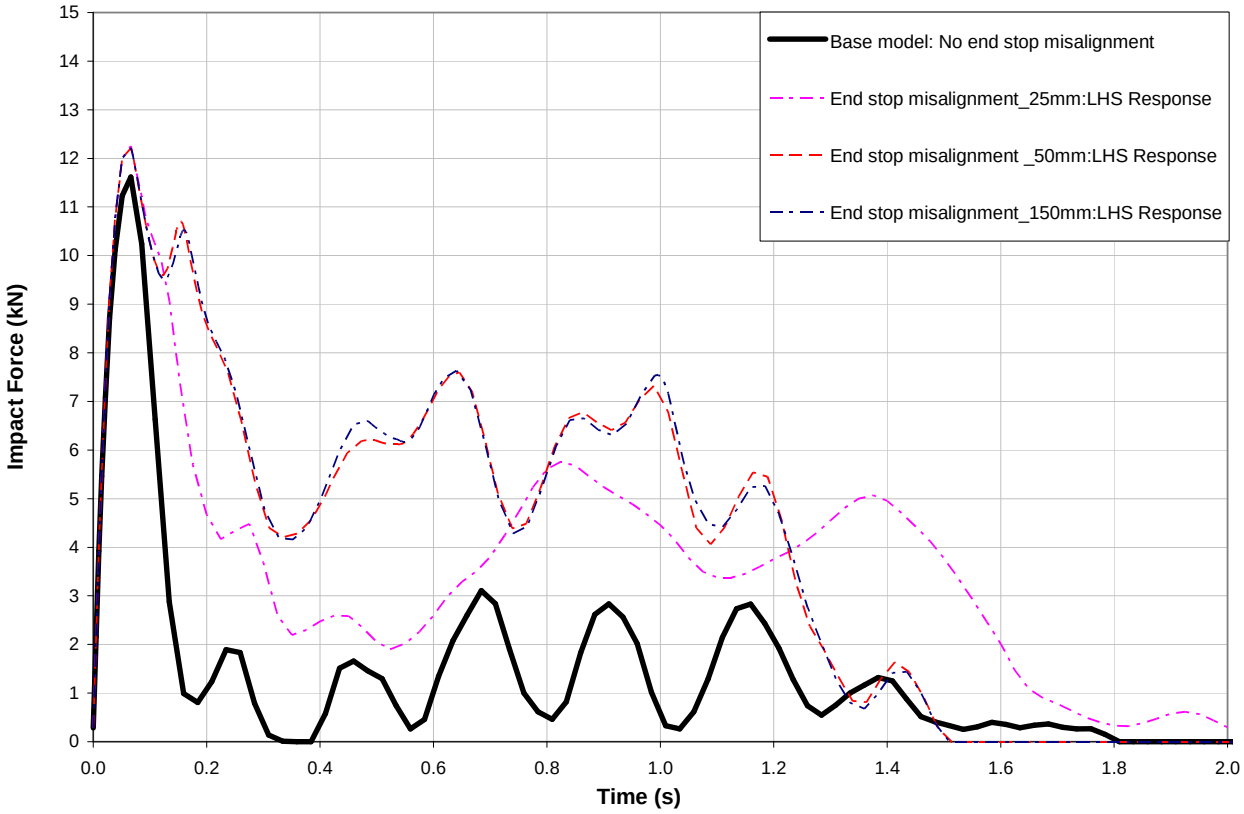

Figure 5.2.2.1 Parameter = End Stop Misalignment: Payload Bottom “Hydraulic Buffers”.

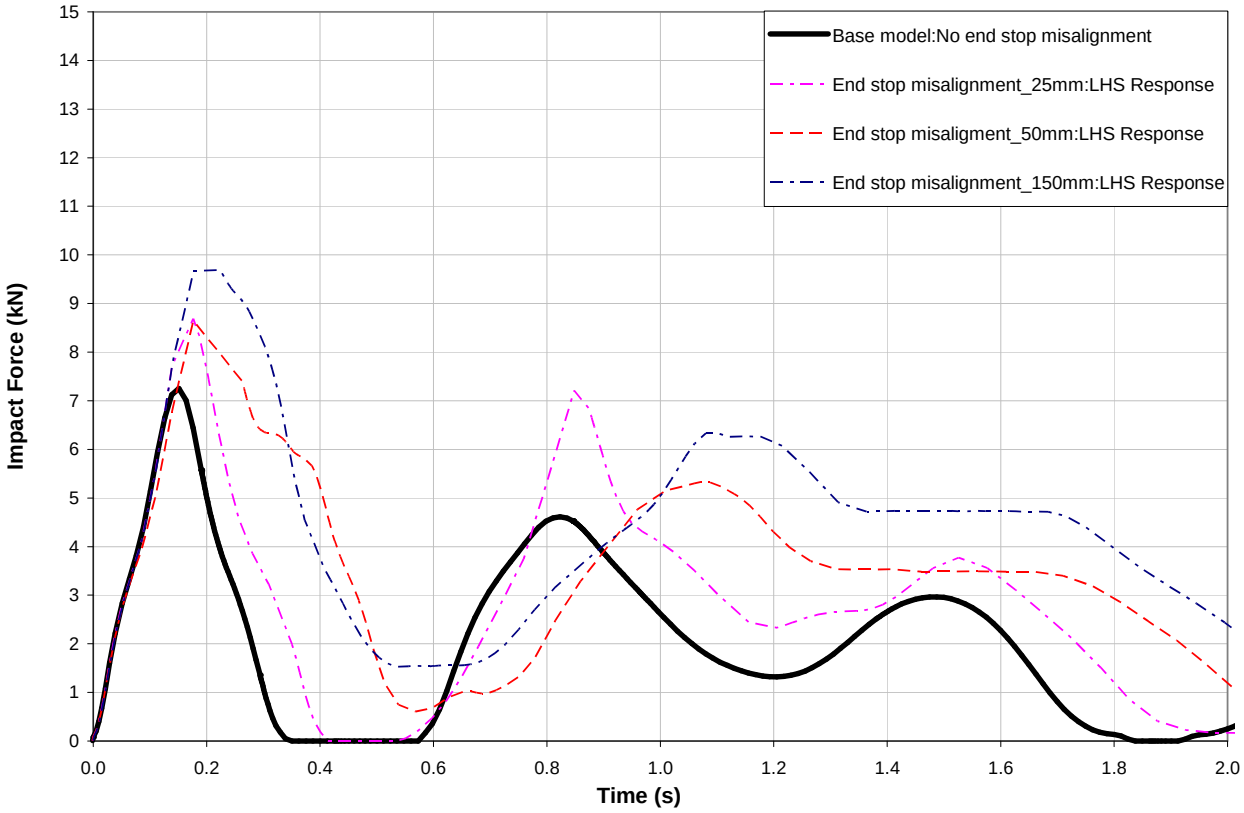

Figure 5.2.2.2 Parameter = End Stop Misalignment: Payload Bottom “Elastomeric Buffers”.

Figures 5.2.2.3 and 5.2.2.4 show the effect of the end stop misalignment on the impact force histories for the single bridge EOHTC fitted with the hydraulic buffers and the single bridge EOHTC fitted with the elastomeric buffers respectively.
The significant information which can be extracted from results obtained are:

- The results obtained for both buffers for the condition of Payload Top follows a trend similar to that obtained for the condition of Payload Bottom.

The numerical differences between the impact forces obtained for the single bridge EOHTC fitted with hydraulic buffers and the single bridge EOHTC fitted with elastomeric buffers for the condition of Payload Top are presented in Table 5.2.2.2

Table 5.2.2.2 Influence of the end stop misalignment on the impact force history: payload top.

End Stop Misalignment (mm)	Hydraulic Buffers		Elastomeric Buffers		Percentage Difference in Impact Force w.r.t the Base Value for Hydraulic Buffers (%)		Percentage Difference in Impact Force w.r.t the Base Value for Elastomeric Buffers (%)	
	1st Impact Force (kN)	2nd Impact Force (kN)	1st Impact Force (kN)	2nd Impact Force (kN)	1st Impact	2nd Impact	1st Impact	2nd Impact
Base value	11.56	5.61	7.48	8.05	NA	NA	NA	NA
Misalignment = 25mm	12.20	9.59	9.10	10.11	5.5	70.9	21.7	25.6
Misalignment = 50mm	12.20	7.60	9.78	7.04	5.5	35.5	30.7	-12.5
Misalignment = 150mm	12.21	7.63	9.72	8.11	5.6	36.0	29.9	0.7

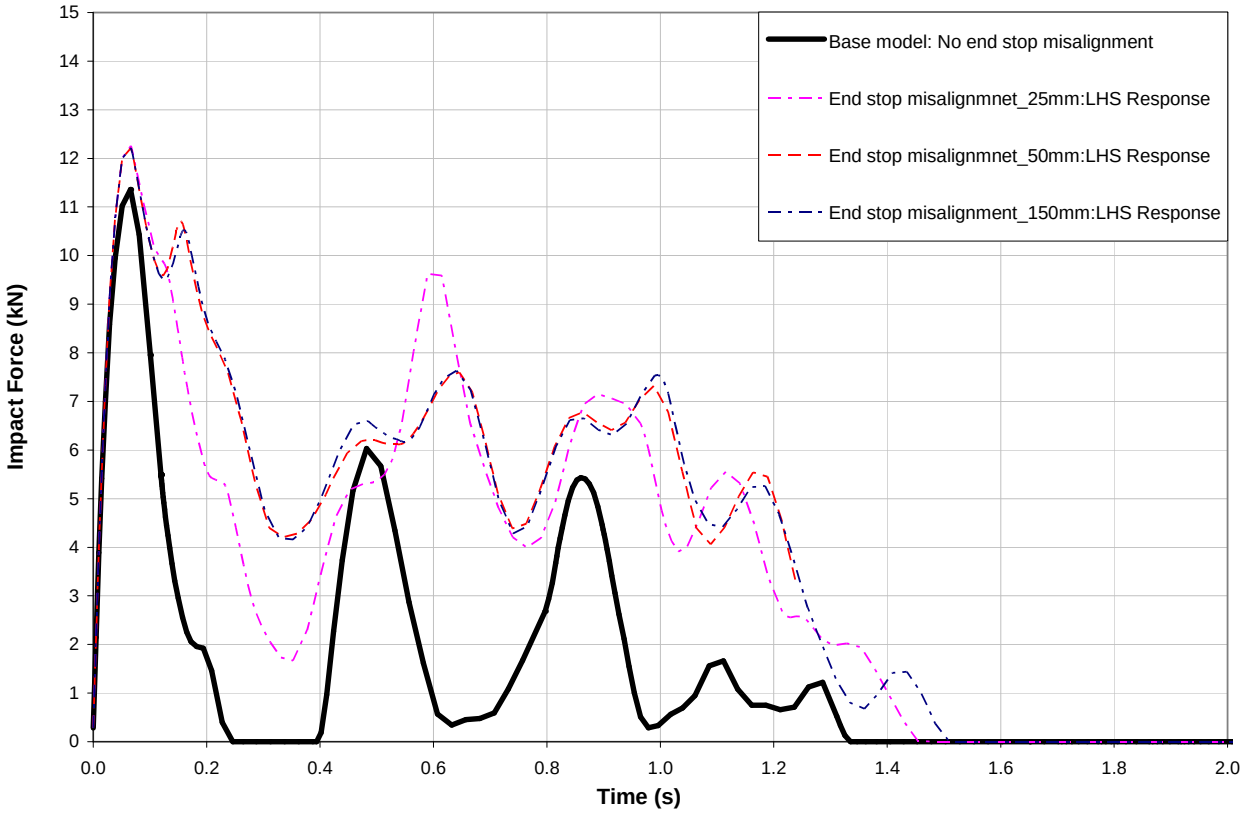

Figure 5.2.2.3 Parameter = End Stop Misalignment: Payload Top “Hydraulic Buffers”.

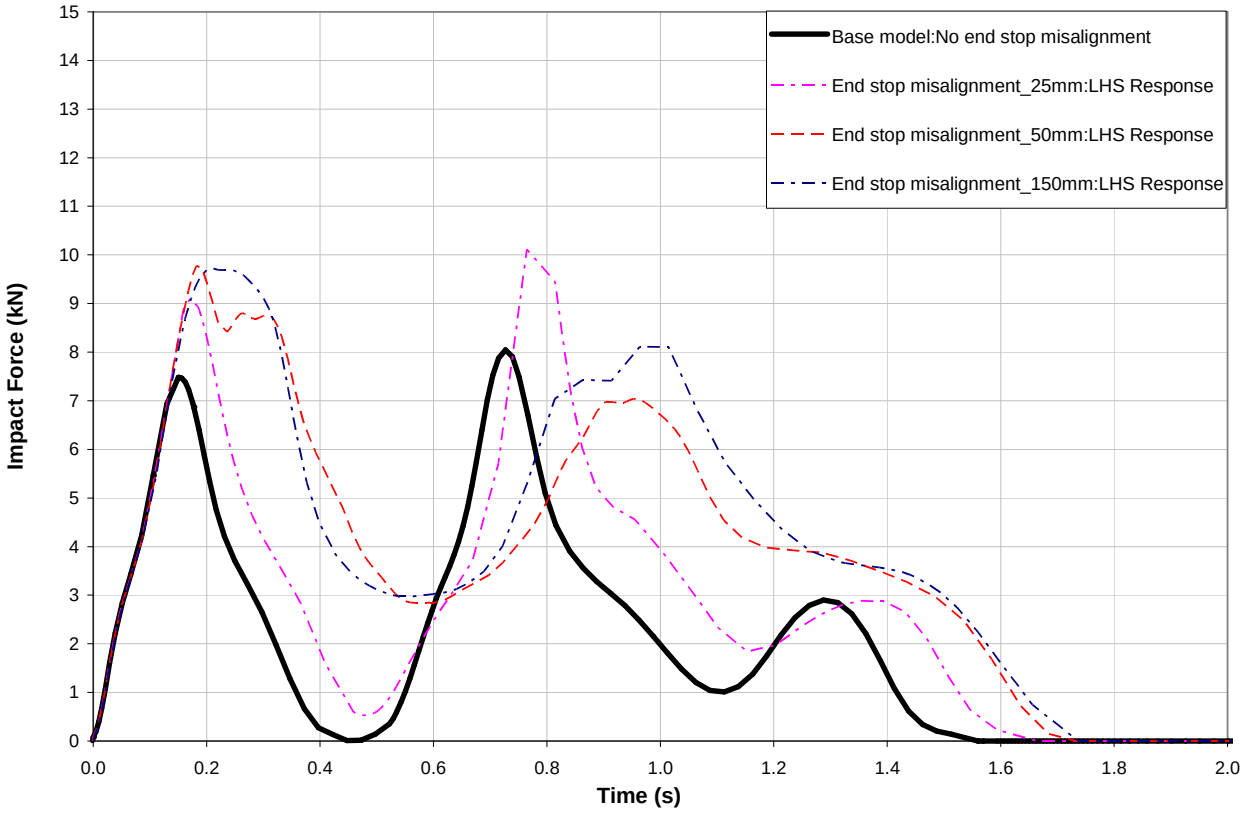

Figure 5.2.2.4 Parameter = End Stop Misalignment: Payload Top “Elastomeric Buffers”.

5.2.3 Effect of the Crab and Payload Eccentricity on the Impact Force History

Figures 5.2.3.1 and 5.2.3.2 show the effect of the crab and payload eccentricity on the impact force histories for the single bridge EOHTC fitted with the hydraulic buffers and the single bridge EOHTC fitted with the elastomeric buffers respectively. Eccentricity of the crab and payload is to the left hand side (LHS) of the crane bridge. The results presented here are for the condition of Payload Bottom. The significant information which can be extracted from the results obtained are:

- The 1st and 2nd impact peaks follow the same trend for both the hydraulic and elastomeric buffers. As the eccentricity of the crab and payload increases, there is a corresponding increase in the impact force obtained on the LHS end stop.

.

The numerical differences between the impact forces for the single bridge EOHTC fitted with hydraulic buffers and the single bridge EOHTC fitted with the elastomeric buffers are presented in Table 5.2.3.1**.**

Table 5.2.3.1 Influence of the crab and payload eccentricity on the impact force history: payload bottom

Crab and Payload Eccentricity (m)	**Hydraulic Buffers**		**Elastomeric Buffers**		**Percentage Difference in Impact Force w.r.t the Base Value for Hydraulic Buffers (%)**		**Percentage Difference in Impact Force w.r.t the Base Value for Elastomeric Buffers (%)**	
	1st Impact Force (kN)	**2nd Impact Force (kN)**	**1st Impact Force (kN)**	**2nd Impact Force (kN)**	**1st Impact**	**2nd Impact**	**1st Impact**	**2nd Impact**
Base value	11.57	1.95	7.26	4.61	NA	NA	NA	NA
Eccentricity from Reference point = 1.695m	12.43	3.09	7.94	5.28	7.43	58.5	9.4	14.5
Eccentricity from Reference point = 3.39m	13.10	3.36	8.85	6.05	13.22	72.3	21.9	31.2

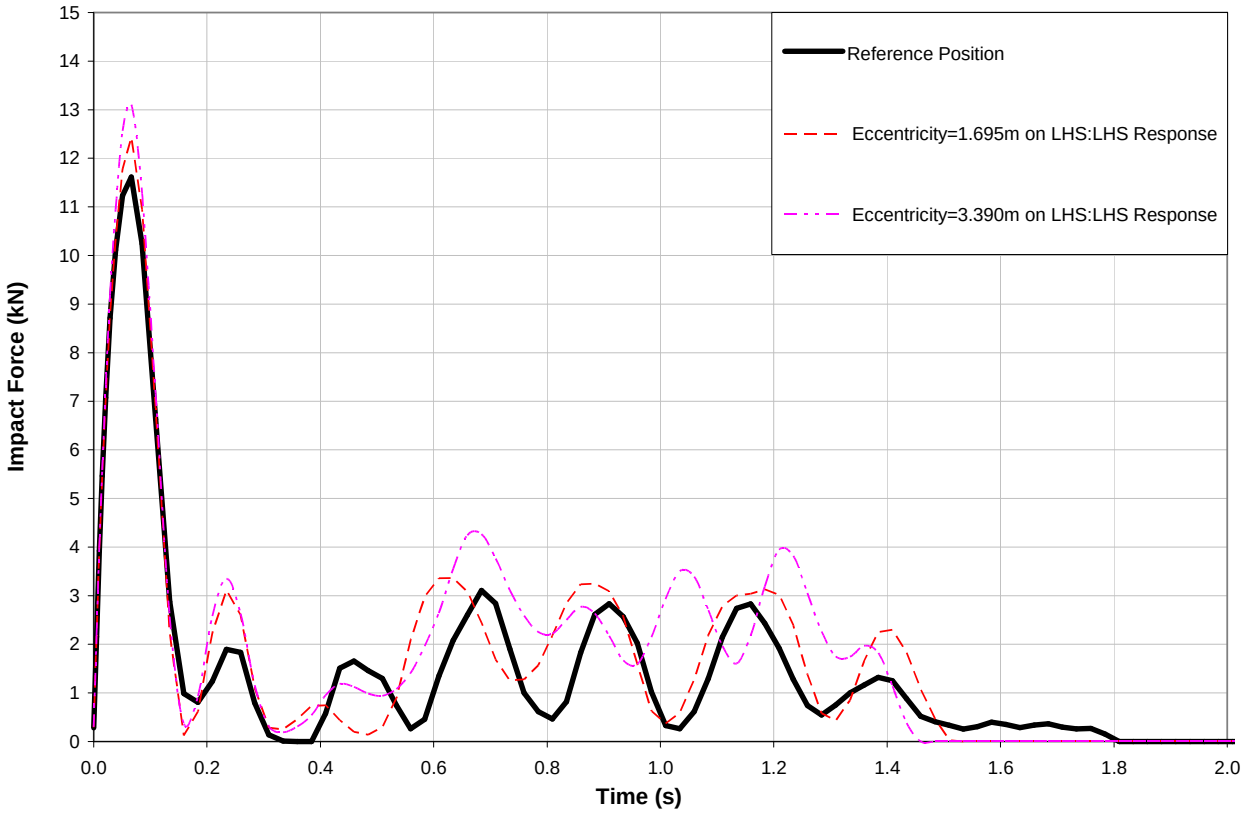

Figure 5.2.3.1 Parameter = Crab and Payload Eccentricity: Payload Bottom “Hydraulic Buffers”.

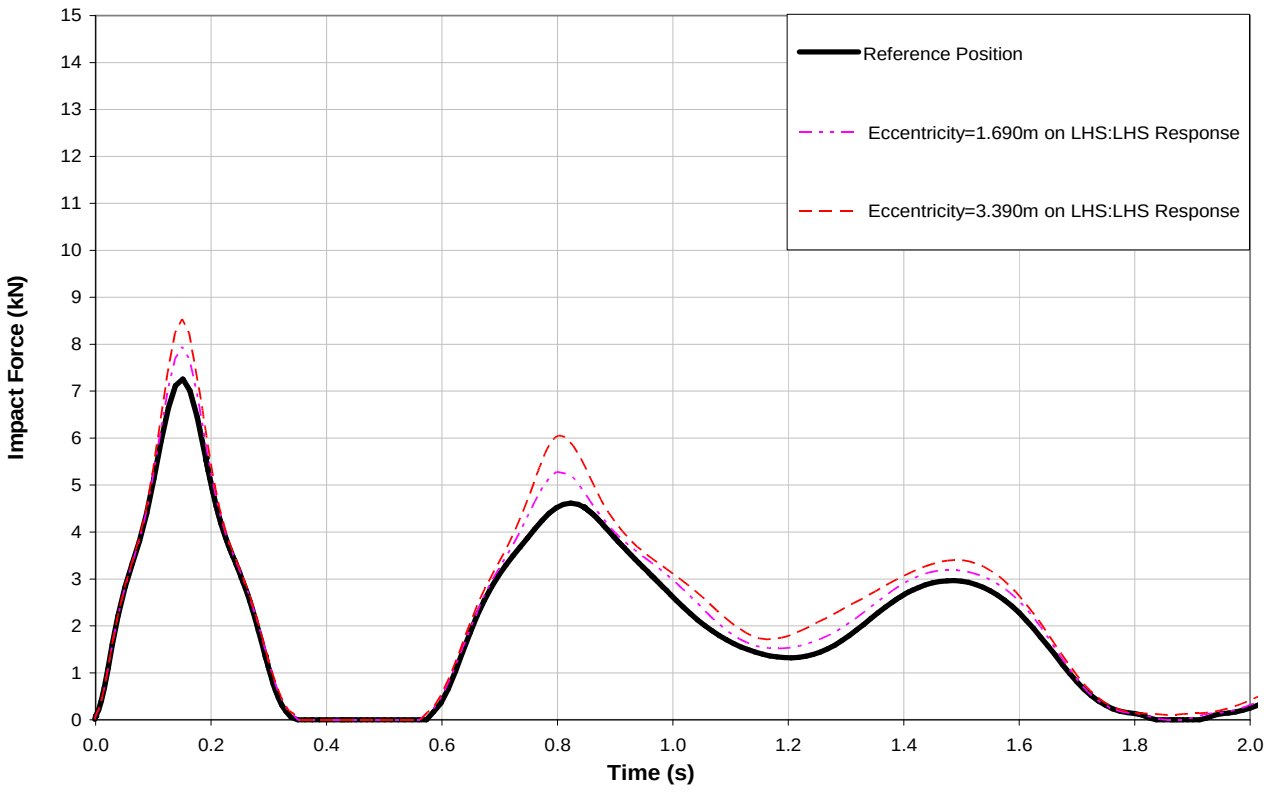

Figure 5.2.3.2 Parameter = Crab and Payload Eccentricity: Payload Bottom “Elastomeric Buffers”.

Figures 5.2.3.3 and 5.2.3.4 show the effect of the crab and payload eccentricity on the impact force histories for the single bridge EOHTC fitted with the hydraulic buffers and the single bridge EOHTC fitted with the elastomeric buffers respectively. The results presented here are for the condition of Payload Top. The significant information which can be extracted from the results obtained are:

- The 1st and 2nd impact peaks follow the same trend for both the hydraulic and the elastomeric buffers. As the crab and payload increases, there is a corresponding increase in the impact force obtained.

The numerical differences between the impact forces for the EOHTC fitted with hydraulic buffers and the EOHTC fitted with the elastomeric buffers are presented in Table 5.2.3.2

Table 5.2.3.2 Influence of crab and payload eccentricity on the impact force history: payload top

Crab and Payload Eccentricity (m)	**Hydraulic Buffers**		**Elastomeric Buffers**		**Percentage Difference in Impact Force w.r.t the Base Value for Hydraulic Buffers (%)**		**Percentage Difference in Impact Force w.r.t the Base Value for Elastomeric Buffers (%)**	
	1st Impact Force (kN)	**2nd Impact Force (kN)**	**1st Impact Force (kN)**	**2nd Impact Force (kN)**	**1st Impact**	**2nd Impact**	**1st Impact**	**2nd Impact**
Base value	11.56	5.61	7.48	8.05	NA	NA	NA	NA
Eccentricity from Reference point= 1.695m	12.32	6.53	8.56	8.83	6.5	16.4	14.4	9.7
Eccentricity from Reference point= 3.39m	13.07	7.37	9.39	9.04	13.06	31.4	25.5	12.3

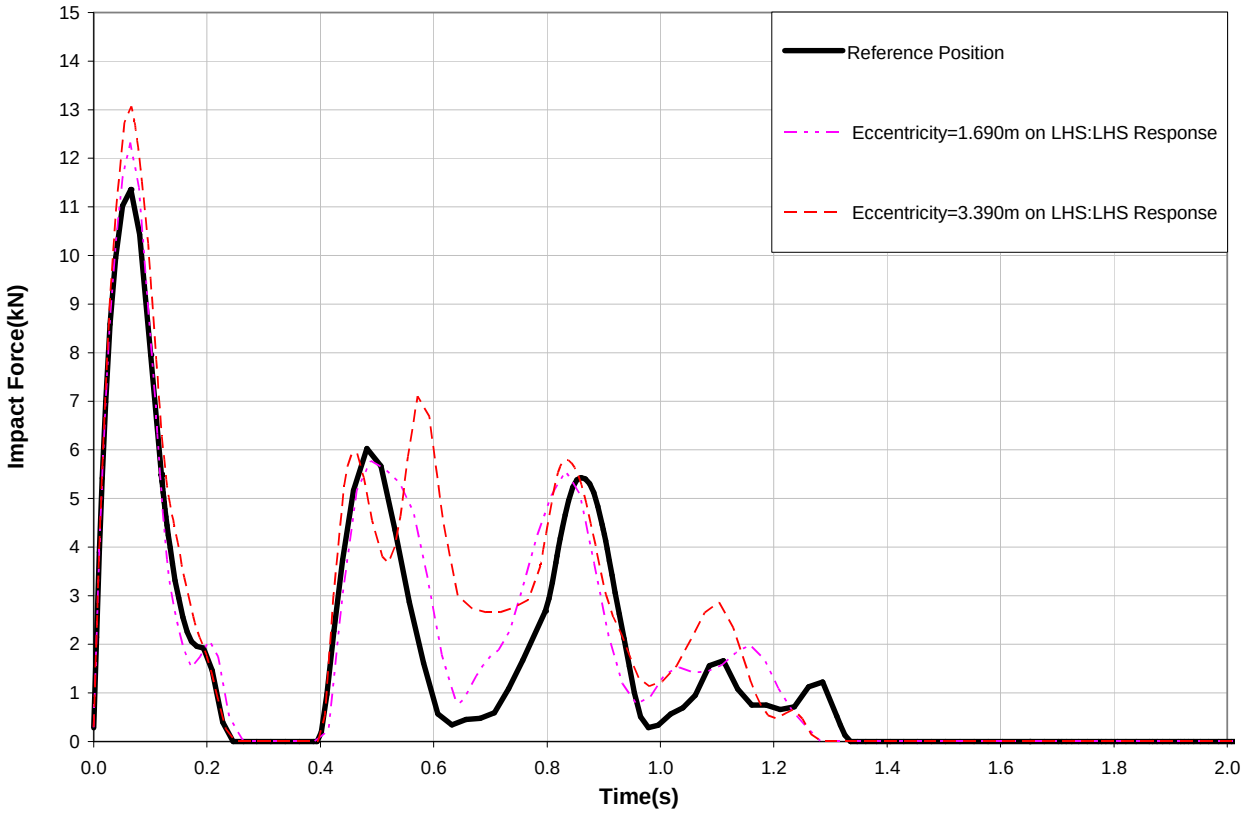

Figure 5.2.3.3 Parameter = Crab and Payload Eccentricity: Payload Top “Hydraulic Buffers”.

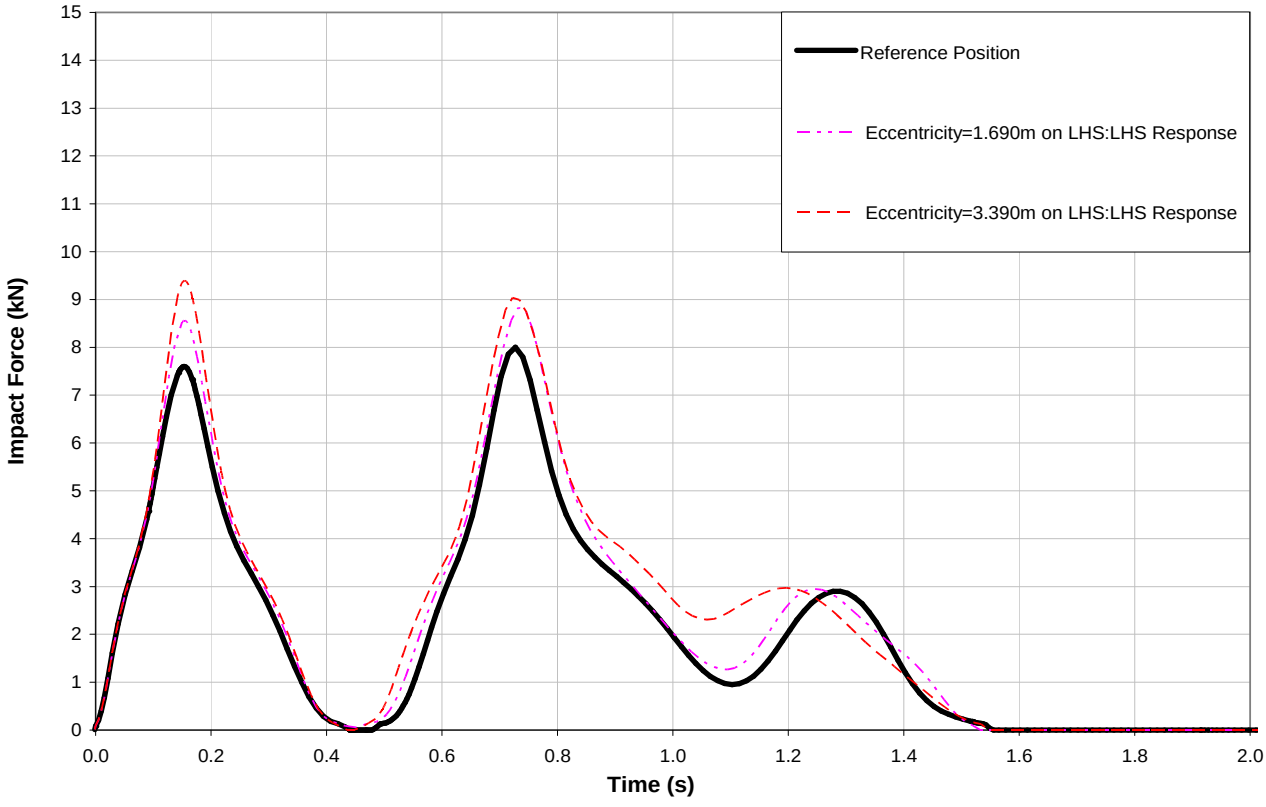

Figure 5.2.3.4 Parameter = Crab and Payload Eccentricity: Payload Top “Elastomeric Buffers”.

5.2.4 Effect of the Impact Velocity on the Impact Force History

Figures 5.2.4.1 and 5.2.4.2 show the effect of the impact velocity on the impact force histories for the single bridge EOHTC fitted with the hydraulic buffers and the single bridge EOHTC fitted with the elastomeric buffers respectively. The results presented here are for the condition of Payload Bottom. The significant information which can be extracted from the results obtained are:

- The 1st impact peaks follow the same trend for the hydraulic and the elastomeric buffers. As the impact velocity increases, there is a corresponding increase in the impact force obtained.
- For the hydraulic buffers, the parameter has a minimal influence on the 2nd impact peak.

The numerical differences between the impact forces for the single bridge EOHTC fitted with hydraulic buffers and the single bridge EOHTC fitted with the elastomeric buffers are presented in Table 5.2.4.1

Table 5.2.4.1 Influence of the impact velocity on the impact force history: payload bottom

Impact Velocity (m/s)	**Hydraulic Buffers**		**Elastomeric Buffers**		**Percentage Difference in Impact Force w.r.t the Base Value for Hydraulic Buffers (%)**		**Percentage Difference in Impact Force w.r.t the Base Value for Elastomeric Buffers (%)**	
	1st Impact Force (kN)	**2nd Impact Force (kN)**	**1st Impact Force (kN)**	**2nd Impact Force (kN)**	**1st Impact**	**2nd Impact**	**1st Impact**	**2nd Impact**
Base value 0.55m/s	11.57	1.95	7.26	4.61	NA	NA	NA	NA
0.385m/s	8.05	0.79	3.90	2.72	-30.4	-59.5	-46.3	-41.0
0.50 m/s	10.46	0.80	5.82	3.70	-9.6	-59.0	-19.8	-19.7
0.60 m/s	12.85	0.91	8.97	7.05	11.1	-53.3	23.6	52.9

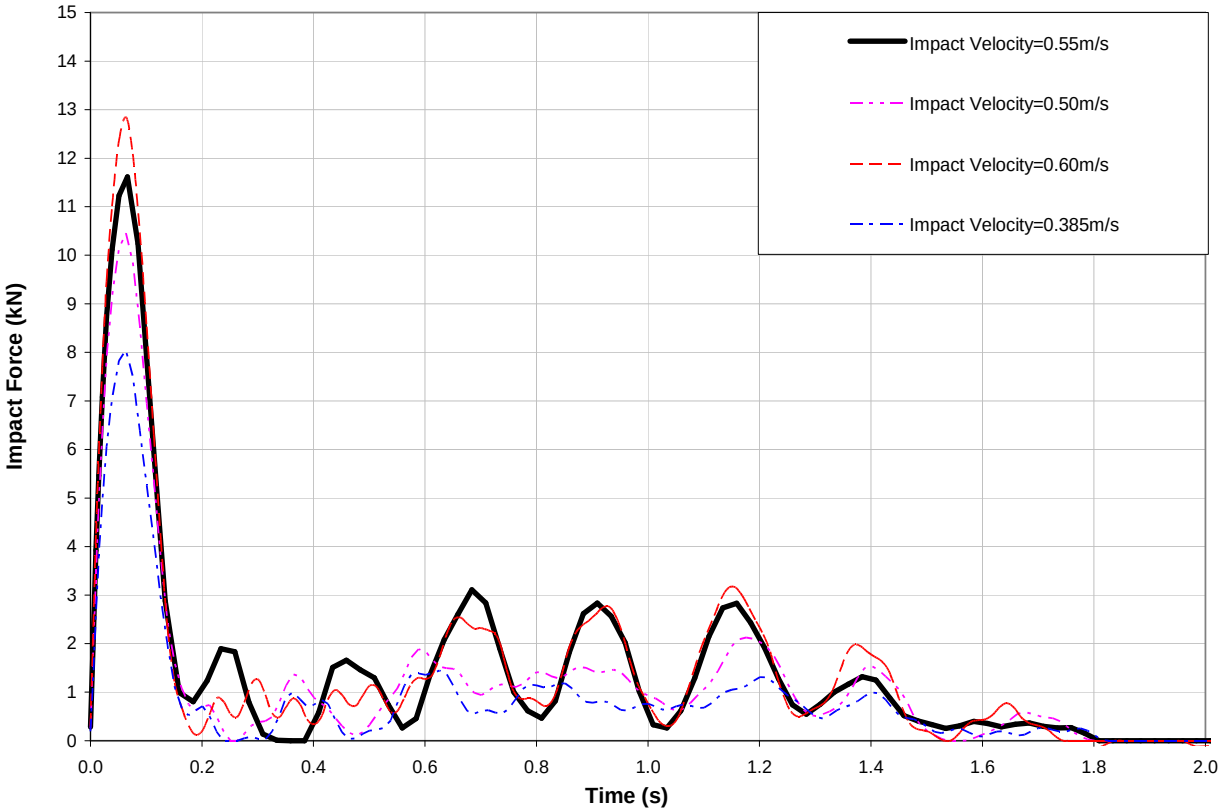

Figure 5.2.4.1 Parameter = Impact Velocity: Payload Bottom "Hydraulic Buffers".

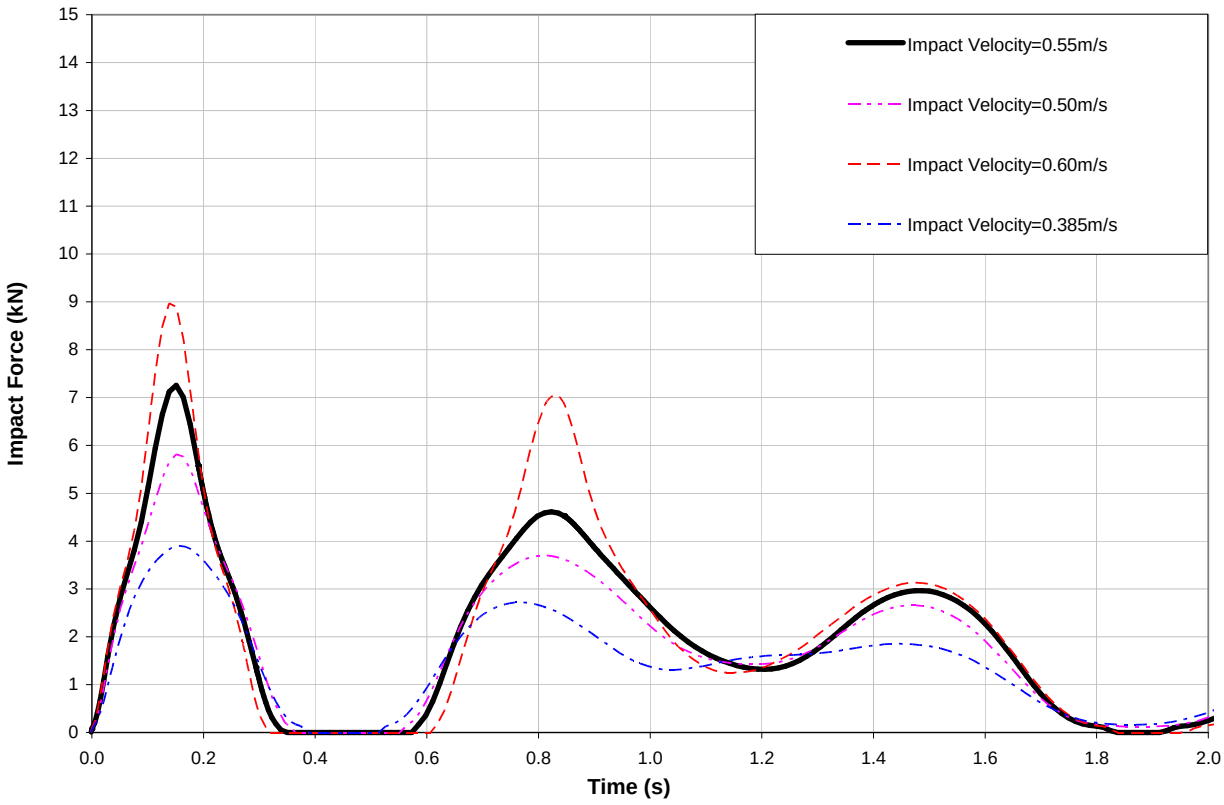

Figure 5.2.4.2 Parameter = Impact Velocity: Payload Bottom "Elastomeric Buffers"

Figures 5.2.4.3 and 5.2.4.4 show the effect of the impact velocity on the impact force histories for the single bridge EOHTC fitted with the hydraulic buffers and the single bridge EOHTC fitted with the elastomeric buffers respectively. The results presented here are for the condition of Payload Top. The significant information which can be extracted from the results obtained are:

- The results obtained for both buffers follow a similar trend to that obtained for the condition of Payload Bottom. As the impact velocity increases, there is a corresponding increase in the 1st impact force obtained.

The numerical differences between the impact forces for the single bridge EOHTC fitted with hydraulic buffers and the single bridge EOHTC fitted with the elastomeric buffers are presented in Table 5.2.4.2

Table 5.2.4.2 Influence of the impact velocity on the impact force history: payload top

Impact Velocity (m/s)	**Hydraulic Buffers**		**Elastomeric Buffers**		**Percentage Difference in Impact Force w.r.t the Base Value for Hydraulic Buffers (%)**		**Percentage Difference in Impact Force w.r.t the Base Value for Elastomeric Buffers (%)**	
	1st Impact Force (kN)	**2nd Impact Force (kN)**	**1st Impact Force (kN)**	**2nd Impact Force (kN)**	**1st Impact**	**2nd Impact**	**1st Impact**	**2nd Impact**
Base value 0.55 m/s	11.56	5.61	7.48	8.05	NA	NA	NA	NA
0.385 m/s	8.03	5.03	3.67	3.68	-30.5	-10.3	-50.9	-54.3
0.50 m/s	10.13	6.12	6.06	6.17	-12.4	9.1	-19.0	-23.4
0.60 m/s	12.56	7.70	9.31	10.34	8.7	37.3	24.5	28.4

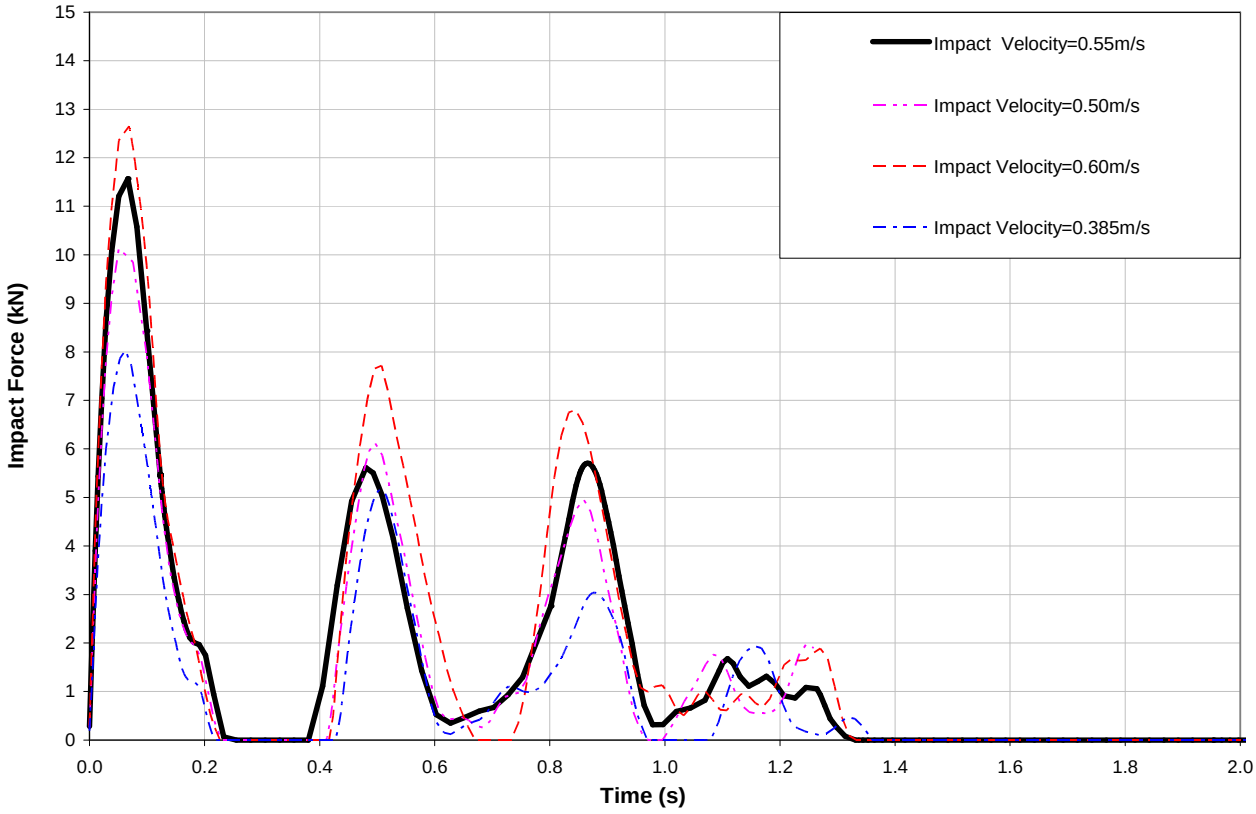

Figure 5.2.4.3 Parameter = Impact Velocity: Payload Top "Hydraulic Buffers".

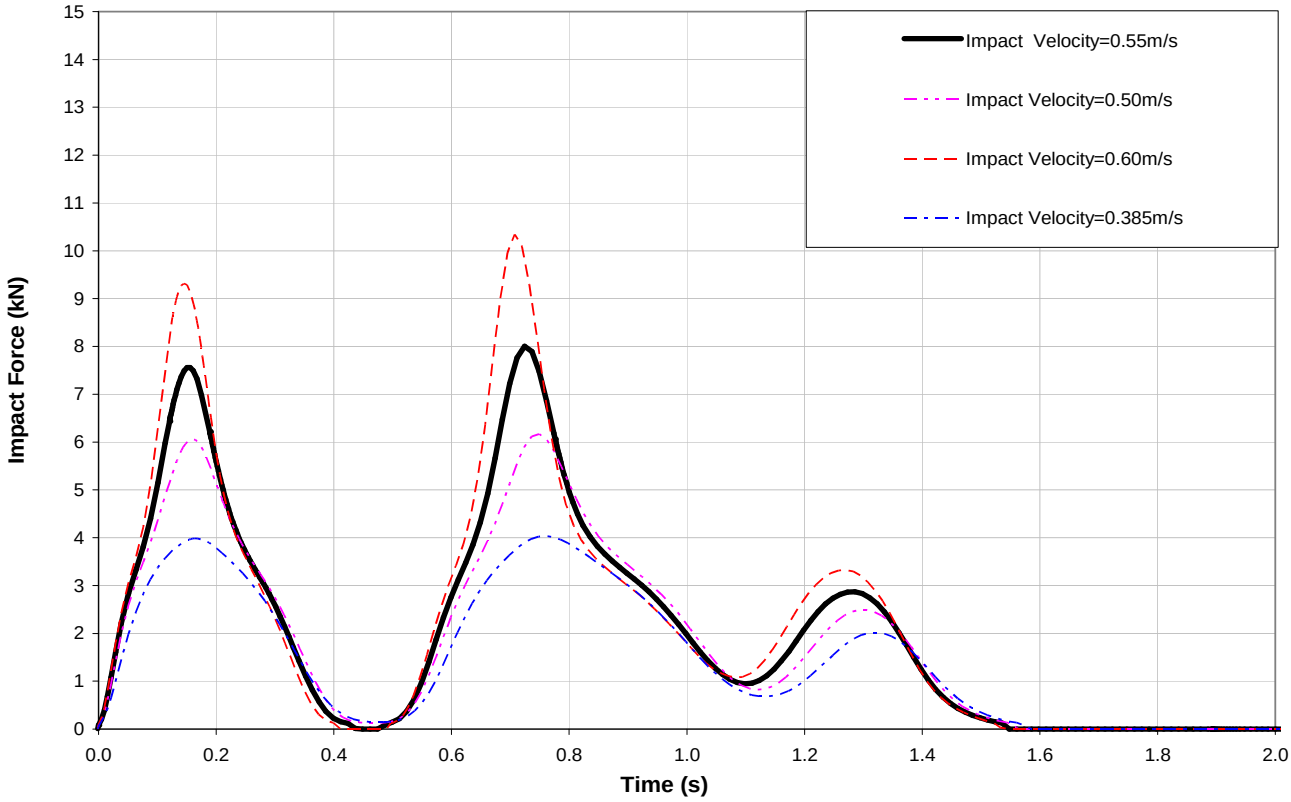

Figure 5.2.4.4 Parameter = Impact Velocity: Payload Top "Elastomeric Buffers".

5.2.5 Effect of Buffer's Damping Characteristics on the impact Force History

Figures 5.2.5.1 and 5.2.5.2 show the effect of the buffer's damping characteristics on the impact force histories for the single bridge EOHTC fitted with the hydraulic buffers and the single bridge EOHTC fitted with the elastomeric buffers respectively. The results presented here are for the condition of Payload Bottom. The significant information which can be extracted from the results obtained are:

- The result obtained follows the same trend for both the hydraulic and elastomeric buffers.
- At 1st impact, the impact peaks increase when the buffers' damping characteristic was omitted from the model.
- The parameter has a significant influence on the 2nd impact peak.

The numerical differences between the impact forces for the single bridge EOHTC fitted with hydraulic buffers and the single bridge EOHTC fitted with the elastomeric buffers are presented in Table 5.2.5.1

Table 5.2.5.1 Influence of the buffer's damping characteristics on the impact force history: payload bottom

Buffer's Damping Characteristics	Hydraulic Buffers		Elastomeric Buffers		Percentage Difference in Impact Force w.r.t the Base Value for Hydraulic Buffers (%)		Percentage Difference in Impact Force w.r.t the Base Value for Elastomeric Buffers (%)	
	1st Impact Force (kN)	2nd Impact Force (kN)	1st Impact Force (kN)	2nd Impact Force (kN)	1st Impact	2nd Impact	1st Impact	2nd Impact
Base value	11.57	1.95	7.26	4.61	NA	NA	NA	NA
No Damping	14.68	17.53	8.71	14.33	26.9	463.7	20.0	210.8

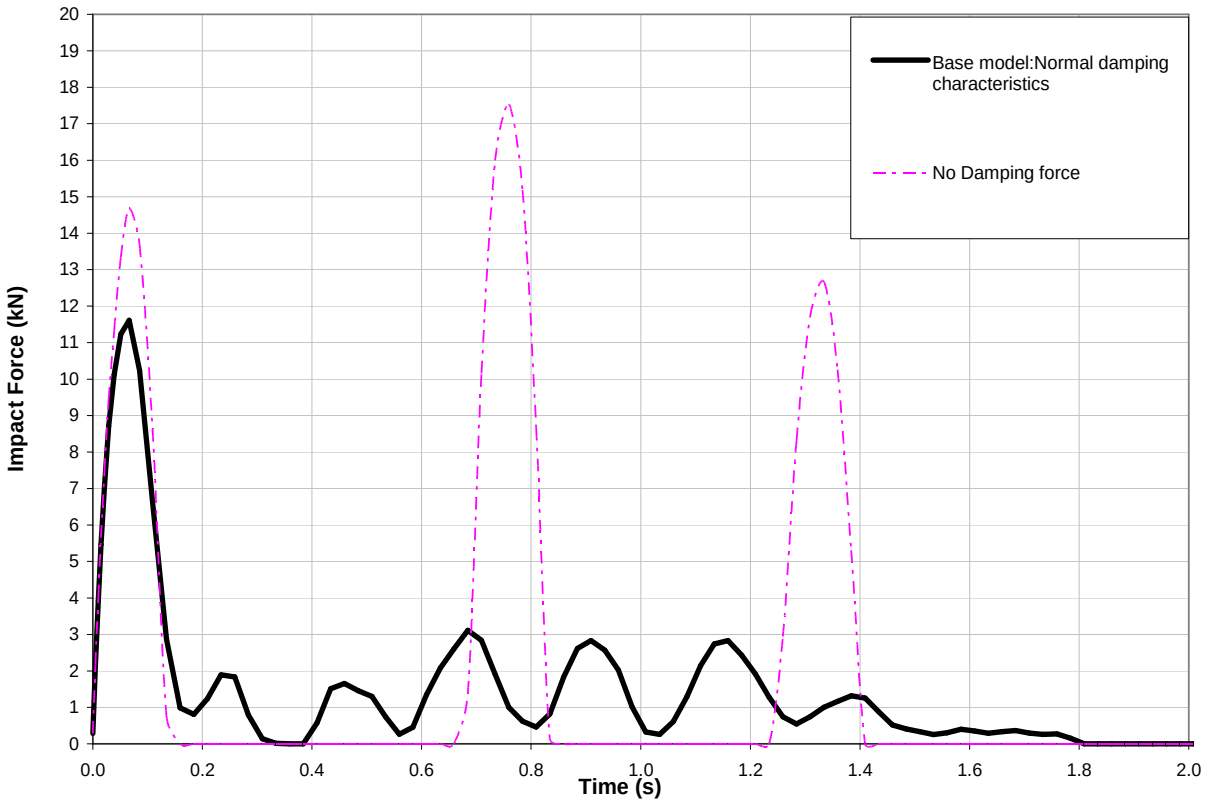

Figure 5.2.5.1 Parameter = Buffer's Damping Characteristics: Payload Bottom "Hydraulic Buffers".

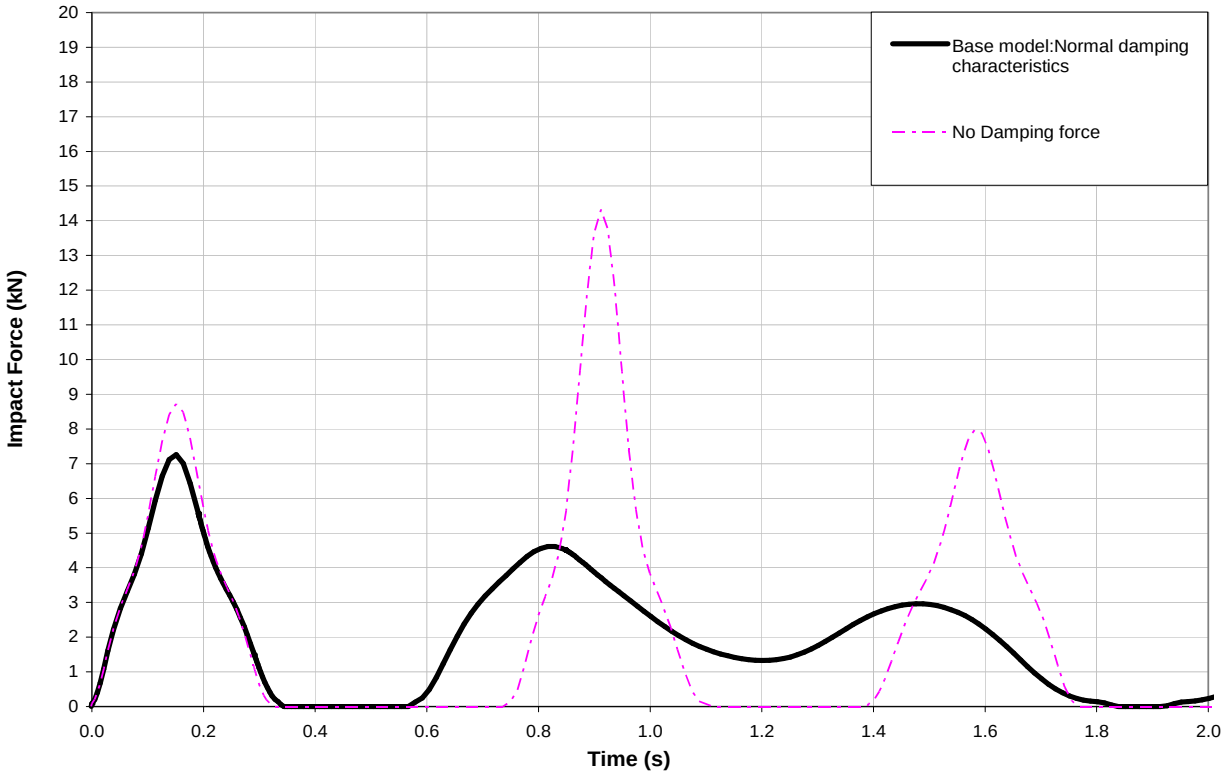

Figure 5.2.5.2 Parameter = Buffer's Damping Characteristics: Payload Bottom "Elastomeric Buffers".

Figures 5.2.5.3 and 5.2.5.4 show the effect of the buffer's damping characteristics on the impact force histories for the single bridge EOHTC fitted with the hydraulic buffers and the single bridge EOHTC fitted with the elastomeric buffers respectively. The results presented here are for the condition of Payload Top. The significant information which can be extracted from the results obtained are:

- The result obtained for both the hydraulic and elastomeric buffers follows a similar trend to that obtained for the condition of Payload Bottom. For the model without the damping characteristics, both the 1st and the 2nd impact peaks were significantly influenced.
- The parameter has a greater influence on the 2nd impact peak.

The numerical differences between the impact forces for the single bridge EOHTC fitted with hydraulic buffers and the single bridge EOHTC fitted with the elastomeric buffers are presented in Table 5.2.5.2

Table 5.2.5.2 Influence of the buffer's damping characteristics on the impact force history: payload top.

Buffer's Damping Characteristics	**Hydraulic Buffers**		**Elastomeric Buffers**		**Percentage Difference in Impact Force w.r.t the Base Value for Hydraulic Buffers (%)**		**Percentage Difference in Impact Force w.r.t the Base Value for Elastomeric Buffers (%)**	
	1st Impact Force (kN)	2nd Impact Force (kN)	1st Impact Force (kN)	2nd Impact Force (kN)	1st Impact	2nd Impact	1st Impact	2nd Impact
Base value	11.56	5.61	7.48	8.05	NA	NA	NA	NA
No Damping	14.54	17.10	9.01	12.48	25.8	204.8	20.5	55.0

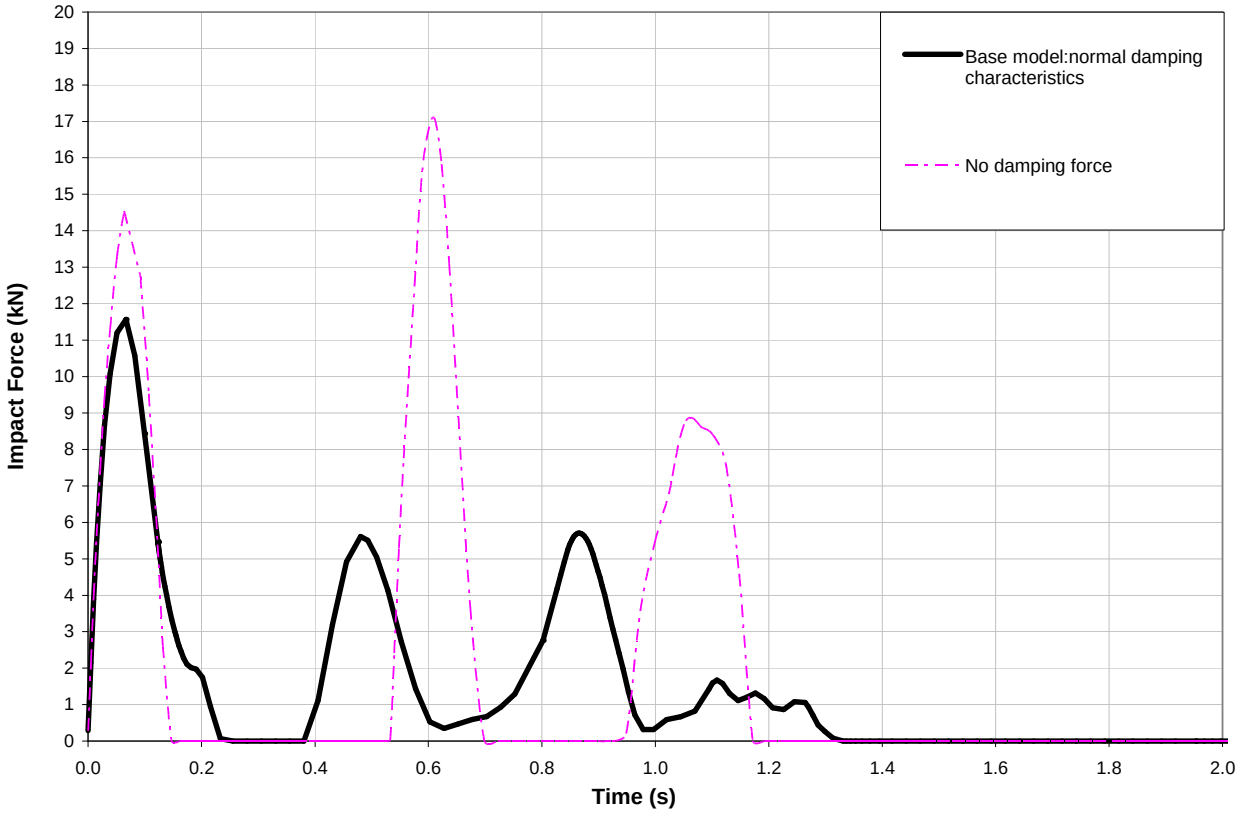

Figure 5.2.5.3 Parameter = Buffer's Damping Characteristics: Payload Top "Hydraulic Buffers"

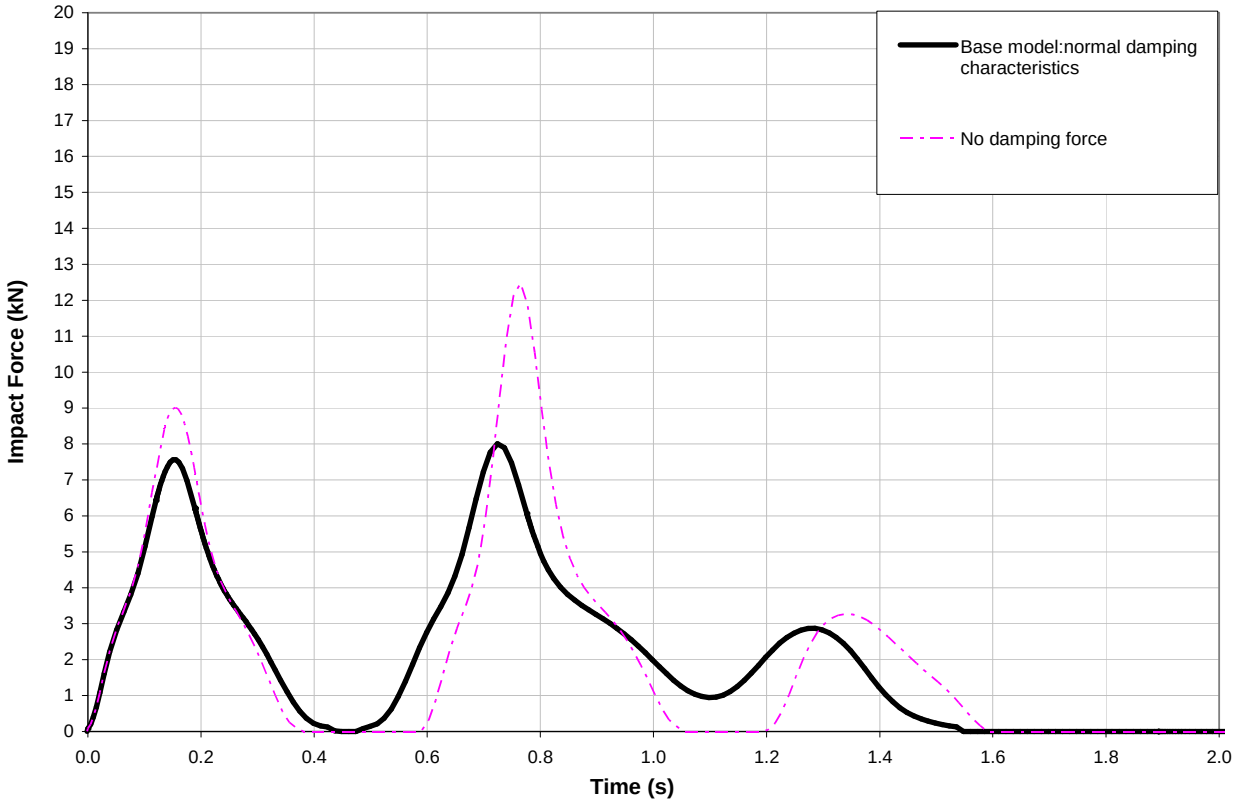

Figure 5.2.5.4 Parameter = Buffer's Damping Characteristics: Payload Top "Elastomeric Buffers"

5.2.6 Effect of the Gantry's Stiffness on the Impact Force History

Figures 5.2.6.1 and 5.2.6.2 show the effect of the gantry's stiffness on the impact force histories for the single bridge EOHTC fitted with the hydraulic buffers and the single bridge EOHTC fitted with the elastomeric buffers respectively. The results presented here are for the condition of Payload Bottom. The significant information which can be extracted from the results obtained are:

- The result obtained for both the hydraulic buffers and the elastomeric buffers follow the same trend. As the gantry's stiffness reduces, there is a corresponding reduction in the impact force peaks.

The numerical differences between the impact forces for the single bridge EOHTC fitted with the hydraulic buffers and the single bridge EOHTC fitted with the elastomeric buffers are presented in Table 5.2.6.1

Table 5.2.6.1 Influence of the gantry's stiffness on the impact force history: payload bottom

Gantry's stiffness (N/m)	**Hydraulic Buffers**		**Elastomeric Buffers**		**Percentage Difference in Impact Force w.r.t the Base Value for Hydraulic Buffers (%)**		**Percentage Difference in Impact Force w.r.t the Base Value for Elastomeric Buffers (%)**	
	1st Impact Force (kN)	**2nd Impact Force (kN)**	**1st Impact Force (kN)**	**2nd Impact Force (kN)**	**1st Impact**	**2nd Impact**	**1st Impact**	**2nd Impact**
Base value	11.57	1.95	7.26	4.61	NA	NA	NA	NA
Weak Spring 1.75×10^5 N/m	9.11	4.63	5.03	6.85	-21.3	137.4	-30.7	48.6
Intermediate spring 1.75×10^6 N/m	9.41	6.06	6.62	5.01	-18.7	210.0	-8.8	8.7
Stiff Spring 1.75×10^7 N/m	11.48	2.17	7.65	4.65	-0.8	11.3	5.4	0.9

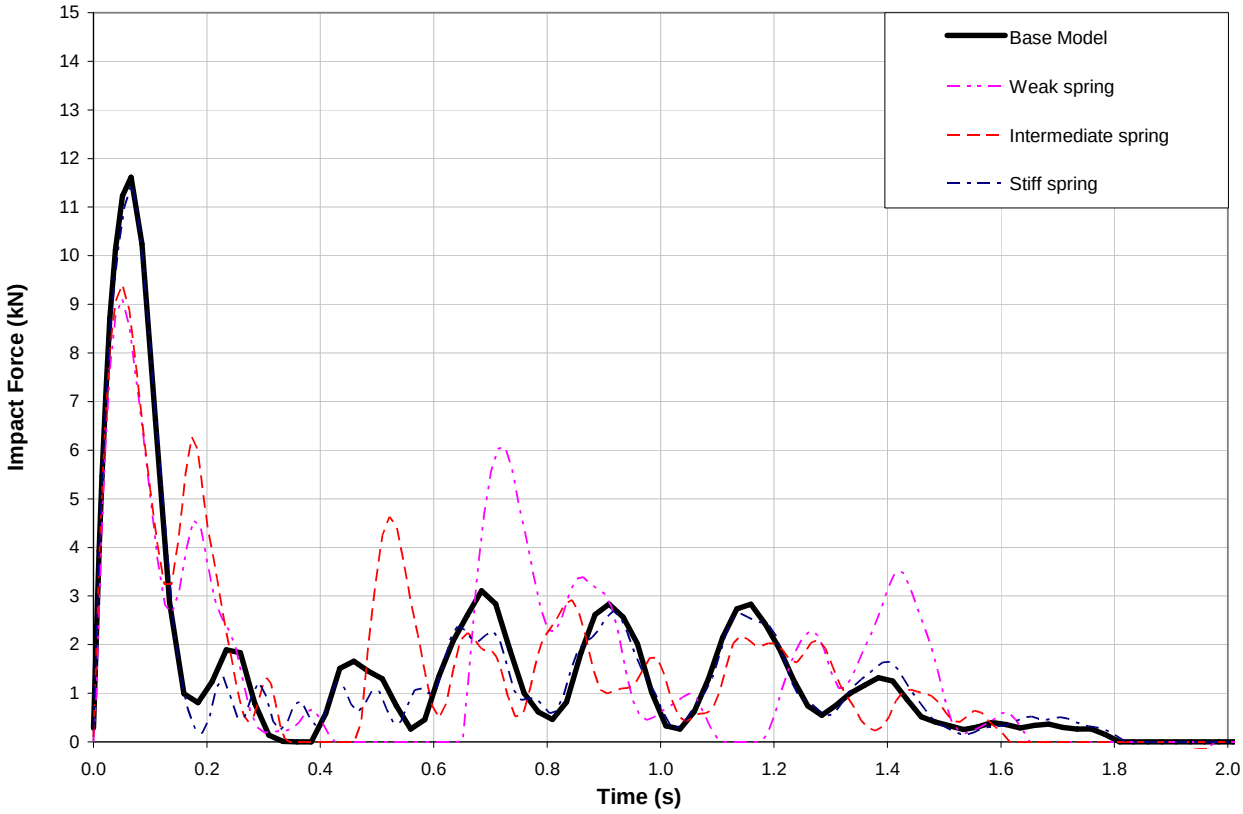

Figure 5.2.6.1 Parameter = Gantry's Stiffness: Payload Bottom "Hydraulic Buffers".

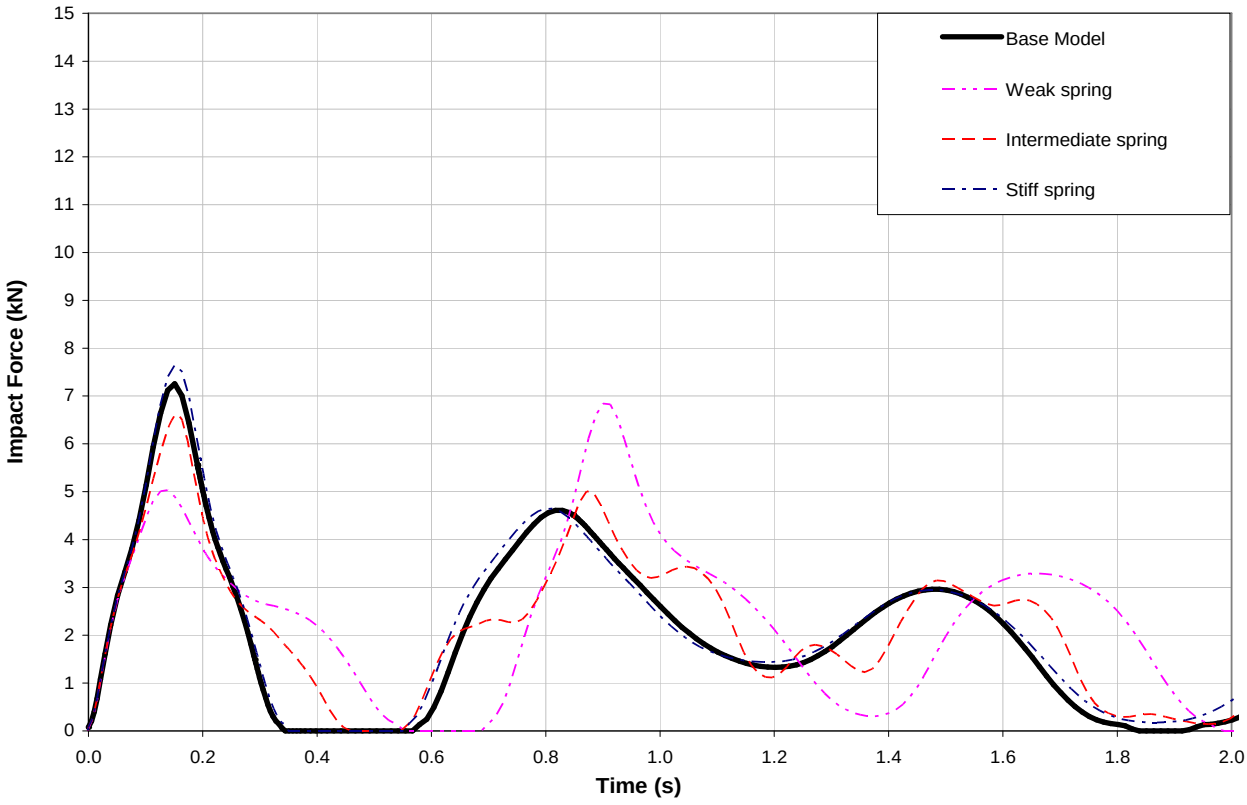

Figure 5.2.6.2 Parameter=Gantry's Stiffness: Payload Bottom "Elastomeric Buffers".

Figures 5.2.6.3 and 5.2.6.4 show the effect of the gantry's stiffness on the impact force histories for the single bridge EOHTC fitted with the hydraulic buffers and the single bridge EOHTC fitted with the elastomeric buffers respectively. The results presented here are for the condition of Payload Top. The significant information which can be extracted from the results obtained are:

- The result obtained for both the hydraulic buffers and the elastomeric buffers follows the same trend obtained for the condition of Payload Bottom where the impact force reduces with a corresponding reduction in the gantry's stiffness.

The numerical differences between the impact forces for the single bridge EOHTC fitted with the hydraulic buffers and the single bridge EOHTC fitted with the elastomeric buffers are presented in Table 5.2.6.2**.**

Table 5.2.6.2 Influence of the gantry's stiffness on the impact force history: payload top

Gantry's Stiffness (mm)	**Hydraulic Buffers**		**Elastomeric Buffers**		**Percentage Difference in Impact Force w.r.t the Base Value for Hydraulic Buffers (%)**		**Percentage Difference in Impact Force w.r.t the Base Value for Elastomeric Buffers (%)**	
	1st Impact Force (kN)	**2nd Impact Force (kN)**	**1st Impact Force (kN)**	**2nd Impact Force (kN)**	**1st Impact**	**2nd Impact**	**1st Impact**	**2nd Impact**
Base value	11.56	5.61	7.48	8.05	NA	NA	NA	NA
Weak Spring 1.75×10^5 N/m	9.15	4.65	4.92	9.01	-20.8	-17.1	-34.2	11.9
Intermediate spring 1.75×10^6 N/m	9.36	6.29	6.52	7.48	-19.0	12.1	-12.8	-7.1
Stiff Spring 1.75×10^7 N/m	11.35	6.69	7.48	7.9	-1.8	19.3	0.0	-1.9

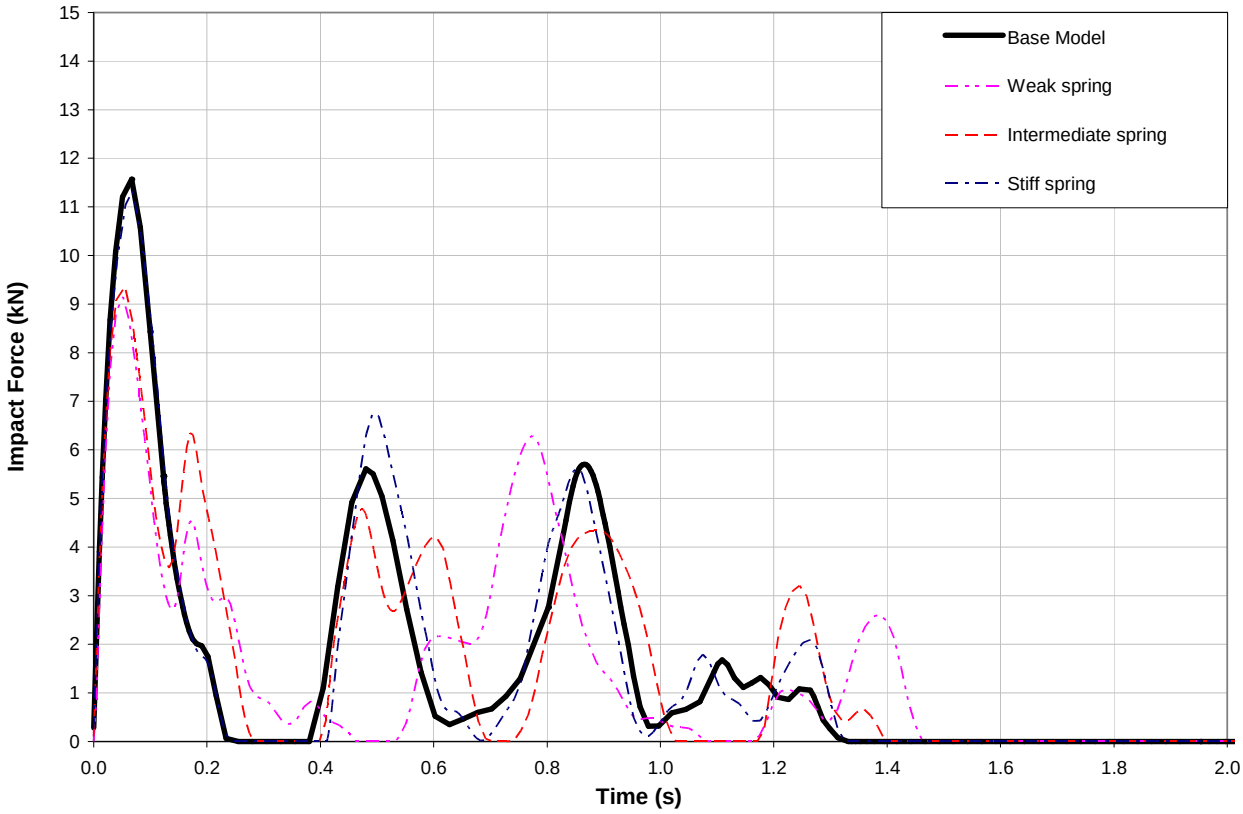

Figure 5.2.6.3 Parameter = Gantry's Stiffness: Payload Top "Hydraulic Buffers".

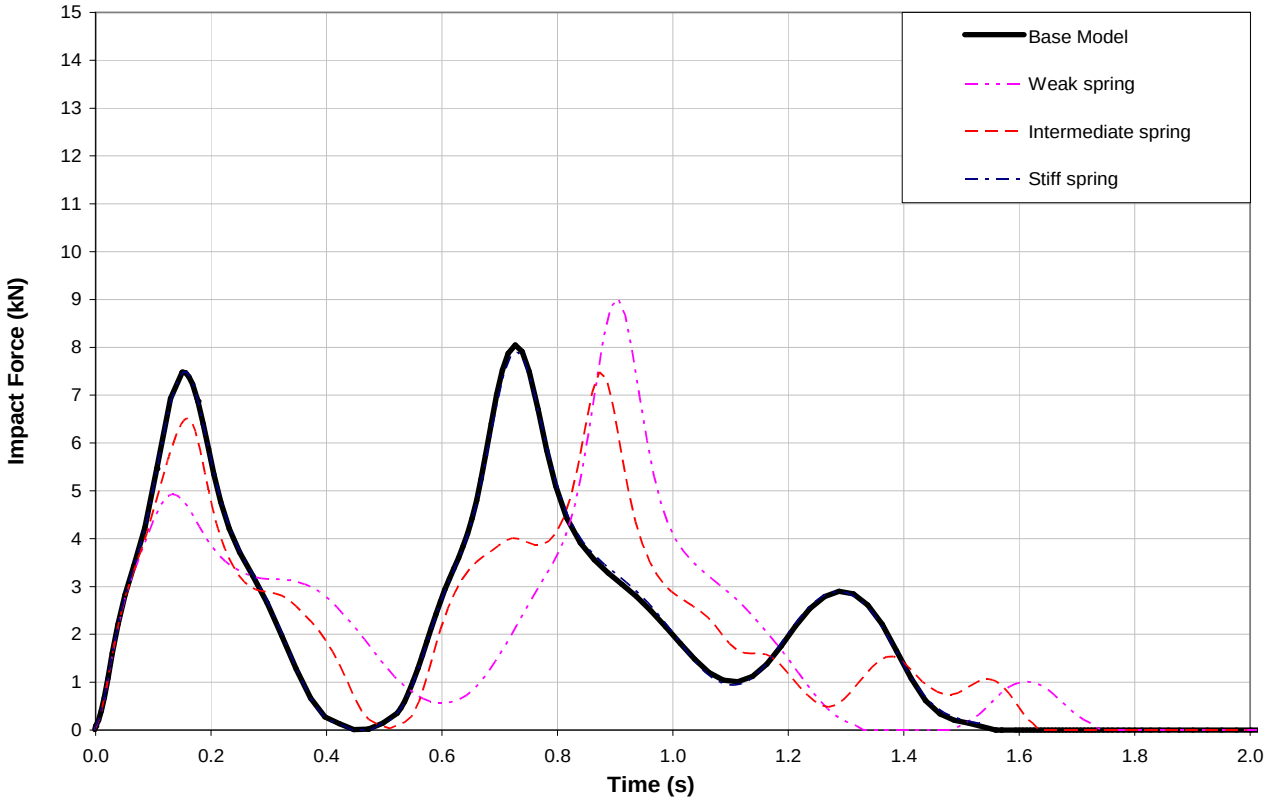

Figure 5.2.6.4 Parameter = Gantry's Stiffness: Payload Top "Elastomeric Buffers".

5.3 Summary of sensitivity analysis (Hydraulic Buffers)

From the sensitivity study conducted on the end stop impact force for the hydraulic buffers, the maximum impact force obtained for each parameter investigated is presented in Table 5.3.1

Table 5.3.1 Summary of sensitivity study

PARAMETERS	CONDITION OF OCCURRENCE	BASE VALUE (kN)	MAXIMUM IMPACT (kN)
Lag Angle	Payload Bottom, 1st impact	11.57	12.40
End Stop Misalignment	Payload Top, 1st impact	11.56	12.21
Crab Eccentricity	Payload Top, 1st impact	11.56	13.26
Velocity at Impact	Payload Bottom, 1st impact	11.57	12.85
Buffer's Damping Characteristics	Payload Bottom, 2nd impact	1.95	17.53
Gantry's Stiffness	Payload Bottom, 1st impact	11.57	11.48

To obtain the maximum end stop impact force from the results presented, the LaGrange multipliers was employed in the same manner as presented in chapter 3. The change in impact force obtained for each parameter at 1st and 2nd impact is presented in Table 5.3.2.

Table 5.3.2 The change in impact force obtained for each parameter when each parameter was varied for 3σ from base value.

PARAMETERS	Payload Bottom		Payload Top	
	1st Impact	2nd Impact	1st Impact	2nd Impact
Base Impact Force *f (0)*	11.57	1.95	11.56	5.61
Lag Angle	1.20	-0.33	1.19	-1.40
End Stop Misalignment	1.97	9.25	2.38	8.26
Crab Eccentricity	1.68	0.22	1.75	1.80
Velocity at Impact	3.59	2.03	3.65	2.39
Buffer's Damping Characteristics	2.80	1.16	2.68	0.23
Gantry's Stiffness	4.85	-1.06	5.40	-2.60

5.4 The Results Obtained from the Constraint Optimization Technique

Using equation 3.4.3.1, the maximum end stop impact force for the 1st impact was obtained for three levels of reliability. The results obtained are presented in Table 5.4.1. The 2nd impact forces were ignored, due to its minimal contribution in the FEA simulations.

Table 5.4.1 Estimated maximum end stop impact force from the 1st impact response

Levels of Reliability (β)	Payload Bottom Power On	Payload Top Power On
β =1	13.65	13.71
β= 2	15.74	15.85
β= 3	17.82	18.00

From Tables 5.4.1 a maximum end stop impact force of 18.00kN occurred at 1st impact for the condition of Payload Top Power On.

5.5 Calculation of the Codified End Stop Impact Force

Using the codes of practice considered in section 3.4.4, codified end stop impact forces were determined. The codified estimates are presented in Tables 5.5.1 and 5.5.2. The codified results were determined using the manufacturer's hydraulic buffer selection curve presented in Figure 5.5.1 according to the procedure given by the codes and described in section 3.4.4. For SANS 10160-6:2010, it was impossible to obtain the end stop impact force for a velocity of 0.55m/sec. Figure 5.5.1 shows that the manufacturer limits the kinetic energy to be absorbed by the DPH 25 to 340Nm. The kinetic energy resulting from the total mass of the crane and payload at a velocity of 0.55m/s is 1113.3N/m which is greater than the kinetic energy limit enforced by the manufacturer on the buffer. Hence no end stop impact force was obtained for SANS 1016-6:2010. Also it must be noted that for SABS 0160:1989, the kinetic energy obtained for an impact velocity of 0.6m/s is greater than 340N/m. Thus no end stop impact force was obtained at this velocity. Figure 5.5.2 shows the comparison made between the codified end stop impact forces and the constraint optimization impact force for three levels of reliability.

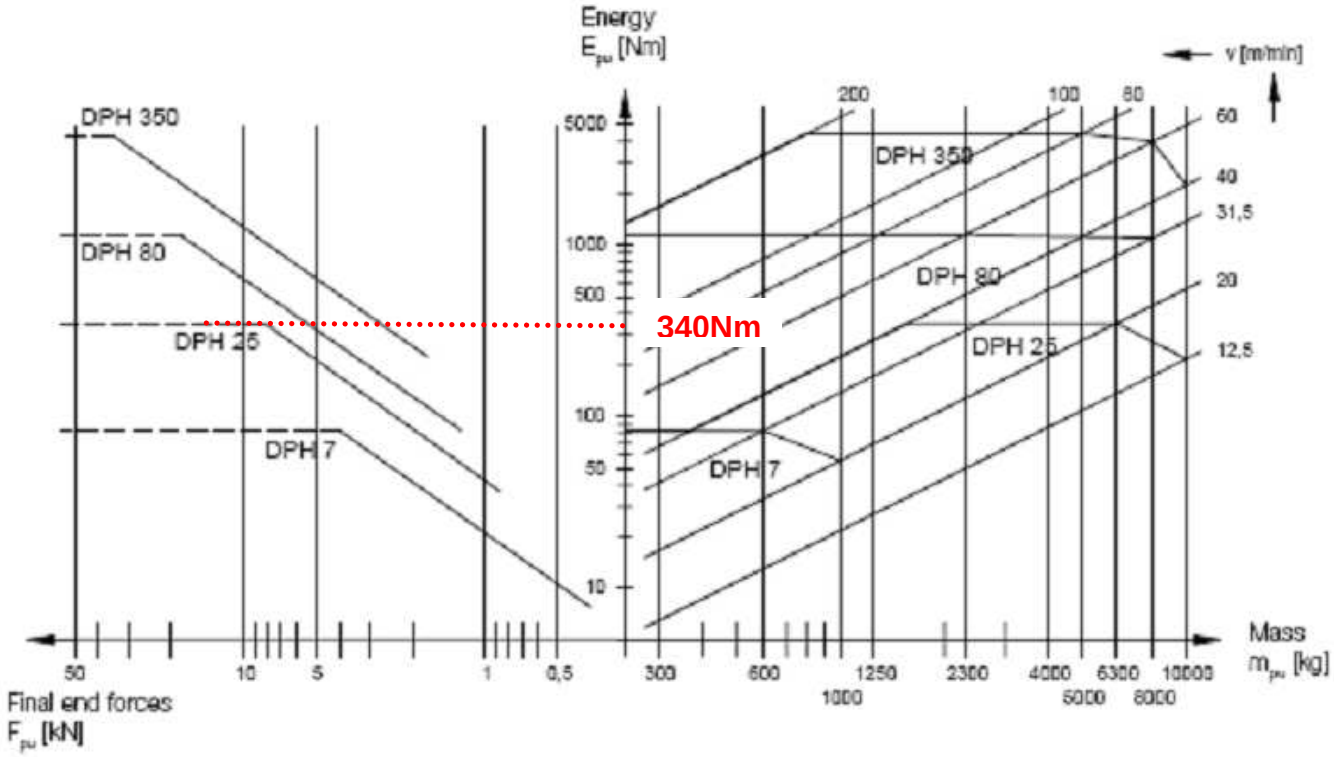

Figure 5.5.1 DEMAG'S hydraulic buffer selection graph

Table 5.5.1 Estimation of the end stop impact force per end stop according to DEMAG

DEMAG	Velocity (m/s)	E_{PU} = MV²/9965 (N/m)	Force (kN)
Mass= 2233kg	0.3	73	2.2
	0.4	129	3.3
	0.5	202	4.1
	0.55	244	5.3
	0.6	290	6.1

Table 5.5.2 Estimation of the end stop impact force per end stop according to SABS 0160:1989

SABS 0160:1989 (method a)	Force = mass x 9.81			Impact Force= 21.9kN
SABS 0160:1989 (method b) Mass = 2233kg	Velocity(m/s)	E_{PU} = MV²/7200 (N/m)	Force (kN)	Lesser of method (a) & (b)
	0.3	100	2.9	2.9
	0.4	179	5.0	5.0
	0.5	279	6.1	6.1
	0.55	337	7.4	7.4
	0.6	402 >> $E_{PU\ ALL}$	NA	NA
For the SABS 1989, use the lesser value between the two methods				

To compare the codified end stop impact forces obtained with that of the FEA end stop impact force, the FEA maximum impact force obtained is superimposed on the codified impact forces. This is presented in Figure 5.5.2.

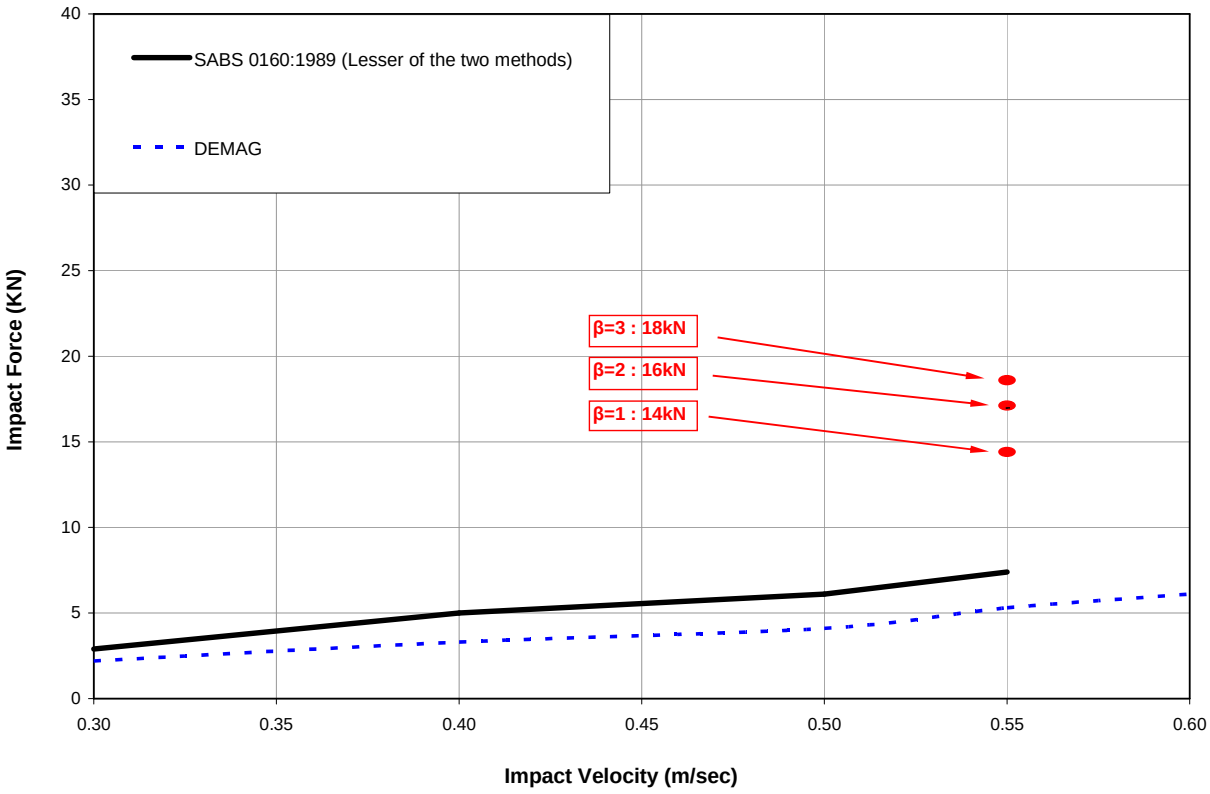

Figure 5.5.2 Codified and Constraint Optimization Impact Force for the Single Bridge EOHTC Fitted with Hydraulic Buffers

CHAPTER 6: DISCUSSIONS, CONCLUSIONS AND RECOMMENDATIONS

6.1 Discussions and conclusions

The purpose of this investigation was to estimate the maximum end stop impact force for an electric over head travelling crane (EOHTC) fitted with hydraulic buffers. Also this research investigated the influence of the stiffness of the EOHTC on the end stop impact force. Literature reviewed reveal that several factors influence the end stop impact force. In the course of this research, the parameters identified were used to determine its effect on the end stop impact force. Also, during the investigation more parameters were identified. This section deals with the summary of some pertinent facts identified in the course of this investigation.

6.1.1 Crane Bridge's Stiffness

The South African loading code SANS 10160 assumes that the crane acts as a rigid body; hence it estimates the end stop impact force using rigid body mechanics, McKenzie, (2007). From the experimental and the FEA simulations conducted in this investigation, it was observed this is not absolutely correct. The results obtained from the FEA simulations reveals that the behaviour of the EOHTC is largely dependent on the stiffness of the crane bridge and the end carriages. This was particularly exhibited in the simulations conducted to investigate the effect of the end stop misalignment and crab eccentricity on impact force histories. For these two cases, it was discovered that at impact, both the crane bridges and the end carriages are capable of undergoing lateral deformation and significant skewing depending on the EOHTC flexibility.

McKenzie, in her investigation on the simulation of wheel load on the EOHTC, conducted numerical simulations on a single bridge EOHTC to determine how it skews under different load cases. One of the load cases considered for the situation is the failure of one of the electric motors. For this condition, the torque was disengaged from the eastern wheels (eastern wheels are represented in Figure 6.1.1.1). This load case yields a scenario where impact occurs first at the end stop with the running motors. This is a replica of the situation of the end stop misalignment considered in this investigation. The result from this load case revealed that both the crane bridges and the end carriages skewed in the course of crane operation. Figure 6.1.1.1 gives a representation of the skewed crane for this load case. It can be seen from Figure 6.1.1.1 that both the crane bridge and end carriages skewed significantly. In the course of this investigation, FEA simulations were conducted on a double bridge EOHTC for a load case where one end stop was misaligned. Figures 6.1.1.2 and 6.1.1.3 show the lateral deflection of the wheels at impact for the double bridge EOHTC and the single bridge EOHTC respectively. These figures represent the condition where the LHS

(western) end stop was misaligned by 50mm. The misalignment is in opposite direction of travel of the crane .That is, the western end stop is 50mm closer to the EOHTC at any point in time. The layout of this misalignment is presented in Figure 3.3.2.1 of chapter 3 of this document. It can be seen from Figures 6.1.1.2 and 6.1.1.3 that the wheels skewed through a wider distance for the single bridge EOHTC than for the double bridge EOHTC. For the double bridge EOHTC, the crane bridge and end carriages were prevented from bowing thus preventing significant skewing to occur at impact. This prevented the EOHTC from significantly compressing the RHS buffer at impact, while the LHS buffer (buffer at the misaligned end stop) is left to absorb a larger percentage of the impacting mass. Figure 6.1.1.4 shows the compression of buffers at impact for the double and single bridge EOHTC. It can be seen that, for the double bridge EOHTC, the RHS buffer was hardly compressed at impact. While for the single bridge EOHTC, both buffers compressed significantly.

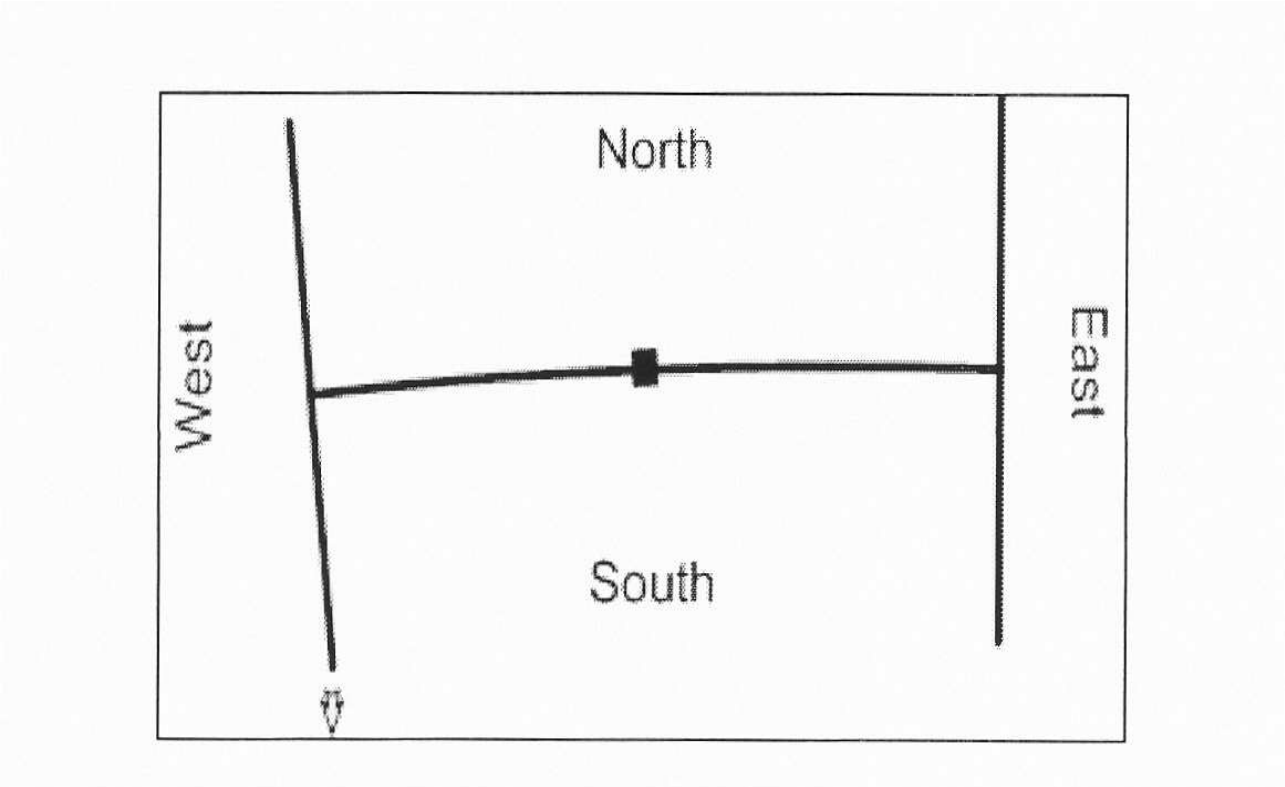

Figure 6.1.1.1 Flexing of the crane bridge and end carriages due to skewing: Load case_ Failure of one of the motors. (McKenzie 2007)

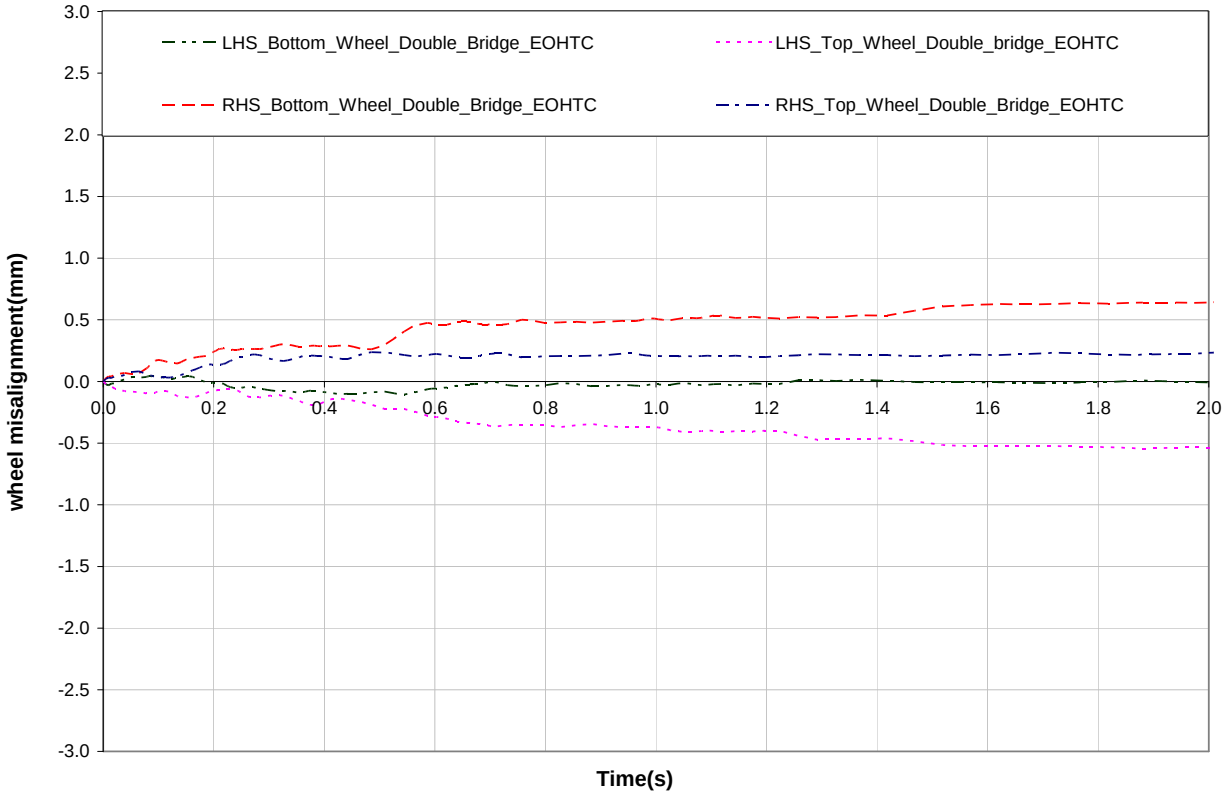

Figure 6.1.1.2 Lateral wheel displacement history at impact for the “Double Bridge EOHTC”

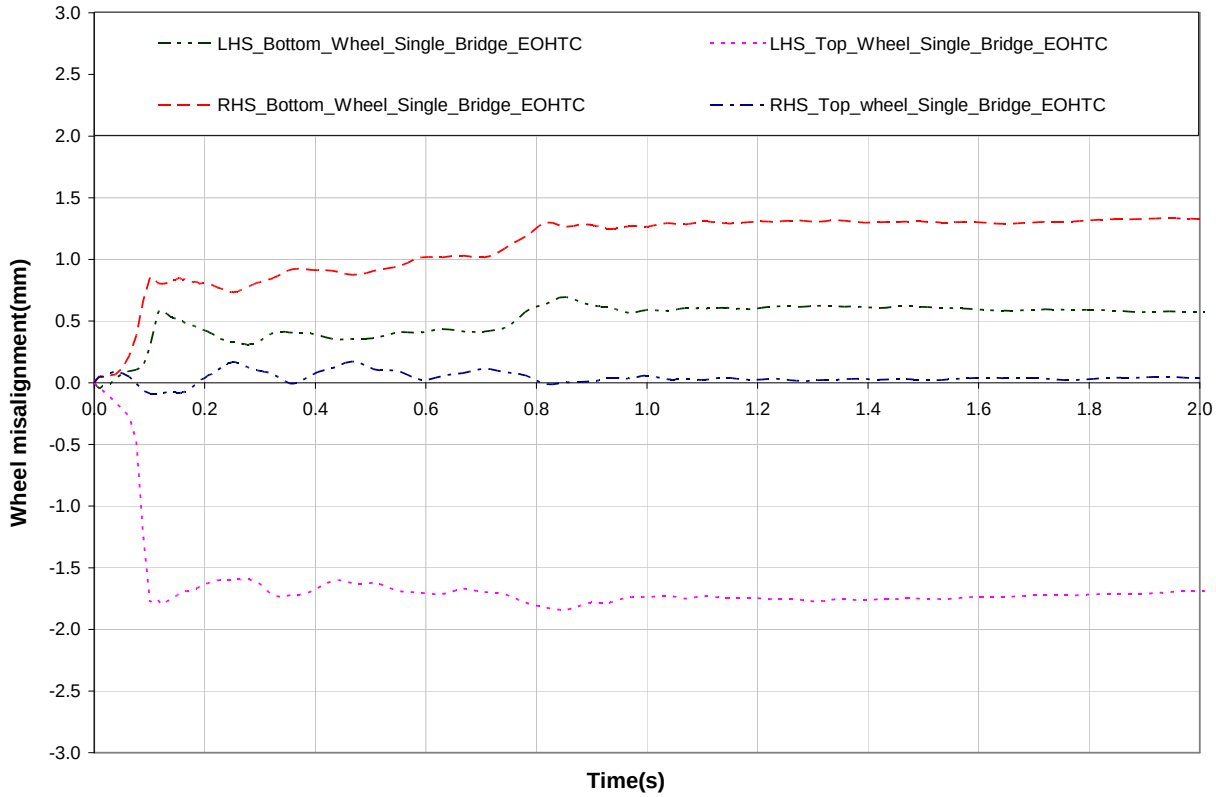

Figure 6.1.1.3 Lateral wheel displacement history at impact for the “Single Bridge EOHTC”

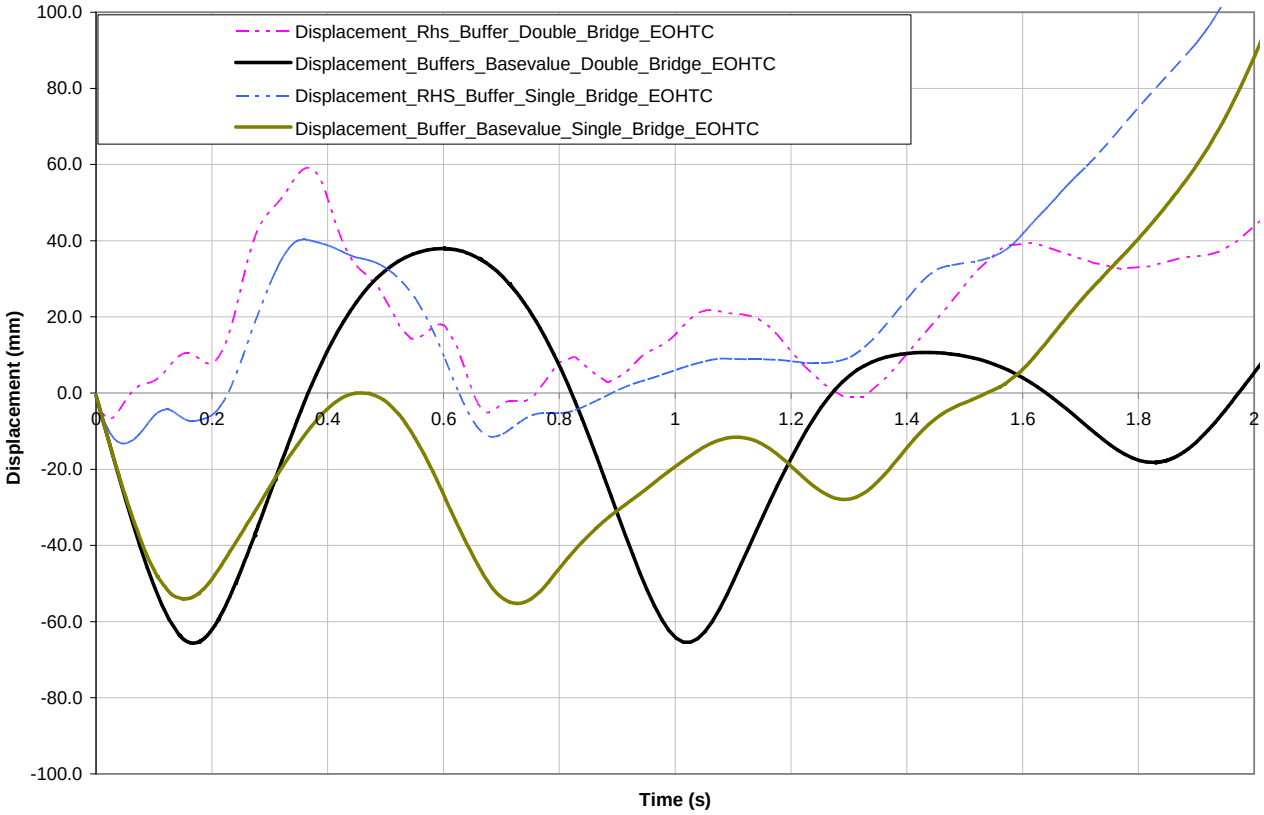

Figure 6.1.1.4 Displacement of the buffers at impact for a 50mm misalignment of the LHS end stop .

Another load cases considered by McKenzie is for the situation of skewing induced by an eccentric payload. From this load case, she identified that in response to the skewing induced by the eccentric payload, to maintain equilibrium, both the crane bridge and the end carriages flexed throughout the crane travel. FEA simulations were conducted on the double bridge EOHTC for the same load case. From the results obtained from this simulation, it was observed that both the crane bridges and the end carriage were prevented from undergoing significant skewing which the eccentric payload would have induced. The impact histories obtained for this load case presented in section 3.3.3 shows that the crab and payload eccentricity has a greater influence on the single bridge EOHTC than for the double crane bridge EOHTC.

The skewing observed from the two aforementioned load cases is largely dependent on the stiffness of the crane bridge and end carriages. It can therefore be concluded that the stiffness of the crane bridge and the end carriages have a significant influence on the end stop impact force history. Hence the concept of rigid body mechanics is not accurate for all load cases.

6.1.2 Buffer's Force displacement Function

The force displacement function of a buffer determines its response under impact force. Different buffers have different force displacement function and thus varying responses to impact.

Literature reviewed reveals that elastomeric buffers have non- linear force displacement curve. Figure 6.1.2.1 shows a representation of the force displacement curve of the elastomeric buffers obtained from impact tests. The non-linearity of the elastomeric buffer implies that variation in the impacting mass will yield a non-linear trend.

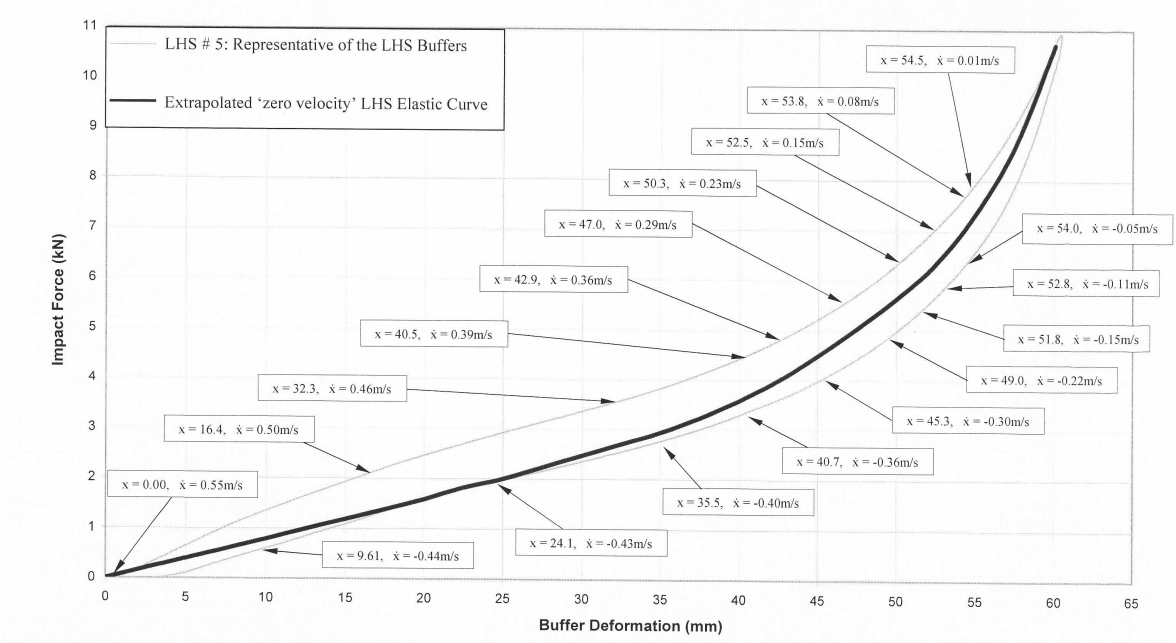

Figure 6.1.2.1 A representation of the force displacement curve of the elastomeric buffers obtained from impact test. (Haas, 2007)

In the course of the investigation, the force displacement curve for hydraulic buffers for a non constant strain was obtained from impact test on the crane. The result obtained is presented in Figure 6.1.2.2. The result presented shows that the buffers deformed by only 13mm at a non constant strain. Due to the deceleration rate of the buffers, the result for higher deformation could not be obtained from the impact test. This made it difficult to accurately estimate the force displacement function of the hydraulic buffers. However, for the fraction of the buffers compressed under impact, the result shows that the hydraulic buffer investigated has a linear force trend until a maximum impact force of 10.4kN was obtained, after which the force reduces gradually to zero.

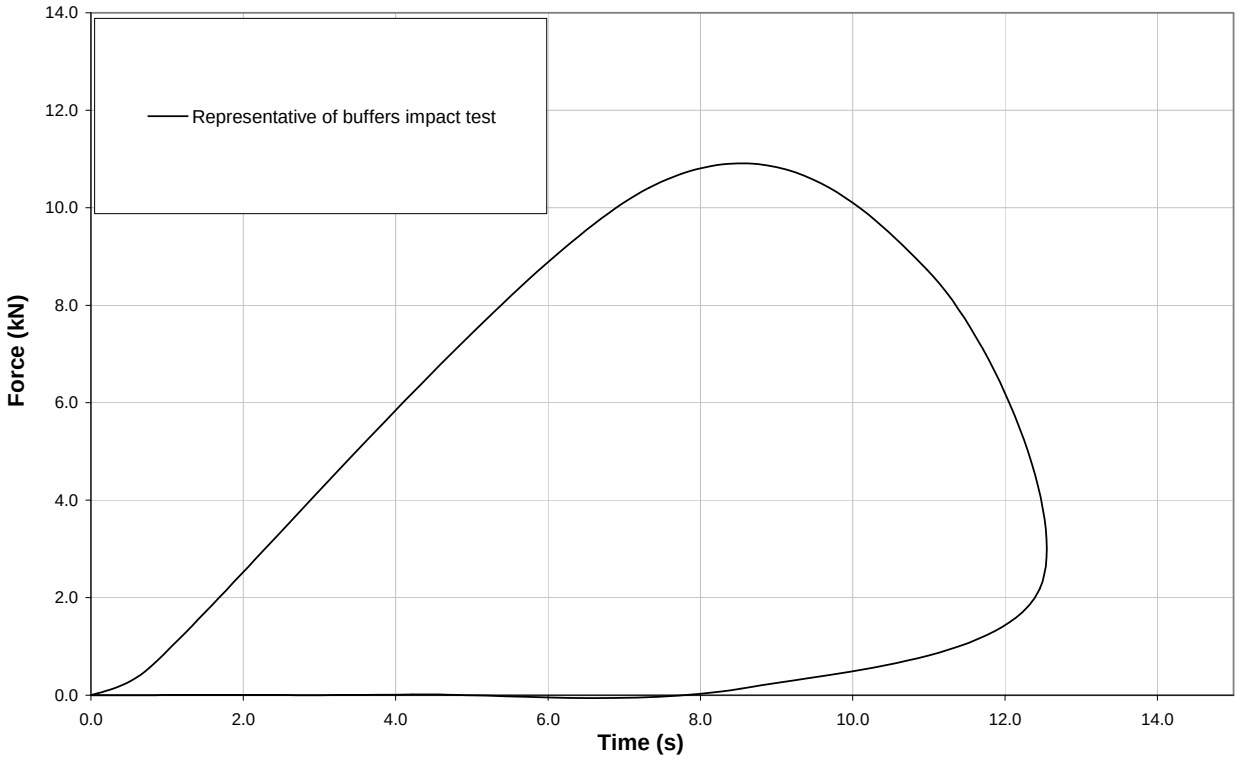

Figure 6.1.2.2 A representation of the force displacement curve of the hydraulic buffers obtained from impact test

6.1.3 Viscosity of the Hydraulic Fluid

In chapter 4, it was discovered that the capacity of the hydraulic buffer is dependent on the viscosity of the hydraulic fluid in the buffers. DEMAG's catalogue reveals that a Newtonian fluid was used for the manufacturing of the DEMAG DPH 25 hydraulic buffer. Experimental test results revealed that at high viscosity, the capacity of the hydraulic buffer is greatly increased. The viscosity of a Newtonian fluid reduces with high temperature. This implies that the buffer's damping capacity reduces with an increase in the temperature of the hydraulic fluid. Figure 6.1.3.1 shows a representation of the buffers damping capacity under repetitive loading. From these tests, it was impossible to accurately determine the time it takes for the hydraulic fluid in the buffer to cool down. The notable observation made from this result is that the full capacity of the hydraulic buffers is not fully utilised when the viscosity of the fluid is low. Hence this investigation reveals that the hydraulic buffer's capacity is greatly influenced by the viscosity of the hydraulic fluid.

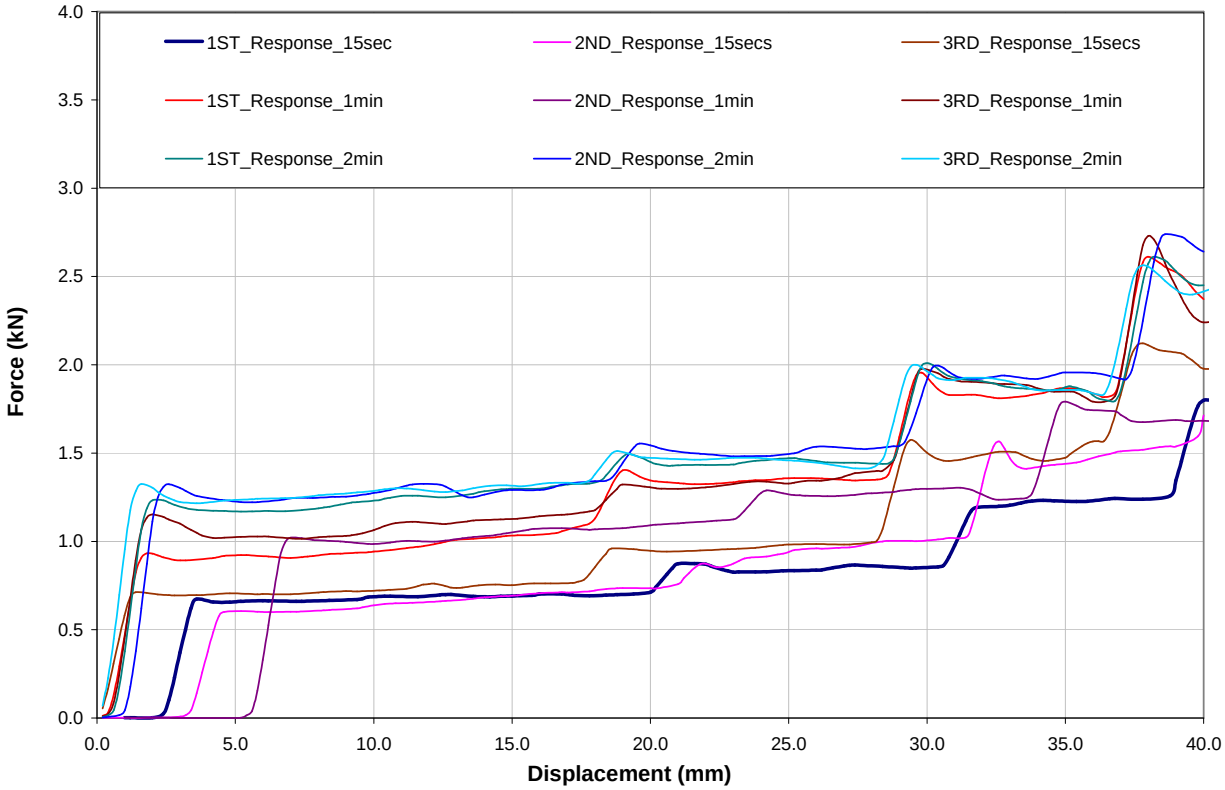

Figure 6.1.3.1 A representation of the damping capacity of the DEMAG DPH hydraulic buffer.

6.1.4 Comparison of the Results Obtained from the Constraint Optimization Technique and the Codified Estimation of the End Stop Impact Force.

Using a constraint optimization technique, the maximum end stop impact force was obtained from the FEA impact histories for the double bridge EOHTC fitted with elastomeric buffers and for the single bridge EOHTC fitted with hydraulic buffers. The maximum end stop impact force was calculated for three levels of reliability. Also, the codified estimates of the maximum end stop impact force was obtained for the double bridge EOHTC fitted with elastomeric buffers and for the single bridge EOHTC fitted with hydraulic buffers.

For the double bridge EOHTC fitted with elastomeric buffers, comparison was made between the maximum end stop impact force obtained for this case and the maximum end stop impact force obtained for a single bridge fitted with elastomeric buffers. Figures 6.1.4.1 and 6.1.4.2 presents the comparisons made for the double and the single bridge EOHTC respectively. Figure 6.1.4.1 shows that at a level of reliability β = 3, the maximum end stop impact force of 21kN was obtained for the double bridge EOHTC. Comparing this result with the codified impact forces, the previous loading

code, SABS 0160:1989, estimates the end stop impact force at a velocity of 0.55m/s as 19.5kN. At the same velocity, the current loading code, SANS 10160 estimates the end stop impact force as 35kN. This reveals that SABS 0160:1989 underestimates end stop impact force by 7% while SANS 10160 overestimates end stop impact force by 67%

For the single bridge EOHTC fitted with elastomeric buffers, an end stop impact force of 14.54kN was obtained for a level of reliability of $\beta = 3$. SABS 0160:1989 estimates end stop impact force as 12kN while SANS 10160 estimates end stop impact force as 23.9kN.

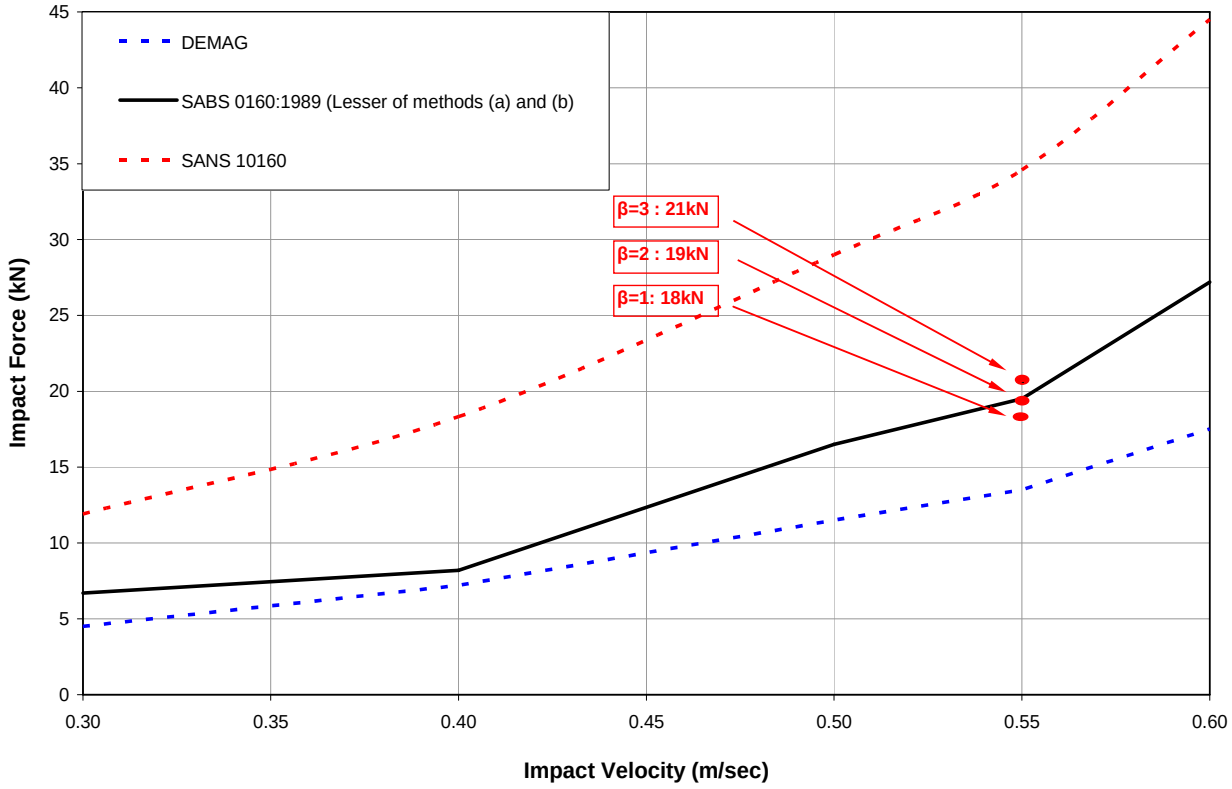

Figure 6.1.4.1 Comparison of the Codified and Constraint Optimization Impact Forces for the Double Bridge EOHTC fitted with Elastomeric Buffer

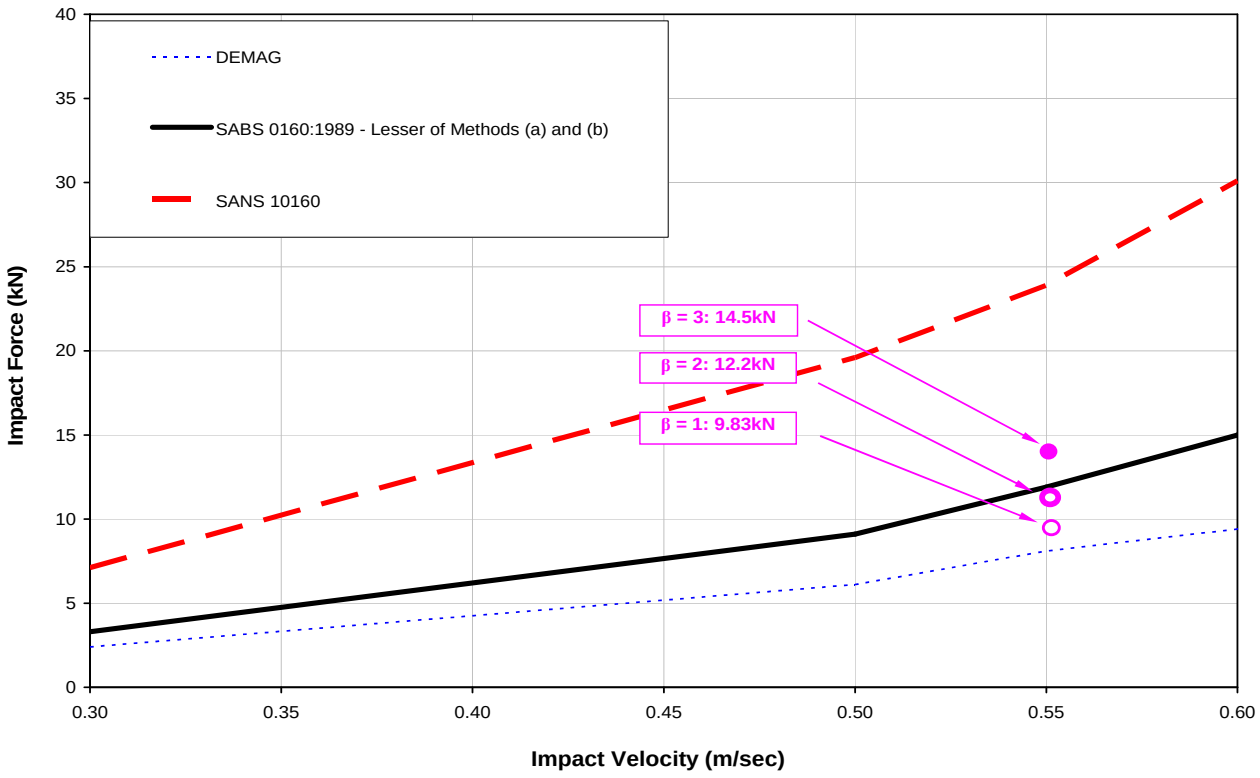

.

Figure 6.1.4.2 Comparison of the Codified and Constraint Optimization Impact Forces for the Single Bridge EOHTC fitted with Elastomeric Buffers.

For the single bridge EOHTC fitted with the hydraulic buffers, the kinetic energy obtained from the total mass of the crane and payload at an impact velocity 0.55m/s is greater than the maximum kinetic energy the buffer can absorb as specified by the manufacturer. Figure 6.1.4.3 shows that, the DPH 25 hydraulic buffer is insufficient to absorb a kinetic energy greater than 340N/m. Also, the South African loading code SANS 10160, state that the kinetic energy obtained from the total mass of the crane and payload should be used in determining the impact force. However, unlike the previous loading code, the current loading code does not explicitly state if the impact force obtained is for one of the end stops or for both end stops. The high kinetic energy obtained from the total mass considered made it impossible to obtain the end stop impact force for SANS 10160. In other words, according to the guidelines given by the current loading code SAN 10160-6:2010, the DPH 25 hydraulic buffer is insufficient to absorb the impact force for the 5-Ton single bridge EOHTC considered in this investigation. SABS 0160:1989, and DEMAG considers only the mass of the crane in estimating the kinetic energy on each end stop. Hence, it was possible to estimate the end stop impact forces for these codes. It must however be noted that for SABS 0160:1989 , the kinetic energy obtained for an impact velocity of 0.6m/s is greater than 340N/m. Thus no end stop impact force was obtained for this velocity. Figure 6.1.4.4 shows the comparison made between the codified results and the constraint optimization result. From the result presented, for a level of reliability

β = 3, SABS 0160:1989 underestimates impact force by 60% and DEMAG underestimates end stop impact force by 73%. No further comparison could be made.

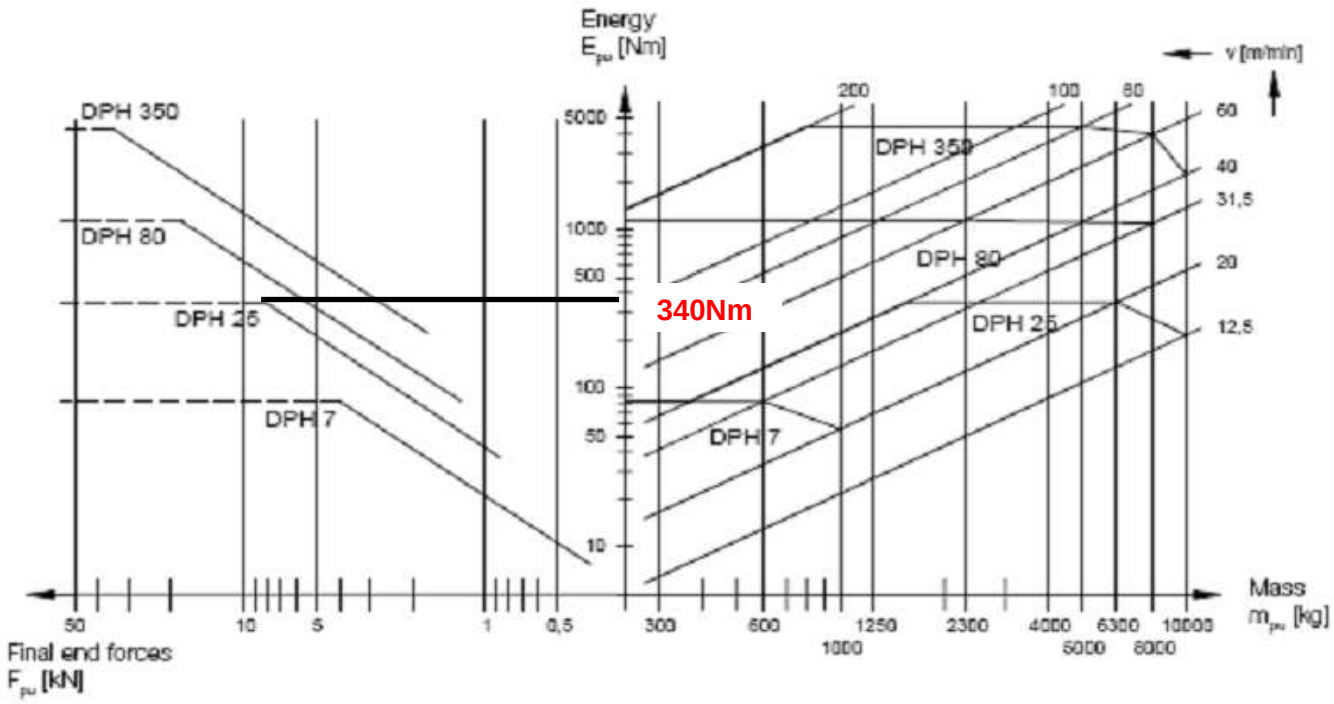

Figure 6.1.4.3 DEMAG'S Information on Hydraulic buffers

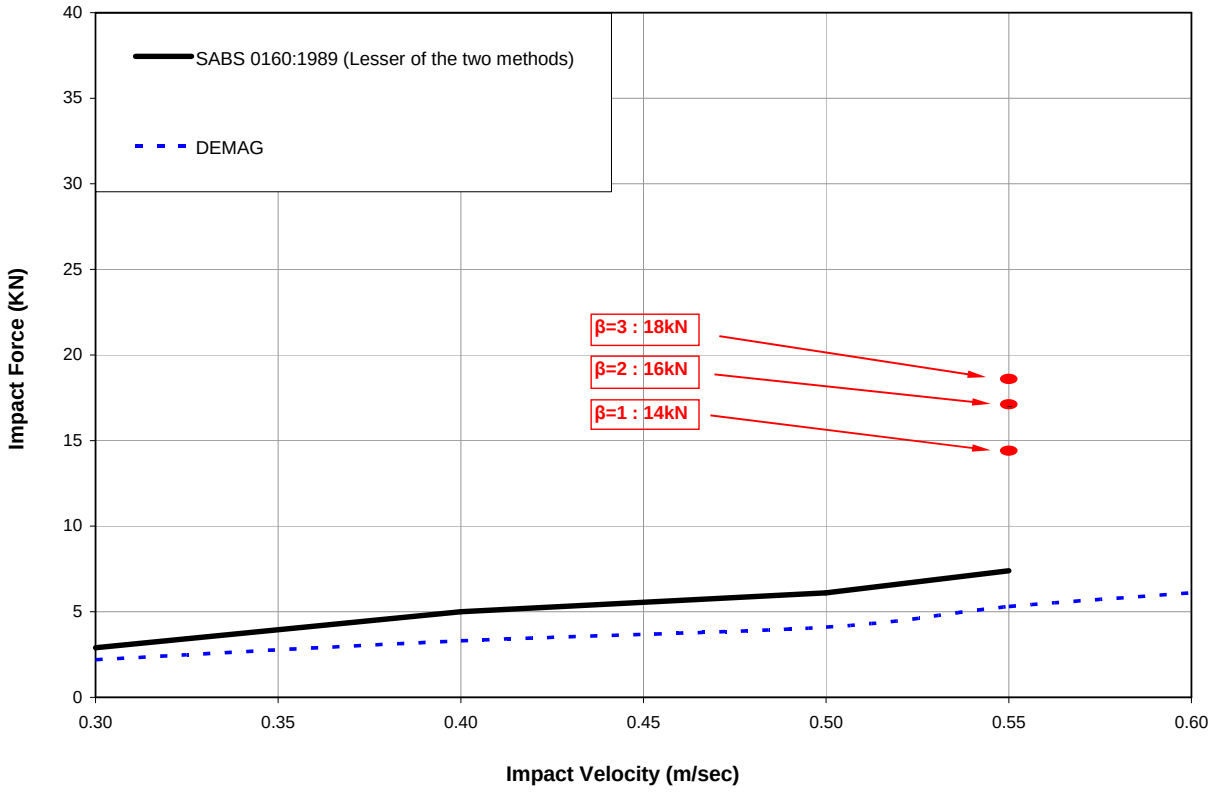

Figure 6.1.4.4 Comparison of the Codified and Constraint Optimization Impact Force for the Single Bridge EOHTC fitted with Hydraulic Buffers.

6.2 Recommendations.

In the course of this investigation, certain parameters were identified to significantly influence end stop impact force. However it was impossible to adequately quantify their influence on the end stop impact force. Hence, it is recommended that such observations should be investigated and clarified with further research. In view of this, the following areas are recommended for further clarifications.

- Numerical estimation of end stop impact force for an EOHTC fitted with hydraulic buffers for different masses of EOHTC. For this investigation, the mass of the EOHTC should be added as a parameter in the constraint optimization technique to obtain the maximum end stop impact force.

- Investigation into the temperature gradient of the hydraulic oil in the hydraulic buffer. For this investigation, the temperature gradient of the hydraulic fluid should be obtained experimentally and the hydraulic buffers should be modelled using temperature dependent data (non-isothermal spring).

REFERENCES:

I. Abaqus, www.abaqus.com

II. De Lange, J.H., (2007), "*An Experimental Investigation into the Behaviour of a 5-ton Electric Overhead Travelling Crane and its Supporting Structures",* Master's Degree Thesis, Department of Civil Engineering, University of Stellenbosch.

III. Demag DRS Wheel Block System's Catalogue, www.demag.com

IV. Dymond, J.S., (2005), *"Reliability Based Codification for the Design of Overhead Travelling Cranes and its Supporting Structures",* Doctorate Degree Dissertation, Department of Civil Engineering, University of Stellenbosch.

V. Haas, T.N., (2007), "*Numerical (FEA) Evaluation of Crane End Buffer Impact Forces",* Doctorate Degree Dissertation, Department of Civil Engineering, University of Stellenbosch.

VI. Kit, P.G., (1996), "*Hydraulic Buffers for the Protection of Buildings, Cranes and Operators from Impact Damage",* A Paper Presentation at the Convention of Association of Iron and Steel Engineers.

VII. Kohlhass, S., (2004), *"Impact Forces on End stops for Overhead Travelling Cranes and Supporting Structures",* Research Report, University of Stellenbosch

VIII. McKenzie, K., (2007), *"The Numerical Simulations of Wheel Loads on Electric Overhead Travelling Crane Supporting Structure"* Master's Degree Thesis, Department of Civil Engineering, University of Stellenbosch.

IX. Oguamanam, D.C.D., (2001), *"Dynamics of a Three-Dimensional Overhead Cranes System",* Journal of Sound and Vibration

X. Perez-Winkler, A.R., (2003), *"An investigation of Overhead Crane Wheel/ rail/ Girder Interaction*", Master's Degree Thesis, Departmental of Civil Engineering, University of Stellenbosch.

XI PDH course content, www.PDHcenter,com

XII South African Institute of steel Construction Handbook.

XIII SABS 0160:1989 (As amended 1990), “South Africa Standard: *Code of practice: The general procedure and Loadings to Be Applied In the Design Of Buildings”,* The council of the South African Bureau of Standards, Pretoria, 1990.

XIV SANS 10160-6:2010 “South Africa National Standards 10160: *Basis of Structural Design and actions for Building and Industrial structures, Section 6, Action Induced by Cranes and Machineries.*

XV Taylor device inc. “History Design and Application of Fluid Dampers in Structural Engineering”